DISSERTATION

THEORIES AND SIMULATIONS OF POLYMERS USING COARSE-GRAINED MODELS

Submitted by

Delian Yang

Department of Chemical and Biological Engineering

In partial fulfillment of the requirements

For the Degree of Doctor of Philosophy

Colorado State University

Fort Collins, Colorado

Fall 2014

Doctoral Committee:

Advisor: David (Qiang) Wang

Travis S. Bailey
Ashok Prasad
Grzegorz Szamel

ABSTRACT

THEORIES AND SIMULATIONS OF POLYMERS USING COARSE-GRAINED MODELS

Full atomistic simulations of many-chain systems such as polymer melts are not feasible at present due to their formidable computational requirements. Molecular simulations with coarse-grained (CG) models have to be used instead, which interact with soft potentials that allow complete particle overlapping. One advantage of soft potentials is that it allows to simulate systems with experimentally accessible fluctuations and correlations because the invariant degree of polymerization $\bar{\mathcal{N}}$ (controlling the system fluctuations and correlations) and the polymer chain length N are decoupled using soft potentials. Another advantage is that it provides a powerful means for unambiguously and quantitatively revealing the effects of fluctuations and correlations of polymers when comparing simulation results with corresponding theoretical predictions based on the same model systems thus without any parameter fitting.

Using the recently proposed fast lattice Monte Carlo (FLMC) simulations and the corresponding lattice self-consistent field (LSCF) calculations based on the same model system, where multiple occupancy of lattice sites is allowed, we studied the coil-globule transition (CGT) of one-mushroom polymeric systems and the fused-separated transition (FST) of two-mushroom polymeric systems. With soft potential, we systematically constructed the phase diagrams of one- and two-mushroom systems using LSCF theory, which neglects the interchain fluctuations and correlations. The LSCF predictions were then directly compared with the simulation results without any parameter-fitting, the fluctuation/correlation effects on these phase transitions are then unambiguously quantified.

Similarly, for disordered symmetric diblock copolymers in continuum, we directly compared the thermodynamic and structural properties from fast off-lattice Monte Carlo simulations, integral equation (IE) theories (including the reference interaction site model and polymer reference interaction site model), and Gaussian fluctuation theory based on the same model systems, and unambiguously quantified the consequences of various theoretical approximations and the validity of these theories in describing the fluctuations/correlations in disordered diblock copolymers.

In order to answer the questions of how to obtain the CG model and how the CG level affects the properties of CG model, we then performed systematic and simulation-free coarse graining of homopolymer melts. In this work, we proposed a systematic and simulation-free strategy for structure-based coarse graining of homopolymer melts, where each chain of N_m monomers is uniformly divided into N segments, with the spatial position of each segment corresponding to the center-of-mass of its monomers. We used integral-equation theories, instead of molecular simulations, to obtain the structural and thermodynamic properties of both original and CG systems, and quantitatively examined how the effective pair potentials between CG segments and the thermodynamic properties of CG systems vary with N. Our coarse-graining strategy is much faster than those using molecular simulations and provides the quantitative basis for choosing the appropriate N-values. Taking the simple hard-core Gaussian thread model (K. S. Schweizer and J. G. Curro, Chem. Phys. **149**, 105 (1990)) as the original system, we demonstrated our strategy and compared in detail the various integral-equation theories and closures for coarse graining. Our numerical results showed that the effective CG potentials using various closures can be collapsed approximately onto the same curve for different N, and that structure-based coarse graining cannot give the thermodynamic consistency between original and CG systems at any $N < N_m$.

The CG potential from structure-based coarse graining can further be used to parameterize CG potentials with a given analytic functional form containing finite number of

parameters, which is much more convenient to use in molecular simulations than the numerically tabulated CG potentials from structure-based coarse graining. In this work, we applied our systematic and simulation-free strategy to the recently proposed relative-entropy-based coarse graining, which minimizes the information loss quantified by the relative entropy. The values of relative entropy obtained from relative-entropy-based coarse graining with different CG potential functional forms can further be compared to determine the appropriate functional form or number of parameters.

Note that the ideal-chain conformations were used in both structure-based and relative-entropy-based coarse-graining strategies, which is not valid for systems with strong pair interactions or small $\bar{\mathcal{N}}$, self-consistent integral equation theory can be used to obtain more accurate intrachain pair correlations. In order to improve the quality of coarse graining, our proposed systematic and simulation-free coarse-graining strategy can be further combined with the self-consistent integral equation theory. This work will be remained for future researchers.

ACKNOWLEDGEMENTS

I would like to first express my deepest appreciation to my advisor, Professor David (Qiang) Wang, for his outstanding guidance and providing me with an excellent atmosphere for doing research. With his guidance in my research activities, such as theory derivations and understanding, paper writing, presentations, and computer programming, I have gradually developed a deep understanding of the nature of science and engineering, and the efficient ways to address a problem. In one word, he totally changed my original scientific research world and leads to my future success.

Second, my deepest gratitude is extended to my committee members: Professor Travis S. Bailey, Professor Ashok Prasad, and Professor Grzegorz Szamel. They also helped me to broaden my perspective on both theories and applications of engineering and applied physics.

I would also thank my fellow group members, Dr. Xinghua Zhang, Dr. Pengfei Zhang, and Mr. Jing Zong for their kind help of both theoretical calculations and simulations during my PhD study. The help from all the stuff and colleagues of Chemical and Biological Engineering Department is also deeply appreciated.

Financial support for this work was provided by NSF CAREER Award CBET-0847016 and Department of Energy Award DE-FG02-07ER46448, which are gratefully acknowledged.

TABLE OF CONTENTS

LIST OF FIGURES

CHAPTER 1

INTRODUCTION

1.1 Advantages of Coarse-Grained Model Using Soft Potentials

Full atomistic simulations of many-chain systems such as polymer melts are not feasible at present due to their formidable computational requirements. Molecular simulations with coarse-grained (CG) models where each segment represents, for example, the center-of-mass of a group of atoms/monomers, have to be used instead. While atoms interact with hard excluded-volume interactions (e.g., the Lennard-Jones (LJ) potential) and cannot overlap, at high levels of coarse graining the segments can certainly overlap and should therefore interact with soft potentials that allow complete particle overlapping. For example, Grosberg et al. first showed that the effective interaction potential between two polymer coils with (hard) excluded volume in a dilute solution is finite (i.e., on the order of k_BT with k_B being the Boltzmann constant and T the thermodynamic temperature), even when their centers-of-mass completely overlap.[1]

A less intuitive reason for using soft potentials is the following: The fluctuations of polymeric systems are mainly controlled by the invariant degree of polymerization defined as $\bar{\mathcal{N}} \equiv (nR_{e,0}^3/V)^2$ for chains each of N_m monomers of size b, where n denotes the number of chains in volume V and $R_{e,0} \sim \sqrt{N_m}b$ is the root-mean-square end-to-end distance of an ideal chain. For dense polymeric systems such as concentrated polymer solutions or melts with hard excluded-volume interactions, $V \sim nN_mb^3$; $\bar{\mathcal{N}}$ is therefore on the same order of magnitude as N_m, which has typical experimental values of $\gtrsim 10^3$. In most molecular simulations of many-chain systems using CG models with hard excluded-volume interactions (e.g., the bead-spring model[2] or the self- and mutual-avoiding walk (SMAW) on a lattice), the number

of segments N on each chain (or $\bar{\mathcal{N}}$) is $\lesssim 10^2$, which means that the fluctuations studied in such conventional molecular simulations are not in the experimentally accessible range in most cases; in other words, by reducing N_m to N, CG models with hard excluded-volume interactions exaggerate the system fluctuations. With soft potentials, however, $\bar{\mathcal{N}}$ and N are decoupled; one can therefore simulate systems with experimentally accessible fluctuations (i.e., with $\bar{\mathcal{N}} \gtrsim 10^3$),[3] while N becomes a chain discretization parameter that does not correspond to the actual chain length used in experiments; in other words, systematic coarse graining with different N can be done at constant $\bar{\mathcal{N}}$. This point is crucial for understanding CG models with soft potentials.

Using the CG models with soft potentials, Wang recently proposed the fast lattice Monte Carlo (FLMC) simulation,[4] where multiple occupancy of lattice sites (MOLS) is allowed in contrast to SMAW used in conventional lattice Monte Carlo (MC) simulations. As explained in Ref. [4], FLMC simulation has great advantages over conventional molecular simulations with hard excluded-volume interactions in the study of equilibrium properties of soft matter such as polymers. For example, it provides a powerful means for unambiguously and quantitatively revealing the effects of fluctuations and correlations by comparing simulation results with the corresponding lattice field theories, such as the lattice self-consistent field (LSCF) theory and lattice Gaussian fluctuation (LGF) theory, based on the same model system. This has been demonstrated in a series of studies of Wang and coworkers on the structural and thermodynamic properties of compressible homopolymer melts in either bulk[5] or thin film[4,6] and those of grafted homopolymers in an either implicit[7] or explicit[8,9] solvent, where no phase transition occurs.

In Chapter 2, we therefore quantify the effects of fluctuations and correlations on phase transitions, taking (homo)polymer mushrooms in a poor solvent as our model systems, which undergoes the coil-globule transition as the solvent quality varies.[10,11] In this work, based on our CG lattice model with MOLS, we systematically construct the phase diagrams of one-mushroom systems as a function of the average polymer volume fraction $\bar{\phi}_{\mathrm{A}}$ and the

Flory-Huggins interaction parameter χ between polymer segments and solvent molecules. While one expects that the simulation results approach the LSCF predictions with increasing average segment number density ρ_0, contradiction to this expectation leads us to the discovery of a second-order symmetric-asymmetric transition (SAT) in polymer mushrooms in a poor solvent (i.e., in the globule state), which, to the best of our knowledge, has not been reported in the literature. Once we understand the behaviors of one mushroom, we then systematically construct the phase diagrams of two-mushroom systems, which undergoes fused-separated transition (FST) with varying solvent quality, as a function of $\bar{\phi}_{\rm A}$, χ, and the grafting distance d using LSCF calculations. We further investigate the coupling of FST with CGT and SAT of each mushroom, and unambiguously quantify the fluctuation/correlation (F/C) effects on FST.

The above study on F/C effects of one and two mushrooms is performed on a lattice, in Chapter 3 we then examine the F/C effects of disordered symmetric diblock copolymers in continuum. In a recent paper of our group,[12] the authors systematically quantified the F/C effects on the ordered-disordered transition (ODT) of compressible symmetric DBC with soft potential in the experimentally acceptable $\bar{\mathcal{N}}$ range by comparing the results of fast off-lattice Monte Carlo (FOMC) simulations[13] and random phase approximation (RPA)[14] based on the same Hamiltonian. In Chapter 3 of this report, the F/C effects in disordered phase will be unambiguously quantified based on the same model system, by comparing the thermodynamic and structural properties obtained from FOMC simulations and various theories, including self-consistent field (SCF) theory,[15] Gaussian fluctuation (GF) theory,[15] and integral equation theories (i.e., the reference interaction site model (RISM)[16–19] and polymer reference interaction site model (PRISM)[20–22]). The compared quantities include the internal energy, entropy, Helmholtz free energy, pressure, constant-volume heat capacity, chain/block dimensions, and various structure factors and correlation functions in the system.

1.2 Systematic Coarse Graining Using Integral Equation Theories

While the CG model with soft potentials has great advantages as explained above, there are still some open questions, such as how to obtain the CG model and how the CG level affects the properties of CG model. There are various levels at which a polymer chain with full atomistic (chemical) details can be coarse-grained: The lowest level is probably the united-atom (UA) model, interacting via bonding, bending, torsion-angle, and non-bonded (typically LJ) potentials. The highest level is to represent each chain by a single soft particle, as done for example by Grosberg et al.[1] Coarse-grained models at intermediate levels are also widely used, such as the bead-spring model proposed by Grest and Kremer,[2] where polymer segments (beads) interact only via bonding (finitely extendable nonlinear elastic) and non-bonded (truncated and shifted purely repulsive LJ) interactions.[1]

For a given original system, an issue to be addressed in systematic coarse graining is therefore how the interaction potentials and the properties of CG models vary with the CG level $l = N_m/N$. On the other hand, due to its reduced degrees of freedom (thus chain conformational entropy), a CG model cannot exactly reproduce the original system in all aspects. In order to choose the appropriate CG level, it is therefore necessary to quantify how well the structural, thermodynamic and dynamic properties of the original system are reproduced by CG models with different CG levels. In spite of the numerous papers on coarse graining of polymeric systems, such systematic coarse graining has rarely been done, especially for polymer melts. Ashbaugh et al applied a coarse-graining method that matches the structural correlations between an original system and CG models with $l = 4 \sim 96$, and examined the effects of l on the structural correlations.[23] Similar work was done by Chen et al.[24] They both found that, for $l \gtrsim 16$, soft potentials naturally arise from coarse graining and the segments can completely overlap.

On the other hand, in most work on coarse graining, molecular simulations (i.e., molecular dynamics or Monte Carlo simulations) are used to obtain the structural and/or thermodynamic properties of both original and CG systems that need to be matched. This is computationally very expensive, particularly for original systems with large N_m ($\gtrsim 100$). Practical use of this kind of coarse-graining strategies is further defeated by the well-known problem of transferability (i.e., the CG pair potentials determined at one set of thermodynamic conditions cannot be transferred to another set of conditions because they are state-dependent).[25] In Chapter 4, we therefore propose the simulation-free strategy of systematic coarse graining: we use integral equation theories,[16,22] instead of molecular simulations, to obtain the structural and thermodynamic properties of both original and CG systems. Here we perform structure-based coarse graining for an original model system with continuous Gaussian chains (CGC) and δ-function potential,[26] where the interchain direct and total correlation functions are obtained by matching their segmental interchain radial distribution functions between the CG and original systems, using the method firstly propose by Krakoviack et al.[27] and further developed by Guenza and coworkers,[28–30] referred to structure-based coarse graining. In this work, we systematically examine the effect of CG level on the CG potential, interchain pressure and internal energy per chain, which provides a quantitative basis for choosing the CG level.

On the other hand, the structure-based coarse graining gives numerical potentials, which is not convenient for further theoretical and simulation studies with CG model. In order to obtain an analytical CG potential independent of segment pairs and to improve the quality of coarse graining, the coarse-graining strategy using a relative entropy framework[31,32] was performed in Chapter 5. In the relative entropy framework, which minimizes the information loss due to coarse graining, the Helmholtz free energy per chain must be calculated, which is usually not easy to obtain in molecular simulations. With integral equation theories, however, it can be readily calculated using the thermodynamic integration. The functional form of pair potential is taken as suggested by our structure-based coarse graining, and its

parameters are obtained by minimizing the relative entropy. This greatly reduces the number of adjustable parameters compared to the structure-based coarse graining. The minimized relative entropy with different CG potential functional forms can further be compared to determine the appropriate functional form or number of parameters. To the best of our knowledge, relative-entropy-based coarse graining has not been applied to polymeric systems.

Finally, in the above structure-based and relative-entropy-based coarse-graining strategies, the use of ideal-chain conformations is an assumption based on the fact that the excluded-volume effects are screened by the surrounding identical chains for large $\bar{\mathcal{N}}$ systems. For systems with strong pair interactions or small $\bar{\mathcal{N}}$, molecular simulations or the self-consistent integral equation (SCIE) theories should be used to obtain more accurate intrachain pair correlations functions.[33–36] This interesting work is remained for *future* researchers to examine the effects of more accurate single-chain structure factor by combining SCIE theories with either structure- or relative-entropy-based coarse graining. In SCIE theories, the intra- and interchain correlation functions are obtained self-consistently by combining P/RISM equation with single-chain simulation in a solvation potential (effectively accounting the interchain correlations), and the so-obtained single-chain conformations are then used in the above coarse-graining procedures.

1.3 List of Publications

In this section, all of the publications (including the unpublished work) in my Ph.D. study are listed in the following.

1. D. Yang, J. Zong, and Q. Wang, "Fluctuation/Correlation Effects in Symmetric Diblock Copolymers: Direct Comparisons between Fast Off-Lattice Monte Carlo Simulations and Integral Equation Theories", J. Chem. Phys., to be submitted.

2. D. Yang and Q. Wang, "Systematic and Simulation-Free Coarse-graining of Homopolymer Melts: A Relative-Entropy-Based Study", J. Chem. Phys., submitted.

3. D. Yang and Q. Wang, "Systematic and Simulation-Free Coarse-graining of Homopolymer Melts: A Structure-Based Study", J. Chem. Phys., submitted.

4. P. Zhang, D. Yang and Q. Wang, "Quantitative Study of the Fluctuation and Correlation Effects in Incompressible Homopolymer Melts", J. Phys. Chem. B, in press.

5. D. Yang and Q. Wang, "Structural and Phase Transitions of One and Two Polymer Mushrooms in Poor Solvent", J. Chem. Phys., **140**, 194902 (2014).

6. D. Yang and Q. Wang, "Unified View on Mean-Field Order of Coil-Globule Transition", ACS Macro Lett. **2**, 952 (2013).

7. P. Sandhu, J. Zong, D. Yang, and Q. Wang, "On the Comparisons Between Dissipative Particle Dynamics Simulations and Self-Consistent Field Calculations of Diblock Copolymer Microphase Separation", J. Chem. Phys. **138**, 194904 (2013).

REFERENCES

[1] A. Yu. Grosberg, P. G. Khalatur, and A. R. Khokhlov, Makromol. Chem., Rapid Commun. **3**, 709 (1982).

[2] G. S. Grest and K. Kremer, Phys. Rev. A **33**, 3628 (1986).

[3] J. Zong and Q. Wang, J. Chem. Phys. **139**, 124907 (2013).

[4] Q. Wang, Soft Matter **5**, 4564 (2009); *ibid.* **5**, 6206 (2010).

[5] P. Zhang, X. Zhang, B. Li, and Q. Wang, Soft Matter **7**, 4461 (2011).

[6] P. Zhang, D. Yang, and Q. Wang, J Phys. Chem. B in press (2014).

[7] P. Zhang, B. Li, and Q. Wang, Macromolecules **44**, 7837 (2011).

[8] P. Zhang, B. Li, and Q. Wang, Macromolecules **45**, 2537 (2012).

[9] P. Zhang and Q. Wang, J. Chem. Phys. **140**, 044904 (2014).

[10] C. Williams, F. Brochard, and H. L. Frisch, Ann. Rev. Phys. Chem. **32**, 433 (1981).

[11] B. M. Baysal and F. E. Karasz, Macromol. Theory Simul. **12**, 627 (2003).

[12] J. Zong and Q. Wang, J. Chem. Phys. **139**, 124907 (2013).

[13] Q. Wang and Y. Yin. J. Chem. Phys. **130**, 104903 (2009).

[14] L. Leibler, Macromolecules **13**, 1602 (1980).

[15] G. H. Fredrickson, *The Equilibrium Theory of Inhomogeneous Polymers* (Oxford Press, New York, 2006).

[16] D. Chandler and H. C. Anderson, J. Chem. Phys. **57**, 1930 (1972).

[17] L. J. Lowden amd D. Chandler, J. Chem. Phys. **59**, 6587 (1973).

[18] L. J. Lowden amd D. Chandler, J. Chem. Phys. **61**, 5228 (1974).

[19] L. J. Lowden amd D. Chandler, J. Chem. Phys. **62**, 4246 (1975).

[20] J. G. Curro and K. S. Schweizer, Macromolecules **20**, 1928 (1987).

[21] J. G. Curro and K. S. Schweizer, J. Chem. Phys. **87**, 1842 (1987).

[22] K. S. Schweizer and J. G. Curro, Phys. Rev. Lett. **58**, 246 (1987).

[23] H. A. Patel, S. K. Kumar, and S. Garde, J. Chem. Phys. **122**, 104908 (2005).

[24] L.-J. Chen, H.-J. Qian, Z.-Y. Lu, Z.-S. Li, and C.-C. Sun, J. Phys. Chem. B **110**, 24093 (2006).

[25] A. A. Louis, J. Phys.: Condens. Matter **14**, 9187 (2002).

[26] K. S. Schweizer and J. G. Curro, Chem. Phys. **149**, 105 (1990).

[27] V. Krakoviack, J. P. Hansen, and A. A. Louis, Europhys. Lett. **58**, 53 (2002).

[28] A. J. Clark and M. G. Guenza, J. Chem. Phys. **132**, 044902 (2010).

[29] A. J. Clark, J. McCarty, I. Y. Lyubimov, and M. G. Guenza, Phys. Rev. Lett. **109**, 168301 (2012).

[30] A. J. Clark, J. McCarty, and M. G. Guenza, J. Chem. Phys. **139**, 124906 (2013).

[31] M. S. Shell, J. Chem. Phys. **129**, 144108 (2008).

[32] A. Chaimovich and M. S. Shell, J. Chem. Phys. **134**, 094112 (2011).

[33] K. S. Schweizer, K. G. Honnell, and J. G. Curro, J. Chem. Phys. **96**, 3211 (1992).

[34] A. Yethiraj and J. G. Curro, J. Chem. Phys. **97**, 1455 (1992).

[35] J. Melenkevitz, K. S. Schweizer, and J. G. Curro, Macromolecules **26**, 6190 (1993).

[36] D. G. Gromov and J. J. de Pablo, J. Chem. Phys. **103**, 8247 (1995).

CHAPTER 2

STRUCTURAL AND PHASE TRANSITIONS OF ONE AND TWO POLYMER MUSHROOMS IN POOR SOLVENT

2.1 Introduction

The fast lattice Monte Carlo (FLMC) simulation was recently proposed,[1] where multiple occupancy of lattice sites (MOLS) is allowed in contrast to the self- and mutual-avoiding walk (SMAW) used in conventional lattice Monte Carlo (MC) simulations. As explained in Ref. [1], FLMC simulation has great advantages over conventional molecular simulations with hard excluded-volume interactions (e.g., the Lennard-Jones potential in continuum or SMAW on a lattice) in the study of equilibrium properties of soft matter such as polymers. For example, it provides a powerful means for unambiguously and quantitatively revealing the effects of fluctuations and correlations when compared with the corresponding lattice field theories based on the same model system. This has been demonstrated in our series of studies on the structural and thermodynamic properties of compressible homopolymer melts in either bulk[2] or thin film[1] and those of grafted homopolymers in an either implicit[3] or explicit[4,5] solvent, where no phase transition occurs. In this work, we quantify the effects of fluctuations and correlations on phase transitions, taking (homo)polymer mushrooms in a poor solvent as our model systems.

It is well known that a polymer chain immersed in a small-molecule solvent undergoes the coil-globule transition (CGT) between the expanded (coil) and collapsed (globule) states as the solvent quality changes, which has been the subject of extensive research.[6,7] It is also known that a polymer mushroom exhibits similar CGT.[8–11] In line with our previous

work on grafted polymers,[3–5] here we consider CGT of a flexible and uncharged polymer mushroom on a planar, homogeneous and neutral (non-selective) substrate, and immersed in an explicit and poor solvent. We use a coarse-grained lattice model with MOLS, and define a mushroom as a group of n chains each of N segments end-grafted at the same point onto a substrate. Each of these segments represents, for example, the center of mass of a group of real monomers on a chain, and soft potentials (e.g., MOLS) emerges naturally from the coarse-graining process.[12,13] With soft potentials that allow complete particle overlapping, N becomes a chain discretization (or coarse-graining) parameter that does not correspond to the actual chain length used in experiments,[14] and, as shown in detail below, a mean-field theory (i.e., the widely applied polymer self-consistent field (SCF) theory[15]) neglecting the system fluctuations/correlations becomes exact in the limit of $n \to \infty$. Furthermore, comparisons between our FLMC simulations at finite n with the corresponding SCF results based on the same model system (thus without any parameter-fitting) can unambiguously and quantitatively reveal the fluctuation/correlation effects neglected by the theory.[1]

An analogous off-lattice study of the fluctuation/correlation effects on the order-disorder transition (ODT) of symmetric diblock copolymers was recently reported by our group.[14] In that case, it is well known that the mean-field theory predicts ODT to be a second-order phase transition,[16] and that the system fluctuations stabilize the disordered phase and change ODT to a weak first-order phase transition.[17] In the case of CGT of a ungrafted chain, a Flory-type[18] mean-field theory, which is similar to but simpler than SCF theory, is commonly used;[19–26] the transition order predicted by this or SCF[27,28] theory, however, has been controversial until our very recent work (see Appendix A),[29] where we clarified that CGT, at the mean-field level, can be either a first-order transition, a critical point, or a crossover for finite N (referred to as the "type I" behavior), and only in the limit of $N \to \infty$ becomes a second-order transition with respect to the solvent quality characterized by either the second virial coefficient (also known as the excluded-volume parameter) v,[24,27] the Flory-Huggins interaction parameter χ, or the temperature.[29]

The phase behavior of a mushroom, on the other hand, has rarely been reported in the literature. Halperin[30] and Tang and Szleifer[11] extended the above Flory-type mean-field theory for a ungrafted chain to chains end-grafted onto a substrate. While they used different elastic free-energy expressions from that in Ref. [19], their results for a mushroom show that it exhibits the "type I" phase behavior. The analysis performed in our resent work[29] is therefore also applicable to one-mushroom systems. In addition, Milik and Orszagh[8,9] performed MC simulations to study CGT of a grafted chain obeying the self-avoiding walk on a diamond lattice, and found continuous variation of the chain dimension with monomer-monomer interaction (i.e., the solvent quality). Due to the finite chain lengths used there (or in any conventional simulation studies), however, the order of CGT cannot be determined.

In this work, based on our coarse-grained lattice model with MOLS, where each lattice site is occupied by totally ρ_0 polymer segments and solvent molecules, we systematically construct the phase diagrams of one-mushroom systems as a function of the average polymer volume fraction $\bar{\phi}_{\rm A} \equiv nN/\rho_0 V$, where V denotes the total number of lattice sites, and the Flory-Huggins interaction parameter χ between polymer segments and solvent molecules at the same lattice site. While one expects that the simulation results approach the SCF predictions with increasing n (i.e., ρ_0), contradiction to this expectation leads us to the discovery of a second-order symmetric-asymmetric transition (SAT) in polymer mushrooms in a poor solvent (i.e., in the globule state), which, to the best of our knowledge, has not been reported in the literature. In the asymmetric globule states, the rotational symmetry around the substrate normal passing through the grafting point is broken in each individual configuration but preserved by the degeneracy of different orientations of these asymmetric configurations.

On the other hand, in a multi-mushroom system mushrooms can interact with each other. For example, as the solvent quality decreases, two or more adjacent mushrooms can fuse together, forming the so-called "surface micelles"[10] or "clusters".[11] In this work we also study two-mushroom systems, which exhibit a fused-separated transition (FST)

as the solvent quality varies. This FST can further be coupled with CGT and SAT of each mushroom, and has rarely been studied in the literature. Williams[10] studied a two-mushroom system in a poor solvent using scaling arguments, and found that the critical grafting distance (i.e., the boundary between the fused and separated states of the two mushrooms) $d_c \propto N^{2/3}$, larger than the overlapping threshold between two isolated globules ($\propto N^{1/3}$) due to the monomer-monomer effective attraction. Using SCF calculations in continuum with continuous Gaussian chains in an explicit solvent, Pattanayek et al.[31] predicted $d_c = 5.4a$ at $\chi N = 30$, where a denotes the polymer statistical segment length, but they did not give the $\bar{\phi}_{\rm A}$ value for their case. Moreover, the above studies did not examine the effects of other parameters in the two-mushroom system, such as $\bar{\phi}_{\rm A}$ and χ.

We therefore systematically construct the phase diagrams of two-mushroom systems using LSCF calculations, as a function of $\bar{\phi}_{\rm A}$, χ, and d. We further investigate the coupling of FST with CGT and SAT of each mushroom. Finally, we compare FLMC results at finite n with LSCF predictions based on the same model system, to unambiguously quantify the fluctuation/correlation effects on FST.

2.2 Model and Methods

2.2.1 Model system

We consider incompressible homopolymer systems of m chains each consisting of N segments (A) and $n_{\rm S}$ solvent molecules (S) on a 3D lattice of totally V sites. Each polymer segment or solvent molecule occupies one lattice site, and each lattice site is occupied by totally $\rho_0 = (mN + n_{\rm S})/V \geq m$ segments and solvent molecules. The first segment of each chain is fixed at $x = 1$, and an impenetrable substrate is placed at $x = 0$, which cannot be occupied by either polymer segments or solvent molecules. Note that the number of chains grafted at each grafting point $n = m$ for one-mushroom systems and $m/2$ for two-mushroom systems. The lattice size V is chosen to be large enough. Specifically, for one-mushroom systems we choose $L_x = N$ and $L_y = L_z = 2N - 1$ with all chains grafted at $(1, 0, 0)$, where L_x, L_y and

L_z are the number of lattice sites in the corresponding direction; for two-mushroom systems we choose $L_x = N$, $L_y = 2N - 1$, and $L_z = 2N + d_{\max}$ with $d_{\max}$ denoting the maximum value of the separation distance d between the two grafting points placed at $y = 0$.

The canonical-ensemble configuration integral of the systems is

$$\mathcal{Z} = \prod_{k=1}^{m} \prod_{s=1}^{N} \sum_{\mathbf{R}_{k,s}} \cdot \prod_{k=1}^{n_{\rm S}} \sum_{\mathbf{r}_k} \cdot \exp\left(- \sum_{k=1}^{m} \beta h_k^C - \beta \mathcal{H}^E \right) \cdot \prod_{\mathbf{r}} \delta_{\hat{\rho}_{\rm A}(\mathbf{r}) + \hat{\rho}_{\rm S}(\mathbf{r}), \rho_0}, \tag{2.1}$$

where $\mathbf{R}_{k,s}$ denotes the lattice position of the $s^{\rm th}$ segment on the $k^{\rm th}$ chain, $\mathbf{r}_k$ denotes the lattice position of the $k^{\rm th}$ solvent molecule, the summations are over all the allowed positions of polymer segments and solvent molecules, respectively, $\beta \equiv 1/k_B T$ with k_B denoting the Boltzmann constant and T the thermodynamic temperature, and $\delta_{\hat{\rho}_{\rm A}(\mathbf{r}) + \hat{\rho}_{\rm S}(\mathbf{r}), \rho_0}$ denotes the Kronecker δ-function imposing the incompressibility constraint on lattice site $\mathbf{r}$. $h_k^C = \sum_{l=1}^{N-1} u_{k,l}^{\rm b}$ is the Hamiltonian of the $k^{\rm th}$ chain due to its connectivity with $u_{k,l}^{\rm b}$ denoting the bonding energy of the $l^{\rm th}$ bond of the $k^{\rm th}$ chain. In this work we use the BFM2 lattice, which has six bonds of length 1 and twelve bonds of length $\sqrt{2}$ (in units of the lattice spacing) with equal *a priori* probabilities for bonds of different lengths (i.e., the parameter λ defined in Ref. [32] takes the value of 1/2); such a lattice minimizes the lattice anisotropy.[32] We thus have $\beta u_{k,l}^{\rm b} = 0$ for bonds of length 1, $\ln 2$ for bonds of length $\sqrt{2}$, and ∞ if the chain connectivity is not maintained. The Hamiltonian due to non-bonded interactions $\mathcal{H}^E$ is given by

$$\beta \mathcal{H}^E = \frac{\chi}{\rho_0} E = \frac{\chi}{\rho_0} \sum_{\mathbf{r}} \hat{\rho}_{\rm A}(\mathbf{r}) \hat{\rho}_{\rm S}(\mathbf{r}), \tag{2.2}$$

where χ is the Flory-Huggins parameter denoting the repulsion between an A segment and a S molecule at the same lattice site, $E \equiv \sum_{\mathbf{r}} \hat{\rho}_{\rm A}(\mathbf{r}) \hat{\rho}_{\rm S}(\mathbf{r})$ denotes the total number of A-S pairs at the same lattice site in the system, and $\hat{\rho}_{\rm A}(\mathbf{r}) \equiv \sum_{k=1}^{m} \sum_{s=1}^{N} \delta_{\mathbf{r}, \mathbf{R}_{k,s}}$ and $\hat{\rho}_{\rm S}(\mathbf{r}) \equiv \sum_{k=1}^{n_{\rm S}} \delta_{\mathbf{r}, \mathbf{r}_k}$ are the microscopic densities of A segments and S molecules at lattice site $\mathbf{r}$, respectively.

With the incompressibility constraint, i.e., $\hat{\rho}_{\rm A}(\mathbf{r}) + \hat{\rho}_{\rm S}(\mathbf{r}) = \rho_0$ at all $\mathbf{r}$, Eq. (2.1) can be re-written as

$$\mathcal{Z} = \prod_{k=1}^{m} \prod_{s=1}^{N} \sum_{\mathbf{R}_{k,s}} \cdot \frac{n_{\rm S}!}{\prod_{\mathbf{r}} [\rho_0 - \hat{\rho}_{\rm A}(\mathbf{r})]!} \exp\left(- \sum_{k=1}^{m} \beta h_k^C - \beta \mathcal{H}^E \right) \cdot \prod_{\mathbf{r}} \theta(\rho_0 - \hat{\rho}_{\rm A}(\mathbf{r})), \tag{2.3}$$

where $\theta(x) = 1$ if $x \geq 0$ and 0 otherwise, and the factor $n_{\rm S}!/\prod_{\mathbf{r}}[\rho_0 - \hat{\rho}_{\rm A}(\mathbf{r})]!$ is the number of different ways of arranging the solvent molecules for a given configuration $\{\mathbf{R}_{k,s}\}$ of all chains and corresponds to the solvent entropy.

2.2.2 Lattice self-consistent field (LSCF) theory

In order to transform the above particle-based configuration integral to a field-based one, we insert into Eq. (2.1) the following identities

$$1 = \left(\frac{\rho_0}{2\pi}\right)^{2V} \prod_j \int \mathcal{D}\phi_j \mathcal{D}\omega_j \exp\left\{\sum_{\mathbf{r}} \omega_j(\mathbf{r})[\rho_0 \phi_j(\mathbf{r}) - \hat{\rho}_j(\mathbf{r})]\right\}, \tag{2.4}$$

$$\prod_{\mathbf{r}} \delta_{\sum_j \hat{\rho}_j(\mathbf{r}),\rho_0} = \frac{1}{(2\pi)^V} \int \mathcal{D}\eta \exp\left\{-\rho_0 \sum_{\mathbf{r}} \eta(\mathbf{r}) \left[\sum_j \phi_j(\mathbf{r}) - 1\right]\right\}, \tag{2.5}$$

where $\phi_j(\mathbf{r})$ is the normalized density (volume fraction) field of species j (=A,S) constrained to $\hat{\rho}_j(\mathbf{r})/\rho_0$, $\omega_j(\mathbf{r})$ is the conjugate field imposing the constraint, and $\eta(\mathbf{r})$ is the conjugate field enforcing the incompressibility constraint. We then have

$$\begin{aligned}
\mathcal{Z} &= \frac{\rho_0^{2V}}{(2\pi)^{3V}} \int \mathcal{D}\phi_{\rm A} \mathcal{D}\omega_{\rm A} \mathcal{D}\phi_{\rm S} \mathcal{D}\omega_{\rm S} \mathcal{D}\eta \\
&\quad \cdot \exp\left\{\frac{\rho_0}{N} \sum_{\mathbf{r}} \left[\sum_j \omega_j(\mathbf{r})\phi_j(\mathbf{r}) - \chi N \phi_{\rm A}(\mathbf{r})\phi_{\rm S}(\mathbf{r}) - \eta(\mathbf{r})\Big(\sum_j \phi_j(\mathbf{r}) - 1\Big)\right]\right\} \\
&\quad \cdot \exp\left[n_{\rm S}(\ln Q_{\rm S} + \ln V) + \sum_{k=1}^{m} (\ln Q_k + \ln \mathcal{G})\right] \\
&\sim \int \mathcal{D}\phi_{\rm A} \mathcal{D}\omega_{\rm A} \mathcal{D}\phi_{\rm S} \mathcal{D}\omega_{\rm S} \mathcal{D}\eta \exp\left\{-[(mN + n_{\rm S})/N]\beta f_c\right\},
\end{aligned} \tag{2.6}$$

where $\mathcal{G} \equiv \prod_{s=1}^{N} \sum_{\mathbf{R}_{k,s}} \cdot \exp\left(-\beta h_k^C\right) = V(2z/3)^{N-1}$ with $z = 18$ denoting the coordination number of BFM2 lattice, and Q_k and $Q_{\rm S}$ are the single-chain partition function of the $k^{\rm th}$ chain and the single-particle partition function of a solvent molecule, respectively, given by

$$Q_k = \prod_{s=1}^{N} \sum_{\mathbf{R}_{k,s}} \cdot \exp\left[-\beta h_k^C - \sum_{s=1}^{N} \omega_{\rm A}(\mathbf{R}_{k,s})/N\right] \Big/ \mathcal{G}, \tag{2.7}$$

$$Q_{\rm S} = \sum_{\mathbf{r}} \exp[-\omega_{\rm S}(\mathbf{r})/N]/V. \tag{2.8}$$

Note that we have re-scaled variables according to $N\omega_j(\mathbf{r}) \rightarrow \omega_j(\mathbf{r})$ and $N\eta(\mathbf{r}) \rightarrow \eta(\mathbf{r})$. Finally the statistical weight βf_c is given by

$$\begin{aligned}\beta f_c &= \frac{1}{V}\sum_{\mathbf{r}}\Big\{\chi N\phi_{\rm A}(\mathbf{r})\phi_{\rm S}(\mathbf{r}) - \sum_j \omega_j(\mathbf{r})\phi_j(\mathbf{r}) + \eta(\mathbf{r})\Big[\sum_j \phi_j(\mathbf{r}) - 1\Big]\Big\} \\ &\quad -\frac{\bar{\phi}_{\rm A}}{m}\sum_{k=1}^{m}\ln Q_k - N\bar{\phi}_{\rm S}\ln Q_{\rm S}, \end{aligned} \tag{2.9}$$

where $\bar{\phi}_{\rm A} \equiv mN/\rho_0 V$ and $\bar{\phi}_{\rm S} = 1 - \bar{\phi}_{\rm A}$ are the volume fractions of A and S, respectively, in the system, and we have neglected a constant factor in $\mathcal{Z}$.

If we define $q_{k,s}(\mathbf{r})$ as the one-end-integrated propagator corresponding to the probability of finding a partial chain of s segments that starts from the grafting point of the $k^{\rm th}$ chain and ends at $\mathbf{r}$, and $q^*_t(\mathbf{r})$ corresponding to the probability of finding a partial chain of t segments that starts anywhere in the system and ends at $\mathbf{r}$, they satisfy the recursive relations given by

$$\begin{aligned} q_{k,1}(\mathbf{r}) &= \exp[-\omega_{\rm A}(\mathbf{r})/N]\delta_{\mathbf{r},\mathbf{g}_k}, \\ q_{k,s+1}(\mathbf{r}) &= \exp[-\omega_{\rm A}(\mathbf{r})/N]\left[\frac{1}{12}\sum_{\mathbf{r}_{n,1}} q_{k,s}(\mathbf{r}_{n,1}) + \frac{1}{24}\sum_{\mathbf{r}_{n,\sqrt{2}}} q_{k,s}(\mathbf{r}_{n,\sqrt{2}})\right]; \end{aligned} \tag{2.10}$$

$$\begin{aligned} q^*_1(\mathbf{r}) &= \exp[-\omega_{\rm A}(\mathbf{r})/N], \\ q^*_{t+1}(\mathbf{r}) &= \exp[-\omega_{\rm A}(\mathbf{r})/N]\left[\frac{1}{12}\sum_{\mathbf{r}_{n,1}} q^*_t(\mathbf{r}_{n,1}) + \frac{1}{24}\sum_{\mathbf{r}_{n,\sqrt{2}}} q^*_t(\mathbf{r}_{n,\sqrt{2}})\right], \end{aligned} \tag{2.11}$$

where $\mathbf{g}_k$ is the grafting point of the $k^{\rm th}$ chain, and $\sum_{\mathbf{r}_{n,1}}$ and $\sum_{\mathbf{r}_{n,\sqrt{2}}}$ denote summations over the neighboring sites of $\mathbf{r}$ with bond length of 1 and $\sqrt{2}$, respectively. We can then re-write Q_k as

$$Q_k = \frac{1}{V}\sum_{\mathbf{r}} q_{k,s}(\mathbf{r})q^*_{N-s+1}(\mathbf{r})\exp[\omega_{\rm A}(\mathbf{r})/N]. \tag{2.12}$$

By setting $\delta\beta f_c/\delta\phi_j(\mathbf{r}) = \delta\beta f_c/\delta\omega_j(\mathbf{r}) = \delta\beta f_c/\delta\eta(\mathbf{r}) = 0$, and noting $q_{k,s}(\mathbf{r})$ and Q_k are the same for chains grafted at the same point, we obtain the following LSCF equations

$$\omega_{\rm A}(\mathbf{r}) = \chi N\phi_{\rm S}(\mathbf{r}) + \eta(\mathbf{r}), \tag{2.13}$$

$$\omega_{\rm S}(\mathbf{r}) = \chi N\phi_{\rm A}(\mathbf{r}) + \eta(\mathbf{r}), \tag{2.14}$$

$$\phi_{\rm A}(\mathbf{r}) = \frac{\bar{\phi}_{\rm A}}{n_g N}\exp[\omega_{\rm A}(\mathbf{r})/N]\sum_{i=1}^{n_g}\frac{1}{Q_i}\sum_{s=1}^{N} q_{i,s}(\mathbf{r})q^*_{N-s+1}(\mathbf{r}), \tag{2.15}$$

$$\phi_{\rm S}(\mathbf{r}) = \frac{\bar{\phi}_{\rm S}}{Q_{\rm S}}\exp[-\omega_{\rm S}(\mathbf{r})/N], \tag{2.16}$$

$$1 = \phi_{\rm A}(\mathbf{r}) + \phi_{\rm S}(\mathbf{r}), \tag{2.17}$$

where n_g denotes the number of different grafting points. Because the conjugate fields can be shifted by an arbitrary constant without changing βf_c and the density fields, we set $Q_{\rm S} = \bar{\phi}_{\rm S}$ to obtain a unique solution. For given $\omega_{\rm A}(\mathbf{r})$, Eqs. (2.15) and (2.17) are used to calculated $\phi_{\rm A}(\mathbf{r})$ and $\phi_{\rm S}(\mathbf{r})$, respectively, then $\omega_{\rm S}(\mathbf{r})$ is calculated as $\omega_{\rm S}(\mathbf{r}) = -N\ln\phi_{\rm S}(\mathbf{r})$ according to Eq. (2.16), and finally a new conjugate field $\omega_{\rm A}(\mathbf{r})$ is obtained as $\omega_{\rm A}(\mathbf{r}) = \omega_{\rm S}(\mathbf{r}) + \chi N[\phi_{\rm S}(\mathbf{r}) - \phi_{\rm A}(\mathbf{r})]$ according to Eqs. (2.13) and (2.14). The LSCF equations can be solved using the Anderson mixing method[33,34] with the convergence criterion of $\max_{\{\mathbf{r}\}}|[\omega_{\rm A}(\mathbf{r}) - \omega_{\rm S}(\mathbf{r})]/\chi N + 2\phi_{\rm A}(\mathbf{r}) - 1| \le 10^{-10}$.

Once LSCF equations are solved, we calculate the mean-field Helmholtz free energy per chain of N segments (or per N lattice sites) $\beta f_c^{\rm LSCF}$ according to Eq. (2.9), the internal energy per chain due to bonding interactions as

$$\beta u_{c,\rm b}^{\rm LSCF} = \frac{\ln 2}{24}\frac{\bar{\phi}_{\rm A}}{n_g}\sum_{i=1}^{n_g}\sum_{s=1}^{N-1}\sum_{\mathbf{r}}\sum_{\mathbf{r}_{n,\sqrt{2}}}\frac{q_{i,s}(\mathbf{r})q^*_{N-s}(\mathbf{r}_{n,\sqrt{2}})}{VQ_i}, \tag{2.18}$$

the internal energy per chain due to non-bonded interactions $\beta u_{c,\rm nb}^{\rm LSCF} \equiv \chi N\sum_{\mathbf{r}}\phi_{\rm A}(\mathbf{r})\phi_{\rm S}(\mathbf{r})/V$, and the entropy per chain $s_c^{\rm LSCF}/k_{\rm B} = \beta(u_c^{\rm LSCF} - f_c^{\rm LSCF})$ with the internal energy per chain $u_c = u_{c,\rm b} + u_{c,\rm nb}$. In order to obtain the most stable solution of LSCF equations (i.e., with the lowest $\beta f_c^{\rm LSCF}$), we further use the combinatorial screening method proposed by Drolet and Fredrickson[35] with different random initial guesses.

For one-mushroom systems, in order to characterize the coil-globule transition (CGT) we define the chain expansion factor $\alpha^2 \equiv R_e^2/R_{e,0}^2$, where $R_{e,0}^2 = (N-1)\bar{b^2}$ is the mean-square end-to-end distance of an ideal (non-interacting) ungrafted chain with the mean-square bond length (in units of the square of lattice spacing) $\bar{b^2} = 1.5$, and LSCF calculations

give the mean-square chain end-to-end distance $R_e^2 = \sum_{\mathbf{r}} q_{1,N}(\mathbf{r})(\mathbf{r}-\mathbf{g})^2/VQ_1$, where the only grafting point $\mathbf{g} = (1,0,0)$. For two-mushroom systems, in order to characterize the fused-separated transition (FST) we define the fusion factor $\gamma \equiv I_{xx}/I_{xx,0}$, where $I_{xx} \equiv \sum_{\mathbf{r}} \phi(\mathbf{r})[(y-y_c)^2 + (z-z_c)^2]$ is the moment of inertia around the symmetry (x) axis of the system for real grafted chains with y_c and z_c being the y- and z-coordinate, respectively, of the center between the two grafting points, and $I_{xx,0}$ is the corresponding value for ideal grafted chains.

2.2.3 Fast lattice Monte Carlo (FLMC) simulations

We perform FLMC simulations in a canonical ensemble according to Eq. (2.3), and use three types of trial moves – local moves, bond-rotation,[1] and partial exchange – with a fraction of $0.2, 0.4$, and 0.4, respectively. For the local moves we randomly displace a randomly chosen free chain-end (end-rotation) or interior segment (hopping), and for partial exchange moves we exchange two randomly chosen partial chains (including their free end but not their grafted end) that have the same length and start from the same lattice site. All trial moves must maintain the chain connectivity, substrate impenetrability, and system incompressibility (by switching polymer segments with solvent molecules), and are accepted according to the probability $\mathcal{P}_{\rm acc}(o \to n) = \min[1, W_o/W_n \exp(-\beta\Delta\mathcal{U})]$, where $\Delta\mathcal{U} \equiv \mathcal{U}_n - \mathcal{U}_o$ is the energy difference between the trial (n) and old (o) configurations with $\mathcal{U} \equiv \sum_{k=1}^{m} h_k^C + \mathcal{H}^E$ denoting the total energy of a configuration, and $W \equiv \prod_{\mathbf{r}}[\rho_0 - \hat{\rho}_{\rm A}(\mathbf{r})]!$ is due to the solvent entropy. The initial configurations are randomly generated and about $(1 \sim 40) \times 10^6$ Monte Carlo steps (MCS) are performed in each simulation, where one MCS is defined as mN trial moves. The error bar of each ensemble-averaged quantity is estimated as three times its standard deviation, with the statistical correlation among samples collected after equilibration taken into account by the correlation function method.[36]

We further use replica exchange (RE)[37] of configurations at different (adjacent) χ values, which greatly reduces the sample correlation. RE is attempted every $10 \sim 20$ MCS, and the

acceptance criterion for swapping two configurations i and j at χ_i and χ_j, respectively, is

$$\mathcal{P}_{\rm acc}^{\rm RE} = \min\{1, \exp[(\chi_i - \chi_j)(E_i - E_j)/\rho_0]\}. \tag{2.19}$$

We also use the self-consistent multiple histogram reweighting technique to analyze the simulation results.[38] For totally R simulation runs performed at different χ_i ($i = 1, ..., R$), we collect the histogram $H_i(E, E_{\rm b}, \psi)$ at each χ_i, where $E_{\rm b}$ denotes the number of bonds of length $\sqrt{2}$, and ψ denotes R_e^2 (for one-mushroom systems) or I_{xx} (for two-mushroom systems). Setting $\mathcal{Z}_1 = 1$, we then have $R - 1$ independent equations

$$\sum_E \frac{\sum_{E_{\rm b}} \sum_\psi \sum_{j=1}^R H_j(E, E_{\rm b}, \psi) g_j^{-1}}{\mathcal{Z}_i \sum_{j=1}^R \exp\left[(\chi_i - \chi_j)E/\rho_0\right] M_j g_j^{-1} \mathcal{Z}_j^{-1}} = 1, \qquad i = 2, \ldots, R, \tag{2.20}$$

where M_i is the total number of collected samples after equilibration in the $i^{\rm th}$ simulation, $g_i \equiv 1 + 2\tau_i$ with τ_i being the correlation length of E in the $i^{\rm th}$ simulation, and $\mathcal{Z}_i$ is the canonical-ensemble configuration integral at χ_i. Once these equations are solved using the Newton's method,[39] we obtain the values of $\mathcal{Z}_i$ ($i = 2, \ldots, R$) and then calculate the quantity $\mathcal{Z}(\chi) p_b(\chi, E, E_{\rm b}, \psi)$ as

$$\mathcal{Z}(\chi) p_b(\chi, E, E_{\rm b}, \psi) = \frac{\sum_{i=1}^R H_i(E, E_{\rm b}, \psi) g_i^{-1}}{\sum_{i=1}^R \exp\left[(\chi - \chi_i)E/\rho_0\right] M_i g_i^{-1} \mathcal{Z}_i^{-1}}, \tag{2.21}$$

where $\mathcal{Z}(\chi)$ is the canonical-ensemble configuration integral at any χ within our simulation range and can be obtained from $\mathcal{Z}(\chi) = \sum_E \sum_{E_{\rm b}} \sum_\psi \mathcal{Z}(\chi) p_b(\chi, E, E_{\rm b}, \psi)$ with p_b satisfying $\sum_E \sum_{E_{\rm b}} \sum_\psi p_b(\chi, E, E_{\rm b}, \psi) = 1$. We finally calculate the ensemble averages $\langle R_e^2 \rangle$, $\langle I_{xx} \rangle$ and $\langle E \rangle$ as, for example, $\langle R_e^2 \rangle = \sum_E \sum_{E_{\rm b}} \sum_{R_e^2} R_e^2 p_b(\chi, E, E_{\rm b}, R_e^2)$, and the constant-volume heat capacity $C_V/k_B \equiv \beta^2(\langle \mathcal{U}^2 \rangle - \langle \mathcal{U} \rangle^2)/m$, the bonded internal energy per chain $\beta u_{c,{\rm b}}^{\rm FLMC} = (\ln 2)\bar{\phi}_{\rm A} \langle E_{\rm b} \rangle / m$, the non-bonded internal energy per chain $\beta u_{c,{\rm nb}}^{\rm FLMC}(\chi) = \chi N \langle E \rangle / \rho_0^2 V$, and the difference in the Helmholtz free energy per chain between the system at χ and that at χ_1

$$\beta \Delta f_c^{\rm FLMC}(\chi) = -(N/\rho_0 V) \ln \mathcal{Z}(\chi), \tag{2.22}$$

where χ_1 is usually taken to be the smallest χ-value used in our simulations. Similarly, we have the non-bonded internal energy difference per chain $\beta \Delta u_{c,{\rm nb}}^{\rm FLMC}(\chi)$ and the entropy

difference per chain $\Delta s_c^{\mathrm{FLMC}}(\chi)/k_B = \beta\left[\Delta u_c^{\mathrm{FLMC}}(\chi) - \Delta f_c^{\mathrm{FLMC}}(\chi)\right]$. The transition point χ^* is determined by $(\mathrm{d}C_V/\mathrm{d}\chi)|_{\chi^*} = 0$. To estimate the statistical errors of χ^* and the peak value C_V^*, we calculate them using the first- and second-half of our samples collected after equilibration, respectively, and take as the error bar three times their largest deviation from those determined using all the samples.

2.3 Results and Discussions

In the following, we first examine one-mushroom systems, where we construct the phase diagrams of CGT using LSCF theory and compare LSCF predictions with FLMC results at various $n = m$, where m denotes the total number of chains in the system, to quantify the effects of fluctuations and correlations in the system. In this comparison we find a second-order SAT for one-mushroom systems, which is confirmed by both LSCF calculations and FLMC simulations. Once we understand one-mushroom systems, we then study how two mushrooms interact with each other (i.e., the coupling among CGT and SAT of one mushroom and FST of two mushrooms) by constructing the phase diagrams of two-mushroom systems using LSCF theory, and compare LSCF predictions with FLMC results at various $n = m/2$, where n denotes the number of chains grafted at each grafting point, to quantify the effects of fluctuations and correlations. Unless specified otherwise, we fix $N = 40$ in this work.

2.3.1 One-mushroom systems

Here LSCF results are controlled by two parameters: the Flory-Huggins χ parameter and the ratio $n/\rho_0 = \bar{\phi}_{\mathrm{A}} V/N$; note that LSCF results are exact in the limit of the total number of polymer segments and solvent molecules at each lattice site $\rho_0 \to \infty$, or equivalently $n \to \infty$. The third parameter, namely ρ_0 (or equivalently n), appears in FLMC simulations and controls the system fluctuations/correlations.

2.3.1.1 Coil-globule transition (CGT) and phase diagrams from LSCF calculations

We first assume that the mushroom is symmetric about both the x-y and x-z planes passing through the grafting point at $(1, 0, 0)$. This symmetry assumption is intuitive and reduces the solution domain of our LSCF calculations to one quarter of the system size. Fig. 2.1(a) shows how the expansion factor α^2 varies with χ at $n/\rho_0 = 1/5$. Two different states are found in the range of $1.393 < \chi < 1.450$ by gradually increasing or decreasing χ in our LSCF calculations. The Helmholtz free energy per chain βf_c of these two states shown in Fig. 2.1(b) indicates that the coil (C) state, which has larger α^2, is more stable (i.e., having lower βf_c) for $\chi < \chi^*_{\rm CGT} = 1.412$, while the globule (G) state, which has smaller α^2, is more stable for $\chi > \chi^*_{\rm CGT}$; a first-order CGT occurs at $\chi^*_{\rm CGT}$, where the two states co-exist (i.e., having the same βf_c). Clearly, the globule state has lower bonded internal energy per chain $\beta u_{c,\rm b}$ than the coil state (data not shown). Fig. 2.1(b) further shows that the globule state also has lower non-bonded internal energy per chain $\beta u_{c,\rm nb}$ than the coil state, due to its denser mushroom structure and thus the less polymer-solvent contact; Figs. 2.1(c) and 2.1(d) show the polymer segmental density profiles $\phi_{\rm A}(x, y = 0, z)$ of the coil and globule states, respectively, at $\chi^*_{\rm CGT}$. The stability of the globule state at $\chi > \chi^*_{\rm CGT}$ is therefore due to its lower internal energy per chain βu_c. The coil state, on the other hand, has higher entropy per chain s_c/k_B than the globule state (data not shown), which favors its stability at $\chi < \chi^*_{\rm CGT}$. Finally, we cannot find the coil state for $\chi > 1.450$ and the globule state for $\chi < 1.393$, which may correspond to the spinodal points at $n/\rho_0 = 1/5$.

Fig. 2.1(a) also shows how α^2 varies with χ at $n/\rho_0 = 1/3$, where only one LSCF solution can be found at any χ and α^2 decreases continuously with increasing χ. We therefore have a crossover, instead of a phase transition, between the coil and globule states in this case, as supported by the continuity of $\mathrm{d}^2\beta f_c/\mathrm{d}\chi^2$ at all χ (data not shown).

Fig. 2.2(a) shows how α^2 of the stable state varies with χ for several values of n/ρ_0, where the binodal curve is obtained by connecting the two co-existing points at each n/ρ_0 where a first-order CGT occurs. The critical point, located at $(n/\rho_0)_c \approx 0.276$ and $\chi_c \approx 1.224$ with

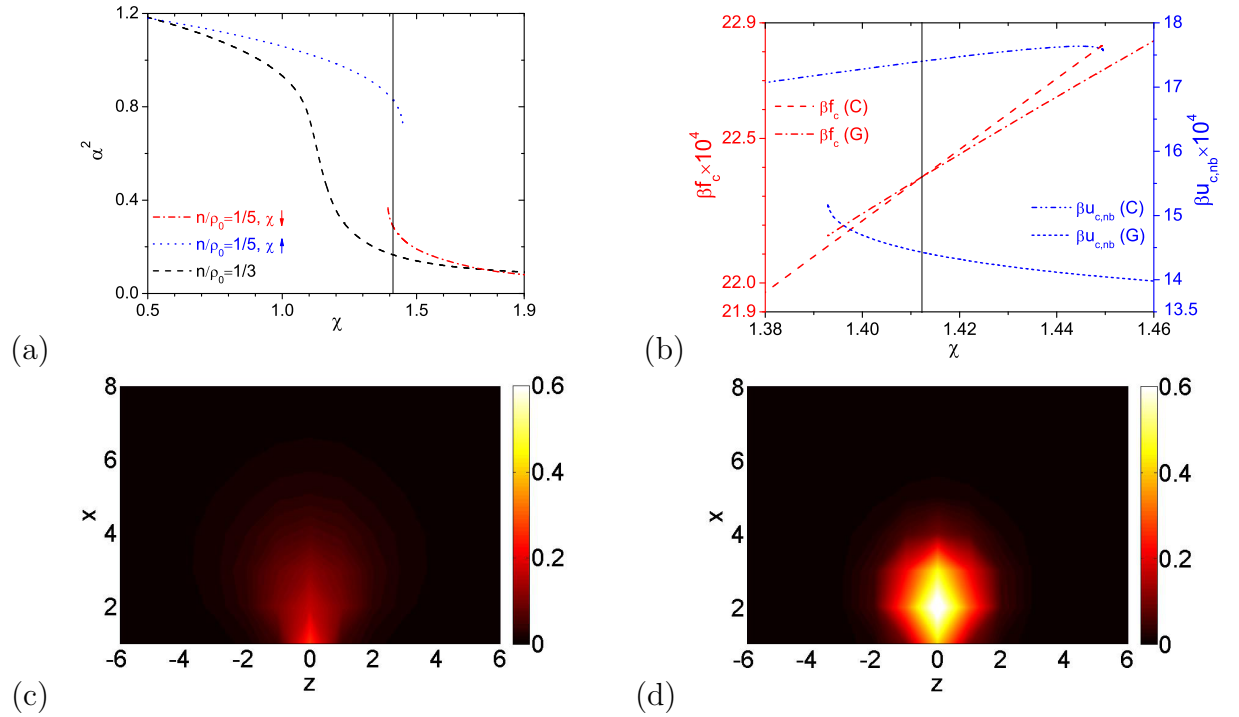

Figure 2.1: LSCF results of one-mushroom systems of $N = 40$: (a) chain expansion factor α^2 as a function of χ at $n/\rho_0 = 1/3$ and $1/5$, where the arrow pointing up (down) indicates gradual increase (decrease) of χ; (b) Helmholtz free energy per chain βf_c and non-bonded internal energy per chain $\beta u_{c,\mathrm{nb}}$ of the coil (C) and globule (G) states as a function of χ at $n/\rho_0 = 1/5$; (c) polymer segmental density profile $\phi_\mathrm{A}(x, y = 0, z)$ of the coil state at $\chi^*_\mathrm{CGT} = 1.412$ and $n/\rho_0 = 1/5$; and (d) $\phi_\mathrm{A}(x, y = 0, z)$ of the globule state at $\chi^*_\mathrm{CGT} = 1.412$ and $n/\rho_0 = 1/5$. The vertical line in parts (a) and (b) marks $\chi^*_\mathrm{CGT} = 1.412$.

$\alpha_c^2 \approx 0.585$, is estimated using the classical critical exponents from the Landau theory,[40] i.e., $|\alpha_c^2 - \alpha^2| \propto [(n/\rho_0)_c - n/\rho_0]^{1/2}$ and $|\alpha_c^2 - \alpha^2| \propto (\chi - \chi_c)^{1/3}$, where n/ρ_0, χ and α^2 are taken from the binodal curve. We therefore see that CGT is a crossover for $n/\rho_0 > (n/\rho_0)_c$ but a first-order phase transition for $n/\rho_0 < (n/\rho_0)_c$ (i.e., the "type I" behavior); in the latter case, α^2 of the stable state exhibits a discontinuity at χ^*_CGT, which increases with decreasing n/ρ_0.

To examine the effects of the grafting substrate, we also perform LSCF calculations for a group of chains of $N = 40$ with one end all fixed at the center of a box of size $L_x = L_y = L_z = 2N - 1$ (i.e., without the grafting substrate, referred to as the system

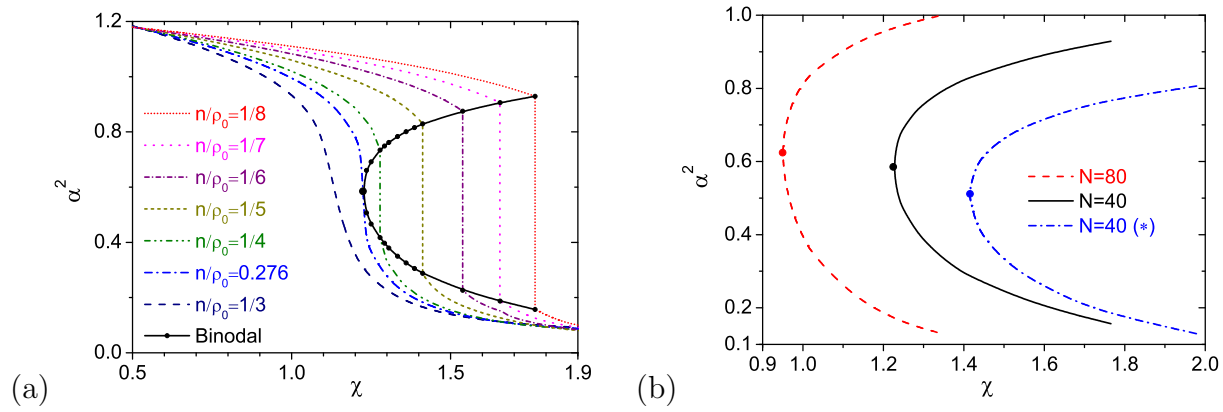

Figure 2.2: LSCF phase diagrams of one-mushroom systems with (a) $N = 40$ and (b) $N = 40$ and 80. In part (b), the results for the system "$*$" are also shown. The critical point of the one-mushroom system with $N = 40$ is located at $(n/\rho_0)_c \approx 0.276$ and $\chi_c \approx 1.224$ with $\alpha_c \approx 0.585$, that of the one-mushroom system with $N = 80$ is located at $(n/\rho_0)_c \approx 0.317$ and $\chi_c \approx 0.950$ with $\alpha_c \approx 0.624$, and that of the system "$*$" with $N = 40$ is located at $(n/\rho_0)_c \approx 0.204$ and $\chi_c \approx 1.415$ with $\alpha_c \approx 0.512$. See main text for details.

"$*$"), the binodal curve of which is shown in Fig. 2.2(b). Comparing with the mushroom of $N = 40$, we see that the grafting substrate shifts the critical point to smaller χ_c and larger $(n/\rho_0)_c$, thus resulting in larger change of α^2 at the same χ where the first-order CGT occurs. Note that the critical point of system "$*$" is located at $\chi_c \approx 1.415$, which is different from that given by the Flory-Huggins theory, $\chi_c^{\rm FH} = (1/N + 1)/2 + 1/\sqrt{N} \approx 0.671$ for a homogeneous system of $N = 40$, due to the inhomogeneity of the former. Fig. 2.2(b) also shows that, compared to the case of $N = 40$, a larger chain length of $N = 80$ moves the binodal curve towards smaller χ. This trend is qualitatively consistent with the Flory-type mean-field theory of CGT of a ungrafted chain in an explicit solvent,[29] which predicts $\chi_c \approx 0.656$ for $N = 40$ and 0.608 for $N = 80$.

As mentioned in Introduction, the Flory-type mean-field study first reported by Ptitsyn et al.[19–21] was extended later by Halperin[30] and Tang and Szleifer[11] to a single chain grafted on a planar substrate. Since the mean-field theory is exact in the limit of $\rho_0 \to \infty$, these studies actually correspond to our LSCF calculations for the "$*$" and one-mushroom systems,

respectively. To see the correspondence between our explicit-solvent model and their implicit-solvent models, we rewrite Eq. (2.3) by Taylor-expanding $\ln[1-\hat{\rho}_{\rm A}(r)/\rho_0]$ at small $\hat{\rho}_{\rm A}(\mathbf{r})/\rho_0 < 1$ to the third order as[4]

$$\mathcal{Z} \sim \prod_{k=1}^{n}\prod_{s=1}^{N}\sum_{\mathbf{R}_{k,s}} \cdot \exp\left\{-\sum_{k=1}^{n}\beta h_k^C - \sum_{\mathbf{r}}\left[\frac{1}{2}(1-2\chi)\frac{\hat{\rho}_{\rm A}^2(\mathbf{r})}{\rho_0} + \frac{1}{6}\frac{\hat{\rho}_{\rm A}^3(\mathbf{r})}{\rho_0^2}\right]\right\}, \tag{2.23}$$

Assuming uniform distribution of polymer segments within the chain volume $V_c = \alpha^3 N^{3/2} l^3/k$, where l is the lattice spacing and k a numerical factor (e.g., $k = 6/\pi$), we have the non-bonded interaction energy per chain as

$$\beta u_c^{\rm Flory} = \frac{1}{2}k(1-2\chi)\left(\frac{n}{\rho_0}\right)N^{1/2}\alpha^{-3} + \frac{1}{6}k^2\left(\frac{n}{\rho_0}\right)^2\alpha^{-6}. \tag{2.24}$$

Our model therefore gives the second and third virial coefficients $v = (1-2\chi)(n/\rho_0)$ and $w = (n/\rho_0)^2$, and our parameters can be mapped to p and q defined in Ref. [20] as $q = k(1-2\chi)(n/\rho_0)N^{1/2}/2$ and $p = k^2(n/\rho_0)^2/3$. While this mapping is not exact due to the different models used (for example, implicit vs. explicit solvents, and lattice vs. continuum chains), our results are consistent with theirs, namely, the system has the "type I" behavior at finite N.

CGT of a single grafted chain obeying the self-avoiding walks (SAW) has also been studied via lattice Monte Carlo simulations.[8,9] To qualitatively relate our model system to the SAW chain, we can equate $\bar{\phi}_{\rm A}$ to that of a single grafted SAW chain of length $N_{\rm SAW}$ on a lattice of $L_x = N_{\rm SAW}$ and $L_y = L_z = 2N_{\rm SAW} - 1$, which gives $N_{\rm SAW} = (N-1/2)/\sqrt{n/\rho_0} + 1/2$. This correspondence is again not exact due to the difference in the non-bonded interactions between our model and those for the SAW chain.

2.3.1.2 Symmetry-breaking in the globule state

Here we fix $n/\rho_0 = 1/5$. Fig. 2.3 compares the expansion factor α^2 from FLMC simulations at various n with the LSCF prediction obtained under the symmetry assumption. We see that FLMC results approach LSCF prediction with increasing n in the coil state, as expected.

In the globule state, however, unexpected "overshooting" (i.e., $\alpha^2_{\rm FLMC} < \alpha^2_{\rm LSCF}$) occurs for $n \geq 16$.

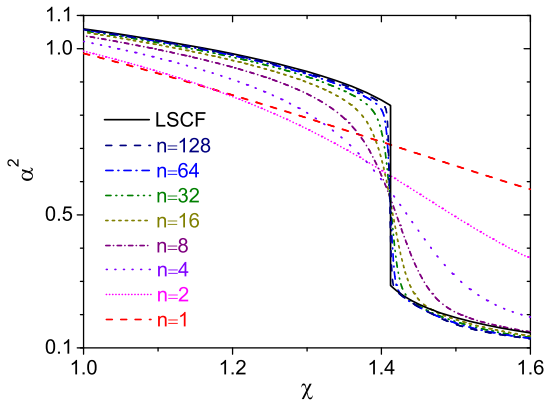

Figure 2.3: Comparison of α^2 between LSCF calculations under the symmetry assumption (see main text for details) and FLMC simulations at various n for one-mushroom system at $n/\rho_0 = 1/5$ and $N = 40$.

Re-solving LSCF equations for the entire system (i.e., without the symmetry assumption) at $\chi = 1.6$, we find two asymmetric globule states (denoted by "A1" and "A2") in addition to the symmetric globule state (denoted by "Sym"). Figs. 2.4(a)∼2.4(c) show the segmental density profiles averaged over the x-direction, $\sum_{x=1}^{L_x} \phi_{\rm A}(x,y,z)/L_x$, of these three states, respectively. For "Sym" [Fig. 2.4(a)], we see that it is symmetric about *both* the y- and z-axes; since the grafting substrate is homogeneous, such rotational symmetry around the x-axis (on a lattice) is intuitively expected. For the asymmetric states, however, this rotational symmetry is broken in each *individual* configuration; that is, "A1" [Fig. 2.4(b)] is symmetric about one diagonal line but not the other, and "A2" [Fig. 2.4(c)] is symmetric about either the y- or z-axis but not both. Of course, due to the homogeneity of the grafting substrate, the configurations shown in Figs. 2.4(b) and 2.4(c) can be rotated by any integer multiple of 90° around the x-axis, which preserves the rotational symmetry.

Fig. 2.4(d) shows how α^2 and βf_c of these states obtained from LSCF calculations vary with χ. "A1" and "A2" can be found only for $\chi > \chi^*_{\rm SAT} = 1.447$, where both α^2 and βf_c increase in the order of "A1", "A2", and "Sym". This is also the case for $\beta u_{c,\rm nb}$ as shown in

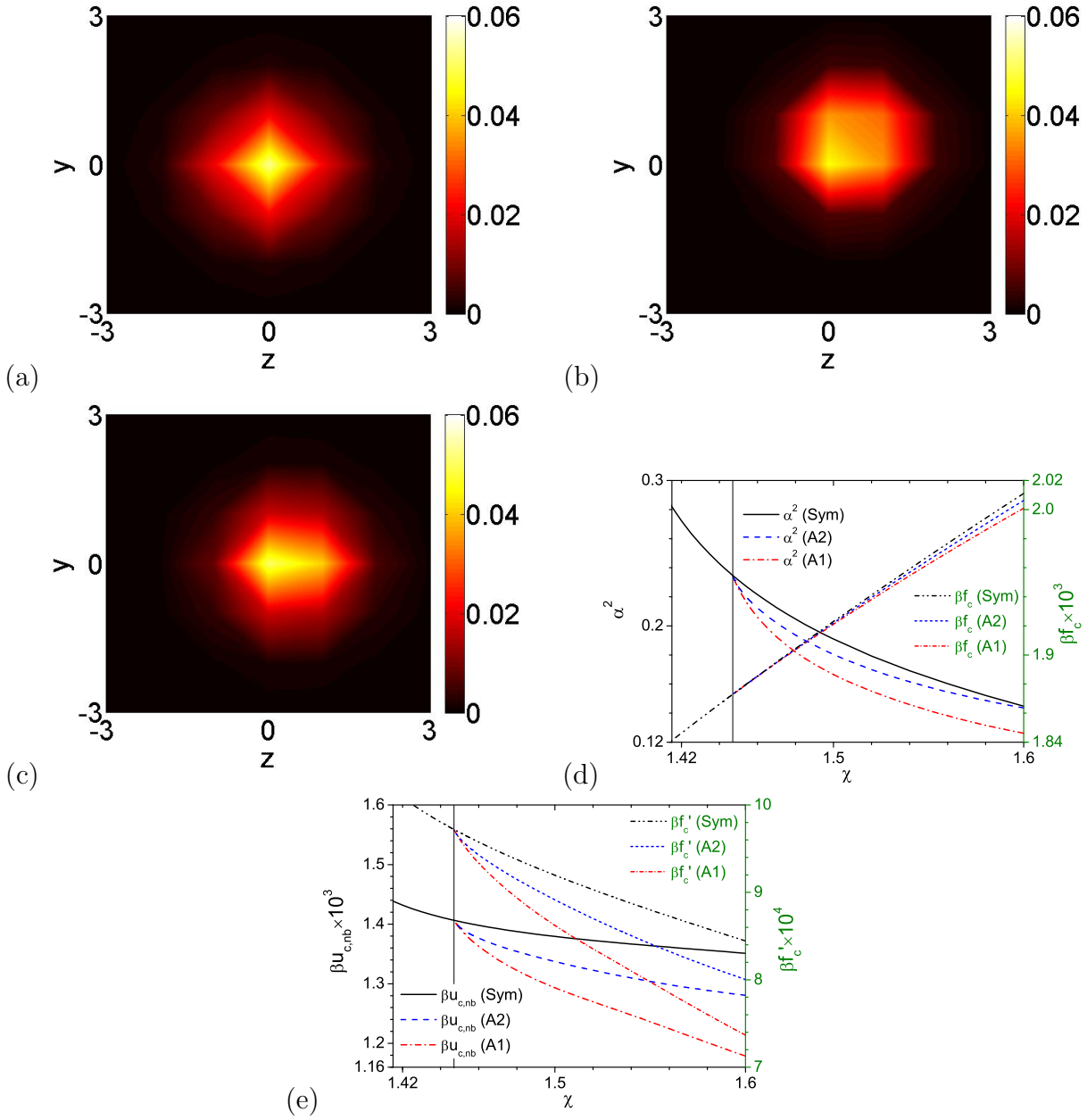

Figure 2.4: LSCF results of one-mushroom systems at $n/\rho_0 = 1/5$ and $N = 40$: (a) polymer segmental density profile $\sum_{x=1}^{L_x} \phi_{\rm A}(x,y,z)/L_x$ in the symmetric state "Sym", (b) that in the asymmetric state "A1", (c) that in the asymmetric state "A2", (d) α^2 and βf_c of the three states, and (e) $\beta u_{c,\rm nb}$ and $\beta f_c' \equiv {\rm d}(\beta f_c)/{\rm d}\chi$ of these states. $\chi = 1.6$ in parts (a)$\sim$(c). The vertical line in parts (d) and (e) marks $\chi^*_{\rm SAT} = 1.447$.

Fig. 2.4(e), as well as for $\beta u_{c,\rm b}$, βu_c and s_c/k_B (data not shown) within the χ-range studied here. "A1" is therefore the most stable state at $\chi > \chi^*_{\rm SAT}$, due to its most compact structure and thus the lowest $\beta u_{c,\rm b}$ and $\beta u_{c,\rm nb}$. Fig. 2.4(e) further shows that ${\rm d}(\beta f_c)/{\rm d}\chi$ of these states

is continuous at $\chi^*_{\rm SAT}$, but $\mathrm{d}^2(\beta f_c)/\mathrm{d}^2\chi$ is clearly not; the symmetric-asymmetric transition (SAT) is therefore a second-order phase transition.

Some discussion on the lattice effects is in order here. While the differences between "A1" and "A2", as well as their discrete set of orientations, are due to the use of a lattice, the occurrence of SAT is not. Our LSCF calculations suggest that, in continuum, the symmetric state should have rotational symmetry around the x-axis, and for $\chi > \chi^*_{\rm SAT}$ an asymmetric state stabilized by its lower βu_c should appear with smaller α^2 and βf_c than the symmetric state; in this asymmetric state, the rotational symmetry is broken in each *individual* configuration but preserved by the degeneracy of different orientations of these asymmetric configurations (which corresponds to the degeneracy of the four different orientations of "A1" or "A2" on a lattice). To the best of our knowledge, the asymmetric state and SAT of one-mushroom systems in the globule state have not been reported in the literature.

To check the existence of asymmetric states in FLMC simulations, we calculate the histogram of the mushroom center-of-mass, $\mathbf{r}_{\rm cm} \equiv \sum_{\mathbf{r}} \mathbf{r}\phi_{\rm A}(\mathbf{r}) / \sum_{\mathbf{r}} \phi_{\rm A}(\mathbf{r})$, from our collected configurations. Fig. 2.5 shows the distributions of $(y_{\rm cm}, z_{\rm cm})$ for $n = 64$ at various χ, where we clearly see that the mushroom changes from "Sym" to "A1" as χ increases: At $\chi = 1.4$ [Fig. 2.5(a)] the mushroom is in the coil state and the distribution of $(y_{\rm cm}, z_{\rm cm})$ exhibits rotational symmetry around the origin; at $\chi = 1.45$ [Fig. 2.5(b)], which is close to the LSCF prediction of $\chi^*_{\rm SAT} = 1.447$, an interesting square distribution appears due to the co-existence of symmetric and asymmetric states; as χ further increases to 1.5 [Fig. 2.5(c)) and 1.6 [Fig. 2.5(d)], "A1" becomes dominant and the distribution exhibits four distinguished points along the diagonal lines due to the degeneracy of the four orientations of "A1". On the other hand, Figs. 2.6(a)$\sim$2.6(c) show the distributions of $(y_{\rm cm}, z_{\rm cm})$ for $n = 2$, 8, and 16 at $\chi = 1.6$, indicating it changes from "Sym" to "A1" as n increases.

We can further transform $\mathbf{r}_{\rm cm}$ into the spherical coordinates, with the grafting point as the origin and $\theta_{\rm cm} \in [0, \pi/2)$ being the angle between $\mathbf{r}_{\rm cm}$ and the x-axis. Fig. 2.7(a) shows how

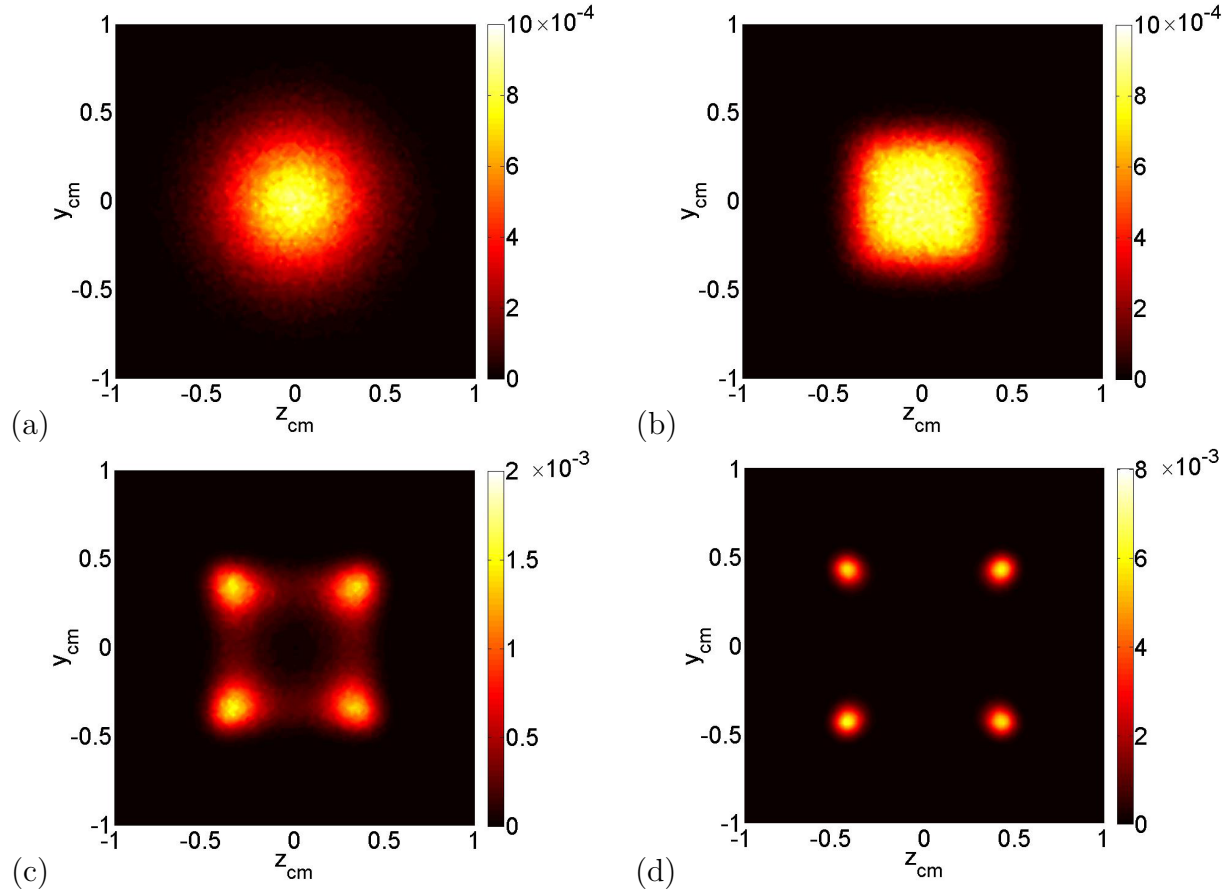

Figure 2.5: Histogram of the mushroom center-of-mass in the y-z plane, $(y_{\rm cm}, z_{\rm cm})$, obtained from FLMC simulations of one-mushroom system of $n = 64$ at (a) $\chi = 1.4$, (b) $\chi = 1.45$, (c) $\chi = 1.5$, and (d) $\chi = 1.6$. $n/\rho_0 = 1/5$ and $N = 40$.

the ensemble average $\langle|\mathbf{r}_{\rm cm}|\rangle$ from FLMC simulations at different n varies with χ, along with the corresponding LSCF predictions for the three states. While $\langle|\mathbf{r}_{\rm cm}|\rangle$ monotonically decreases with increasing χ in the LSCF prediction for "Sym" (due to the decreased mushroom size) and in the FLMC results for $n \leq 16$, it exhibits a minimum in the LSCF predictions for "A1" and "A2" (due to their broken rotational symmetry) and in the FLMC results for $n \geq 32$. Furthermore, the FLMC results at the largest number of grafted chains $n = 128$, where the system fluctuations are the smallest, closely follow the LSCF prediction for "A1". Our FLMC simulations therefore confirm the mean-field predictions of asymmetric states and SAT, and show that they are gradually destroyed by increasing system fluctuations.

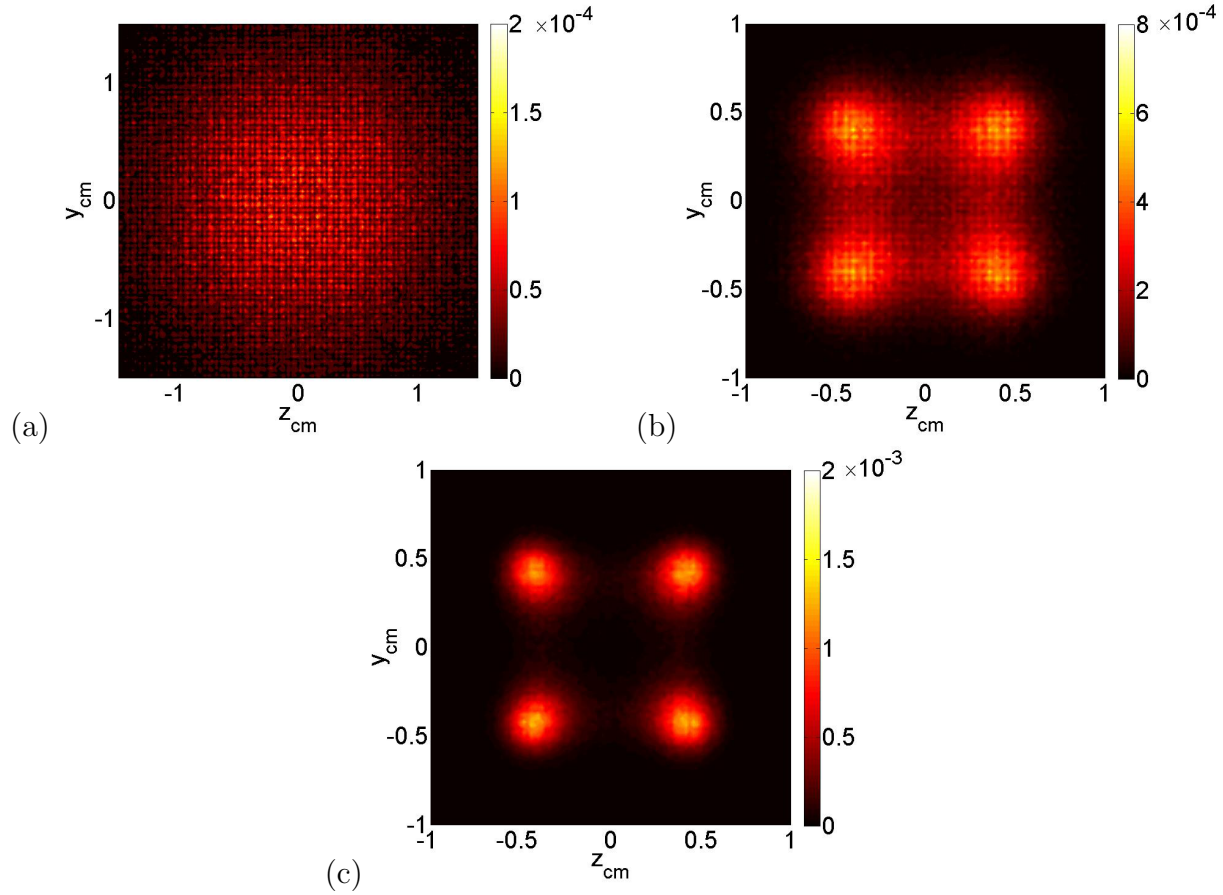

Figure 2.6: Histogram of the mushroom center-of-mass in the y-z plane, $(y_{\rm cm}, z_{\rm cm})$, obtained from FLMC simulations of one-mushroom systems of (a) $n = 2$, (b) $n = 8$, and (c) $n = 16$ at $\chi = 1.6$. $n/\rho_0 = 1/5$ and $N = 40$.

The same is found in $\langle\theta_{\rm cm}\rangle$ shown in Fig. 2.7(b). Here we see that, in the coil state (i.e., at $\chi \lesssim 1.4$), $\langle\theta_{\rm cm}\rangle$ is almost independent of χ, is positive due to the system fluctuations, and decreases with increasing n (which reduces the fluctuations); the least-squares fitting for $n \geq 16$ gives $\langle\theta_{\rm cm}\rangle \propto n^{-0.49}$. In the globule state, $\langle\theta_{\rm cm}\rangle$ increases with increasing χ, and at $\chi = 1.6$ almost coincides (for $n \geq 16$) with the LSCF prediction for "A1"; these results are consistent with those shown in Fig. 2.5. On the other hand, Fig. 2.7(b) clearly shows that the asymmetric states and SAT are not found for $n \leq 4$.

Finally, as mentioned above, LSCF predictions are exact in the limit of $\rho_0 \to \infty$ (or equivalently $n \to \infty$), and we expect that FLMC results approach LSCF predictions at large

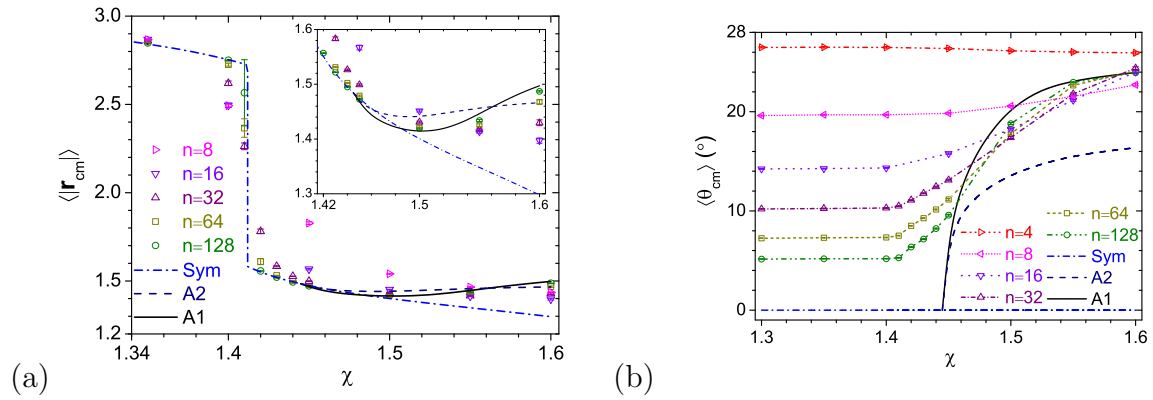

Figure 2.7: Comparisons between the ensemble-averaged components of the mushroom center-of-mass, $\mathbf{r}_{\rm cm}$, in the spherical coordinates (see main text for details) obtained from FLMC simulations of one-mushroom systems at various n and the corresponding LSCF predictions for the three states: (a) $\langle|\mathbf{r}_{\rm cm}|\rangle$ and (b) $\langle\theta_{\rm cm}\rangle$. The inset of part (a) enlarges the results in the globule state. $n/\rho_0 = 1/5$ and $N = 40$.

n. This is indeed found if we take LSCF predictions to be those in the most stable state (i.e., "A1" for $\chi > \chi^*_{\rm SAT}$), as shown in Fig. 2.8(a) (which can be compared with Fig. 2.3), except in the small region of $1.418 < \chi < 1.452$. This remaining "overshooting" can be explained by Fig. 2.7(b), which shows that $\langle\theta_{\rm cm}\rangle$ from FLMC simulations starts to increase at χ-values smaller than $\chi^*_{\rm SAT} = 1.447$; in other words, the system fluctuations change the location of SAT from $\chi^*_{\rm SAT}$ predicted by LSCF theory.

2.3.1.3 Quantifying fluctuation effects

Fig. 2.8(b) shows that, at $n/\rho_0 = 1/5$, α^2 from FLMC simulations, $\alpha^2_{\rm FLMC}$, approaches LSCF prediction, $\alpha^2_{\rm LSCF}$, at a rate of $1/n$ at large n in both the coil and globule states, except near the transitions (e.g., at $\chi = 1.4$ and 1.5). Similar results are found at other n/ρ_0-values (data not shown), and for $\beta\Delta f_c$ [Fig. 2.8(c)], $\beta\Delta u_{c,\rm nb}$ [Fig. 2.8(d)], as well as $\beta\Delta u_{c,\rm b}$, $\beta\Delta u_c$, $\Delta s_c/k_B$, and $\sqrt{\sum_{\mathbf{r}}[\phi_{\rm A,LSCF}(\mathbf{r}) - \phi_{\rm A,FLMC}(\mathbf{r})]^2/V}$ (data not shown); to calculate the last quantity for $\chi > \chi^*_{\rm SAT}$, we rotate each collected configuration in FLMC simulations by an angle of integer multiples of $\pi/2$ in the y-z plane such that $0 \le \varphi_{\rm cm} < \pi/2$, and use $\phi_{\rm A,LSCF}(\mathbf{r})$ of "A1" corresponding to the orientation shown in Fig. 2.4(b). Note that this $1/n$ scaling has also

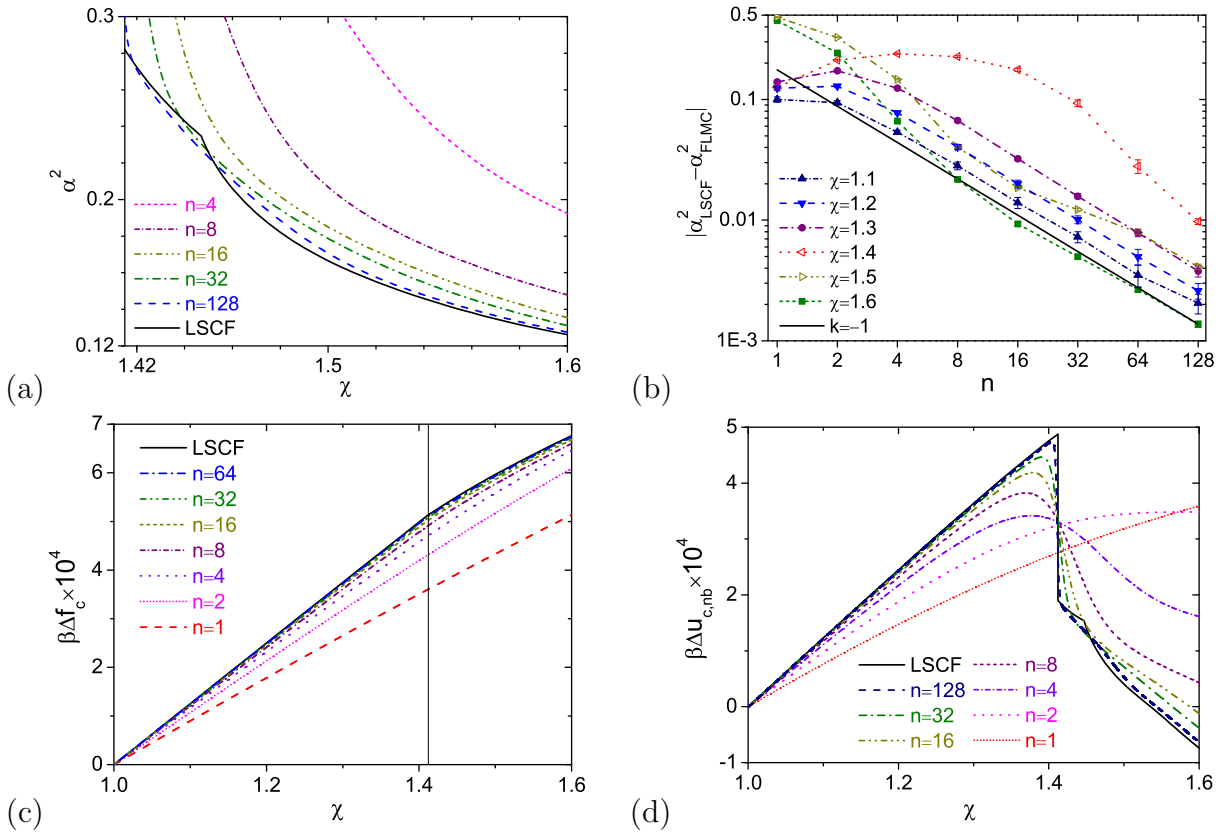

Figure 2.8: Comparisons between FLMC results of one-mushroom systems at various n and the corresponding LSCF predictions of the most stable state (i.e., "Sym" for $\chi < \chi^*_{\rm SAT} = 1.447$ and "A1" for larger χ): (a) α^2; (b) $|\alpha^2_{\rm LSCF} - \alpha^2_{\rm FLMC}|$ on a logarithmic plot, where $\alpha^2_{\rm FLMC} < \alpha^2_{\rm LSCF}$ for $\chi = 1.1 \sim 1.4$ and $\alpha^2_{\rm FLMC} > \alpha^2_{\rm LSCF}$ for $\chi = 1.5$ and 1.6, and "$k = -1$" denotes a straight line of slope -1; (c) $\beta\Delta f_c \equiv \beta[f_c(\chi) - f_c(\chi = 1)]$, where the vertical line marks $\chi^*_{\rm CGT} = 1.412$; and (d) $\beta\Delta u_{c,\rm nb} \equiv \beta[u_{c,\rm nb}(\chi) - u_{c,\rm nb}(\chi = 1)]$. $n/\rho_0 = 1/5$ and $N = 40$.

been found in our previous studies on the fluctuation effects in various systems using FLMC simulations.[2–5]

To examine the fluctuation effects on CGT, Fig. 2.9 shows the distribution of α^2 at $n/\rho_0 = 1/5$ obtained from FLMC simulations at $\chi^*_{\rm CGT} = 1.412$. For small n (≤ 8), the distribution has only one broad peak due to the large fluctuations in the system. As n increases and thus fluctuations decrease, it exhibits two peaks with position approaching α^2 for the coil and globule state, respectively, predicted by LSCF calculations.

Fig. 2.10(a) shows the constant-volume heat capacity C_V/k_B obtained from FLMC simulations as a function of χ for various n at $n/\rho_0 = 1/5$. As n increases, C_V/k_B develops a

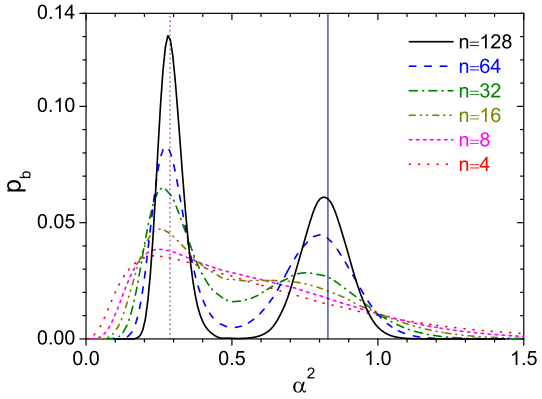

Figure 2.9: Distributions of α^2 obtained from FLMC simulations of one-mushroom systems of various n at $\chi^*_{\rm CGT} = 1.412$ predicted by LSCF theory. The two vertical lines mark the corresponding LSCF prediction of α^2 in the coil and globule states, respectively. $n/\rho_0 = 1/5$ and $N = 40$.

higher and sharper peak, with its position approaching $\chi^*_{\rm CGT}$ given by LSCF calculations. Fig. 2.10(b) shows that the peak value $C^*_V/k_B \propto n$ at large n, consistent with the LSCF result that CGT is a first-order phase transition. In Fig. 2.10(a), we can also see a second peak in C_V/k_B for $n \geq 32$, the position of which approaches $\chi^*_{\rm SAT}$ given by LSCF calculations with increasing n. Since SAT is a second-order phase transition, our FLMC data give $C^*_V/k_B \propto n^{0.17}$ for this peak as shown in Fig. 2.10(b).

Finally, we examine the behavior of C_V/k_B at $n/\rho_0 = 1/3$, where CGT is a crossover. Fig. 2.10(c) show that, as n increases, C_V/k_B also develops a higher and sharper peak with its position approaching $\chi^*_{\rm CGT} = 1.135$ given by LSCF calculations (which is determined by $({\rm d}^2\chi/{\rm d}(\alpha^2)^2)|_{\chi^*_{\rm CGT}} = 0$). The peak value C^*_V/k_B, however, increases much slower with increasing n than in the $n/\rho_0 = 1/5$ case as shown in Fig. 2.10(b), and should remain finite in the limit of $n \to \infty$ for a crossover. Note that, in Fig. 2.10(c), we can also find a second peak in C_V/k_B corresponding to SAT at $\chi^*_{\rm SAT} = 1.217$ given by LSCF calculations.

2.3.2 Two-mushroom systems

For two-mushroom systems, the two grafting points are placed at $x = 1$ and $y = 0$, and are separated by distance d (in units of lattice spacing) along the z direction. We therefore have

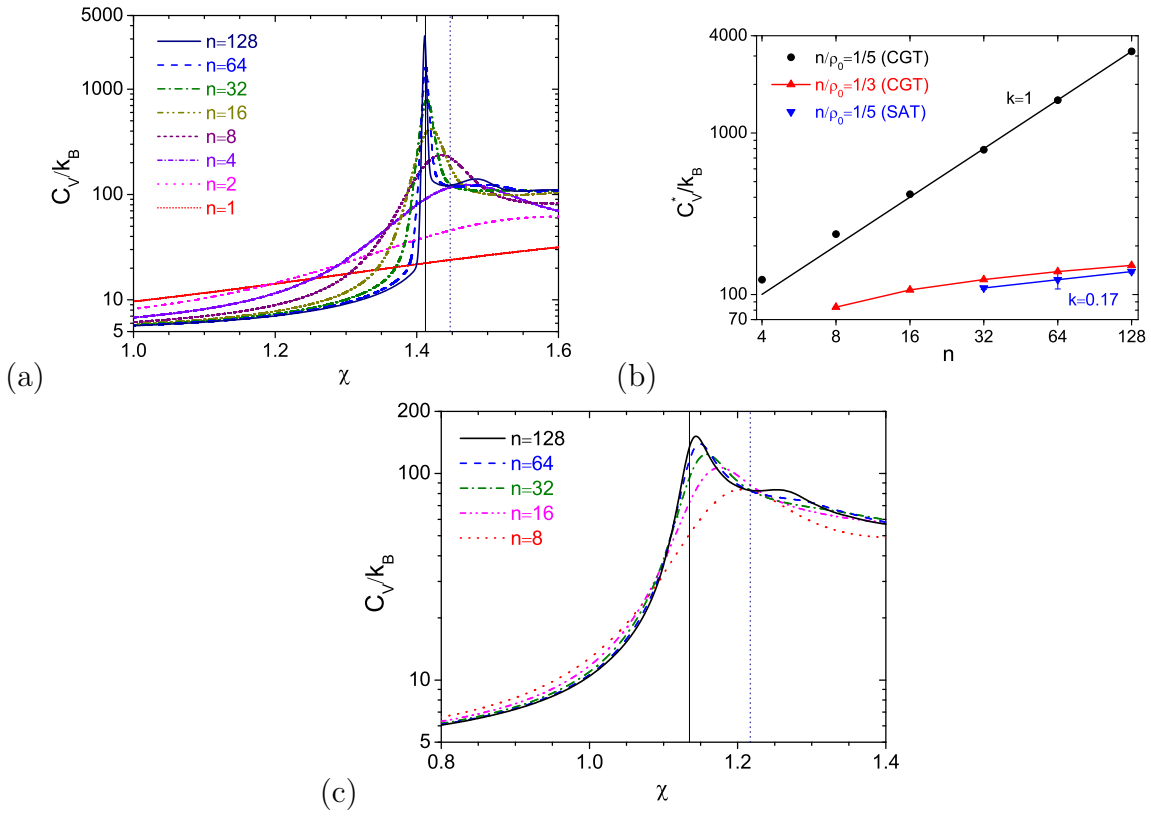

Figure 2.10: Constant-volume heat capacity C_V obtained from FLMC simulations of one-mushroom systems with various n at (a) $n/\rho_0 = 1/5$ and (c) $n/\rho_0 = 1/3$, where the vertical lines mark $\chi^*_{\rm CGT} = 1.412$ (solid) and $\chi^*_{\rm SAT} = 1.447$ (dotted) in part (a) and $\chi^*_{\rm CGT} = 1.135$ (solid) and $\chi^*_{\rm SAT} = 1.217$ (dotted) in part (c). Part (b) shows how the peak values C^*_V corresponding to CGT and SAT vary with n on a logarithmic plot, where the k-value near each fitted line gives its slope.

three controlling parameters in LSCF calculations: d, χ, and $n/\rho_0 = \bar{\phi}_{\rm A}V/2N$. Similar to one-mushroom systems, LSCF predictions are exact in the limit of $\rho_0 \to \infty$ (or equivalently $n \to \infty$). The fourth parameter, namely ρ_0 (or equivalently n), appears in FLMC simulations and controls the system fluctuations/correlations.

2.3.2.1 Phase diagrams from LSCF calculations

In LSCF calculations, we assume that the system is symmetric about both the x-y plane passing through the center of the two grafting points and the x-z plane passing through the grafting points, which reduces the solution domain to one quarter of the system size. On

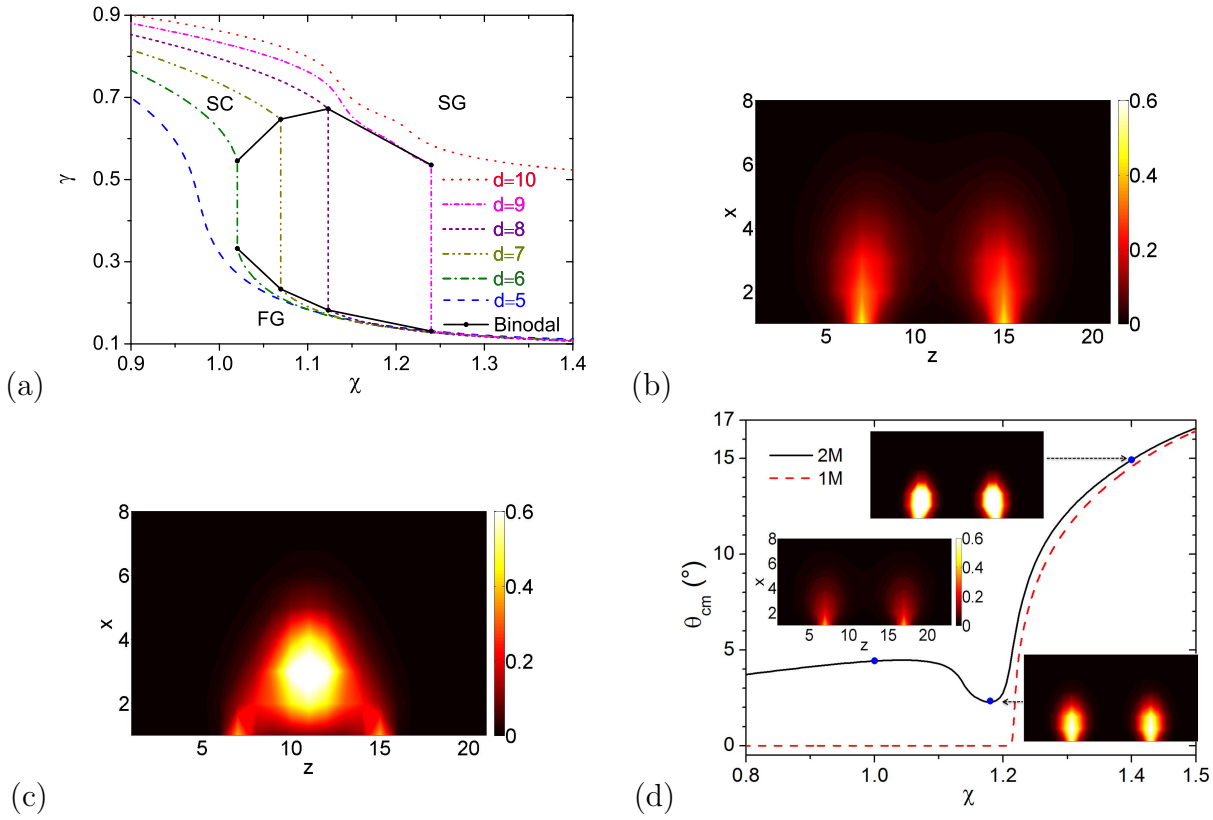

Figure 2.11: LSCF results of two-mushroom systems at $n/\rho_0 = 1/3$ and $N = 40$: (a) phase diagram in terms of the fusion factor γ as a function of χ, (b) $\phi_{\rm A}(x, y = 0, z)$ in the separated state at $\chi^*_{\rm FST} = 1.123$ and $d = 8$, (c) $\phi_{\rm A}(x, y = 0, z)$ in the fused state at $\chi^*_{\rm FST} = 1.123$ and $d = 8$, and (d) $\theta_{\rm cm}$ of each mushroom in the two-mushroom (2M) system at $d = 10$, where the insets show $\phi_{\rm A}(x, y = 0, z)$ at various χ (marked by dots), and the corresponding result of the one-mushroom (1M) system at $n/\rho_0 = 1/3$ is also shown. See main text for details.

the other hand, our LSCF calculations performed for the entire system (i.e., without the symmetry assumption) confirm that such symmetric solution (where each mushroom is in the asymmetric state "A2") has the lowest free energy per chain βf_c, due to the effective attraction between the two mushrooms in a poor solvent.

Fig. 2.11(a) shows how the fusion factor γ varies with χ at various d and $n/\rho_0 = 1/3$. For small separations (i.e., $d \leq 5$), only one solution can be found at any χ and the system exhibits a continuous crossover between the fused (small γ) and separated (large γ) states. For intermediate separations (i.e., $6 \leq d \leq 9$), a first-order fused-separated transition (FST) occurs at $\chi^*_{\rm FST}$, which increases with increasing d; the binodal curve is obtained by connecting

the two co-existing points at each d. Finally, for large separations (i.e., $d \geq 10$), the two mushrooms stay separated regardless of the solvent quality.

Figs. 2.11(b) and 2.11(c) show the segmental density profiles $\phi_{\rm A}(x, y = 0, z)$ in the separated and fused states, respectively, at $\chi^*_{\rm FST} = 1.123$ for $d = 8$ and $n/\rho_0 = 1/3$. Note that, in the corresponding one-mushroom system (i.e., at $n/\rho_0 = 1/3$), CGT is a crossover occurring at $\chi^*_{\rm CGT} = 1.135$; each mushroom in the separated state is therefore in the coil state, as shown in Fig. 2.11(b). In the fused state, the two mushrooms fuse together to avoid the unfavorable contact with the poor solvent, resulting in a denser polymeric system (thus lower solvent entropy) than in the separated state. The increased segmental density in turn puts the fused mushroom in the globule state, as shown in Fig. 2.11(c). While chains are stretched towards the middle of the system for the two mushrooms to fuse together, they are also collapsed in the fused globule, resulting in lower bonded internal energy per chain $\beta u_{c,\rm b}$ and smaller chain expansion factor α^2 than in the separated state. The fused state therefore has both lower internal energy per chain βu_c and lower entropy per chain s_c/k_B (data not shown), and their competition leads to FST.

For the $d = 10$ case shown in Fig. 2.11(a), we see two regions where γ varies quickly with χ: one is around $\chi = 1.136$ corresponding to the crossover between the coil and globule states of each mushroom, and the other is around $\chi = 1.214$ corresponding to SAT of each mushroom; these values are very close to $\chi^*_{\rm CGT} = 1.135$ and $\chi^*_{\rm SAT} = 1.217$, respectively, of the corresponding one-mushroom system. Fig. 2.11(d) shows that $\theta_{\rm cm}$ of each mushroom, characterizing its asymmetry, varies non-monotonically with χ: in a poor solvent, the two mushrooms attract thus lean towards each other, resulting in the gradual increase of $\theta_{\rm cm}$ with increasing χ for $\chi < 1.040$. The crossover from the coil to the globule state of each mushroom, however, greatly shrinks the mushroom size thus reduces their attraction, resulting in the decrease of $\theta_{\rm cm}$ with increasing χ for $1.040 < \chi < 1.180$. For $\chi > 1.180$, the quick increase of $\theta_{\rm cm}$ with increasing χ is mainly due to SAT of each mushroom. In Fig. 2.11(d), we also plot $\theta_{\rm cm}$ of the corresponding one-mushroom system; the difference between the two curves is due

to the attraction in the two-mushroom system, which for $\chi > \chi^*_{\rm SAT} = 1.217$ monotonically decreases with increasing χ due to the decreasing size of each mushroom.

In Fig. 2.11(a), these two regions can also be seen in the separated state at $d = 9$, but not in the fused state of systems at $d \leq 8$. For the latter systems in such a poor solvent, the increased segmental density due to the fusion of the two mushrooms puts them in the globule state, with the (partial) globule formed by each mushroom being strongly asymmetric (i.e., analogous to "A2" with $\varphi_{\rm cm} = 0$ or π). In other words, both the crossover between the coil and globule states and SAT of each mushroom are pre-empted by FST. Two-mushroom systems therefore have three different states: separated coils (SC), separated globules (SG), and fused globule (FG), as marked in Fig. 2.11(a); co-existence of SC/FG and that of SG/FG are found in the region encompassed by the binodal curve.

We further note that, $\chi^*_{\rm FST} = 1.240 > \chi^*_{\rm CGT}$ at $d = 9$, which means each mushroom in the separated state is in the globule state (i.e., SG). Fusion of the two mushrooms therefore results in abrupt increase of $\beta u_{c,\rm b}$ and α^2 (in contrast to the $d \leq 8$ cases) due to the strong chain-stretching towards the middle of the system. On the other hand, the fused state still has both lower βu_c and lower s_c/k_B (data not shown), and their competition leads to FST. The excessive chain-stretching required for the two mushrooms at larger separations (e.g., $d = 10$) to fuse together explains why FST does not occur in such cases.

Fig. 2.12(a) shows that qualitatively the same behavior is found for the two-mushroom systems at $n/\rho_0 = 1/5$, except that a first-order CGT occurs at $\chi^*_{\rm CGT} = 1.412$, the same value as given by LSCF calculations of the corresponding one-mushroom system (i.e., at $n/\rho_0 = 1/5$). Fig. 2.12(b) shows how α^2 varies with χ and d for this case. We see that in FG state α^2 increases with increasing d due to the increased chain-stretching for the two mushrooms to fuse together, and that α^2 for $d = 10 \sim 12$ exhibits a discontinuity at CGT of the corresponding one-mushroom system. In addition, α^2 for $d = 10$ and 11 exhibits another discontinuity at $\chi^*_{\rm FST} = 1.451$ and 1.730, respectively, due to FST of the two-mushroom system, which does not occur at larger separation (i.e., $d = 12$).

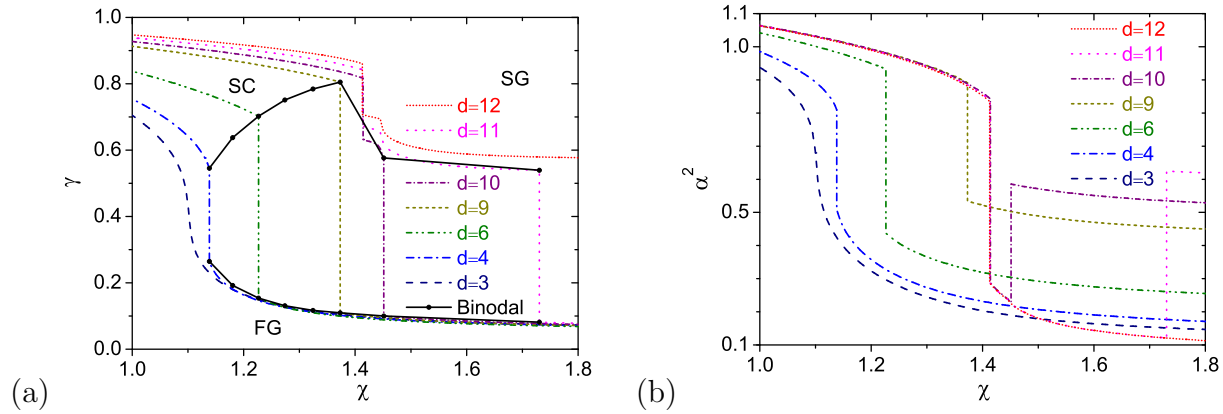

Figure 2.12: LSCF results of two-mushroom systems at $n/\rho_0 = 1/5$ and $N = 40$: (a) phase diagram and (b) the corresponding α^2 as a function of χ.

2.3.2.2 Quantifying fluctuation effects

Taking the case of $n/\rho_0 = 1/3$ and $d = 8$ as an example, here we examine how FLMC results approach LSCF predictions with increasing n. The results for γ are shown in Fig. 2.13(a), which is analogous to Fig. 2.3 or 2.8(a) without the complication of "overshooting" at large n. Fig. 2.13(b) further shows that $\gamma_{\rm FLMC}$ obtained from FLMC simulations approaches the corresponding LSCF prediction $\gamma_{\rm LSCF}$ at a rate of $1/n$ at large n in both the separated and the fused states. Similar results are found for $\beta\Delta f_c$ [Fig. 2.13(c)], $\beta\Delta u_{c,\rm nb}$ [Fig. 2.13(d)], as well as $\beta\Delta u_{c,\rm b}$, $\beta\Delta u_c$, and $\Delta s_c/k_B$ (data not shown).

Finally, Fig. 2.14(a) shows the constant-volume heat capacity C_V/k_B obtained from FLMC simulations as a function of χ for various n. As n increases, C_V/k_B develops a higher and sharper peak, with its position approaching $\chi^*_{\rm FST} = 1.123$ given by LSCF calculations. Fig. 2.14(b) further shows that the peak value $C^*_V/k_B \propto n^{1.2}$ and its position $\chi^*_{\rm FLMC}$ approaches the LSCF prediction at a rate of $n^{-1.2}$ at large n, where the scaling is somewhat different from that for one-mushroom systems.

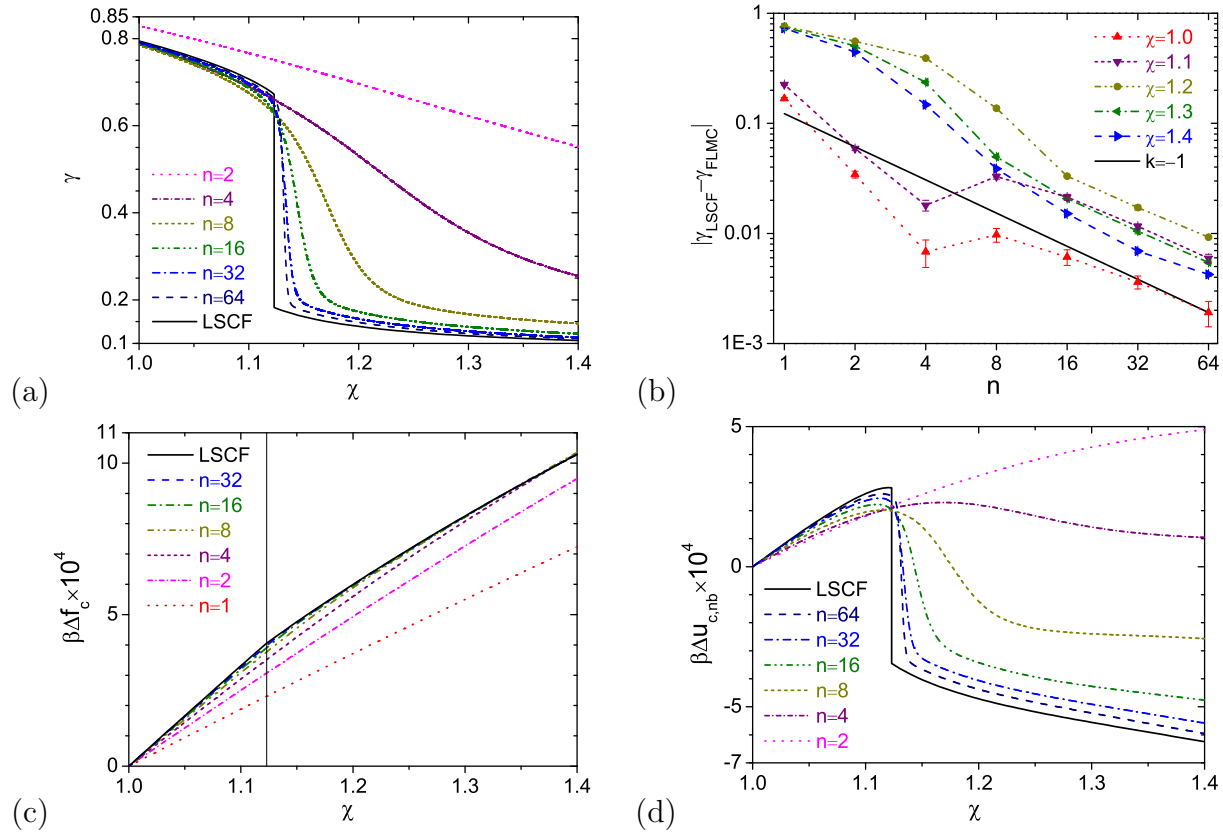

Figure 2.13: Comparisons between FLMC results of two-mushroom systems at various n and the corresponding LSCF predictions: (a) γ; (b) $|\gamma_{\rm LSCF} - \gamma_{\rm FLMC}|$ on a logarithmic plot, where $\gamma_{\rm FLMC} < \gamma_{\rm LSCF}$ for $\chi = 1.0$ and 1.1 (except at $n = 1$ and 2) and $\gamma_{\rm FLMC} > \gamma_{\rm LSCF}$ for $\chi = 1.2 \sim 1.4$, and "$k = -1$" denotes a straight line of slope -1; (c) $\beta\Delta f_c \equiv \beta[f_c(\chi) - f_c(\chi = 1)]$, where the vertical line marks $\chi^*_{\rm FST} = 1.123$; and (d) $\beta\Delta u_{c,\rm nb} \equiv \beta[u_{c,\rm nb}(\chi) - u_{c,\rm nb}(\chi = 1)]$. $n/\rho_0 = 1/3$, $d = 8$, and $N = 40$.

2.4 Conclusions

Using the recently proposed fast lattice Monte Carlo (FLMC) simulations[1] and corresponding lattice self-consistent field (LSCF) calculations based on the same model system, where each lattice site is occupied by totally $\rho_0 > 1$ polymer segments and solvent molecules, we have studied the coil-globule transition (CGT) of one-mushroom systems and the fused-separated transition (FST) of two-mushroom systems. Here a polymer mushroom is formed by a group of n flexible and uncharged homopolymer chains each of N segments end-grafted at the same point onto a planar, homogeneous and neutral (non-selective) substrate, and

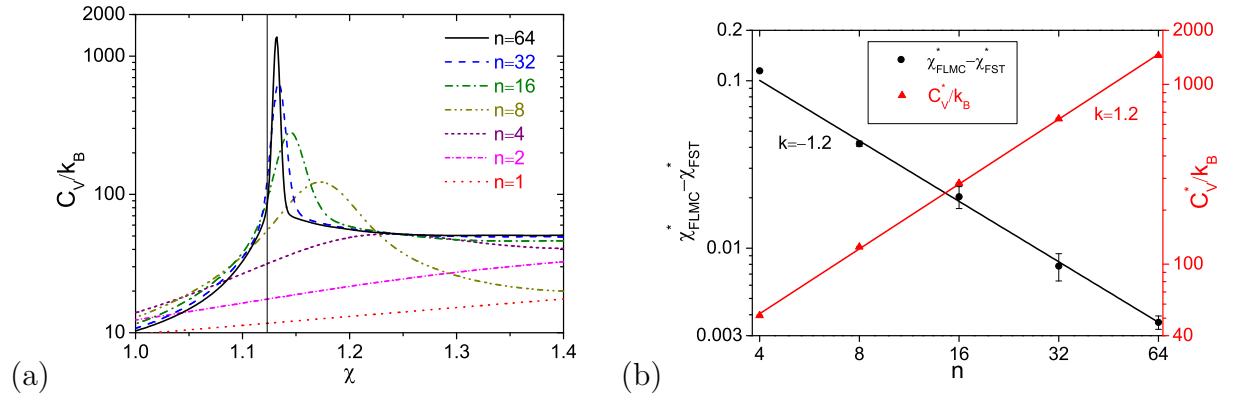

Figure 2.14: FLMC simulations of two-mushroom systems of various n: (a) constant-volume heat capacity C_V, where the vertical line marks the LSCF prediction $\chi^*_{\rm FST} = 1.123$; and (b) logarithmic plots of its peak value C^*_V corresponding to FST and its peak location $\chi^*_{\rm FLMC}$, where the k-value near each fitted line gives the slope. $n/\rho_0 = 1/3$, $d = 8$, and $N = 40$.

immersed in an explicit solvent. With soft potential that allows complete particle overlapping, N becomes a chain discretization parameter that does not correspond to the actual chain length used in experiments,[14] and in the limit of $n \to \infty$ the LSCF theory neglecting the system fluctuations/correlations becomes exact. Furthermore, direct comparisons between our FLMC simulations at finite n with the corresponding LSCF results, without any parameter-fitting, can unambiguously and quantitatively reveal the fluctuation/correlation effects on phase transitions such as CGT and FST.[1]

Using LSCF calculations, we have systematically constructed the phase diagrams of one-mushroom systems as a function of the average polymer volume fraction $\bar{\phi}_{\rm A} \equiv nN/\rho_0 V$, and the Flory-Huggins interaction parameter χ between polymer segments and solvent molecules at the same lattice site. With $N = 40$ used in most cases, CGT of the one-mushroom system is found to be of the first-order when $n/\rho_0 < (n/\rho_0)_c$ and a crossover when $n/\rho_0 > (n/\rho_0)_c$; the critical point is located at $(n/\rho_0)_c \approx 0.276$ and $\chi_c \approx 1.224$. The globule state has lower chain expansion factor α^2, bonded internal energy per chain $\beta u_{c,\rm b}$, non-bonded internal energy per chain $\beta u_{c,\rm nb}$, and entropy per chain s_c/k_B than the coil state. The grafting substrate shifts the critical point to smaller χ_c and larger $(n/\rho_0)_c$, and a larger chain length of $N = 80$ shifts it to $\chi_c \approx 0.950$ and $(n/\rho_0)_c \approx 0.317$.

While one expects that the simulation results approach the LSCF predictions with increasing n (i.e., ρ_0), which is indeed found in the coil state of one-mushroom systems, contradiction to this expectation leads us to the discovery of a second-order symmetric-asymmetric transition (SAT) in such systems in a poor solvent (i.e., in the globule state), which occurs at $\chi^*_{\rm SAT}$. In the asymmetric globule states, the rotational symmetry around the substrate normal passing through the grafting point is broken in each individual configuration but preserved by the degeneracy of different orientations of these asymmetric configurations. At given $\chi > \chi^*_{\rm SAT}$, our LSCF calculations show that the asymmetric states have lower α^2, $\beta u_{c,\rm b}$, $\beta u_{c,\rm nb}$, and s_c/k_B than the symmetric state. The existence of asymmetric globule states and SAT are confirmed by both LSCF calculations and FLMC simulations. Our simulations further show that the asymmetric states and SAT are gradually destroyed by increasing system fluctuations, which also change the location of SAT from $\chi^*_{\rm SAT}$ predicted by the LSCF theory. To the best of our knowledge, the asymmetric states and SAT of polymer mushrooms have not been reported in the literature.

For one-mushroom systems, taking LSCF predictions to be those in the most stable state, we find that FLMC results of various quantities (including α^2, the polymer segmental density profile, and the differences from a reference state in the Helmholtz free energy per chain βf_c, $\beta u_{c,\rm b}$, $\beta u_{c,\rm nb}$, and s_c/k_B) approach the corresponding LSCF predictions at a rate of $1/n$ at large n in both the coil and globule states, except near the transitions. We further find that the peak value of the constant-volume heat capacity $C^*_V/k_B \propto n$ at large n when CGT is a first-order transition, but increases much slower with increasing n and should remain finite in the limit of $n \to \infty$ when it is a crossover. We also find that $C^*_V/k_B \propto n^{0.17}$ at large n for the second-order SAT.

We have also studied two-mushroom systems, which exhibit FST as the solvent quality varies. We find that FST is a crossover for small d, the distance between the grafting points of the two mushrooms, and a first-order phase transition for intermediate d. In the latter case, the fused state, where the two mushrooms stretch and fuse together to avoid the unfavorable

contact with the poor solvent, has lower βu_c and s_c/k_B than the separated state, and their competition leads to FST occurring at $\chi^*_{\rm FST}$, which increases with increasing d. For large d, FST does not occur due to the excessive chain-stretching required for the two mushrooms to fuse together. Using LSCF calculations, we have systematically constructed the phase diagrams of two-mushroom systems as a function of $\bar{\phi}_{\rm A}$, χ, and d. We find three different states of two-mushroom systems: separated coils, separated globules, and fused globule, and that both CGT and SAT of each mushroom could be pre-empted by FST.

Finally, similar to one-mushroom systems, we find that the FLMC results of various quantities (including the fusion factor γ and the differences from a reference state in βf_c, $\beta u_{c,\rm b}$, $\beta u_{c,\rm nb}$, and s_c/k_B) in two-mushroom systems approach the corresponding LSCF predictions at a rate of $1/n$ at large n in both the separated and fused states. We also find that $C^*_V/k_B \propto n^{1.2}$ at large n when FST is a first-order transition.

REFERENCES

[1] Q. Wang, Soft Matter **5**, 4564 (2009); *ibid.* **5**, 6206 (2010).

[2] P. Zhang, X. Zhang, B. Li, and Q. Wang, Soft Matter **7**, 4461 (2011).

[3] P. Zhang, B. Li, and Q. Wang, Macromolecules **44**, 7837 (2011).

[4] P. Zhang, B. Li, and Q. Wang, Macromolecules **45**, 2537 (2012).

[5] P. Zhang and Q. Wang, J. Chem. Phys. **140**, 044904 (2014).

[6] C. Williams, F. Brochard, and H. L. Frisch, Ann. Rev. Phys. Chem. **32**, 433 (1981).

[7] B. M. Baysal and F. E. Karasz, Macromol. Theory Simul. **12**, 627 (2003).

[8] M. Milik and A. Orszagh, Ploymer **30**, 681 (1989).

[9] M. Milik and A. Orszagh, Ploymer **31**, 506 (1990).

[10] D. R. M. Williams, J. Phys. II France **3**, 1313 (1993).

[11] H. Tang and I. Szleifer, Euro. phys. Lett. **28**, 19 (1994).

[12] H. S. Ashbaugh, H. A. Patel, S. K. Kumar, and S. Garde, J. Chem. Phys. **122**, 104908 (2005).

[13] L.-J. Chen, H.-J. Qian, Z.-Y. Lu, Z.-S. Li, and C.-C. Sun, J. Phys. Chem. B **110**, 24093 (2006).

[14] J. Zong and Q. Wang, J. Chem. Phys. **139**, 124907 (2013).

[15] G. H. Fredrickson, *The Equilibrium Theory of Inhomogeneous Polymers* (University Press, Oxford, 2006).

[16] L. Leibler, Macromolecules **13**, 1602 (1980).

[17] G. H. Fredrickson and E. Helfand, J. Chem. Phys. **87**, 697 (1987).

[18] P. J. Flory, *Principles of Polymer Chemistry* (Cornell university Press, Ithaca, 1952).

[19] O. B. Ptitsyn and Yu. Ye. Eizner, Biofizika **10**, 3 (1965).

[20] O. B. Ptitsyn, A. K. Kron, and Yu. Ye. Eizner, J. Polym. Sci.: Part C **16**, 3509 (1968).

[21] Yu. Ye. Eizner, Polym. Sci. USSR. **11**, 409 (1969).

[22] P. G. de Gennes, J. Phys. (Paris) **36**, L55 (1975).

[23] C. B. Post and B. H. Zimm, Biopolym. **18**, 1487 (1979).

[24] I. C. Sanchez, Macromolecules **12**, 980 (1979).

[25] T. M. Birshtein and V. A. Pryamitsyn, Macromolecules **24**, 1554 (1991).

[26] A. Y. Grosberg and D. V. Kuznetsov, Macromolecules **25**, 1970 (1992).

[27] M. A. Moore, J. Phys. A: Math. Gen. **10**, 305 (1977).

[28] M. Muthukumar, J. Chem. Phys. **81**, 6272 (1984).

[29] D. Yang and Q. Wang, ACS Macro Lett. **2**, 952 (2013).

[30] A. Halperin, J. Phys. France **49**, 547 (1988).

[31] S. K. Pattanayek, T. T. Pham, and G. G. Pereira, J. Chem. Phys. **122**, 214908 (2005).

[32] Q. Wang, J. Chem. Phys. **131**, 234903 (2009).

[33] R. B. Thompson, K. Ø. Rasmussen, and T. Lookman, J. Chem. Phys. **120**, 31 (2004).

[34] M. W. Matsen, Eur. Phys. J. E **30**, 361 (2009).

[35] F. Drolet and G. H. Fredrickson, Phys. Rev. Lett. **83**, 4317 (1999).

[36] D. Frenkel and B. Smit, Appendix D in *Understanding Molecular Simulation: From Algorithms to Applications* (Academic Press, San Diego, 2002).

[37] R. H. Swendsen and J. S. Wang, Phys. Rev. Lett. **57**, 2607 (1986).

[38] A. M. Ferrenberg and R. H. Swendsen, Phys. Rev. Lett. **63**, 1195 (1989).

[39] W. H. Press, S. A. Teukolsky, W. T. Vetterling, and B. P. Flannery, Chap. 9 in *Numerical Recipes in C*, 2nd ed. (Cambridge University Press, New York, 1992).

[40] H. B. Callen, Chap. 10 in *Thermodynamics and an Introduction to Thermostatistics* (John Wiley & Son, New York, 1985).

CHAPTER 3

FLUCTUATION/CORRELATION EFFECTS IN DISORDERED SYMMETRIC DIBLOCK COPOLYMERS

3.1 Introduction

Diblock copolymers (DBC) have attracted great interest not only due to their applications (e.g., in nanotechnology) but also the underlying physics, especially for its behavior of microphase transition.[1] The system fluctuation/correlation (F/C) effects plays very important role in both ordered and disordered phases for DBC systems. Unfortunately, the studies of F/C effects in conventional simulations of multi-chain systems with hard-core repulsions are not in the experimentally accessible $\bar{\mathcal{N}}$ range in most cases (at most 100 or so), where the invariant degree of polymerization $\bar{\mathcal{N}} \equiv (nR_{e,0}^3/V)^2$ controls the system fluctuations for n monodisperse copolymer chains in volume V with $R_{e,0}$ denoting the root-mean-square end-to-end distance of an ideal chain;[2] in contrast, with soft potentials one can study systems of much larger $\bar{\mathcal{N}}$ values, like presented in the recent paper[3] by our group (referred to as Paper I hereafter). Furthermore the use of soft potential allow us to directly compare the results of simulation and various theories, and thus to quantify the F/C effects neglected or treated approximately in theories, based on the same model system without any parameter fitting.

In Paper I, the authors systematically quantify the F/C effects on the ordered-disordered transition (ODT) of compressible symmetric DBC with soft potential in the experimental acceptable $\bar{\mathcal{N}}$ range by comparing the results of fast off-lattice Monte Carlo (FOMC) simulations[4] and random phase approximation (RPA)[5] based on the same Hamiltonian. In this work, on the other hand, the F/C effects on the structural and thermodynamic properties

of compressible DBC with soft potential in disordered phase will be investigated based on the same model system thus without any parameter-fitting. To do this, we directly compare the simulation results to the self-consistent field (SCF) theory,[6] Gaussian fluctuation (GF) theory[6] and integral equation (IE)[7–9] theory, which consider different levels of fluctuation and/or correlations.

Polymer field theories, in particular the well developed SCF theory, have been widely applied to various polymeric systems. Due to neglecting the interchain F/C effects in the system, SCF theory provides a well understood reference for the F/C effects study, which still preserves the intrachain correlations among different segments due to the bonding interactions. On the other hand, systematic one-loop expansions can be used to incorporate these effects into the field theories.[10] The Zero-order expansion leads to the SCF theory, and the second-order expansion leads to the GF theory.[6] Based on Leibler's RPA analysis[5] up to the fourth order in mean field, about 25 years ago, Fredrickson and Helfand (FH) presented so far the most influential fluctuation theory for DBC, which used the Hartree analysis of Brazovskii[11] and the Ohta-Kawasaki effective Hamiltonian[12] for the "standard" model of incompressible DBC melts of continuous Gaussian chains with Dirac δ-function interactions. Based on the one-loop approximation and the renormalization treatment of homopolymer blends of Wang,[13] Morse and co-workers[14–17] developed a renormalized one-loop theory for both incompressible DBC and homopolymer blends to correct the structure factor predicted by RPA and to obtain an effective Flory-Huggins interaction parameter. In the present study, for the purpose of study of F/C effects, we only consider the GF theory applied for compressible DBC containing fluctuations and correlations at the Gaussian level.

The second theory we use in this study is the integral equation (IE) theory, including the reference interaction site model (RISM)[19–22] and polymer reference interaction site model (PRISM),[7–9] which describe the relation between the intrachain and interchain pair correlation functions (PCF) by the well known Ornstein-Zernike (OZ) equation,[18] where the local packing and density fluctuations are described. The OZ equation was first introduced by

Ornstein and Zernike[18] for spherical monatomic liquid systems, which was extended to a simple molecular system leading to the so called RISM theory by Chandler and Anderson,[19] where the intrachain PCF are considered and thus the correlations can be propagated both intrachainly and interchainly. The RISM theory of Chandler and Anderson was then extended to the polymer liquid systems by Curro and Schweizer,[9] and this application is the well known PRISM theory, which was successfully used in various polymer liquid systems including homopolymer melts,[23] polymer blends[24] and copolymers.[25–28] In their PRISM theory, comparing the RISM theory, the interchain PCFs are considered independent on the interacting site pair position and thus the chain end effects are neglected, which is only valid for ring chains or infinite long chains. Additionally, they also considered the fact that the excluded-volume effects are screened by the surrounding identical chains for large $\bar{\mathcal{N}}$ systems, and thus the intrachain PCFs are assumed to exhibit ideal-chain behavior. On the other hand, as the temperature decreases for copolymers, polymer blends or polymer solution, the ideal-chain assumption is not valid any more; to solve this problem the self-consistent IE (SCIE) theory[29–32] was proposed, where the P/RISM equation was combined with single-chain simulation in solvation potential.[33,34] For the purpose of study of F/C effects, here we do not consider the SCIE theory, but use the RISM theory with chain conformations of ideal chains or from FOMC simulations in this study.

RISM equation defines the interchain direct PCF, $c(r)$, but it cannot be solved without a specific closure approximation, which gives the relation between $c(r)$ and the interchain total PCF, $h(r)$. The commonly used atomic closure includes the mean spherical approximation (MSA) closure,[35] Percus-Yevick (PY) closure[36] and hypernetted chain (HNC) closure,[37] where the PY closure can be considered as the linear version of HNC closure with respect of the indirect PCF $\gamma(r) = h(r) - c(r)$ and the MSA closure is obtained by expanding HNC closure to the first order of $h(r)$. While MSA closure can make the RISM equation to be solved analytically, its prediction disagrees with most experimental and simulation results. As we explained in the next section, the RISM theory with MSA closure is equivalent to

the GF theory, containing fluctuations and correlations only at the Gaussian level. The PY closure and HNC closure were both successfully applied for various polymer systems, but considering that the PY closure is more applicable for the repulsive short-range potential,[38] like the dissipative particle dynamic (DPD) potential[39] used in this study, the PY closure will be used in most cases here. Note that the above closure are originally proposed for hard-core repulsion, i.e., $h(r) = -1$ inside of the hard-core diameter, here we extend their applications to the whole interaction range for soft potential, like the treatment for penetrable spheres.[40–42] In addition to PY closure, we also consider one more closure. Viererblová et al[42] tested various closures for penetrable spheres and found that one closure proposed by Zhou[43] (referred to Zhou closure) gives the most accuracy at high density and interaction strength, which has never been investigated for polymeric system. But due to its own limitation of application, here we apply Zhou closure to our model systems in some cases for illustrative purpose.

As mentioned early, the F/C effects plays very important role in both ordered and disordered phases for DBC systems. On the other hand, in the comparison among simulations and theories, the SCF theory neglects all of the interchain fluctuations and correlations, the GF theory only considers the fluctuations in the Gaussian level, RISM theory with PY closure considers the correlations in the "PY level", and in the FOMC simulations all kinds of fluctuations and correlations are included. But as shown in the next section, both fluctuation and correlation effects can be reflected by a structural or thermodynamic property, for example the structure factor or the internal energy. Therefore, we can directly compare the structural or thermodynamic properties from all the methods considered in this study, and their difference thus reflects the F/C effects for the system; and one key point here is that the comparison is based on the same model system with soft potential and thus the F/C effects can be unambiguously quantified without any parameter fitting.

This Chapter is structured as follows. In the second section, we firstly introduce our model system with soft DPD potential and define some notations, where the discrete Gaussian chain

(DGC) model is used, following some simple description about FOMC; then the derivation of GF theory and P/RISM theories are simply presented, where the equations of how to calculate the interested structural and thermodynamic properties are also presented. In the third section, these properties are compared among FOMC simulations and theories, including the block/chain mean-square end-to-end distances, the bonding and non-bonded internal energy per chain and pressure, the Helmholtz free energy per chain, the non-bonded constant-volume heat capacity, and the structure factors. We then make some conclusions and remarks in the fourth section.

3.2 Model and Methods

3.2.1 Model system

In our model system, we consider compressible DBC systems of n chains in continuum, each consisting of N segments at a chain number density $\rho_c \equiv n/V$ with V being the system volume. Each polymer chain has $N_{\rm A}$ A-type segments followed by $N_{\rm B}$ B-type segments, and $N = N_{\rm A} + N_{\rm B}$; for symmetric DBC $N_{\rm A} = N_{\rm B}$. The canonical-ensemble partition function of the system is

$$\mathcal{Z} = \frac{1}{n!} \prod_{k=1}^{n} \prod_{s=1}^{N} \int \mathrm{d}\mathbf{R}_{k,s} \cdot \exp\left\{-\beta \mathcal{H}^C - \beta \mathcal{H}^E\right\}, \tag{3.1}$$

where $\mathcal{H}^C = \sum_{k=1}^{n} h_k^C$ is the Hamiltonian due to the chain connectivity, with h_k^C denoting the contribution of the $k^{\rm th}$ chain, described by the discrete Gaussian chain (DGC) model in 3D, i.e.,

$$\beta h_k^C = \frac{3}{2a^2} \sum_{s=1}^{N-1} \left(\mathbf{R}_{k,s+1} - \mathbf{R}_{k,s}\right)^2, \tag{3.2}$$

where $\beta \equiv 1/k_B T$ with k_B being the Boltzmann constant and T the thermodynamic temperature, a denotes the effective bond length (assumed to be the same for both A and B blocks), and $\mathbf{R}_{k,s}$ denotes the spatial position of the $s^{\rm th}$ segment on the $k^{\rm th}$ chain. The non-bonded Hamiltonian $\mathcal{H}^E = \mathcal{H}^E_\kappa + \mathcal{H}^E_\chi$, with $\mathcal{H}^E_\kappa$ and $\mathcal{H}^E_\chi$ are respectively given by

$$\mathcal{H}^E_\kappa = \frac{1}{2\kappa\rho_0} \int \mathrm{d}\mathbf{r}\mathrm{d}\mathbf{r}' \left[\hat{\rho}_{\rm A}(\mathbf{r}) + \hat{\rho}_{\rm B}(\mathbf{r})\right] u_0(|\mathbf{r} - \mathbf{r}'|) \left[\hat{\rho}_{\rm A}(\mathbf{r}') + \hat{\rho}_{\rm B}(\mathbf{r}')\right] - \frac{nN}{2\kappa\rho_0} u_0(0), \tag{3.3}$$

$$\mathcal{H}_{\chi}^{E} = \frac{\chi}{\rho_0} \int \mathrm{d}\mathbf{r}\mathrm{d}\mathbf{r}' \hat{\rho}_{\mathrm{A}}(\mathbf{r}) u_0(|\mathbf{r}-\mathbf{r}'|) \hat{\rho}_{\mathrm{B}}(\mathbf{r}'), \tag{3.4}$$

where Eq. (3.3) is due to the system compressibility characterized by the generalized Helfand compressibility κ,[44] with the last term used to deduct the self-interaction, and Eq. (3.4) models the repulsion between A and B segments with the generalized Flory-Huggins interaction parameter χ. $\rho_0 \equiv nN/V$ is the average segmental density, and the microscopic densities of A and B segments are defined as $\hat{\rho}_{\mathrm{A}}(\mathbf{r}) \equiv \sum_{k=1}^{n} \sum_{s=1}^{N_{\mathrm{A}}} \delta(\mathbf{r}-\mathbf{R}_{k,s})$ and $\hat{\rho}_{\mathrm{B}}(\mathbf{r}) \equiv \sum_{k=1}^{n} \sum_{s=N_{\mathrm{A}}+1}^{N} \delta(\mathbf{r}-\mathbf{R}_{k,s})$, respectively. $u_0(|\mathbf{r}-\mathbf{r}'|)$ is the normalized and isotropic pair potential, i.e., $\int \mathrm{d}\mathbf{r} u_0(|\mathbf{r}-\mathbf{r}'|) = k_B T$, and is taken to be $\beta u_0(r) = (15/2\pi\sigma^3)(1-r/\sigma)^2\theta(\sigma-r)$ as commonly used in the dissipative particle dynamics (DPD) simulations,[39] with $r \equiv |\mathbf{r}|$ being the separation distance between two segments, σ the finite interaction range, and $\theta(r)$ the Heaviside step-function. The soft repulsive pair potential between two segments s and s' is therefore given by

$$\beta u_{s,s'}(r) = \begin{cases} \frac{N}{\kappa}\frac{\beta u_0(r)}{\rho_0 N} & \text{if } s \text{ and } s' \text{ are of the same type} \\ (\frac{N}{\kappa} + \chi N)\frac{\beta u_0(r)}{\rho_0 N} & \text{otherwise} \end{cases}. \tag{3.5}$$

which recovers the hard-sphere potential as $N/\kappa \to \infty$.

Alternatively, $\mathcal{H}^E$ can be rewritten as

$$\beta\mathcal{H}^E = \frac{nN}{2\kappa}\left[1 - \frac{\beta u_0(0)}{\rho_0}\right] + n\chi N f_{\mathrm{A}} f_{\mathrm{B}} + \frac{N}{\kappa} E_{\kappa} + \chi N E_{\chi} \tag{3.6}$$

where $E_{\kappa} \equiv (1/2\rho_0)\int \mathrm{d}\mathbf{r}\mathrm{d}\mathbf{r}' \delta\hat{\boldsymbol{\rho}}(\mathbf{r})\cdot\mathbf{u}_{\kappa}(|\mathbf{r}-\mathbf{r}'|)\delta\hat{\boldsymbol{\rho}}(\mathbf{r}')$ and $E_{\chi} \equiv (1/2\rho_0)\int \mathrm{d}\mathbf{r}\mathrm{d}\mathbf{r}' \delta\hat{\boldsymbol{\rho}}(\mathbf{r})\cdot\mathbf{u}_{\chi}(|\mathbf{r}-\mathbf{r}'|)\delta\hat{\boldsymbol{\rho}}(\mathbf{r}')$ measure the "contact" of all segments (regardless of their type) and that between A and B segments, respectively, beyond the mean-field values (i.e., those for random mixing of all segments). Here the vector $\delta\hat{\boldsymbol{\rho}}(\mathbf{r}) \equiv \hat{\boldsymbol{\rho}}(\mathbf{r}) - \boldsymbol{\rho}_0$, $\hat{\boldsymbol{\rho}}(\mathbf{r}) = [\hat{\rho}_{\mathrm{A}}(\mathbf{r}), \hat{\rho}_{\mathrm{B}}(\mathbf{r})]^T$ and $\boldsymbol{\rho}_0 = \rho_0[f_{\mathrm{A}}, f_{\mathrm{B}}]^T$ with $f_{\mathrm{A}} \equiv N_{\mathrm{A}}/N$ and $f_{\mathrm{B}} = 1 - f_{\mathrm{A}}$ being the average volume fraction of A and B blocks, respectively, and the 2×2 matrices $\mathbf{u}_{\kappa}(\mathbf{r}) \equiv [\beta u_0(\mathbf{r})/N]\begin{bmatrix} 1 & 1 \\ 1 & 1 \end{bmatrix}$ and $\mathbf{u}_{\chi}(\mathbf{r}) \equiv [\beta u_0(\mathbf{r})/N]\begin{bmatrix} 0 & 1 \\ 1 & 0 \end{bmatrix}$. The non-bonded internal energy per chain is then given by

$$\beta u_{c,\mathrm{nb}} \equiv \frac{\langle \beta\mathcal{H}^E \rangle}{n} = \frac{N}{2\kappa}\left[1 - \frac{\beta u_0(0)}{\rho_0}\right] + \chi N f_{\mathrm{A}} f_{\mathrm{B}} + \frac{N}{\kappa}\frac{\langle E_{\kappa}\rangle}{n} + \chi N \frac{\langle E_{\chi}\rangle}{n}, \tag{3.7}$$

and the difference in the Helmholtz free energy per chain from the reference state at $N/\kappa = \chi N = 0$ (i.e., ideal chains) can be calculated via the thermodynamic integration as

$$\beta\Delta f_c = \frac{N}{2\kappa}\left[1 - \frac{\beta u_0(0)}{\rho_0}\right] + \chi N f_{\rm A} f_{\rm B} + \frac{1}{n}\int_0^{N/\kappa} \langle E_\kappa \rangle_{N/\kappa,\chi N=0}\, {\rm d}\left(\frac{N}{\kappa}\right) + \frac{1}{n}\int_0^{\chi N} \langle E_\chi \rangle_{N/\kappa,\chi N}\, {\rm d}\left(\chi N\right). \tag{3.8}$$

Finally, the fluctuations of E_κ and E_χ are given by

$$\sigma_\kappa^2 \equiv \left\langle E_\kappa^2 \right\rangle - \left\langle E_\kappa \right\rangle^2 = -\frac{\partial \left\langle E_\kappa \right\rangle}{\partial(N/\kappa)} \tag{3.9}$$

$$\sigma_\chi^2 \equiv \left\langle E_\chi^2 \right\rangle - \left\langle E_\chi \right\rangle^2 = -\frac{\partial \left\langle E_\chi \right\rangle}{\partial(\chi N)} \tag{3.10}$$

$$\sigma_{\kappa,\chi}^2 \equiv \left\langle E_\kappa E_\chi \right\rangle - \left\langle E_\kappa \right\rangle \left\langle E_\chi \right\rangle = -\frac{\partial \left\langle E_\kappa \right\rangle}{\partial(\chi N)} = -\frac{\partial \left\langle E_\chi \right\rangle}{\partial(N/\kappa)}, \tag{3.11}$$

from which the non-bonded constant-volume heat capacity is calculated as

$$\frac{C_{V,\rm nb}}{k_B} = \frac{1}{n}\left[(N/\kappa)^2\sigma_\kappa^2 + (\chi N)^2\sigma_\chi^2 + 2(N/\kappa)(\chi N)\sigma_{\kappa,\chi}^2\right]. \tag{3.12}$$

3.2.2 Fast off-lattice Monte Carlo (FOMC) simulations

We perform FOMC simulations of the above model system in a canonical ensemble with trial moves of hopping,[4] reptation,[4] pivot,[3] and box-length change,[3] where replica-exchange of configurations at different χN is used to further improve the sampling efficiency; more details are given in Paper I. Note that our simulations are preformed in a variable-length, rectangular parallelepipedal box with the periodic boundary conditions applied in all direction. For the disordered phase close to the order-disordered transition (ODT), the box-length change trial moves are needed to eliminate the effects of the periodic boundary conditions on the system fluctuations.[3]

In our simulations, we calculate $E_\kappa = (1/2\rho_0 N)\sum_{k,k'=1}^{n}\sum_{s,s'=1}^{N}\beta u_0(|\mathbf{R}_{k,s} - \mathbf{R}_{k',s'}|) - n/2$ and $E_\chi = (1/\rho_0 N)\sum_{k,k'=1}^{n}\sum_{s=1}^{N_{\rm A}}\sum_{s'=N_{\rm A}+1}^{N}\beta u_0(|\mathbf{R}_{k,s} - \mathbf{R}_{k',s'}|) - n/4$, and their fluctuations according to Eqs. (3.9)$\sim$(3.11) using the second-order finite central difference after their ensemble averages are obtained.

3.2.3 Polymer field theories

Here we start from the same model system as in Sec. 3.2.1 and insert the identity $1 = \prod_{\mathrm{P=A,B}} \int \mathcal{D}\rho_{\mathrm{P}} \mathcal{D} \left(\omega_{\mathrm{P}}/2\pi\right) \exp\left\{\int \mathrm{d}\mathbf{r} i\omega_{\mathrm{P}}(\mathbf{r})[\rho_{\mathrm{P}}(\mathbf{r}) - \hat{\rho}_{\mathrm{P}}(\mathbf{r})]\right\}$ into Eq. (3.1), where $\rho_{\mathrm{P}}(\mathbf{r})$ is the density field constrained to $\hat{\rho}_{\mathrm{P}}(\mathbf{r})$ and $\omega_{\mathrm{P}}(\mathbf{r})$ is the conjugate field imposing this constraint. The partition function can finally be re-written as

$$\begin{aligned}\mathcal{Z} =& \prod_{\mathrm{P}} \int \mathcal{D}\rho_{\mathrm{P}} \mathcal{D} \left(\frac{\omega_{\mathrm{P}}}{2\pi}\right) \cdot \exp\left\{-\beta \mathcal{F}[\rho_{\mathrm{P}}, \omega_{\mathrm{P}}]\right\} \\ =& \exp\left\{-\beta \mathcal{F}^{id}\right\} \prod_{\mathrm{P}} \int \mathcal{D}\rho_{\mathrm{P}} \cdot \exp\left\{-\beta \mathcal{H}^{E}[\rho_{\mathrm{A}}, \rho_{\mathrm{B}}]\right\} \\ & \times \prod_{\mathrm{P}} \mathcal{D} \left(\frac{\omega_{\mathrm{P}}}{2\pi}\right) \cdot \exp\left\{-\beta \mathcal{F}^{en}[\rho_{\mathrm{A}}, \rho_{\mathrm{B}}, \omega_{\mathrm{A}}, \omega_{\mathrm{B}}]\right\}, \end{aligned} \tag{3.13}$$

where $\beta\mathcal{F}^{id} \equiv -\ln(G^n/n!)$ is the Helmholtz free energy of ideal chains with $G \equiv \prod_{s=1}^{N} \int \mathrm{d}\mathbf{R}_s \cdot \exp\left\{-\beta h^C\right\}$, and $\beta\mathcal{F}^{en} \equiv -\sum_{\mathrm{P}} \int \mathrm{d}\mathbf{r} i\omega_{\mathrm{P}}(\mathbf{r})\rho_{\mathrm{P}}(\mathbf{r}) - n \ln Q[i\omega_{\mathrm{A}}, i\omega_{\mathrm{B}}]$ is the entropic contribution from chain configurations with the single-chain partition function $Q \equiv \prod_{s=1}^{N} \int \mathrm{d}\mathbf{R}_s \cdot \exp\left\{-\beta h^C - i\sum_{s=1}^{N_{\mathrm{A}}} \omega_{\mathrm{A}}(\mathbf{R}_s) - i\sum_{s=N_{\mathrm{A}}+1}^{N} \omega_{\mathrm{B}}(\mathbf{R}_s)\right\} \Big/ G$.

3.2.3.1 Self-consistent field (SCF) theory

The SCF solution, $\boldsymbol{\omega}^* \equiv [\omega_{\mathrm{A}}^*(\mathbf{r}), \omega_{\mathrm{B}}^*(\mathbf{r})]^T$ and $\boldsymbol{\rho}^* \equiv [\rho_{\mathrm{A}}^*(\mathbf{r}), \rho_{\mathrm{B}}^*(\mathbf{r})]^T$, is obtained under the mean-field approximation $[\delta\mathcal{F}^{en}/\delta i\omega_{\mathrm{P}}(\mathbf{r})]\big|_{\boldsymbol{\omega}^*,\boldsymbol{\rho}^*} = [\delta(\mathcal{H}^E + \mathcal{F}^{en})/\delta\rho_{\mathrm{P}}(\mathbf{r})]\big|_{\boldsymbol{\omega}^*,\boldsymbol{\rho}^*} = 0$. In this study we only consider the homogeneous phase, i.e., $\boldsymbol{\rho}^* = \boldsymbol{\rho}_0$ and $\boldsymbol{\omega}^* = \mathbf{0}$. SCF theory then gives $\langle E_\kappa \rangle^{\mathrm{SCF}} = \langle E_\chi \rangle^{\mathrm{SCF}} = 0$, $\beta\Delta f_c^{\mathrm{SCF}} = \beta u_{c,\mathrm{nb}}^{\mathrm{SCF}} = (N/2\kappa)[1-\beta u_0(0)/\rho_0] + \chi N f_{\mathrm{A}} f_{\mathrm{B}}$ with $u_{c,\mathrm{nb}}$ being the non-bonded internal energy per chain, the difference in the entropy per chain from the ideal-chain reference state $\Delta s_c^{\mathrm{SCF}}/k_B = \beta u_{c,\mathrm{b}}^{\mathrm{SCF}} = 1.5(N-1)$ with $u_{c,\mathrm{b}}$ being the bonding energy per chain, the pressure due to the bonding interactions $\beta P_{\mathrm{b}}^{\mathrm{SCF}} = -\rho_c(N-1)$ and that due to the non-bonded interactions $\beta P_{\mathrm{nb}}^{\mathrm{SCF}} = \rho_c(N/2\kappa + \chi N f_{\mathrm{A}} f_{\mathrm{B}})$, and the constant-volume heat capacity $C_V^{\mathrm{SCF}}/k_B = C_{V,\mathrm{b}}^{\mathrm{SCF}}/k_B = 1.5(N-1)$ with $C_{V,\mathrm{b}}$ being the bonding contribution and the non-bonded contribution $C_{V,\mathrm{nb}}^{\mathrm{SCF}} = 0$. As for the chain dimensions, SCF theory gives random walk for a homogeneous system, e.g., $R_{e,\mathrm{SCF}}^2 = (N-1)a^2$.

3.2.3.2 Random-phase approximation (RPA) and Gaussian-fluctuation (GF) theory

In RPA analysis,[4,5,45] the fields are re-written as $\boldsymbol{\omega}(\mathbf{r}) = \boldsymbol{\omega}^* + \delta\boldsymbol{\omega}(\mathbf{r})$ and $\boldsymbol{\rho}(\mathbf{r}) = \boldsymbol{\rho}^* + \delta\boldsymbol{\rho}(\mathbf{r})$, where $\boldsymbol{\omega}(\mathbf{r})$ and $\boldsymbol{\rho}(\mathbf{r})$ are defined similarly to $\hat{\boldsymbol{\rho}}(\mathbf{r})$. The single-chain partition function can then be expanded to the second order in $\delta\boldsymbol{\omega}(\mathbf{r})$ as

$$\ln Q[i\boldsymbol{\omega}] \approx \ln Q[i\boldsymbol{\omega}^*] - \frac{N}{2V}\int \frac{\mathrm{d}\mathbf{q}}{(2\pi)^3}\delta\hat{\boldsymbol{\omega}}(\mathbf{q})\cdot\mathbf{S}_1(q)\delta\hat{\boldsymbol{\omega}}(-\mathbf{q}). \tag{3.14}$$

where $\delta\hat{\boldsymbol{\omega}}(\mathbf{q})$ denotes the Fourier transform of $\delta\boldsymbol{\omega}(\mathbf{r})$ with $\mathbf{q}$ being the wavevector, $\mathbf{S}_1(q)$ is the single-chain structure factor matrix with its element $S_{1,\mathrm{PP'}}(q)$ being the intrachain correlation functions between P and P′ blocks, and $q = |\mathbf{q}|$. For an ideal DGC, $S_{1,\mathrm{AA}}(q) = NP(f_\mathrm{A}, q)$, $S_{1,\mathrm{BB}}(q) = NP(1-f_\mathrm{A}, q)$, and $S_{1,\mathrm{AB}}(q) = S_{1,\mathrm{BA}}(q) = [NP(1,q) - S_{1,\mathrm{AA}}(q) - S_{1,\mathrm{BB}}(q)]/2$, where $P(f,q) \equiv \left[fN - B(q)\left(2 + fNB(q) - 2B(q)^{fN}\right)\right]/N^2\left(1-B(q)\right)^2$ and $B(q) \equiv \exp(-a^2q^2/6)$. We then write the second-order term of the statistical weight $\mathcal{F}$ as

$$\beta\mathcal{F}^{(2)}_{\mathrm{RPA}} = \frac{1}{2\rho_0}\int \frac{\mathrm{d}\mathbf{q}}{(2\pi)^3}\delta\hat{\boldsymbol{\rho}}(\mathbf{q})\cdot[\mathbf{S}^{\mathrm{RPA}}_\rho(q)]^{-1}\delta\hat{\boldsymbol{\rho}}(-\mathbf{q}), \tag{3.15}$$

where $\delta\beta\mathcal{F}^{(2)}_{\mathrm{RPA}}/\delta\delta\hat{\boldsymbol{\omega}}(\mathbf{q}) = 0$ is used, and

$$\mathbf{S}^{\mathrm{RPA}}_\rho \equiv \begin{bmatrix} \frac{N}{\kappa}\beta\hat{u}_0/N + S^{-1}_{1,\mathrm{AA}} & (\frac{N}{\kappa}+\chi N)\beta\hat{u}_0/N + S^{-1}_{1,\mathrm{AB}} \\ (\frac{N}{\kappa}+\chi N)\beta\hat{u}_0/N + S^{-1}_{1,\mathrm{AB}} & \frac{N}{\kappa}\beta\hat{u}_0/N + S^{-1}_{1,\mathrm{BB}} \end{bmatrix}^{-1} = (\mathbf{S}_0 + \mathbf{S}_1^{-1})^{-1}, \tag{3.16}$$

with the matrix $\mathbf{S}_0 \equiv (N/\kappa)\hat{\mathbf{u}}_\kappa + \chi N\hat{\mathbf{u}}_\chi$ due to the non-bonded interactions. For symmetric DBC, $S_{1,\mathrm{AA}} = S_{1,\mathrm{BB}}$ and we can diagonalize the matrix $(\mathbf{S}^{\mathrm{RPA}}_\rho)^{-1}$ to obtain Eqs. (A6) and (A7) in Ref. [4]. At the mean-field ODT $\chi^*_{\mathrm{MF}}N$, $(\mathbf{S}^{\mathrm{RPA}}_\rho)^{-1}$ is singular at the most unstable mode q^*, which gives the corresponding lamellar period $L^*_{0,\mathrm{MF}} = 2\pi/q^*$.[4,45] Alternatively, we can write

$$\beta\mathcal{F}^{(2)}_{\mathrm{RPA}} = \frac{1}{2\rho_0}\int \frac{\mathrm{d}\mathbf{q}}{(2\pi)^3}\delta\hat{\boldsymbol{\omega}}(\mathbf{q})\cdot[\mathbf{S}^{\mathrm{RPA}}_\omega(q)]^{-1}\delta\hat{\boldsymbol{\omega}}(-\mathbf{q}), \tag{3.17}$$

where $\delta\beta\mathcal{F}^{(2)}_{\mathrm{RPA}}/\delta\delta\hat{\boldsymbol{\rho}}(\mathbf{q}) = 0$ is used and $\mathbf{S}^{\mathrm{RPA}}_\omega = (\mathbf{S}_0^{-1} + \mathbf{S}_1)^{-1}$; $\chi^*_{\mathrm{MF}}N$ and q^* can also be obtained from the singularity of $(\mathbf{S}^{\mathrm{RPA}}_\omega)^{-1}$.

Substituting Eq. (3.14) into Eq. (3.13) and evaluating the Gaussian integrals over $\delta\hat{\boldsymbol{\omega}}(\mathbf{q})$ and $\delta\hat{\boldsymbol{\rho}}(\mathbf{q})$, we can approximate the partition function $\mathcal{Z}$ by

$$\begin{aligned}\mathcal{Z}^{\mathrm{GF}} &= \exp\left\{-\beta\mathcal{F}^{id}\right\}\exp\left\{-n\beta\Delta f_c^{\mathrm{SCF}}\right\}\int\mathcal{D}\boldsymbol{\rho}\exp\left\{-\frac{1}{2\rho_0}\int\frac{\mathrm{d}\mathbf{q}}{(2\pi)^3}\delta\hat{\boldsymbol{\rho}}(\mathbf{q})\cdot\mathbf{S}_0(q)\delta\hat{\boldsymbol{\rho}}(-\mathbf{q})\right\}\\ &\quad\cdot\int\mathcal{D}\left(\frac{\delta\boldsymbol{\omega}}{2\pi}\right)\exp\left\{\int\frac{\mathrm{d}\mathbf{q}}{(2\pi)^3}\left[i\delta\hat{\boldsymbol{\omega}}(\mathbf{q})\cdot\delta\hat{\boldsymbol{\rho}}(-\mathbf{q})-\frac{\rho_0}{2}\delta\hat{\boldsymbol{\omega}}(\mathbf{q})\cdot\mathbf{S}_1(q)\delta\hat{\boldsymbol{\omega}}(-\mathbf{q})\right]\right\}\\ &= \exp\left\{-\beta\mathcal{F}^{id}\right\}\exp\left\{-n\beta\Delta f_c^{\mathrm{SCF}}\right\}\prod_{\mathbf{q}}\Big[\det[\mathbf{S}_1(q)\mathbf{S}_0(q)+\mathbf{I}]\Big]^{-1/2},\end{aligned}\tag{3.18}$$

which gives

$$\beta\Delta f_c^{\mathrm{GF}} = \beta\Delta f_c^{\mathrm{SCF}} + \frac{1}{2\rho_c}\int\frac{\mathrm{d}\mathbf{q}}{(2\pi)^3}\ln\det[\mathbf{S}_1(q)\mathbf{S}_0(q)+\mathbf{I}]\tag{3.19}$$

with $\mathbf{I}$ being a 2×2 unit matrix.

3.2.4 Quantities calculated from Gaussian fluctuation theory

3.2.4.1 Mean-square end-to-end distances, bonding energy and bonding pressure

Adopting the method of Wang,[46] for two segments e_1 and e_2 on the same chain we introduce an auxiliary parameter η and define $\beta\mathcal{H}^C(\eta)\equiv\beta\mathcal{H}^C+(3\eta/2a^2)\sum_{k=1}^{n}(\mathbf{R}_{k,e_2}-\mathbf{R}_{k,e_1})^2$. We then have the partition function at given η as

$$\mathcal{Z}(\eta) = \frac{G(\eta)^n}{n!}\int\mathcal{D}\boldsymbol{\rho}\exp\left\{-\beta\mathcal{H}^E\right\}\int\mathcal{D}\left(\frac{\boldsymbol{\omega}}{2\pi}\right)\exp\left\{\int\mathrm{d}\mathbf{r}[i\boldsymbol{\omega}(\mathbf{r})\cdot\boldsymbol{\rho}(\mathbf{r})+n\ln Q(\eta)\right\},\tag{3.20}$$

where $Q(\eta)\equiv\prod_{s=1}^{N}\int\mathrm{d}\mathbf{R}_s\cdot\exp\Big\{-\beta h^C-i\sum_{s=1}^{N_{\mathrm{A}}}\omega_{\mathrm{A}}(\mathbf{R}_s)-i\sum_{s=N_{\mathrm{A}}+1}^{N}\omega_{\mathrm{B}}(\mathbf{R}_s)-(3\eta/2a^2)(\mathbf{R}_{e_2}-\mathbf{R}_{e_1})^2\Big\}\Big/G(\eta)$ and $G(\eta)\equiv\prod_{s=1}^{N}\int\mathrm{d}\mathbf{R}_s\cdot\exp\left\{-\beta h^C-(3\eta/2a^2)(\mathbf{R}_{e_2}-\mathbf{R}_{e_1})^2\right\}$. The mean-square distance between e_1 and e_2, $R^2(e_1,e_2)$, is then given by $R^2(e_1,e_2) = -(2a^2/3n)[\partial\ln\mathcal{Z}(\eta)/\partial\eta]|_{\eta=0} = \left\langle\sum_{k=1}^{n}(\mathbf{R}_{k,e_2}-\mathbf{R}_{k,e_1})^2\right\rangle/n$.

Next, we expand $\ln Q(\eta)$ to the second order in $\delta\boldsymbol{\omega}(\mathbf{r})$ as

$$\ln Q(\eta)\approx\ln Q^*(\eta)-\frac{N}{2V}\int\frac{\mathrm{d}\mathbf{q}}{(2\pi)^3}\delta\hat{\boldsymbol{\omega}}(\mathbf{q})\cdot\mathbf{S}_1(q,\eta,e_1,e_2)\delta\hat{\boldsymbol{\omega}}(-\mathbf{q}),\tag{3.21}$$

where $\mathbf{S}_1(q,\eta,e_1,e_2)$ is a 2×2 matrix with its (P,P') element being the Fourier transform of $(V/N)\,[\delta^2\ln Q(\eta)/\delta i\omega_{\mathrm{P}}(\mathbf{r})\delta i\omega_{\mathrm{P}'}(\mathbf{r}')]|_{\boldsymbol{\omega}^*}$. Substituting it into Eq. (3.20) and performing the Gaussian integrals, we obtain

$$R^2_{\mathrm{GF}}(e_1,e_2) = R^2_{\mathrm{SCF}}(e_1,e_2)+\frac{a^2}{3\rho_c}\int\frac{\mathrm{d}\mathbf{q}}{(2\pi)^3}\mathrm{tr}\left[\mathbf{S}_{\omega}^{\mathrm{RPA}}(q)\mathbf{S}'_{1,\eta=0}(q,e_1,e_2)\right],\tag{3.22}$$

where $R^2_{\rm SCF}(e_1,e_2)=(e_2-e_1)a^2$ is the SCF prediction, and, at given η, the single-chain structure factor $\mathbf{S}_1(q,\eta,e_1,e_2)$ and $\mathbf{S}'_{1,\eta=0}(q,e_1,e_2)\equiv[\partial\mathbf{S}_1(q,\eta,e_1,e_2)/\partial\eta]|_{\eta=0}$ are derived in the following. Note that, $\mathbf{S}'_{1,\eta=0}(q,1,N)$ is equivalent to $-\sum_{\mathbf{r},\mathbf{r}'}H(\mathbf{q},-\mathbf{q},\mathbf{r}-\mathbf{r}')/N$ defined in Ref. [47]; since RPA [Eq. (3.21)] is the only approximation used here and we obtain the same results as in Ref. [47], the additional approximation used in the Appendix of Ref. [47] turns out to be exact at the RPA level.

The mean-square chain end-to-end distance can be obtained as $R^2_{e,\rm GF}=R^2_{\rm GF}(1,N)$, and the mean-square block end-to-end distance $R^2_{eb,\rm GF}=R^2_{\rm GF}(1,N_{\rm A})$ [or $R^2_{\rm GF}(N_{\rm A}+1,N)$ for symmetric DBC]. Finally the bonding energy can be evaluated as

$$\beta u^{\rm GF}_{c,\rm b}=\beta u^{\rm SCF}_{c,\rm b}+\frac{1}{2\rho_c}\int\frac{\mathrm{d}\mathbf{q}}{(2\pi)^3}\mathrm{tr}\left[\mathbf{S}^{\rm RPA}_{\omega}(q)\mathbf{S}_{1\rm b^2}(q)\right], \tag{3.23}$$

where $\mathbf{S}_{1\rm b^2}(q)\equiv\sum_{s=1}^{N-1}\mathbf{S}'_{1,\eta=0}(q,s,s+1)$, and the bonding pressure is given by

$$\beta P^{\rm GF}_{\rm b}=\beta P^{\rm SCF}_{\rm b}-\frac{1}{3}\int\frac{\mathrm{d}\mathbf{q}}{(2\pi)^3}\mathrm{tr}\left[\mathbf{S}^{\rm RPA}_{\omega}(q)\mathbf{S}_{1\rm b^2}(q)\right]. \tag{3.24}$$

3.2.4.2 Non-bonded internal energy and non-bonded pressure

Using Eq. (3.18) and the second-order cumulant moment of the Gaussian distribution,[6] we obtain the ensemble average of E_κ and E_χ in GF theory as

$$\langle E_\kappa\rangle^{\rm GF}=\frac{V}{2}\int\frac{\mathrm{d}\mathbf{q}}{(2\pi)^3}\mathrm{tr}[\mathbf{S}^{\rm RPA}_{\rho}(q)\hat{\mathbf{u}}_\kappa(q)], \tag{3.25}$$

$$\langle E_\chi\rangle^{\rm GF}=\frac{V}{2}\int\frac{\mathrm{d}\mathbf{q}}{(2\pi)^3}\mathrm{tr}[\mathbf{S}^{\rm RPA}_{\rho}(q)\hat{\mathbf{u}}_\chi(q)], \tag{3.26}$$

the non-bonded internal energy is then given by

$$\beta u^{\rm GF}_{c,\rm nb}=\beta u^{\rm SCF}_{c,\rm nb}+\frac{1}{2\rho_c}\int\frac{\mathrm{d}\mathbf{q}}{(2\pi)^3}\mathrm{tr}[\mathbf{S}^{\rm RPA}_{\rho}(q)\mathbf{S}_0(q)]. \tag{3.27}$$

Alternatively, one can use $\beta u^{\rm GF}_{c,\rm nb}=(N/\kappa)[\partial\beta\Delta f^{\rm GF}_c/\partial(N/\kappa)]+\chi N[\partial\beta\Delta f^{\rm GF}_c/\partial(\chi N)]$ to obtain the same results.

Similarly, the non-bonded pressure is given by

$$\beta P^{\rm GF}_{\rm nb}=\beta P^{\rm SCF}_{\rm nb}-\frac{1}{6}\int\frac{\mathrm{d}\mathbf{q}}{(2\pi)^3}\mathrm{tr}[\mathbf{S}^{\rm RPA}_{\rho}(q)\mathbf{S}'_0(q)], \tag{3.28}$$

where $\mathbf{S}'_0 \equiv (\beta\hat{u}'_0/N)\begin{bmatrix} N/\kappa & N/\kappa+\chi N \\ N/\kappa+\chi N & N/\kappa \end{bmatrix}$ with $\beta u'_0(r) \equiv r\mathrm{d}\beta u_0(r)/\mathrm{d}r$.

3.2.4.3 Non-bonded constant-volume heat capacity

The fluctuations of E_κ and E_χ in GF theory are given by

$$\left(\sigma^2_\kappa\right)^{\mathrm{GF}} = \frac{V}{2}\int \frac{\mathrm{d}\mathbf{q}}{(2\pi)^3}\mathrm{tr}\Big[[\mathbf{S}^{\mathrm{RPA}}_\rho(q)\hat{\mathbf{u}}_\kappa(q)]^2\Big], \tag{3.29}$$

$$\left(\sigma^2_\kappa\right)^{\mathrm{GF}} = \frac{V}{2}\int \frac{\mathrm{d}\mathbf{q}}{(2\pi)^3}\mathrm{tr}\Big[[\mathbf{S}^{\mathrm{RPA}}_\rho(q)\hat{\mathbf{u}}_\chi(q)]^2\Big], \tag{3.30}$$

$$\left(\sigma^2_{\kappa,chi}\right)^{\mathrm{GF}} = \frac{V}{2}\int \frac{\mathrm{d}\mathbf{q}}{(2\pi)^3}\mathrm{tr}\Big[\mathbf{S}^{\mathrm{RPA}}_\rho(q)\hat{\mathbf{u}}_\kappa(q)\mathbf{S}^{\mathrm{RPA}}_\rho(q)\hat{\mathbf{u}}_\chi(q)\Big], \tag{3.31}$$

where we have used Eq. (3.18) and the fourth-order cumulant moment of the Gaussian distribution[6] to calculate the ensemble average; these results can also be obtained from Eqs. (3.9)∼(3.11). The GF prediction of $C_{V,\mathrm{nb}}$ is then given by

$$\frac{C^{\mathrm{GF}}_{V,\mathrm{nb}}}{k_B} = \frac{1}{2\rho_c}\int \frac{\mathrm{d}\mathbf{q}}{(2\pi)^3}\mathrm{tr}\Big[[\mathbf{S}^{\mathrm{RPA}}_\rho(q)\mathbf{S}_0(q)]^2\Big]. \tag{3.32}$$

Note that at given N/κ and χN, the GF predictions of ΔR^2_e, ΔR^2_{eb}, $\beta\Delta u_{c,\mathrm{b}}$, $\beta\Delta u_{c,\mathrm{nb}}$, $C_{V,nb}$, $\beta\Delta f_c$, and $\Delta s_c/k_B$ are all proportional to ρ_c^{-1}, which is independent of the system dimensionality, and in the limit of $\rho_c \to \infty$ the SCF prediction is exact.

3.2.4.4 Single chain structure factors at given η for the R^2_e calculation

Here we derive $\mathbf{S}'_{1,\eta=0}(q,e_1,e_2) = [\partial\mathbf{S}_1(q,\eta,e_1,e_2)/\partial\eta]|_{\eta=0}$ used for the calculation of $\langle R^2(e_1,e_2)\rangle$ in GF theory for $e_2 > e_1$. Firstly, for the (A, A) element, we have

$$\begin{aligned}
&\left.\frac{\partial S_{1,\mathrm{AA}}}{\partial\eta}\right|_{\eta=0} = \int \mathrm{d}(\mathbf{r}-\mathbf{r}')\frac{\partial}{\partial\eta}\left[\frac{V}{N}\frac{1}{Q^*(\eta)}\frac{\delta^2 Q(\eta)}{\delta i\omega_{\mathrm{A}}(\mathbf{r})\delta i\omega_{\mathrm{A}}(\mathbf{r}')}\bigg|_{\boldsymbol{\omega}^*}\right]\Bigg|_{\eta=0}\exp[-i\mathbf{q}\cdot(\mathbf{r}-\mathbf{r}')] \\
&= \frac{3}{2a^2N}\sum_{t,t'=1}^{N_{\mathrm{A}}}\left[\langle\exp[-i\mathbf{q}\cdot(\mathbf{R}_t-\mathbf{R}_{t'})]\rangle_0\langle(\mathbf{R}_{e_2}-\mathbf{R}_{e_1})^2\rangle_0 - \langle\exp[-i\mathbf{q}\cdot(\mathbf{R}_t-\mathbf{R}_{t'})](\mathbf{R}_{e_2}-\mathbf{R}_{e_1})^2\rangle_0\right] \\
&= \frac{3}{N}\sum_{t'=1}^{N_{\mathrm{A}}-1}\sum_{t=t'+1}^{N_{\mathrm{A}}}\Big[(e_2-e_1)B(q)^{|s'-s|} - \langle\exp[-i\mathbf{q}\cdot(\mathbf{R}_t-\mathbf{R}_{t'})](\mathbf{R}_{e_2}-\mathbf{R}_{e_1})^2/a^2\rangle_0\Big]
\end{aligned} \tag{3.33}$$

which corresponds to the correlation between $\exp[-i\mathbf{q}\cdot(\mathbf{R}_t - \mathbf{R}_{t'})]$ and $(\mathbf{R}_{e_2} - \mathbf{R}_{e_1})^2$ in the ideal-chain ensemble, depending on the positions of relevant segments along a chain. If $e_2 > e_1 \geq N_\mathrm{A}$, apparently, $\exp[-i\mathbf{q}\cdot(\mathbf{R}_t - \mathbf{R}_{t'})]$ and $(\mathbf{R}_{e_2} - \mathbf{R}_{e_1})^2$ are uncorrelated, and thus the above equation goes to 0; otherwise, for $e_1 < e_2 \leq N_\mathrm{A}$, we have

$$\left.\frac{\partial S_{1,\mathrm{AA}}}{\partial \eta}\right|_{\eta=0} = \frac{a^2q^2}{3N}\left\{\sum_{t'=1}^{e_1-1}\sum_{t=e_1+1}^{e_2}(t-e_1)^2B(q)^{t-t'} + \sum_{t'=1}^{e_1-1}\sum_{t=e_2+1}^{N_\mathrm{A}}(e_2-e_1)^2B(q)^{t-t'} + \sum_{t'=e_1}^{e_2-1}\sum_{t=t'+1}^{e_2}(t-t')^2B(q)^{t-t'} + \sum_{t'=e_1}^{e_2-1}\sum_{t=e_2+1}^{N_\mathrm{A}}(e_2-t')^2B(q)^{t-t'}\right\}, \tag{3.34}$$

and for $e_1 \leq N_\mathrm{A} - 1$ and $e_2 \geq N_\mathrm{A} + 1$, we have

$$\left.\frac{\partial S_{1,\mathrm{AA}}}{\partial \eta}\right|_{\eta=0} = \frac{a^2q^2}{3N}\left\{\sum_{t'=1}^{e_1-1}\sum_{t=e_1+1}^{N_\mathrm{A}}(t-e_1)^2B(q)^{t-t'} + \sum_{t'=e_1}^{N_\mathrm{A}-1}\sum_{t=t'+1}^{N_\mathrm{A}}(t-t')^2B(q)^{t-t'}\right\}. \tag{3.35}$$

Similarly, for $e_1 < e_2 \leq N_\mathrm{A} + 1$, the (B, B) element $[\partial S_{1,\mathrm{BB}}(q,\eta,e_1,e_2)/\partial\eta]|_{\eta=0} = 0$; otherwise, for $e_2 > e_1 \geq N_\mathrm{A} + 1$, we have

$$\left.\frac{\partial S_{1,\mathrm{BB}}}{\partial \eta}\right|_{\eta=0} = \frac{a^2q^2}{3N}\left\{\sum_{t'=N_\mathrm{A}+1}^{e_1-1}\sum_{t=e_1+1}^{e_2}(t-e_1)^2B(q)^{t-t'} + \sum_{t'=N_\mathrm{A}+1}^{e_1-1}\sum_{t=e_2+1}^{N}(e_2-e_1)^2B(q)^{t-t'} + \sum_{t'=e_1}^{e_2-1}\sum_{t=t'+1}^{e_2}(t-t')^2B(q)^{t-t'} + \sum_{t'=e_1}^{e_2-1}\sum_{t=e_2+1}^{N}(e_2-t')^2B(q)^{t-t'}\right\}, \tag{3.36}$$

and for $e_2 \geq N_\mathrm{A} + 2$ and $e_1 \leq N_\mathrm{A}$, we have

$$\left.\frac{\partial S_{1,\mathrm{BB}}}{\partial \eta}\right|_{\eta=0} = \frac{a^2q^2}{3N}\left\{\sum_{t'=N_\mathrm{A}+1}^{e_2-1}\sum_{t=t'+1}^{e_2}(t-t')^2B(q)^{t-t'} + \sum_{t'=N_\mathrm{A}+1}^{e_2-1}\sum_{t=e_2+1}^{N}(e_2-t')^2B(q)^{t-t'}\right\}. \tag{3.37}$$

Note that $[\partial S_{1,\mathrm{BB}}(q,\eta,e_1,e_2)/\partial\eta]|_{\eta=0} = [\partial S_{1,\mathrm{AA}}(q,\eta,e_1,e_2)/\partial\eta]|_{\eta=0}$ for symmetric DBC.

Finally, for $e_1 < e_2 \leq N_\mathrm{A}$, we have the crossing terms $[\partial S_{1,\mathrm{AB}}(q,\eta,e_1,e_2)/\partial\eta]|_{\eta=0} = [\partial S_{1,\mathrm{BA}}(q,\eta,e_1,e_2)/\partial\eta]|_{\eta=0}$ as

$$\left.\frac{\partial S_{1,\mathrm{AB}}}{\partial \eta}\right|_{\eta=0} = \frac{q^2a^2}{6N}\left\{\sum_{t'=1}^{e_1-1}\sum_{t=N_\mathrm{A}+1}^{N}(e_2-e_1)^2B(q)^{t-t'} + \sum_{t'=e_1}^{e_2-1}\sum_{t=N_\mathrm{A}+1}^{N}(e_2-t')^2B(q)^{t-t'}\right\}, \tag{3.38}$$

for $N_\mathrm{A} + 1 \leq e_1 < e_2$ we have

$$\left.\frac{\partial S_{1,\mathrm{AB}}}{\partial \eta}\right|_{\eta=0} = \frac{q^2a^2}{6N}\left\{\sum_{t'=1}^{N_\mathrm{A}}\sum_{t=e_1}^{e_2-1}(t-e_1)^2B(q)^{t-t'} + \sum_{t'=1}^{N_\mathrm{A}}\sum_{t=e_2}^{N}(e_2-e_1)^2B(q)^{t-t'}\right\}, \tag{3.39}$$

and for $e_1 \leq N_{\rm A}$ and $e_2 \geq N_{\rm A}+1$ we have

$$\left.\frac{\partial S_{1,\rm AB}}{\partial \eta}\right|_{\eta=0} = \frac{q^2a^2}{6N}\left\{\sum_{t'=1}^{e_1-1}\sum_{t=N_{\rm A}+1}^{e_2-1}(t-e_1)^2B(q)^{t-t'} + \sum_{t'=1}^{e_1-1}\sum_{t=e_2}^{N}(e_2-e_1)^2B(q)^{t-t'} + \sum_{t'=e_1}^{N_{\rm A}}\sum_{t=N_{\rm A}+1}^{e_2-1}(t-t')^2B(q)^{t-t'} + \sum_{t'=e_1}^{N_{\rm A}}\sum_{t=e_2}^{N}(e_2-t')^2B(q)^{t-t'}\right\}. \quad (3.40)$$

From the above equations $\mathbf{S}_{1b^2}(q) \equiv \sum_{s=1}^{N-1}\mathbf{S}'_{1,\eta}(q,s,s+1)$ is given by

$$S_{1b^2,\rm AA} = \frac{a^2q^2}{3N}\sum_{s=1}^{N_{\rm A}-1}\sum_{t'=1}^{s}\sum_{t=s+1}^{N_{\rm A}}B(q)^{t-t'} = \frac{a^2q^2}{3}\sum_{s=1}^{N_{\rm A}-1}\frac{[B(q)^s-1][B(q)^{N_{\rm A}}-B(q)^s]}{NB(q)^{s-1}[1-B(q)]^2},$$

$$S_{1b^2,\rm BB} = \frac{a^2q^2}{3N}\sum_{s=N_{\rm A}+1}^{N-1}\sum_{t'=N_{\rm A}+1}^{s}\sum_{t=s+1}^{N}B(q)^{t-t'} = \frac{a^2q^2}{3}\sum_{s=1}^{N_{\rm B}-1}\frac{[B(q)^s-1][B(q)^{N_{\rm B}}-B(q)^s]}{NB(q)^{s-1}[1-B(q)]^2},$$

$$S_{1b^2,\rm AB} = \frac{a^2q^2}{6N}\left[\sum_{s=1}^{N_{\rm A}}\sum_{t'=1}^{s}\sum_{t=N_{\rm A}+1}^{N}B(q)^{t-t'} + \sum_{s=N_{\rm A}+1}^{N-1}\sum_{t'=1}^{N_{\rm A}}\sum_{t=s+1}^{N}B(q)^{t-t'}\right]$$
$$= \frac{a^2q^2}{6N}\left[\sum_{s=1}^{N_{\rm A}}\frac{[B(q)^s-1][B(q)^N-B(q)^{N_{\rm A}}]}{B(q)^{s-1}[1-B(q)]^2} + \sum_{s=1}^{N_{\rm B}-1}\frac{[B(q)^s-1][B(q)^N-B(q)^{N_{\rm B}}]}{B(q)^{s-1}[1-B(q)]^2}\right]. \quad (3.41)$$

Note that, for symmetric DBC, $S_{1b^2,\rm AA} = S_{1b^2,\rm BB}$.

3.2.5 Integral-equation (IE) theories

3.2.5.1 Reference interaction site model (RISM) theory

Due to the small N-values (10 and 20) and thus the large chain-end effects in our study, we employ RISM theory[19] in most cases to study the structural and thermodynamic properties of symmetric DBC in the disordered phase. RISM theory describes the interchain pair correlation functions (PCFs) via the generalized Ornstein-Zernike (OZ) equation given in Fourier space as[19]

$$\hat{\mathbf{h}} = \hat{\boldsymbol{\omega}}\hat{\mathbf{c}}(\hat{\boldsymbol{\omega}} + \rho_c\hat{\mathbf{h}}), \quad (3.42)$$

where the symmetric matrices $\hat{\mathbf{h}}$, $\hat{\boldsymbol{\omega}}$ and $\hat{\mathbf{c}}$ have $N\times N$ elements of $\hat{h}_{s,s'}$, $\hat{\omega}_{s,s'}$ and $\hat{c}_{s,s'}$, respectively; $c_{s,s'}(r)$ and $h_{s,s'}(r) \equiv g_{s,s'}(r)-1$ are the interchain direct and total PCFs, respectively, between the $s^{\rm th}$ segment on one chain and the $s'^{\rm th}$ segment on another, with $g_{s,s'}(r)$ being the interchain radial distribution function; $\omega_{s,s'}(r)$ is the intrachain PCF between the $s^{\rm th}$ and

s'^{th} segments on the same chain with $\hat{\omega}_{s,s'}(q=0)=1$; and we use the short-hand notation $\hat{f} \equiv \int \mathrm{d}\mathbf{r} f(r)\exp(-i\mathbf{q}\cdot\mathbf{r}) = (4\pi/q)\int_0^\infty \mathrm{d}r f(r) r\sin(qr)$ to denote the Fourier transform of $f(r)$.

In this study, we take $\hat{\omega}_{s,s'}$ as an input obtained in two ways: one is calculated directly in FOMC simulations and denoted by $\hat{\omega}^{\text{FOMC}}_{s,s'}$, and the other is given by the ideal DGC model $\hat{\omega}^{\text{DGC}}_{s,s'} = B(q)^{|s-s'|}$.

Eq. (3.42) must be solved together with a closure relating the interchain direct and total PCFs. Here we use the atomic Percus-Yevick (PY) closure[36] in most cases, commonly employed for short-range repulsive pair potentials, which for our soft potential [Eq. (3.5)] is given by

$$c_{s,s'}(r) = \left[1 - e^{\beta u_{s,s'}(r)}\right] g_{s,s'}(r). \tag{3.43}$$

Zhou closure[43] used in some cases in our study is given by

$$c_{s,s'}(r) = \exp\left[-\beta u_{s,s'}(r) + \gamma_{s,s'}(r) - \frac{\gamma^2_{s,s'}(r)}{2[1+\alpha\gamma_{s,s'}(r)]}\right] - \gamma_{s,s'}(r) - 1. \tag{3.44}$$

where $\gamma_{s,s'}(r) \equiv h_{s,s'}(r) - c_{s,s'}(r)$ being the indirect PCFs and the parameter α is a function of the reduced density $\rho^*_0 = \rho_0\sigma^3$ and temperature $T^* = 10\rho_0 N/\epsilon\beta u_0(0)$ with ϵ denoting N/κ for the same block or $N/\kappa + \chi N$ for different blocks, given by $\alpha = 1.0185\exp(T^*) - 0.2685\rho^*_0$. Note that, since $\gamma_{s,s'}(r)$ is not always positive, in the case of $\epsilon \to 0$, i.e., $\alpha \to \infty$, the term in the denominator $1 + \alpha\gamma_{s,s'}(r)$ might be 0 at specific r. Zhou closure is therefore cannot be used for cases of small pair interaction strength.

We solve the RISM equation and closure iteratively. For given $\mathbf{c}^{\text{old}}$, from Eq. (3.42) we obtain

$$\hat{\boldsymbol{\gamma}} = (\mathbf{I} - \rho_c\hat{\boldsymbol{\omega}}\hat{\mathbf{c}}^{\text{old}})^{-1}\left[\hat{\boldsymbol{\omega}}\hat{\mathbf{c}}^{\text{old}}(\hat{\boldsymbol{\omega}} + \rho_c\hat{\mathbf{c}}^{\text{old}}) - \hat{\mathbf{c}}^{\text{old}}\right] \tag{3.45}$$

with $\mathbf{I}$ the identity matrix. We then obtain the new direct PCFs as $c^{\text{new}}_{s,s'}(r) = [\gamma_{s,s'}(r) + 1]\exp[-\beta u_{s,s'}(r)] - 1 - \gamma_{s,s'}(r)$ from the PY closure; the Anderson mixing method[48,49] is used with a convergence criterion $\max_{\{s\geq s',r\}}|[\gamma_{s,s'}(r)+1]\exp[-\beta u_{s,s'}(r)] - g_{s,s'}(r)| \leq 10^{-10}$, where

$\gamma_{s,s'}(r)$ and $g_{s,s'}(r)$ are functions of $c_{s,s'}(r)$ from Eq. (3.45) and we use a cut-off $r_c = 10R_{e,0}$ for $\gamma_{s,s'}(r)$ [i.e., $h_{s,s'}(r)$ and $g_{s,s'}(r)$] and uniformly discretize $[0, r_c]$ into $3,200$ subintervals.

3.2.5.2 Polymer reference interaction site model (PRISM) theory

To highlight the chain-end effects, we compare the RISM predictions with those from PRISM theory in some cases. Following Schweizer[26] and replacing the subscript "s, s'" by "$s\mathrm{P}, s'\mathrm{P}'$", where $\hat{h}_{s\mathrm{P},s'\mathrm{P}'}$, for example, denotes the interchain PCF between the s^{th} segment on P (=A,B) block and the s'^{th} segment on P$'$ block, we can rewrite Eq. (3.42) as

$$\hat{h}_{s\mathrm{P},s'\mathrm{P}'} = \sum_{\mathrm{Q=A,B}} \sum_{\mathrm{Q}'=\mathrm{A,B}} \sum_{t=1}^{N_{\mathrm{Q}}} \sum_{t'=1}^{N_{\mathrm{Q}'}} \left[\hat{\omega}_{s\mathrm{P},s'\mathrm{Q}} \hat{c}_{t\mathrm{Q},t'\mathrm{Q}'} \left(\hat{\omega}_{t'\mathrm{Q}',s'\mathrm{P}'} + \rho_c \hat{h}_{t'\mathrm{Q}',s'\mathrm{P}'} \right) \right]. \tag{3.46}$$

In PRISM theory one assumes $\hat{h}_{s\mathrm{P},s'\mathrm{P}'} = \hat{h}_{\mathrm{P},\mathrm{P}'}$ and $\hat{c}_{s\mathrm{P},s'\mathrm{P}'} = \hat{c}_{\mathrm{P},\mathrm{P}'}$ (which neglects the chain-end effects). The above equation then becomes

$$\hat{h}_{\mathrm{P},\mathrm{P}'} = \sum_{\mathrm{Q=A,B}} \sum_{\mathrm{Q}'=\mathrm{A,B}} \left(\frac{N^2}{N_{\mathrm{P}} N_{\mathrm{P}'}} S_{1,\mathrm{PQ}} \hat{c}_{\mathrm{Q},\mathrm{Q}'} S_{1,\mathrm{Q}'\mathrm{P}'} + \rho_c \frac{N N_{\mathrm{Q}'}}{N_{\mathrm{P}}} S_{1,\mathrm{PQ}} \hat{c}_{\mathrm{Q},\mathrm{Q}'} \hat{h}_{\mathrm{Q}',\mathrm{P}'} \right). \tag{3.47}$$

Multiplying $f_{\mathrm{P}} f_{\mathrm{P}'}$ on both sides of Eq. (3.47) and defining $\hat{H}_{\mathrm{P},\mathrm{P}'} \equiv f_{\mathrm{P}} f_{\mathrm{P}'} \hat{h}_{\mathrm{P},\mathrm{P}'}$, we finally obtain

$$\hat{\mathbf{H}} = \mathbf{S}_1 \hat{\mathbf{C}} (\mathbf{S}_1 + \rho_0 \hat{\mathbf{H}}), \tag{3.48}$$

where the symmetric matrices $\hat{\mathbf{H}}$ and $\hat{\mathbf{C}}$ have 2×2 elements of $\hat{H}_{\mathrm{P},\mathrm{P}'}$ and $\hat{C}_{\mathrm{P},\mathrm{P}'} = \hat{c}_{\mathrm{P},\mathrm{P}'}$, respectively, corresponding to the correlations between P and P$'$ blocks.

3.2.6 Quantities calculated from IE theories

3.2.6.1 Non-bonded properties and free energy

The non-bonded internal energy per chain from IE theories is given by

$$\beta u_{c,\mathrm{nb}}^{\mathrm{IE}} = \beta u_{c,\mathrm{nb}}^{\mathrm{SCF}} + \frac{N}{\kappa} \frac{\langle E_\kappa \rangle^{\mathrm{IE}}}{n} + \chi N \frac{\langle E_\chi \rangle^{\mathrm{IE}}}{n}, \tag{3.49}$$

where

$$\frac{\langle E_\kappa \rangle^{\mathrm{IE}}}{n} = \frac{2\pi}{\rho_0 N} \sum_{s,s'=1}^{N} \int_0^\sigma \mathrm{d}r \left[\omega_{s,s'}(r) + \rho_c h_{s,s'}(r) \right] r^2 \beta u_0(r) \tag{3.50}$$

$$\frac{\langle E_\chi \rangle^{\rm IE}}{n} = \frac{4\pi}{\rho_0 N} \sum_{s=1}^{N_{\rm A}} \sum_{s'=N_{\rm A}+1}^{N} \int_0^\sigma {\rm d}r \left[\omega_{s,s'}(r) + \rho_c h_{s,s'}(r)\right] r^2 \beta u_0(r) \tag{3.51}$$

have both intra- and interchain contributions. Similarly, the non-bonded pressure from IE theories is given by

$$\beta P_{\rm nb}^{\rm IE} = -\frac{2\pi\rho_c}{3} \sum_{s,s'=1}^{N} \int_0^\sigma {\rm d}r \left[\omega_{s,s'\neq s}(r) + \rho_c g_{s,s'}(r)\right] r^2 \frac{{\rm d}\beta u_{s,s'}(r)}{{\rm d}\ln r}. \tag{3.52}$$

We then calculate $\Delta f_c^{\rm IE}$ from Eqs. (3.8), (3.50) and (3.51), and $\Delta s_c^{\rm IE}/k_B = \beta u_{c,\rm b}^{\rm IE} - \beta u_{c,\rm b}^{\rm SCF} + \beta u_{c,\rm nb}^{\rm IE} - \beta \Delta f_c^{\rm IE}$; the calculation of $u_{c,\rm b}^{\rm IE}$ is given below. Finally, the fluctuations of E_κ and E_χ and the non-bonded constant-volume heat capacity are calculated numerically by the second-order finite central difference according to Eqs. (3.9)$\sim$(3.12), (3.50) and (3.51).

3.2.6.2 Chain dimensions, bonding properties and structure factors

Adopting the method of Wang,[46] for two segments e_1 and e_2 on the same chain we introduce an auxiliary parameter η and define $\beta\mathcal{H}^C(\eta) \equiv \beta\mathcal{H}^C + (3\eta/2a^2)\sum_{k=1}^n (\mathbf{R}_{k,e_2} - \mathbf{R}_{k,e_1})^2$. We then have the partition function at given η as

$$\mathcal{Z}(\eta) = \frac{1}{n!} \prod_{k=1}^{n} \prod_{s=1}^{N} \int {\rm d}\mathbf{R}_{k,s} \cdot \exp\left\{ -\beta\mathcal{H}^C - \frac{3\eta}{2a^2} \sum_{k=1}^{n} (\mathbf{R}_{k,e_2} - \mathbf{R}_{k,e_1})^2 - \beta\mathcal{H}^E \right\}. \tag{3.53}$$

The mean-square distance between e_1 and e_2, $R^2(e_1, e_2)$, is then given by

$$R^2(e_1,e_2) = -\left.\frac{2a^2}{3n} \frac{\partial \ln \mathcal{Z}(\eta)}{\partial \eta}\right|_{\eta=0} = R_{e,\rm SCF}^2(e_1,e_2) + \left.\frac{2a^2}{3} \frac{\partial \beta\Delta f_c(\eta)}{\partial \eta}\right|_{\eta=0}, \tag{3.54}$$

where we numerically evaluate the partial derivative by the second-order finite central difference after obtaining $\beta\Delta f_c(\eta)$ via Eq. (3.8); the intrachain PCFs at given η, $\hat{\omega}_{s,s'}(q;\eta,e_1,e_2)$, needed for solving the P/RISM equations are derived in the following. We then have the chain and block mean-square end-to-end distance as $R_{e,\rm IE}^2 = R_{\rm IE}^2(1,N)$ and $R_{eb,\rm IE}^2 = R_{\rm IE}^2(1,N_{\rm A})$, respectively, as well as the mean-square bond length $b_{s,\rm IE}^2 = R_{\rm IE}^2(s,s+1)$ for the $s^{\rm th}$ bond. The bonding energy per chain is then given by $\beta u_{c,\rm b}^{\rm IE} = (3/2a^2)\sum_{s=1}^{N-1} b_{s,\rm IE}^2$, from which we calculate $\beta P_{\rm b} = -(2\rho_c/3)\beta u_{c,\rm b}$.

We also calculate the total structure factor $S_t(q) \equiv \sum_{\mathrm{P,P'}} S_{\mathrm{P,P'}}(q)$, where $S_{\mathrm{PP'}}(q) \equiv \sum_{s\in\mathrm{P}} \sum_{s'\in\mathrm{P'}} \hat{S}_{s,s'}/N$ with $\hat{S}_{s,s'}$ being the (s,s') element of the $N\times N$ matrix $\hat{\mathbf{S}} \equiv \hat{\boldsymbol{\omega}} + \rho_c \hat{\mathbf{h}} = (\hat{\boldsymbol{\omega}}^{-1} - \rho_c \hat{\mathbf{c}})^{-1}$. We further calculate the structure factor $S_\psi(q) \equiv S_{\mathrm{AA}}(q) + S_{\mathrm{BB}}(q) - 2S_{\mathrm{AB}}(q)$ characterizing the composition fluctuations of $\psi(\mathbf{r}) \equiv [\rho_{\mathrm{A}}(\mathbf{r}) - \rho_{\mathrm{B}}(\mathbf{r})]/\rho_0$.

3.2.6.3 Derivation of $\hat{\omega}_{t,t'}(q,\eta,e_1,e_2)$ for chain dimension calculations

Considering one ideal-chain, $\hat{\omega}_{t,t'}(q,\eta,e_1,e_2)$, with $t' \geq t$ for example, can be evaluated by Gaussian integral as

$$\hat{\omega}_{t,t'}(\ q\ ,\eta,e_1,e_2) = \frac{\prod_{s=1}^{N-1}\int \mathrm{d}\mathbf{b}_s \cdot \exp\left\{-\frac{3}{2a^2}\sum_{s=1}^{N-1}\mathbf{b}_s^2 - \frac{3\eta}{2a^2}\left(\sum_{s=e_1}^{e_2-1}\mathbf{b}_s\right)^2 - i\mathbf{q}\cdot\sum_{s=t}^{t'-1}\mathbf{b}_s\right\}}{\prod_{s=1}^{N-1}\int \mathrm{d}\mathbf{b}_s \cdot \exp\left\{-\frac{3}{2a^2}\sum_{s=1}^{N-1}\mathbf{b}_s^2 - \frac{3\eta}{2a^2}\left(\sum_{s=e_1}^{e_2-1}\mathbf{b}_s\right)^2\right\}}$$

$$= \begin{cases} \exp\left\{-\frac{a^2q^2}{6}(t'-t)\right\}, & \text{if } 1\leq t\leq t'\leq e_1 \text{ or } e_2\leq t\leq t'\leq N; \\ \exp\left\{-\frac{a^2q^2}{6}\left[(t'-t) - \frac{(t'-e_1)^2\eta}{(e_2-e_1)\eta+1}\right]\right\}, & \text{if } 1\leq t\leq e_1 \text{ and } e_1+1\leq t'\leq e_2; \\ \exp\left\{-\frac{a^2q^2}{6}\left[(t'-t) - \frac{(e_2-e_1)^2\eta}{(e_2-e_1)\eta+1}\right]\right\}, & \text{if } 1\leq t\leq e_1 \text{ and } e_2+1\leq t'\leq N; \\ \exp\left\{-\frac{a^2q^2}{6}\left[(t'-t) - \frac{(t'-t)^2\eta}{(e_2-e_1)\eta+1}\right]\right\}, & \text{if } e_1+1\leq t\leq t'\leq e_2-1; \\ \exp\left\{-\frac{a^2q^2}{6}\left[(t'-t) - \frac{(e_2-t)^2\eta}{(e_2-e_1)\eta+1}\right]\right\}, & \text{if } e_1+1\leq t\leq e_2-1 \text{ and } e_2\leq t'\leq N; \end{cases} \tag{3.55}$$

Taking the derivative of $\hat{\omega}_{t,t'}(q,\eta,e_1,e_2)$ with respect of η and set $\eta = 0$, we have

$$\left.\frac{\partial\hat{\omega}_{t,t'}}{\partial\eta}\right|_{\eta=0} = \begin{cases} 0, & \text{if } 1\leq t\leq t'\leq e_1 \text{ or } e_2\leq t\leq t'\leq N; \\ \frac{a^2q^2}{6}(t'-e_1)^2B(q)^{t'-t}, & \text{if } 1\leq t\leq e_1 \text{ and } e_1+1\leq t'\leq e_2; \\ \frac{a^2q^2}{6}(e_2-e_1)^2B(q)^{t'-t}, & \text{if } 1\leq t\leq e_1 \text{ and } e_2+1\leq t'\leq N; \\ \frac{a^2q^2}{6}(t'-t)^2B(q)^{t'-t}, & \text{if } e_1+1\leq t\leq t'\leq e_2-1; \\ \frac{a^2q^2}{6}(e_2-t)^2B(q)^{t'-t}, & \text{if } e_1+1\leq t\leq e_2-1 \text{ and } e_2\leq t'\leq N; \end{cases} \tag{3.56}$$

which also leads to $\mathbf{S}'_{1,\eta=0}(q,e_1,e_2)$, for example, the (P, P′) element is given by $(1/N)\sum_{t\in\mathrm{P},t'\in\mathrm{P'}}[\partial\hat{\omega}_{t,t'}(q,\eta,e_1,e_2)/\partial\eta]|_{\eta=0}$.

3.2.7 Relation among IE, GF, and SCF theories

If we assume $1-\exp[\beta u_{s,s'}(r)] \approx -\beta u_{s,s'}(r)$ for small $\beta u_{s,s'}(r)$ and set $g_{s,s'}(r) = 1$ in PY closure [Eq. (3.43)], it is then reduced to $c_{s,s'}(r) = -\beta u_{s,s'}(r)$, the mean-spherical

approximation (MSA) closure[35] used for the penetrable spheres.[40,42] Since $u_{s,s'}(r)$ satisfies $u_{\mathrm{PP}'}(r) = u_{s\mathrm{P},s'\mathrm{P}'}(r)$, the RISM equations are then equivalent to the PRISM equations and we have $C^{\mathrm{RPA}}_{\mathrm{PP}'}(r) = -\beta u_{\mathrm{PP}'}(r)$. Eq. (3.48) thus gives the total structure factor matrix $\mathbf{S} \equiv \mathbf{S}_1 + \rho_0\hat{\mathbf{H}} = (\mathbf{S}_0 + \mathbf{S}_1^{-1})^{-1}$, which is the same as $\mathbf{S}^{\mathrm{RPA}}_\rho$. We therefore refer $C^{\mathrm{RPA}}_{\mathrm{PP}'}(r) = -\beta u_{\mathrm{PP}'}(r)$ as the RPA closure.[50] It is clear that, for all calculated structural and thermodynamic quantities, P/RISM theories with RPA closure (denoted as P/RISM-RPA) and $\omega^{\mathrm{DGC}}_{s,s'}(r)$ are the same as GF theory, which contains only the Gaussian-level fluctuations. One thing to note is that the above assumption of $g_{s,s'}(r) = 1$ is used only to reduce PY closure to RPA closure; P/RISM-RPA or GF theory does not necessarily give $g_{s,s'}(r) = 1$.

On the other hand, in the limit of $\rho_c \to \infty$, Eq. (3.5) gives $\beta u_{s,s'}(r) \to 0$ at finite N/κ and χN, leading to $c_{s,s'}(r) \to 0$ and $h_{s,s'}(r) \to 0$ (or $g_{s,s'}(r) \to 1$) for both P/RISM-PY and P/RISM-RPA (or GF) theories. In this limit, the interchain fluctuation/correlation (F/C) effects can thus be neglected, and both IE and GF theories reduce to SCF theory. In another point of view, all the F/C effects on both structural and thermodynamic properties (beyond the mean-field predictions) for both GF theory and IE theories at large $\bar{\mathcal{N}}$ are proportional to ρ_0^{-1}; this also indicates that both IE and GF theories reduce to the SCF predictions as $\rho_0 \to \infty$.

3.3 Results and Discussions

Setting $R_{e,0}$ as the length scale, we have five parameters in our model system: $\bar{\mathcal{N}} \equiv (nR^3_{e,0}/V)^2$, χN, N/κ, N, and σ/a (or $\sigma/R_{e,0}$); the first three are physical parameters that can be mapped to an experimental system, and the last two are model parameters characterizing the chain discretization and finite interaction range, respectively. In the following, we fix $\bar{\mathcal{N}} = 10^4$, $N = 10$ and $\sigma/a = 0.3$ unless specified otherwise, and examine the effects of N/κ and χN by comparing the results from different methods mainly in three cases: homopolymers at $\chi N = 0$, and DBC at $N/\kappa = 0$ and 50. We use ideal chains at $N/\kappa = \chi N = 0$ as the reference state in all the cases. The error bar of each ensemble-averaged quantity from

FOMC simulation is estimated as three times its standard deviation with the statistical correlation among samples collected after equilibration taken into account by the correlation function method.[51] Note that, because Zhou closure cannot be used for small interactions, it is only applied for homopolymers with $N/\kappa \gtrsim 12$ and DBC for $N/\kappa = 50$ in this study.

3.3.1 Chain dimensions and bonding energy

Fig. 3.1 shows the difference in the mean-square chain and block end-to-end distances from the reference state, ΔR_e^2 and ΔR_{eb}^2, obtained from various theories and FOMC simulations. At $\chi N = 0$ (i.e., homopolymers), we see in Fig. 3.1(a) that ΔR_e^2 obtained from all the methods monotonically increases with increasing $N/\kappa \leq 100$ due to the excluded-volume interaction. At small $N/\kappa \lesssim 1$, ΔR_e^2 is proportional to N/κ, which can be found from the Taylor expansion of Eq. (3.22). While our simulation result here is for $N/\kappa \leq 50$, as N/κ further increases it is expected to converge to a constant similar to Fig. 5(a) in Ref. [47]. GF theory (or equivalently P/RISM-RPA with the intrachain PCF for ideal DGC, $\hat{\omega}_{s,s'}^{\mathrm{DGC}}$) gives surprisingly good predictions within the entire range of our simulation data; in contrast, RISM-PY method with $\hat{\omega}_{s,s'}^{\mathrm{DGC}}$ overestimates ΔR_e^2 for $N/\kappa \gtrsim 2$, and the deviation increases with increasing N/κ and diverges in the limit of $N/\kappa \to \infty$.

For homopolymers, with $e_1 = 1$ and $e_2 = N$, Eqs. (3.8), (3.50) and (3.54) give

$$\Delta R_{e,\mathrm{IE}}^2 = \frac{4\pi a^2}{3\rho_0 N} \sum_{s,s'=1}^{N} \int_0^{N/\kappa} \mathrm{d}\left(\frac{N}{\kappa}\right) \int_0^{\sigma} \mathrm{d}r \left[\frac{\partial \omega_{s,s'}^{\mathrm{DGC}}(r,\eta)}{\partial \eta} + \rho_c \frac{\partial h_{s,s'}(r,\eta,N/\kappa)}{\partial \eta}\right]\Bigg|_{\eta=0} r^2 \beta u_0(r). \tag{3.57}$$

In the limit of $N/\kappa \to \infty$, PY closure gives $h_{s,s'}(r,\eta,N/\kappa) = -1$ for $0 \leq r \leq \sigma$ regardless of η, leading to $[\partial h_{s,s'}(r,\eta,N/\kappa)/\partial\eta]_{\eta=0} = 0$; $\Delta R_{e,\mathrm{IE}}^2$ thus diverges as $N/\kappa \to \infty$. This divergence is clearly due to the use of ideal-chain conformations. On the other hand, RPA closure $\hat{c}(q) = -(N/\kappa)(\beta\hat{u}_0(q)/\rho_0 N)$ gives $\hat{h}_{s,s'}(q,\eta,N/\kappa) = S_1^2(q,\eta)\hat{c}(q)/[1 - \rho_0 S_1(q,\eta)\hat{c}(q)]$ with $S_1(q,\eta) = (1/N)\sum_{s,s'=1}^{N} \hat{\omega}_{s,s'}(q,\eta)$. Eq. (3.57) then becomes

$$\Delta R_{e,\mathrm{GF}}^2 = \frac{a^2}{3\rho_0} \int_0^{N/\kappa} \mathrm{d}\left(\frac{N}{\kappa}\right) \int \frac{\mathrm{d}\mathbf{q}}{(2\pi)^3} \left[\frac{\partial S_1(q,\eta)}{\partial \eta} + \rho_0 \frac{\partial \hat{h}(q,\eta,N/\kappa)}{\partial \eta}\right]\Bigg|_{\eta=0} \beta\hat{u}_0(q). \tag{3.58}$$

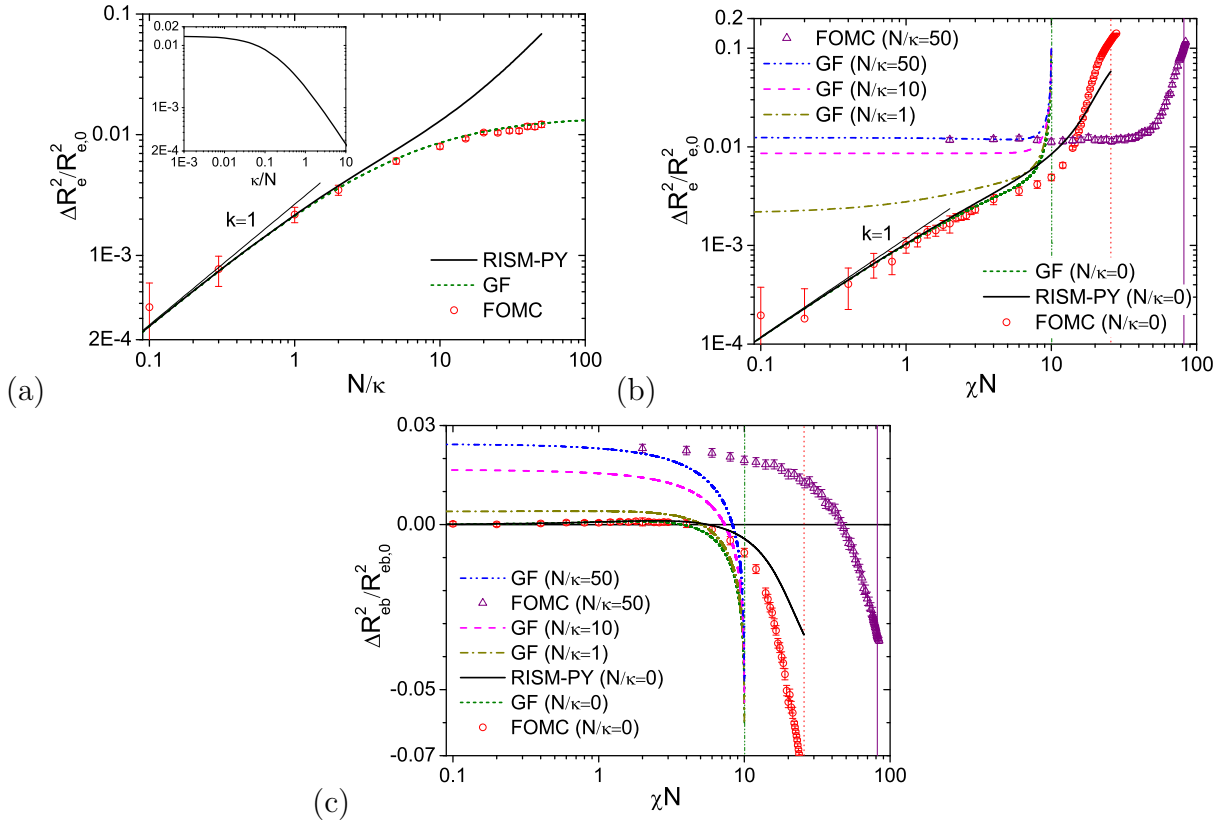

Figure 3.1: Log-log plot of ΔR_e^2 with N/κ for homopolymers (a) and with χN for DBC (b), obtained form different methods. (c) semilogarithmic plot of ΔR_{eb}^2 with χN obtained form different methods. "$k = 1$" in parts (a) and (b) denotes a straight line of slope 1. The vertical lines in parts (b) and (c) denote $\chi^*_{\rm MF}N$ (dash-dot-dot) and $\chi^*_{\rm FOMC}N$ (solid), which have the same meaning in the following figures. The inset of part (a) shows how ΔR_e^2 with κ/N for homopolymers. $N = 10$, $\bar{\mathcal{N}} = 10^4$ and $\sigma/a = 0.3$ are used here and fixed for the following figures unless specified otherwise.

Since $\rho_0 \partial \hat{h}(q,\eta,N/\kappa)/\partial\eta = [1-\rho_0 S_1(q,\eta)\hat{c}(q)]^{-2}[\partial S_1(q,\eta)/\partial\eta] - [\partial S_1(q,\eta)/\partial\eta]$, its second term then cancels with the first term in the integrand of Eq. (3.58), thus eliminating the divergence of $\Delta R^2_{e,\rm IE}$ in the limit of $N/\kappa \to \infty$. With RPA closure, we finally have

$$\Delta R^2_{e,\rm GF} = \frac{a^2}{3\rho_0}\int \frac{{\rm d}\mathbf{q}}{(2\pi)^3}\frac{\beta\hat{u}_0(q)}{P(1,q)\beta\hat{u}_0(q)+\kappa/N}\left.\frac{\partial S_1(q,\eta)}{\partial\eta}\right|_{\eta=0}, \tag{3.59}$$

leading to $\Delta R^2_{e,\rm GF}/R^2_{e,0} \approx 0.0141$ in the limit of $N/\kappa \to \infty$, shown as the inset of Fig. 3.1(a). These results can be compared with those shown in Fig. 5(a) of Ref. [47] obtained on the 1D lattice. That $\Delta R^2_{e,\rm GF}$ does not diverge in this limit is therefore due to the error cancelation between the use of ideal-chain conformations and RPA closure, which may also be the reason

for the surprisingly good prediction of GF theory shown in Fig. 3.1(a). Due to the poor performance of RISM theory for chain dimensions, we do not consider it with Zhou closure here.

For DBC at $N/\kappa = 0$, we see in Fig. 3.1(b) that ΔR_e^2 obtained from all the methods monotonically increase with increasing χN (i.e., the repulsion between A and B segments causes chain-stretching), and both theories give good predictions at small $\chi N \lesssim 1$, where Taylor expansion of Eq. (3.22) gives $\Delta R_{e,\mathrm{GF}}^2 \propto \chi N$ (at $N/\kappa = 0$). For $3 \lesssim \chi N \lesssim 8$ GF theory gives better prediction than RISM-PY theory (both with $\hat{\omega}_{s,s'}^{\mathrm{DGC}}$), while at larger χN the opposite occurs. The latter is due to the divergence of $\Delta R_{e,\mathrm{GF}}^2$ at the mean-field ODT $\chi_{\mathrm{MF}}^* N = 10.047$, where the matrix $(\mathbf{S}_\omega^{\mathrm{RPA}})^{-1}$ becomes singular at the most unstable mode $q_{\mathrm{MF}}^* R_{e,0} = 4.634$. In contrast, we see that both $\Delta R_{e,\mathrm{FOMC}}^2$ and $\Delta R_{e,\text{RISM-PY}}^2$ remains finite even at the ODT $\chi^* N = 25.67$ determined from FOMC simulations. Fig. 3.1(b) further shows that, while $\Delta R_{e,\mathrm{GF}}^2$ monotonically increases with χN at small $N/\kappa \lesssim 10$, at larger N/κ it slightly decreases with increasing χN and exhibits a minimum before diverging at $\chi_{\mathrm{MF}}^* N$ (which is independent of N/κ). This is consistent with our simulation results at $N/\kappa = 50$, where the GF theory still gives good prediction up to $\chi N \lesssim 6$. Due to the poor performance of RISM-PY theory with $\hat{\omega}_{s,s'}^{\mathrm{DGC}}$ for homopolymers at $N/\kappa = 50$ shown in Fig. 3.1(a), we do not consider it for DBC at $N/\kappa = 50$ here.

Fig. 3.1(c) shows the mean-square block end-to-end distance ΔR_{eb}^2. We see that, at $N/\kappa = 0$, ΔR_{eb}^2 obtained from all the methods exhibit a small positive maximum around $\chi N = 2$, and that both theories give good predictions up to $\chi N \lesssim 4$. At larger χN, ΔR_{eb}^2 becomes negative, and GF theory underestimates ΔR_{eb}^2 mainly due to its divergence to $-\infty$ at $\chi_{\mathrm{MF}}^* N$ (again caused by the singularity of $(\mathbf{S}_\omega^{\mathrm{RPA}})^{-1}$); in contrast, RISM-PY theory with $\hat{\omega}_{s,s'}^{\mathrm{DGC}}$ overestimates ΔR_{eb}^2, and both $\Delta R_{eb,\mathrm{FOMC}}^2$ and $\Delta R_{eb,\text{RISM-PY}}^2$ remains finite at $\chi^* N$. We also note that, at small $\chi N \lesssim 1$, the Taylor expansion of Eq. (3.22) gives $\Delta R_{eb,\mathrm{GF}}^2 \propto \chi N$ at $N/\kappa = 0$. On the the hand, for $N/\kappa \gtrsim 10$ $\Delta R_{eb,\mathrm{GF}}^2$ monotonically decreases with increasing χN, which is consistent with our simulation results at $N/\kappa = 50$.

Finally, we examine the difference in the bonding energy per chain from the reference state, $\beta\Delta u_{c,\mathrm{b}}$. For homopolymers, $\beta\Delta u_{c,\mathrm{b}}$ exhibits similar behavior to ΔR_e^2 as expected and is not shown. Fig. 3.2 shows $\beta\Delta u_{c,\mathrm{b}}$ for DBC obtained from various methods, which is similar to Fig. 3.1(c) except that $\beta\Delta u_{c,\mathrm{b}}^{\mathrm{FOMC}}$ exhibits a minimum before $\chi^* N$ and increases with increasing χN after that. This minimum, absent in R_{eb}^2, is clearly due to the contribution of A-B (and nearby) bonds. In fact, the difference in the mean-square bond length of both the fourth and fifth bonds from the reference state, $\Delta R^2(e_1 = 4, e_2 = 5)$ and $\Delta R^2(e_1 = 5, e_2 = 6)$, exhibits similar behavior to ΔR_e^2 shown in Fig. 3.1(b). GF theory, however, cannot capture the minimum in $\beta\Delta u_{c,\mathrm{b}}$ due to the divergence to $-\infty$ of other bonds. In contrast, while RISM-PY theory with $\hat{\omega}_{s,s'}^{\mathrm{DGC}}$ overestimates $\beta\Delta u_{c,\mathrm{b}}$ at $\chi N \gtrsim 4$, it can capture this minimum. Note that, however, the relative difference $\Delta u_{c,\mathrm{b}}/u_{c,\mathrm{b}}^{\mathrm{SCF}}$ is very small, meaning that the effect of χN on the bonding energy is negligible compared to the SCF contribution while $\hat{\omega}_{s,s'}^{\mathrm{DGC}}$ and $\hat{\omega}_{s,s'}^{\mathrm{FOMC}}$ are different.

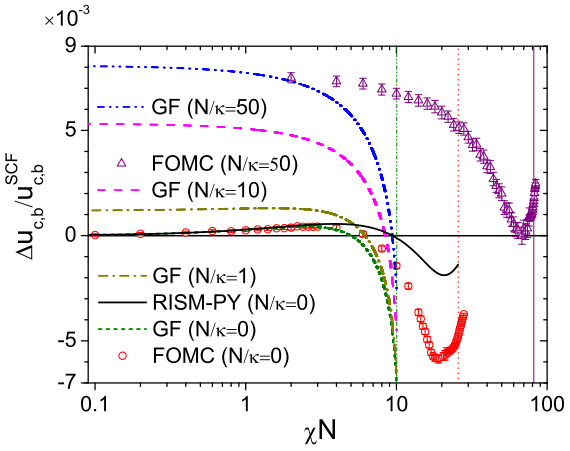

Figure 3.2: Semilogarithmic plot of the bonding energy difference per chain $\beta\Delta u_{c,\mathrm{b}}$ varying with χN for DBC, obtained form different methods.

3.3.2 E_κ, E_χ and their fluctuations

From Eqs. (3.7), (3.8) and (3.12), we see that the non-bonded internal energy per chain $u_{c,\mathrm{nb}}$ and the difference in the Helmholtz free energy per chain from the reference state Δf_c are

directly related to the ensemble averages of E_κ and E_χ, and that the non-bonded constant-volume heat capacity C_V is directly related to their fluctuations. We therefore focus on the behavior of E_κ and E_χ here.

For homopolymers ($\chi N = 0$), we see from Fig. 3.3(a) that $\langle E_\kappa \rangle / n$ obtained from all the methods monotonically decrease with increasing N/κ, because polymer segments reduce their contact (overlap) as their repulsion increases. Since $\bar{\mathcal{N}} = 10^4$ here is below the FCC close packing of theses segments (which corresponds to $\bar{\mathcal{N}} = 2 \times 10^4$),[3] in the limit of $N/\kappa \to \infty$ we have the ground state of hard-sphere chains with $\beta u_{c,\mathrm{nb}} = 0$, which has no fluctuations (i.e., the presence of multiple energy levels) and gives $\langle E_\kappa \rangle / n = [\beta u_0(0)/\rho_0 - 1]/2 \approx 0.6937$. There are, however, correlations in the ground state; that is, the segments cannot overlap. Fig. 3.3(a) shows that RISM-PY theory with $\hat{\omega}^{\mathrm{DGC}}_{s,s'}$ gives very good prediction; even in the limit of $N/\kappa \to \infty$, it gives $\langle E_\kappa \rangle^{\mathrm{IE}} / n \approx 0.7066$, slightly higher (by $< 2\%$) than the above exact value. The deviation is due to the use of ideal-chain conformations. In fact, in this limit we have $h_{s,s'}(r < \sigma) = -1$; Eq. (3.50) then leads to $\langle E_\kappa \rangle^{\mathrm{IE}} / n = (2\pi/\rho_0 N) \sum_{s,s'=1}^{N} \int_0^\sigma \mathrm{d}r \omega^{\mathrm{DGC}}_{s,s'}(r) \beta u_0(r) r^2 - 1/2 \approx 0.7066$. We also note that using $\hat{\omega}^{\mathrm{FOMC}}_{s,s'}$ in RISM-PY theory gives worse prediction (underestimate) than using $\hat{\omega}^{\mathrm{DGC}}_{s,s'}$ for N/κ up to 50 (more clearly seen in Fig. 3.5(a) below); this unexpected result is due to the error cancelation between the use of ideal-chain conformations and PY closure at finite N/κ. As an evidence as shown in the inset, we found that RISM-Zhou theory (with high accuracy at large pair interactions) with $\hat{\omega}^{\mathrm{FOMC}}_{s,s'}$ gives better prediction than using $\hat{\omega}^{\mathrm{DGC}}_{s,s'}$ (more clearly seen in Fig. 3.5(a) below) as expected. We see that the prediction of RISM-Zhou theory with $\hat{\omega}^{\mathrm{FOMC}}_{s,s'}$ is undistinguishable with that from RISM-PY with $\hat{\omega}^{\mathrm{DGC}}_{s,s'}$ up to $N/\kappa = 50$, while RISM-Zhou theory with $\hat{\omega}^{\mathrm{DGC}}_{s,s'}$ overestimates $\langle E_\kappa \rangle / n$.

On the other hand, GF theory only works for $N/\kappa \lesssim 1$ and underestimates $\langle E_\kappa \rangle$ at larger N/κ. For large N/κ, our numerical calculations give $\langle E_\kappa \rangle^{\mathrm{GF}} / n \propto (N/\kappa)^{-0.25}$ (for N/κ up to 10^{10}, not shown), which is different from the lattice case where $\langle E_\kappa \rangle^{\mathrm{GF}} / n \propto (N/\kappa)^{-1}$ was found.[47] At $\chi N = 0$, Eq. (3.25) can be rewritten as $\langle E_\kappa \rangle^{\mathrm{GF}} / n =$

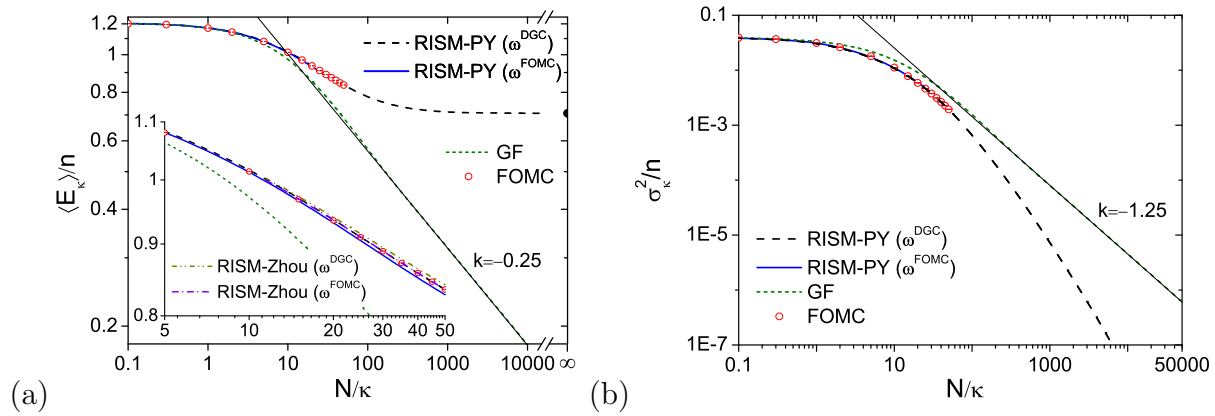

Figure 3.3: Log-log plot of $\langle E_\kappa \rangle$ in part (a) and its fluctuations σ_κ^2 in part (b) as functions of N/κ for homopolymers at $\chi N = 0$ obtained from different methods. "$k = a$" denotes a straight line of slope a.

$(1/4\pi^2\rho_c)\int_0^\infty dqq^2\beta\hat{u}_0(q)P(1,q)/[(N/\kappa)\beta\hat{u}_0(q)P(1,q)+1]$, which corresponds to Eq. (19) in Ref. [47]. With $\beta\hat{u}_0(q) = 1$ on a lattice, we then obtain the "-1" scaling in the limit of $N/\kappa \to \infty$ after the Taylor expansion in terms of κ/N. But for the soft potential used here, $\beta\hat{u}_0(q)$ is not constant and approaches 0 in the limit of $q \to \infty$, which changes the scaling of $\langle E_\kappa \rangle^{\rm GF}/n$ with N/κ. Clearly, $\langle E_\kappa \rangle^{\rm GF} = 0$ in the limit of $N/\kappa \to \infty$ indicates that GF theory does not capture the segment correlations in the ground state.

Fig. 3.3(b) shows the fluctuations of E_κ, σ_κ^2, for homopolymers as a function of N/κ. GF theory again only works for $N/\kappa \lesssim 1$, and overestimates σ_κ^2 at larger N/κ. For large N/κ, our numerical calculations give $\sigma^2_{\kappa,\rm GF} \propto (N/\kappa)^{-1.25}$, consistent with the above behavior of $\langle E_\kappa \rangle^{\rm GF}$ [see Eq. (3.9)]. In contrast, RISM-PY predictions with both $\hat{\omega}^{\rm DGC}_{s,s'}$ and $\hat{\omega}^{\rm FOMC}_{s,s'}$ are in quantitative agreement with our simulation results, and the former decreases more rapidly with increasing N/κ than GF prediction at large N/κ. While our simulation data are only for $N/\kappa \leq 50$, at larger N/κ they are expected to decrease also more rapidly than GF prediction, as found in the 1D lattice case shown in Fig. 3(a) of Ref. [47].

For DBC at $N/\kappa = 0$, we see in Fig. 3.4(a) that $\langle E_\chi \rangle$ obtained from all the methods monotonically decrease with increasing χN, because A and B segments reduce their contact as their repulsion increases. GF theory only works for $\chi N \lesssim 1$, and underestimates $\langle E_\chi \rangle$ at

larger χN; $\langle E_\chi \rangle^{\rm GF}$ diverges to $-\infty$ at $\chi^*_{\rm MF} N$ due to the singularity of the matrix $(\mathbf{S}^{\rm RPA}_\rho)^{-1}$ at the most unstable mode q^*. In contrast, both RISM-PY and FOMC results remain finite even at $\chi^* N$. While RISM-PY theory with both $\hat{\omega}^{\rm FOMC}_{s,s'}$ and $\hat{\omega}^{\rm DGC}_{s,s'}$ overestimates $\langle E_\chi \rangle$ for $\chi N \gtrsim 15$, using $\hat{\omega}^{\rm FOMC}_{s,s'}$ gives better prediction than using $\hat{\omega}^{\rm DGC}_{s,s'}$, as expected.

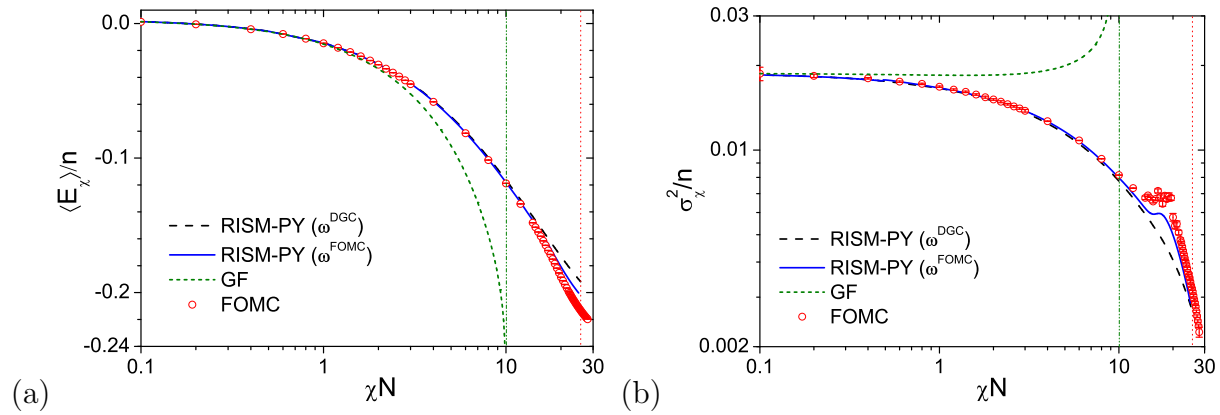

Figure 3.4: Semilogarithmic plot of $\langle E_\chi \rangle$ in part (a) and log-log plot of its fluctuations σ^2_χ in part (b) as functions of χN for DBC at $N/\kappa = 0$, obtained from different methods.

Finally, Fig. 3.4(b) shows the fluctuations of E_χ, σ^2_χ, of DBC at $N/\kappa = 0$. We see that GF prediction increases with increasing χN and diverges to ∞ at $\chi^*_{\rm MF} N$, consistent with the behavior of $\langle E_\chi \rangle^{\rm GF}$ [see Eq. (3.10)]. But this is the wrong trend, as $\langle E_\chi \rangle^{\rm FOMC}$ actually decreases with increasing χN. In contrast, RISM-PY theory gives much better predictions. RISM-PY theory with $\hat{\omega}^{\rm FOMC}_{s,s'}$ gives the closest prediction to our simulation results as expected, and even captures the small shoulder found in our simulations around $\chi N = 16$, which is not captured when ideal-chain formations are used. Note that the only difference in RISM-PY theory is from $\hat{\omega}_{s,s'}$, therefore the shoulder is caused by the stretching between different blocks or the compressing in each block comparing the ideal-chain conformations; for which the behaviors of chain dimension and bonded internal energy around $\chi N = 16$ for DBC at $N/\kappa = 0$ are also evidences, as shown in Fig. 3.1(b) and (c) and Fig. 3.2. Since E_χ can be divided into the intrachain and interchain parts raised by $\hat{\omega}^{\rm FOMC}_{s,s'}$ and $\hat{h}_{s,s'}$ (depending on $\hat{\omega}^{\rm FOMC}_{s,s'}$), respectively, according to Eq.(3.51), σ^2_χ can also be performed in this way. Our data (not shown) shows that the interchain contribution to σ^2_χ

is larger than the intrachain one in the order of at least 10^2. So the small shoulder is mainly an effect of collective behavior of the system, reflected by $\hat{h}_{s,s'}$, while it is originally caused by $\hat{\omega}^{\mathrm{FOMC}}_{s,s'}$, which influences $\hat{h}_{s,s'}$ through RISM equation.

3.3.3 Non-bonded internal energy and constant-volume heat capacity

For homopolymers (i.e., $\chi N = 0$), the non-bonded internal energy per chain $\beta u_{c,\mathrm{nb}}$ is directly calculated from $\langle E_\kappa \rangle$ according to Eq. (3.7) and is shown in Fig. 3.5(a). We see that $\beta u^{\mathrm{GF}}_{c,\mathrm{nb}} \propto N/\kappa$ at small $N/\kappa \lesssim 1$, and that RISM-PY theory with $\hat{\omega}^{\mathrm{DGC}}_{s,s'}$ can quantitatively predict $\beta u_{c,\mathrm{nb}}$ within the range of our simulation data. Its predictions with $\hat{\omega}^{\mathrm{FOMC}}_{s,s'}$, however, are less accurate (smaller) for N/κ up to 50, due to the error cancelation between the use of ideal-chain conformations and PY closure at finite N/κ. As an evidence, similar to the behavior of $\langle E_\kappa \rangle$, RISM-Zhou theory with $\hat{\omega}^{\mathrm{FOMC}}_{s,s'}$ gives better prediction than using $\hat{\omega}^{\mathrm{DGC}}_{s,s'}$ as expected, which is undistinguishable with that from RISM-PY with $\hat{\omega}^{\mathrm{DGC}}_{s,s'}$ up to $N/\kappa = 50$. On the other hand, RISM-PY prediction with $\hat{\omega}^{\mathrm{DGC}}_{s,s'}$ is proportional to N/κ at large N/κ (data not shown), due to the slight deviation of its predicted $\langle E_\kappa \rangle^{\mathrm{IE}}/n$ from the exact value in the limit of $N/\kappa \to \infty$; in other words, $\beta u^{\mathrm{IE}}_{c,\mathrm{nb}}$ diverges instead of approaching 0 in this limit, which is unphysical and due to the use of ideal-chain conformations. $\hat{\omega}^{\mathrm{FOMC}}_{s,s'}$ is therefore needed at large N/κ. Fig. 3.5(a) also shows that GF theory largely underestimates $\beta u_{c,\mathrm{nb}}$ and even gives the wrong trend for $N/\kappa \gtrsim 15$, because it fails to capture the segment correlations. Eq. (3.27) indicates that $\beta u^{\mathrm{GF}}_{c,\mathrm{nb}}$ has two parts: the SCF prediction $\beta u^{\mathrm{SCF}}_{c,\mathrm{nb}} = (N/2\kappa)[1 - \beta u_0(0)/\rho_0] \approx -0.6937 N/\kappa$ and the GF contribution $(N/\kappa)E^{\mathrm{GF}}_\kappa/n \propto (N/\kappa)^{0.75}$ at large N/κ; the former leads to $\beta u_{c,\mathrm{nb}} < 0$ at large N/κ.

Analogous to $\beta u_{c,\mathrm{nb}}$, the constant-volume heat capacity due to the non-bonded interactions $C_{V,\mathrm{nb}}$ is directly calculated from σ^2_κ according to Eq. (3.12). We find that $C_{V,\mathrm{nb}}$ from all the methods is proportional to $(N/\kappa)^2$ at small $N/\kappa \lesssim 1$ and monotonically increases with increasing $N/\kappa \leq 50$ (data not shown). At large N/κ, however, $C^{\mathrm{FOMC}}_{V,\mathrm{nb}}$ is expected to exhibit a maximum and then decrease to zero in the limit of $N/\kappa \to \infty$, where the system

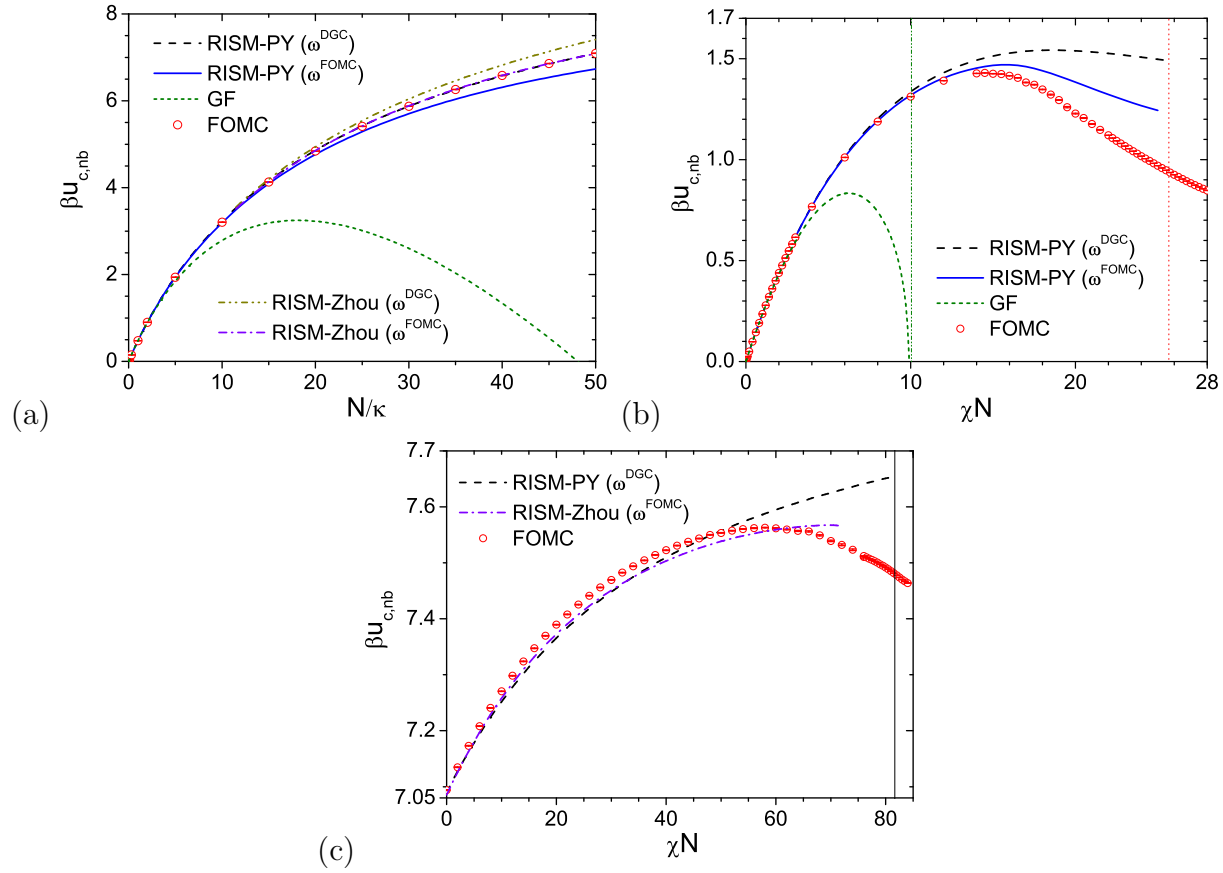

Figure 3.5: Comparison of non-bonded internal energy per chain $\beta u_{c,\mathrm{nb}}$ for homopolymers (a), and for DBC at $N/\kappa = 0$ (b) and $N/\kappa = 50$ (c), obtained from different methods.

is in the ground state; while the same is expected for the RISM-PY prediction with $\omega_{s,s'}^{\mathrm{DGC}}$, $C_{V,\mathrm{nb}}^{\mathrm{GF}} \propto (N/\kappa)^{0.75}$ and diverges in this limit.

For DBC at $N/\kappa = 0$, $\beta u_{c,\mathrm{nb}}$ is directly calculated from $\langle E_\chi \rangle$ according to Eq. (3.7) and is shown in Fig. 3.5(b). We see that $\beta u_{c,\mathrm{nb}}$ from all the methods is proportional to χN at small $\chi N \lesssim 0.1$ (i.e., where $\langle E_\chi \rangle$ is nearly constant), and exhibits a maximum due to the competing SCF contribution of random mixing ($\chi N/4$) and the fluctuation/correlation contribution of A-B segregation (i.e., $\langle E_\chi \rangle$ monotonically decreases with increasing χN as shown in Fig. 3.4(a)). At $N/\kappa = 50$, $\langle E_\kappa \rangle$ also contributes to $\beta u_{c,\mathrm{nb}}$, and we do not consider the RISM-PY with $\hat{\omega}_{s,s'}^{\mathrm{FOMC}}$, RISM-Zhou with $\hat{\omega}_{s,s'}^{\mathrm{DGC}}$ and GF predictions due to their poor performance. Fig. 3.5(c) compares $\beta u_{c,\mathrm{nb}}$ calculated from RISM-PY with $\hat{\omega}_{s,s'}^{\mathrm{DGC}}$, RISM-Zhou

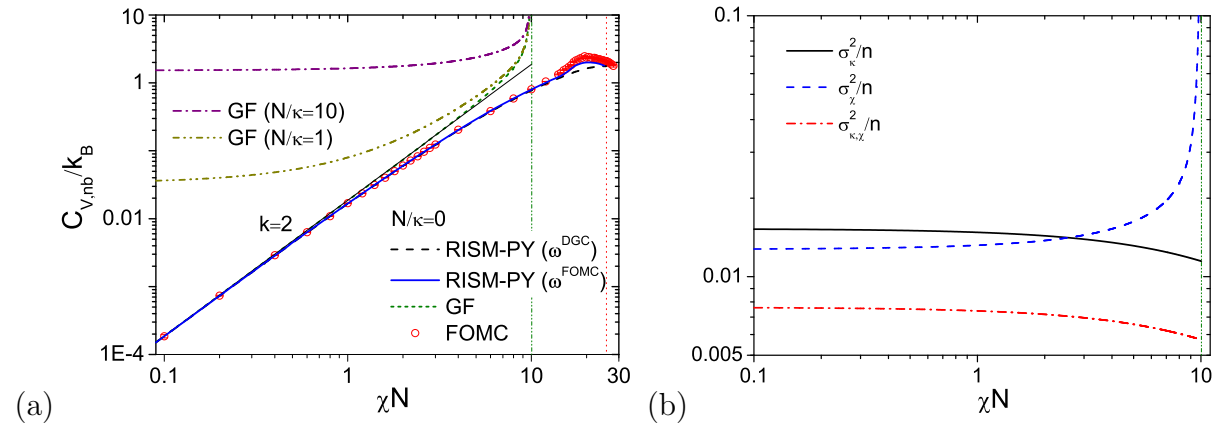

Figure 3.6: (a) The non-bonded constant volume heat capacity $C_{V,\mathrm{nb}}$ as a function of χN for DBC at $N/\kappa = 0$. (b) The fluctuations of the non-bonded "contacts" vary with χN predicted by GF theory at $N/\kappa = 10$. "$k = 2$" in part (a) denotes a straight line of slope 2.

with $\hat{\omega}_{s,s'}^{\mathrm{FOMC}}$ and FOMC simulations. In this case, RISM-PY cannot capture the maximum in $\beta u_{c,\mathrm{nb}}$ before the ODT determined from FOMC simulations; on the other hand, RISM-Zhou with $\hat{\omega}_{s,s'}^{\mathrm{FOMC}}$ gives better prediction and we expect that it can even capture the maximum in $\beta u_{c,\mathrm{nb}}$ (need $\hat{\omega}_{s,s'}^{\mathrm{FOMC}}$ for $\chi N > 70$ to prove this).

Finally, Fig. 3.6(a) shows $C_{V,\mathrm{nb}}$ for DBC at $N/\kappa = 0$, calculated directly from σ_χ^2 shown in Fig. 3.4(b). We see that $C_{V,\mathrm{nb}}^{\mathrm{FOMC}}$ exhibits a maximum before $\chi^* N$, which is captured by RISM-PY theory with $\omega_{s,s'}^{\mathrm{FOMC}}$ but not with $\omega_{s,s'}^{\mathrm{DGC}}$; this behavior can be deduced from the behavior of σ_χ^2. On the other hand, as N/κ increases the χN dependence of $C_{V,\mathrm{nb}}^{\mathrm{GF}}$ is reduced and $C_{V,\mathrm{nb}}^{\mathrm{GF}}$ is even independent of χN at small χN. Regardless of N/κ, $C_{V,\mathrm{nb}}^{\mathrm{GF}}$ diverges at $\chi_{\mathrm{MF}}^* N$, which is caused only by the divergence of σ_χ^2; Fig. 3.6(b) shows that both σ_κ^2 and $\sigma_{\kappa,\chi}^2$ predicted by GF theory decrease with increasing χN and remain finite at $\chi_{\mathrm{MF}}^* N$.

3.3.4 Pressure and free energy

Since the pressure due to the bonding interaction is proportional to the bonding internal energy, here we only examine the difference in pressure from the reference state due to the non-bonded interactions, $\beta \Delta P_{\mathrm{nb}}$, as shown in Fig. 3.7. For homopolymers (i.e., $\chi N = 0$), we see that $\beta \Delta P_{\mathrm{nb}} \propto N/\kappa$ at small $N/\kappa \lesssim 1$, and that RISM-PY theory with $\hat{\omega}_{s,s'}^{\mathrm{DGC}}$ can

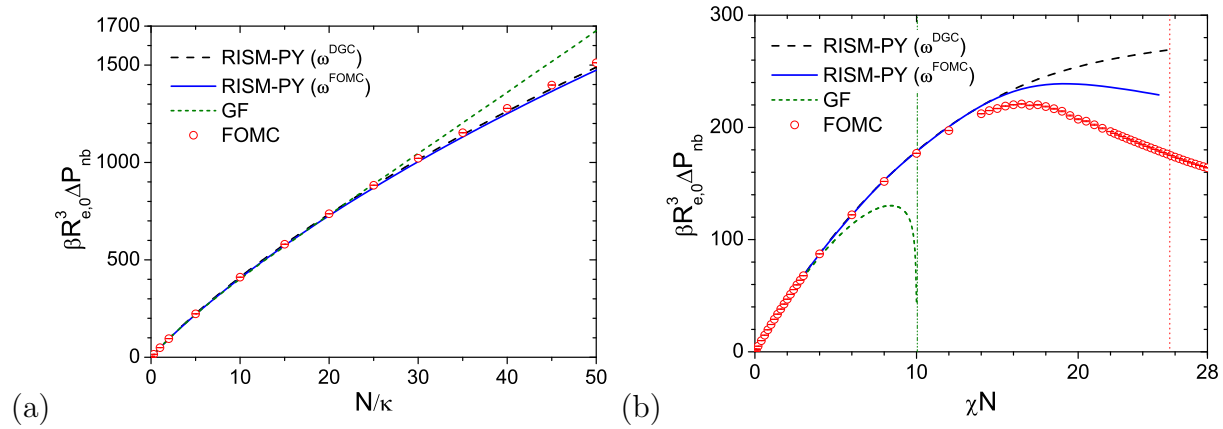

Figure 3.7: Comparison of non-bonded pressure $\beta P_{\rm nb}$ for homopolymers (a), and for DBC at $N/\kappa = 0$ (b), obtained from different methods.

quantitatively predict $\beta\Delta P_{\rm nb}$ within the range of our simulation data. Its predictions with $\hat{\omega}^{\rm FOMC}_{s,s'}$, however, are less accurate (smaller) for N/κ up to 50, due to the same reason for $\beta u_{c,\rm nb}$. We also see that GF theory overestimates $\beta\Delta P_{\rm nb}$ at large $N/\kappa \gtrsim 20$, which is different from that for $\beta u_{c,\rm nb}$. On the other hand, the predictions of RISM-PY with $\hat{\omega}^{\rm DGC}_{s,s'}$ and GF theories are proportional to N/κ at large N/κ, because the SCF contribution dominates at large N/κ, which is proportional to N/κ; in other words, they diverge instead of approaching 0 in the limit of $N/\kappa \to \infty$ due to the use of ideal-chain conformations. For DBC at $N/\kappa = 0$ (as well as at $N/\kappa = 50$, data not shown), as shown in Fig. 3.7(b), the behavior of $\beta\Delta P_{\rm nb}$ is similar to that of $\beta u_{c,\rm nb}$.

Fig. 3.8 shows the χN and N/κ dependence of the difference in the free energy per chain from the reference state, $\beta\Delta f_c$, which is directly calculated from $\langle E_\kappa \rangle$ and $\langle E_\chi \rangle$ according to Eq. (3.8). Similar behaviors to $\beta u_{c,\rm nb}$ are observed for homopolymers at $\chi N = 0$, as shown in Fig. 3.8(a), and the valid N/κ range for RISM-PY theory is larger than $\beta u_{c,\rm nb}$. On the other hand, the RISM-PY prediction with $\hat{\omega}^{\rm DGC}_{s,s'}$ is proportional to N/κ at large N/κ (data not shown); in other words, $\beta f_c^{\rm IE}$ diverges in the limit of $N/\kappa \to \infty$ due to the use of ideal-chain conformations. Fig. 3.8(a) also shows that $\beta\Delta f_c^{\rm GF}$ exhibits a maximum, which can be found from Eq. (3.8) and the behavior of $\langle E_\kappa^{\rm GF} \rangle$ shown in Fig. 3.3(a); the

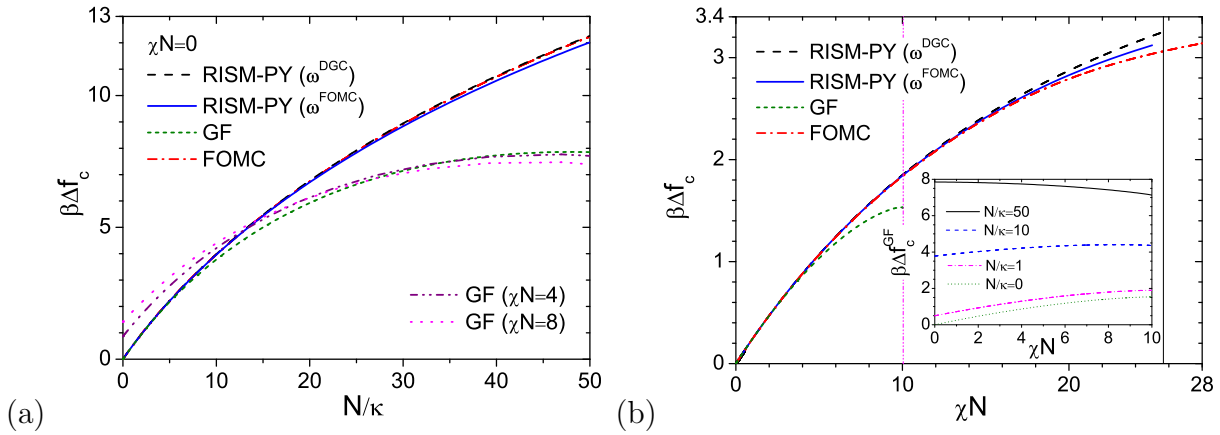

Figure 3.8: Free energy difference per chain $\beta\Delta f_c$ varies with N/κ at $\chi N = 0$ in part (a) and with χN at $N/\kappa = 0$ in part (b), respectively, obtained from different methods. The inset of part (b) compares $\beta\Delta f_c^{\rm GF}$ as a function of χN at different N/κ.

position of the maximum decreases from $N/\kappa \approx 48$ at $\chi N = 0$ to $N/\kappa \approx 43$ at $\chi N = 8$. Additionally, $\beta\Delta f_c^{\rm GF}$ decreases to negative value at large N/κ (data not shown), where the SCF contribution ($-0.6937N/\kappa$) dominates in Eq. (3.8).

For DBC at $N/\kappa = 0$ as shown in Fig. 3.8(b), while $\beta\Delta f_c$ from all the methods is proportional to χN at small $\chi N \lesssim 1$ similar to the behavior of $\beta u_{c,\rm nb}$, they monotonically increase with χN up to $\chi^* N$ ($\chi^*_{\rm MF}$ for GF theory), because the SCF contribution ($\chi N/4$) is always larger than the absolute value of the fluctuation/correlation corrections in Eq. (3.8). Note that $\beta\Delta f_c^{\rm GF}$ does not diverge [as evident from Eq. (3.19) or the behavior of $E_\chi^{\rm GF}/n$] at $\chi^*_{\rm MF}N$, which means that the entropy per chain $\Delta s_c^{\rm GF}/k_B = \beta\Delta u_c^{\rm GF} - \beta\Delta f_c^{\rm GF}$ must diverge just like the non-bonded internal energy, consistent with the divergence of $R^2_{e,\rm GF}$. The inset of this figure shows that at small N/κ, $\beta\Delta f_c^{\rm GF}$ monotonically increases with increasing χN; as N/κ increases, $\beta\Delta f_c^{\rm GF}$ exhibits a maximum before $\chi^*_{\rm MF}N$; and at larger N/κ, $\beta\Delta f_c^{\rm GF}$ monotonically decreases with increasing χN.

Note that, RISM-Zhou closure exhibits similar behaviors for $\beta\Delta P_{\rm nb}$ and $\beta\Delta f_c$ to that of $\beta u_{c,\rm nb}$, we thus do not show its prediction here for clearness of our figures (neither for the following structural properties). In the following, only the ideal-chain conformations are considered.

3.3.5 Structure factors

Fig. 3.9 compares the structure factors $S_t(q)$ and $S_\psi(q)$ at $N/\kappa = 0$ for all methods. The deviation of $S_t(q)$ between RISM-PY method and FOMC simulations is due to the approximations (PY closure and $\omega^{\mathrm{DGC}}_{s,s'}$) in RISM-PY method; and the deviation of $S_t(q)$ between GF theory and FOMC simulations is due to the approximations of $\omega^{\mathrm{DGC}}_{s,s'}$ and the higher-order terms neglected in the random-phase approximation. As shown in Fig. 3.9(a), the RISM-PY predictions of $S_t(q)$ are mainly consistent with the FOMC simulation results far away from the ODT determined from FOMC ($\chi^* N = 25.56$), which is consistent with our previous discussions, but apparently, the GF predictions underestimate $S_t(q)$ except at the ideal-chain case. Note that $S_t(0)$ decreases with increasing χN; this is because $S_t(0)$ is proportional to the isothermal compressibility, which decreases with increasing non-bonded interactions.

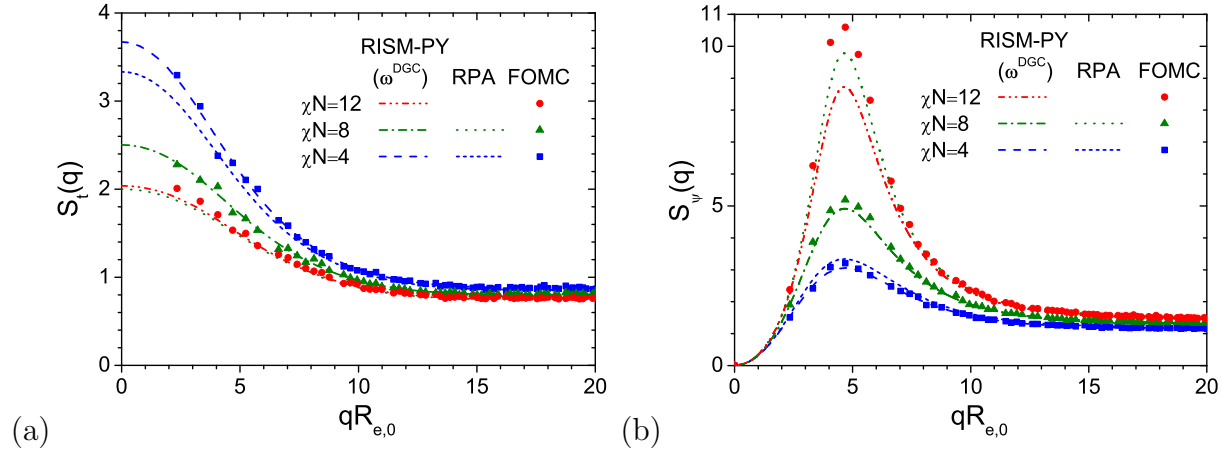

Figure 3.9: Comparison of structure factors $S_t(q)$ in part (a) and $S_\psi(q)$ in part (b), respectively, for different χN, obtained from different methods at $N/\kappa = 0$.

Fig. 3.9(b) shows the structure factor $S_\psi(q)$ characterizing the composition fluctuations in DBC at different χN. We see a growing peak at the most unstable mode q^* as χN increases, and the simulation results lie in-between the RISM and RPA predictions. While RISM-PY underestimates $S_\psi(q)$ (except for ideal chains) and exhibits larger deviation from the FOMC result with increasing χN, it is much better than the RPA prediction. Using $\omega^{\mathrm{FOMC}}_{s,s'}$, RISM-PY method gives better prediction of $S_\psi(q)$ than $\omega^{\mathrm{DGC}}_{s,s'}$, and it lie in-between

the simulation results and the RISM-PY prediction with $\omega_{s,s'}^{\mathrm{DGC}}$ (data not shown). We also note that $\chi N = 12$ is already larger than the mean-field ODT.

3.3.6 Trends of ODT predicted by RISM-PY method

The mean-field ODT χ^*_{MF} is given by RPA; $S_\psi^{-1}(q^*)$ from RPA is a linear function of χ, and $S_\psi^{-1}(q^*) = 0$ at χ^*_{MF}. While $S_\psi^{-1}(q^*)/S_\psi^{-1}(q^*, \chi N = 0)$ from RPA does not depend on σ/a and N/κ, the RISM-PY results do, exhibit non-linear behavior at large χ, and are always positive for finite χ, which means this theory does not give a ODT as it only works for the disordered phase. In this section we therefore analyze the trends of ODT by comparing the rates at which $S_\psi^{-1}(q^*)/S_\psi^{-1}(q^*, \chi N = 0)$ approaches 0 (or how close it is to RPA prediction) obtained from the RISM-PY method with $\hat{\omega}_{s,s'}^{\mathrm{DGC}}$, which captures some of the qualitative behavior of the ODT determined in our recent FOMC simulations of symmetric DBC.[3]

Fig. 3.10(a) shows how the RISM-PY prediction of the peak position q^* varies with χ normalized by the ODT determined from simulations, and we see a unexpected minimum (marked by the symbol) at both $N/\kappa = 0$ and 50. The unexpected increase of q^* at large χ signifies the breakdown of RISM-PY method.

Fig. 3.10(b) shows the N/κ and σ/a dependence of $S_\psi^{-1}(q^*)/S_\psi^{-1}(q^*, \chi N = 0)$ at $\bar{\mathcal{N}} = 10^4$, where the symbols denote the χN value where RISM-PY method the breaks down (same for the other plots in Fig. 3.10). We see that, at given σ/a, $S_\psi^{-1}(q^*)/S_\psi^{-1}(q^*, \chi N = 0)$ predicted by RISM-PY method increases with increasing N/κ and approaches 0 at slower rate. This is because, as N/κ increases, the A-B repulsion characterized by χN becomes relatively weaker, thus requiring larger χN to form lamellae. This behavior is consistent with most cases of the FOMC results, but at $\sigma/a = 1.15$, $\chi^*/\chi^*_{\mathrm{MF}}$ decreases with increasing N/κ for $\bar{\mathcal{N}} \lesssim 1300$ at $N = 10$ or $\bar{\mathcal{N}} \lesssim 2500$ at $N = 20$ in the simulation results, which cannot be explained by IE theories. On the other hand, as σ/a increases, the RISM-PY results approach the RPA prediction (i.e., $S_\psi^{-1}(q^*)/S_\psi^{-1}(q^*, \chi N = 0)$ approaches 0 at faster rate), which is consistent with our FOMC results. This is because, as σ/a increases, the A-B

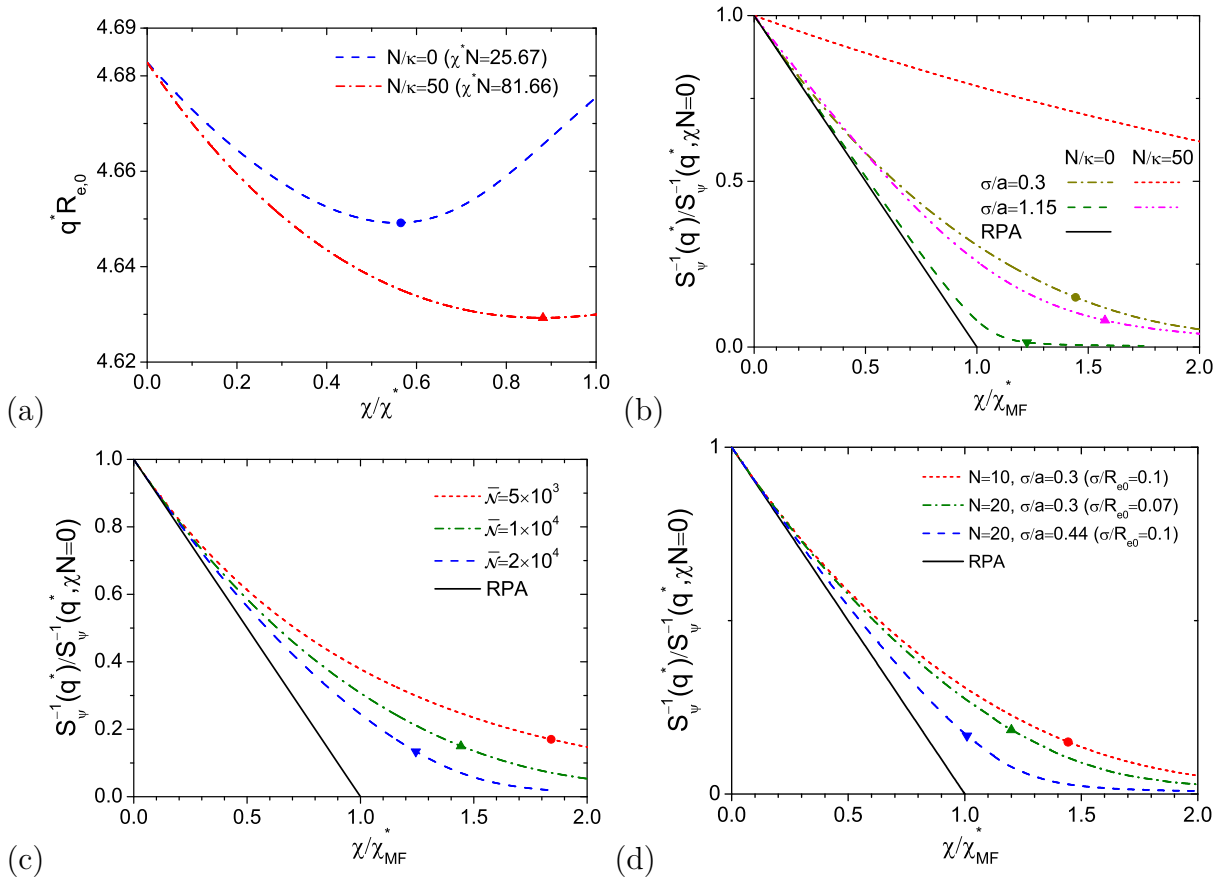

Figure 3.10: (a) The most unstable mode q^* as a function of χ normalized by $\chi^*_{\rm MF}N$ predicted by RISM theory, where χ^*N is the ODT obtained from FOMC simulations. Comparison of $S_\psi^{-1}(q^*)$ predicted by RIMS theory as a function of $\chi/\chi^*_{\rm MF}$ to analyze the effects of σ/a and N/κ in part (b) at $\bar{\mathcal{N}} = 10^4$, the effect of $\bar{\mathcal{N}}$ in part (c) at $N/\kappa = 0$ and $\sigma/a = 0.3$, and the effect of chain discretization in part (d) at $N/\kappa = 0$.

repulsion becomes effectively larger, thus requiring lower χN to form lamellae.

As $\bar{\mathcal{N}}$ increases, Fig. 3.10(c) shows that, at $N/\kappa = 0$ and $\sigma/a = 0.3$, $S_\psi^{-1}(q^*)/S_\psi^{-1}(q^*)|_{\chi N=0}$ approaches 0 faster; in other words, as $\bar{\mathcal{N}}$ increases, the system fluctuations approaches Gaussian-level, which is consistent with out FOMC results.[3]

Finally, we also investigate the effects of the chain length N, as shown in Fig. 3.10(d). At given $\sigma/a = 0.3$ and $N/\kappa = 0$, $S_\psi^{-1}(q^*)/S_\psi^{-1}(q^*, \chi N = 0)$ predicted by RISM-PY method decreases with increasing N and approaches 0 at faster rate. But we note that varying N at constant σ/a exhibits both the short-range correlation and chain discretization effects,

because changing N also changes $R_{e,0}$. To investigate the latter alone, we compare the case of $N = 10$ and $\sigma/a = 0.3$ (i.e. $\sigma/R_{e,0} = 0.1$) with that of $N = 20$ and $\sigma/R_{e,0} = 0.1$. We see that the RISM-PY prediction of $S_\psi^{-1}(q^*)/S_\psi^{-1}(q^*, \chi N = 0)$ approaches 0 also at faster rate with only increasing the chain discretization, which is consistent with the FOMC results. One may expect that the chain discretization effects diminish quickly and the RISM-PY results approach RPA with increasing the chain discretization.

In another point of view, the RPA closure can be obtaind by Taylor expansion from the PY closure with respect to $\beta u_{s,s'}(r)$, which is more accurate for smaller $\beta u_{s,s'}(r)$. Since the maximum value of $\beta u_{s,s'}(r)$, achieved at $r = 0$, linearly varies with $(N/\kappa)\rho_c^{-1}N^{-2}(\sigma/R_{e,0})^{-3}$ (or equivalently $(N/\kappa)\rho_c^{-1}N^{-1/2}(\sigma/a)^{-3}$), smaller N/κ or larger ρ_c (or $\bar{\mathcal{N}}$) makes $\beta u_{s,s'}(r)$ smaller, therefore, Fig. 3.10(b) and 3.10(c) show that as N/κ decreases or $\bar{\mathcal{N}}$ increases, RISM-PY method approaches RPA results. Similarly, as σ/a increases at the same N, $\beta u_{s,s'}(r = 0)$ decreases, Fig. 3.10(b) thus shows that RISM-PY method approaches RPA results with increasing σ/a. Finally, keeping $\sigma/R_{e,0}$ as constant, $\beta u_{s,s'}(r)$ decreases with increasing the chain discretization, which is consistent with the middle two curves in Fig. 3.10(d); on the other hand, comparing the upper two curves in Fig. 3.10(d), since increasing N and decreasing $\sigma/R_{e,0}$ have competing effects on $\beta u_{s,s'}(r)$, the former is clearly more significant than the latter for this case.

3.3.7 Chain-end effects in integral equation theories

The comparison of $\beta\Delta u_{c,\mathrm{nb}}$ and βP_{nb} between RISM and PRISM theories provides us with the chain-end effects neglected in the PRISM theory, shown as in Fig. 3.11 at $N/\kappa = 0$ for instance. We find, with $\omega_{s,s'}^{\mathrm{DGC}}$, both $\beta u_{c,\mathrm{nb}}$ and βP_{nb} from PRISM-PY method are lower than that from RISM-PY at high χN values, meaning that PRISM-PY gives solutions closer to FOMC simulation than RISM-PY, which is conflict with our expectation and it is probably caused by error cancelation between the chain-end effects and the PY closure.

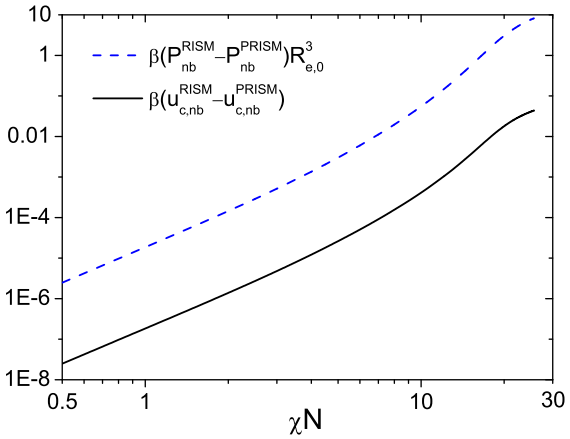

Figure 3.11: Comparison of the non-bonded internal energy per chain $\beta u_{c,\mathrm{nb}}$ and pressure $\beta P R_{e,0}^3$ between RISM and PRISM theories.

To show the chain-end effects in RISM theory, Fig. 3.12 compares the interchain pair radial distribution functions $g_{s,s'}(r)$ at $N/\kappa = 0$ and $\chi N = 10$, which depends significantly on the pair of segments either in the same block or in different blocks. In the same block (A), if we fix the first segment $s = 1$ and change the position of another segment $s' = 1 \to N_\mathrm{A}$ along the chain contour, as in Fig. 3.12(a), $g_{s,s'}(r)$ increases first and then decreases with increasing s' in the range of $0 \le r/R_{e,0} \le 0.5$; Fig. 3.12(b) shows $g_{s,s'}(r)$ with $s = s' = 1 \to N_\mathrm{A}$ and we find it similarly increases first and then decreases with increasing s and the difference is larger than Fig. 3.12(a). Therefore in the same block, the closer to the middle of the chain, the higher excluded-volume effects and the lower interchain pair correlations exhibit. Fig. 3.12(c) and (d) compare the contribution of different pair correlations to the averaged radial distribution function between A and B blocks $g_\mathrm{AB}(r) \equiv (1/N_\mathrm{A}N_\mathrm{B}) \sum_{s\in\mathrm{A},s'\in\mathrm{B}} g_{s,s'}(r)$. This figure shows that all of them have a peak at about $r/R_{e,0} = \sigma/R_{e,0}$, at which $g_{s,s'}(r)$ decreases first and then increases in the order of $(s,s') = (1, N_\mathrm{A}+1), (1, N_\mathrm{A}+2)...(1, N)$ [Fig. 3.12(c)] and in the order of $(s,s') = (1, N), (2, N-1)...(N_\mathrm{A}, N_\mathrm{A}+1)$ [Fig. 3.12(d)]. In the middle of a block the excluded-volume effects play an important role, leading to lower correlations; on the other hand, the A-B repulsion ($\chi N = 10$ here) induces the system to form A-like and B-like clusters, leading to higher interchain pair correlation for ending

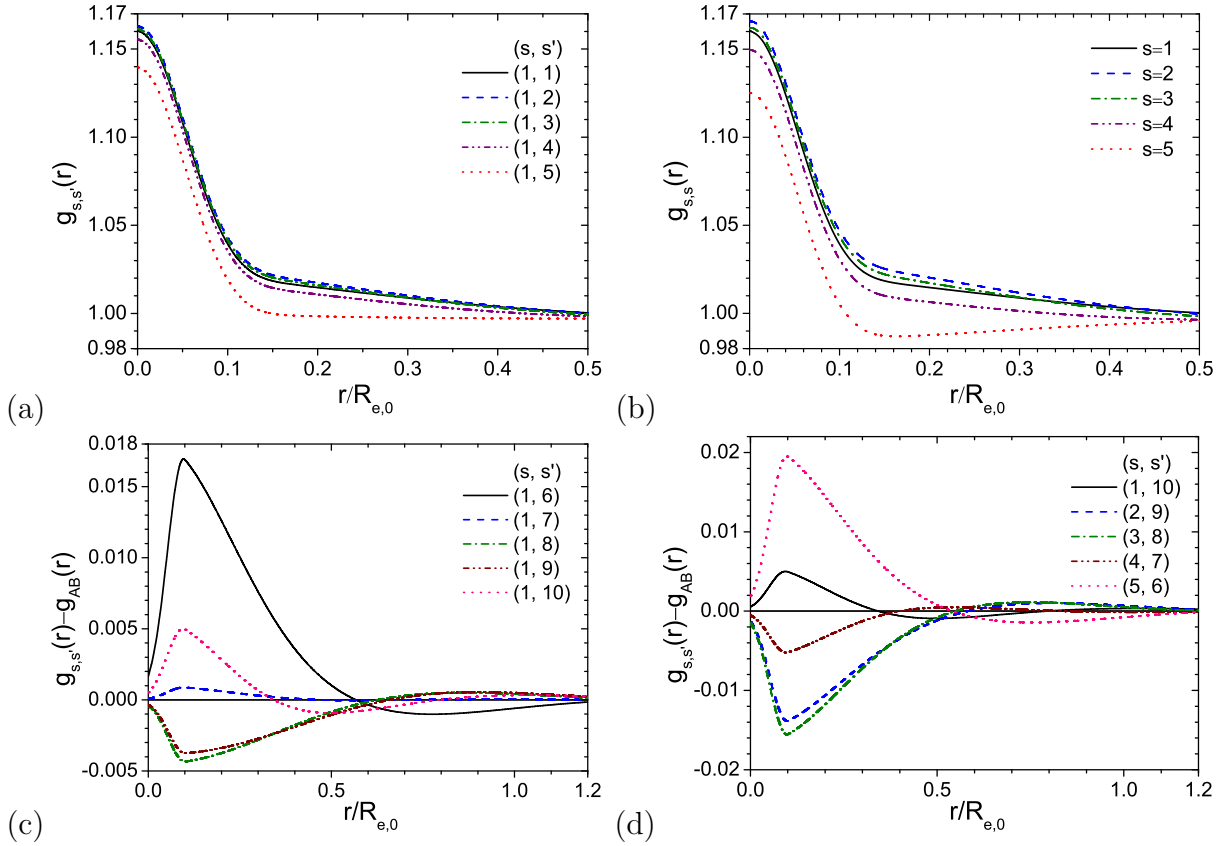

Figure 3.12: Chain end effects in RISM theory by comparing the interchain pair radial distribution functions $g_{s,s'}(r)$ in the same block in parts (a) and (b), and between different blocks in parts (c) and (d), respectively.

segment of each block [$g_{5,6}(r)$ in Fig. 3.12(d)]. Therefore the chain-end effects is mainly influenced by the excluded volume effects and the A-B repulsion, as well as the chain length N, and we expect that as N becomes infinity the chain-end effects can be eliminated.

3.4 Conclusions

To summarize, we have studied the fluctuation/correlation (F/C) effects on the structural and thermodynamic properties of compressible diblock copolymers (DBC) in disordered phase with the soft potential commonly used in dissipative particle dynamic (DPD) simulations, based on the same model system thus without any parameter-fitting, by comparing the fast off-lattice Monte Carlo (FOMC) simulation results to the self-consistent field (SCF)

theory, Gaussian fluctuation (GF) theory and integral equation (IE) theories, which consider different levels of fluctuation and/or correlations.

We first fix $\bar{\mathcal{N}} = 10^4$, $N = 10$ and $\sigma/a = 0.3$, and examine the effects of N/κ and χN by comparing the results from different methods mainly in three cases: homopolymers at $\chi N = 0$, and DBC at $N/\kappa = 0$ and 50, with ideal chains at $N/\kappa = \chi N = 0$ as the reference state in all the cases.

For the chain dimensions of homopolymers, we find that GF theory (or equivalently P/RISM-RPA) gives surprisingly good predictions of ΔR_e^2 within the entire range of our simulation data; in contrast, RISM-PY method with $\hat{\omega}_{s,s'}^{\mathrm{DGC}}$ overestimates ΔR_e^2 for $N/\kappa \gtrsim 2$, and the deviation increases with increasing N/κ and diverges in the limit of $N/\kappa \to \infty$. For DBC at $N/\kappa = 0$, both theories give good predictions of ΔR_e^2 at small $\chi N \lesssim 1$. For $3 \lesssim \chi N \lesssim 8$, GF theory gives better prediction than RISM-PY theory, while at larger χN the opposite occurs. At larger N/κ, ΔR_e^2 slightly decreases with increasing χN and exhibits a minimum before diverging at $\chi_{\mathrm{MF}}^* N$; this is consistent with our simulation results at $N/\kappa = 50$. On the other hand, the mean-square block end-to-end distance, ΔR_{eb}^2, obtained from all the methods at $N/\kappa = 0$ exhibits a small positive maximum around $\chi N = 2$, and both theories give good predictions up to $\chi N \lesssim 4$. For the difference in the bonding energy per chain from the reference state, $\beta \Delta u_{c,\mathrm{b}}$, homopolymers exhibit similar behavior to ΔR_e^2 as expected; DBC exhibits similar to ΔR_{eb}^2, except that $\beta \Delta u_{c,\mathrm{b}}$ obtained from simulations and RISM-PY with $\hat{\omega}_{s,s'}^{\mathrm{FOMC}}$ has a minimum before $\chi^* N$.

On the other hand, for the thermodynamic properties, such as the segment "contacts" $\langle E_\kappa \rangle$ and $\langle E_\chi \rangle$, non-bonded internal energy per chain $\beta u_{c,\mathrm{nb}}$, constant-volume heat capacity $C_{V,\mathrm{nb}}$, pressures βP_{nb} and free energy $\beta \Delta f_c$, while GF theory is consistent with the simulation results at only small interaction strength, it gives poor predictions at large interaction strength and even gives qualitatively incorrect trends. RISM theory with PY closure, however, gives better predictions than GF theory at the interested ranges of interaction strength. Note that, for homopolymers, RISM-PY with $\hat{\omega}_{s,s'}^{\mathrm{DGC}}$ gives better predictions than

with $\hat{\omega}_{s,s'}^{\mathrm{FOMC}}$, which is unexpected, and it is due to the error cancelation between PY closure and ideal-chain conformations; this can also be proved by the behaviors of RISM-Zhou results. For DBC, RISM-PY with $\hat{\omega}_{s,s'}^{\mathrm{FOMC}}$ always gives better predictions than with $\hat{\omega}_{s,s'}^{\mathrm{DGC}}$, and it can even capture some behaviors, that $\hat{\omega}_{s,s'}^{\mathrm{DGC}}$ cannot predict, such as the maximum in the curve of $C_{V,\mathrm{nb}}$.

Finally, we have analyzed the trends of ODT by comparing the rates at which $S_{\psi}^{-1}(q^*)/S_{\psi}^{-1}(q^*, \chi N = 0)$ approaches 0 (or how close it is to RPA prediction) obtained from the RISM-PY method with $\hat{\omega}_{s,s'}^{\mathrm{DGC}}$, which captures some of the qualitative behavior of the ODT determined in our recent FOMC simulations of symmetric DBC.[3] We find that RISM theory with the ideal DGC single-chain structure factor and PY closure gives qualitative consistency of the ODT trend with N/κ, σ/a, $\bar{\mathcal{N}}$ and the chain discretization in most of the cases studied in Ref. [3]; that is, ODT increases with increasing N/κ, decreasing σ/a, decreasing $\bar{\mathcal{N}}$, or decreasing the chain discretization.

REFERENCES

[1] F. S. Bates and G. H. Fredrickson, Annu. Rev. Phys. Chem. **41**, 525 (1990).

[2] G. H. Fredrickson and E. J. Helfand, Chem. Phys. **87**, 697 (1987).

[3] J. Zong and Q. Wang, J. Chem. Phys. **139**, 124907 (2013).

[4] Q. Wang and Y. Yin, J. Chem. Phys. **130**, 104903 (2009).

[5] L. Leibler, Macromolecules **13**, 1602 (1980).

[6] G. H. Fredrickson, *The Equilibrium Theory of Inhomogeneous Polymers* (Oxford Press, New York, 2006).

[7] J. G. Curro and K. S. Schweizer, Macromolecules **20**, 1928 (1987).

[8] J. G. Curro and K. S. Schweizer, J. Chem. Phys. **87**, 1842 (1987).

[9] K. S. Schweizer and J. G. Curro, Phys. Rev. Lett. **58**, 246 (1987).

[10] D. J. Amit, *Field Theory, the Renormalization Group, and Critical Phenomena* (World Scientific Publishing Company, 3rd Ed, 2005).

[11] S. A. Brazovskii, Sov. Phys. JETP **41**, 85 (1975)

[12] T. Ohta and K. Kawasaki, Macromolecules **19**, 2621 (1986).

[13] Z. G. Wang, J. Chem. Phys. **117**, 481 (2002).

[14] P. Grzywacz, J. Qin, and D. C. Morse, Phys. Rev. E **76**, 061802 (2007).

[15] J. Qin and D. C. Morse, J. Chem. Phys. **130**, 224902 (2009).

[16] J. Qin, P. Grzywacz, and D. C. Morse, J. Chem. Phys. **135**, 084902 (2011).

[17] J. Qin and D. C. Morse, Phys. Rev. Lett. **108**, 238301 (2012).

[18] L. S. Ornstein and F. Zernike, Proc. Acad. Sci. (Amsterdam) **17**, 793 (1914).

[19] D. Chandler and H. C. Anderson, J. Chem. Phys. **57**, 1930 (1972).

[20] L. J. Lowden and D. Chandler, J. Chem. Phys. **59**, 6587 (1973).

[21] L. J. Lowden and D. Chandler, J. Chem. Phys. **61**, 5228 (1974).

[22] L. J. Lowden and D. Chandler, J. Chem. Phys. **62**, 4246 (1975).

[23] K. S. Schweizer and J. G. Curro, Macromolecules **21**, 3070 (1988).

[24] K. S. Schweizer and J. G. Curro, Phys. Rev. Lett. **60**, 809 (1988).

[25] K. S. Schweizer, Macromolecules **26**, 6050 (1993).

[26] E. F. David and K. S. Schweizer, J. Chem. Phys. **100**, 7767 (1994).

[27] E. F. David and K. S. Schweizer, J. Chem. Phys. **100**, 7784 (1994).

[28] M. Guenza and K. S. Schweizer, J. Chem. Phys. **106**, 7391 (1997).

[29] K. S. Schweizer, K. G. Honnell, and J. G. Curro, J. Chem. Phys. **96**, 3211 (1992).

[30] A. Yethiraj and J. G. Curro, J. Chem. Phys. **97**, 1455 (1992).

[31] J. Melenkevitz, K. S. Schweizer, and J. G. Curro, Macromolecules **26**, 6190 (1993).

[32] D. G. Gromov and J. J. de Pablo, J. Chem. Phys. **103**, 8247 (1995).

[33] D Chandler, Y. Singn, and D. M. Richardson, J. Chem. Phys. **81**, 1975 (1984).

[34] C. J. Grayce and K. S. Schweizer, J. Chem. Phys. **100**, 6846 (1994).

[35] J. L. Lebowitz and J. K. Percus, Phys. Rev. **144**, 251 (1966).

[36] J. K. Percus and G. J. Yevick, Phys. Rev. **110**, 1 (1958).

[37] J. P. Hansen and I. R. McDonald, *Theory of Simple Liquids* (Academic Press, London, 1976).

[38] D. R. Heine, G. S. Grest, and J. G. Curro, Adv. Polym. Sci. **173**, 209 (2005).

[39] R. D. Groot and P. B. Warren, J. Chem. Phys. **107**, 4423 (1997).

[40] C. N. Likos, M. Watzlawek, and H. Löwen, Phys. Rev. E **58**, 3235 (1998).

[41] G. Yatsenko, E. J. Sambriski, M. A. Nemirovskaya, and M. Guenza, Phys. Rev. Lett. **93**, 257803 (2004).

[42] L. Viererblová, J. Kolafa, S. Labík, and A. Malijevský, Phys. Chem. Chem. Phys. **12**, 254 (2010).

[43] S. Zhou, Commun. Theo. Phys. **46**, 323 (2006).

[44] E. Helfand and Y. Tagami, J. Polym. Sci., Part B: Polym. Lett. **9**, 741 (1971).

[45] Q. Wang, J. Chem. Phys. **129**, 054904 (2008).

[46] Z. G. Wang, Macromolecules **28**, 570 (1995).

[47] P. Zhang, X. Zhang, B. Li, and Q. Wang, Soft Matter **7**, 4461 (2011).

[48] R. B. Thompson, K. Ø. Rasmussen, and T. Lookman, J. Chem. Phys. **120**, 31 (2004).

[49] M. W. Matsen, Eur. Phys. J. E **30**, 361 (2009).

[50] A. A. Louis, P. G. Bolhuis, and J. P. Hansen, Phys. Rev. E **62**, 7961 (2000).

[51] D. Frenkel and B. Smit, *Understanding molecular simulation from algorithms to applications* (Academic Press, London, 2002).

CHAPTER 4

SYSTEMATIC AND SIMULATION-FREE COARSE GRAINING OF HOMOPOLYMER MELTS USING INTEGRAL EQUATION THEORY: A STRUCTURE-BASED STUDY

4.1 Introduction

Full atomistic simulations of many-chain systems such as polymer melts used in experiments are not feasible at present due to their formidable computational requirements. Coarse-grained (CG) models have to be used instead, where each segment represents, for example, the center-of-mass (CM) of a group of atoms/monomers. There are various levels at which a polymer chain with full atomistic (chemical) details can be coarse-grained: The lowest level is probably the united-atom (UA) model, where each methyl or methylene group, for example, is treated as a single interaction site (i.e., UA), and these UAs interact via bonding, bending, torsion-angle, and non-bonded (typically Lennard-Jones, LJ) potentials. The highest level is to represent each chain by a single particle. CG models at intermediate levels are also widely used, such as the bead-spring model where polymer segments (beads) interact only via bonding (finitely extendable nonlinear elastic) and non-bonded (truncated and shifted purely repulsive LJ) potentials with the parameters chosen to prevent chain-crossing.[1]

For a given original system, an issue to be addressed in *systematic coarse graining* is how the interaction potentials and the properties of CG models vary with the coarse-graining level $l \equiv N_m/N$, where N_m denotes the number of monomers on each chain in the original (monodisperse) system, and N the number of segments on each chain in CG system.

Clearly, larger l means computationally more efficient models. On the other hand, due to its reduced degrees of freedom (thus chain conformational entropy), a CG model cannot exactly reproduce the original system in all aspects. In order to choose the appropriate l-values, it is necessary to *quantify* how well the structural and thermodynamic properties of the original system are described by CG models with various l.

In spite of the numerous papers on coarse graining of polymeric systems, such systematic coarse graining has rarely been done, especially for polymer melts. Ashbaugh et al. applied a coarse-graining method that matches the interchain segment radial distribution functions between an original system (UA model of n-alkane melts with $N_m = 16 \sim 96$) and CG models with $l = 4 \sim 96$ (i.e., structure-based coarse graining), and examined the effects of l on the structural correlations.[2] Similar work was done by Chen et al.[3] They both found that, for $l \gtrsim 16$, soft potentials naturally arise from coarse graining and CG segments can completely overlap.[2,3] We note that using soft potentials is the basic idea of the recently proposed fast Monte Carlo (MC) simulations.[4–6]

On the other hand, in most work on coarse graining, molecular simulations (i.e., molecular dynamics or MC simulations) are used to obtain the structural and/or thermodynamic properties of both original and CG systems that need to be matched. This is computationally very expensive, particularly for original systems with large N_m ($> 10^2$), where the statistical uncertainties can be too large for the simulation results to be meaningful due to the difficulty in efficient sampling of configuration space (this is exactly why coarse graining is needed). Practical use of this kind of coarse-graining strategies is further defeated by the well-known problem of transferability (i.e., CG pair potentials determined at one set of thermodynamic conditions cannot be transferred to another set of conditions because they are state-dependent).[7] We therefore propose the *simulation-free strategy of coarse graining*: For polymer melts, instead of molecular simulations, we use integral-equation theories, including the reference interaction site model (RISM),[8] the polymer reference interaction site model (PRISM),[9] and the multi-block PRISM[10] (denoted by BPRISM) theories, to obtain

the structural and thermodynamic properties of both original and CG systems. It has been well established that PRISM theory can predict these properties of polymer melts in quantitative agreement with, but are at least several orders of magnitude faster than, molecular simulations.[11–13]

Introducing CM of each chain (i.e., $N = 1$) as an auxiliary site and neglecting the direct correlations involving these sites, Krakoviack et al. derived the relationship between the monomer-monomer structure factor and the CM structure factor in polymer solutions with PRISM theory.[14] Clark and Guenza extended this work to homopolymer melts, where CM of each segment (i.e., $N > 1$) was introduced and BPRISM theory[10] was used accordingly; only structural correlations for $N \leq 4$, however, were examined.[15] Applying this structure-based coarse-graining approach, with PRISM instead of BPRISM theory, to the original system of hard-core Gaussian thread model,[16] Guenza and co-workers obtained analytical results under several approximations and claimed thermodynamic consistency of the so-obtained CG models;[17–19] that is, the CG models give *exactly* the same interchain internal energy and pressure as the original system regardless of N. As shown in Sec. 4.3.4 below, however, this is actually due to the approximations they used to obtain analytical results.

In this work, we first describe the systematic and simulation-free strategy of structure-based coarse graining, then present our numerical results with the hard-core Gaussian thread model[16] (referred to as the "CGC-δ" model below) as the original system. We compare the various integral-equation theories and closures for coarse graining, as well as the structural and thermodynamic properties of original and CG systems at various N. Our numerical results show that the effective CG potentials for various N and closures can be collapsed approximately onto the same curve, and that structure-based coarse graining cannot give the thermodynamic consistency between original and CG systems at any $N < N_m$.

4.2 Models and Methods

As summarized in Fig. 4.1 at the end of this section, structure-based coarse graining using integral-equation theories has three steps: (1) solve the original system, (2) perform the coarse graining, and (3) obtain CG potentials and properties. In Sec. 4.2.1 we introduce DGC-G model and its limiting case, CGC-δ model; the hard-core CGC-δ model is chosen as the original system for coarse graining in this work. In Sec. 4.2.2 we explain how to solve CGC-δ model with BPRISM theory and the Percus-Yevick (PY) closure,[20] thus completing the first step. The second step is described in Sec. 4.2.3, and the third step in Sec. 4.2.4. Finally, using PRISM instead of BPRISM theory greatly simplifies the calculation in all steps, as described in Sec. 4.2.5.

4.2.1 Models for original system

We consider an original model system of homopolymer melts, which is at the monomer level in continuum, of n chains each consisting of N_m monomers with statistical segment length a at a chain number density $\rho_c \equiv n/V$ with V being the system volume. The non-bonded pair potential between monomers is given by $u_m(r) = (\bar{\kappa}/\rho_c N_m^2) u_{0,m}(r)$, where $\bar{\kappa} \equiv N_m/\kappa \geq 0$ controls the interaction strength with κ being the generalized Helfand compressibility,[21] and $u_{0,m}(r)$ is a normalized isotropic pair potential (i.e., $\int \mathrm{d}\mathbf{r} u_{0,m}(r) = k_B T$ with k_B being the Boltzmann constant and T the thermodynamic temperature), which can be, for example, the Gaussian-core potential, i.e., $\beta u_{0,m}(r) = (3/2\pi\sigma_m^2)^{3/2} \exp\left[-(3/2)(r^2/\sigma_m^2)\right]$ with σ_m denoting the interaction range and $\beta \equiv 1/k_B T$. On the other hand, the chain connectivity can be described by the discrete Gaussian chain (DGC) model based on the concept of statistical segment length. Hereafter we refer to this model as DGC-G model. The invariant degree of polymerization controlling the system fluctuations is then defined as $\bar{\mathcal{N}} \equiv (\rho_c R_{e,0}^3)^2$, where $R_{e,0} = \sqrt{N_m} a$ (for large N_m) is the root-mean-square end-to-end distance of an ideal chain.

In the limit of $N_m \to \infty$ while keeping $R_{e,0}$ and σ_m/a finite, we have $a \to 0$ and $\sigma_m \to 0$; DGC model then becomes the continuous Gaussian chain (CGC) model, and the normalized

potential becomes $\beta u_{0,m}(r) = \delta(r)$. We refer to this limit as CGC-δ model, where the non-bonded pair potential between monomers is given by $\beta u_m(r) = (\bar{\kappa}/\rho_c N_m^2)\delta(r)$. Note that $\beta u_m(r)$ approaches 0 at finite $\bar{\kappa}$ and $\bar{\mathcal{N}}$ in CGC-δ model; this can be shown with that in DGC-G model, written as

$$\beta u_m(r) = \frac{(3/2\pi)^{3/2}\,\bar{\kappa}}{\sqrt{N_m \bar{\mathcal{N}}}(\sigma_m/a)^3} \exp\left[-\frac{3}{2}\frac{N_m (r/R_{e,0})^2}{(\sigma_m/a)^2}\right], \tag{4.1}$$

which clearly approaches 0 as $N_m \to \infty$ at finite $R_{e,0}$, σ_m/a, $\bar{\kappa}$ and $\bar{\mathcal{N}}$. CGC-δ model is commonly used for polymer melts[16] or solutions in an implicit, good solvent,[22] simply because it has the least number of parameters; taking $R_{e,0}$ as the length scale, it has only two (physical) parameters: $\bar{\kappa}$ and $\bar{\mathcal{N}}$. In this study, we perform structure-based coarse graining with the hard-core CGC-δ model (i.e., $\bar{\kappa} \to \infty$)[16] as the original system.

4.2.2 BPRISM theory for CGC-δ model solved with PY closure

For the purpose of coarse graining, we divide each original polymer chain into N subchains (segments) each containing l monomers, such that $Nl = N_m$. For large l, one can assume that the interchain pair correlation functions (PCFs) depend only on the position of segments along the chain contour, i.e., $h_{\alpha i,\beta j}(r) = h^{mm}_{\alpha,\beta}(r)$ and $c_{\alpha i,\beta j}(r) = c^{mm}_{\alpha,\beta}(r)$, where $h_{\alpha i,\beta j}(r)$ and $c_{\alpha i,\beta j}(r)$ denotes the interchain total and direct PCFs, respectively, between the i^{th} monomer in the α^{th} segment on one chain and the j^{th} monomer in the β^{th} segment on another, and the superscript "mm" denotes the monomer-monomer correlations. The well-known RISM theory,[8] which describes the PCFs between monomers via the generalized Ornstein-Zernike equation in Fourier space, then becomes the BPRISM form given by[10]

$$\hat{\mathbf{h}}^{mm} = \hat{\boldsymbol{\omega}}^{mm}\hat{\mathbf{C}}^{mm}(\hat{\boldsymbol{\omega}}^{mm} + \rho_c \hat{\mathbf{h}}^{mm}), \tag{4.2}$$

where $\hat{\mathbf{C}}^{mm} \equiv l^2 \hat{\mathbf{c}}^{mm}$, the symmetric matrices $\hat{\mathbf{h}}^{mm}$ and $\hat{\mathbf{c}}^{mm}$ have $N \times N$ elements with each element denoting the *average* correlation between all monomers in the corresponding segment pairs, the intrachain PCF $\hat{\boldsymbol{\omega}}^{mm}$ is defined as $\hat{\omega}^{mm}_{\alpha,\beta} \equiv \sum_{i,j=1}^{l} \hat{\omega}_{\alpha i,\beta j}/l^2$ (with $\hat{\omega}^{mm}_{\alpha,\beta}(0) = 1$) with $\hat{\omega}_{\alpha i,\beta j}$ being the intrachain monomer-monomer PCF between the i^{th} monomer in the α^{th}

segment and the j^{th} monomer in the β^{th} segment, and we use the short-hand notation $\hat{f} \equiv \int \mathrm{d}\mathbf{r} f(r) \exp(-\sqrt{-1}\mathbf{q}\cdot\mathbf{r}) = (4\pi/q)\int_0^\infty \mathrm{d}r f(r) r \sin(qr)$ to denote the 3D Fourier transform of $f(r)$ with $q \equiv |\mathbf{q}|$ being the length of the wavevector $\mathbf{q}$ and $r \equiv |\mathbf{r}|$. The expressions of $\hat{\omega}^{mm}_{\alpha,\beta}$ for ideal DGC and CGC are given in Ref. [15] and Sec. 4.2.6.

Eq. (4.2) must be solved with a closure relating the interchain direct and total PCFs. For the original CGC-δ system, we use the Percus-Yevick (PY) closure[20] given by

$$c^{mm}_{\alpha,\beta}(r) = \{1 - \exp[\beta u_m(r)]\} g^{mm}_{\alpha,\beta}(r), \tag{4.3}$$

where $g^{mm}_{\alpha,\beta}(r) = h^{mm}_{\alpha,\beta}(r) + 1$ is the interchain radial distribution function. PY closure can be obtained from the hypernetted-chain (HNC) closure, $c^{mm}_{\alpha,\beta}(r) = -\beta u_m(r) + h^{mm}_{\alpha,\beta}(r) - \ln g^{mm}_{\alpha,\beta}(r)$,[23] by Taylor expanding $\exp[\gamma^{mm}_{\alpha,\beta}(r)]$ to the first order, where the indirect PCF $\gamma^{mm}_{\alpha,\beta}(r) \equiv h^{mm}_{\alpha,\beta}(r) - c^{mm}_{\alpha,\beta}(r)$. HNC closure also leads to the random phase approximation (RPA) closure, $c^{mm}_{\alpha,\beta}(r) = -\beta u_m(r)$,[24,25] by Taylor expanding $\ln[1+h^{mm}_{\alpha,\beta}(r)]$ to the first order.

At finite $\bar{\kappa}$ and $\bar{\mathcal{N}}$, since $\beta u_m(r)$ approaches 0 as shown in Sec. 4.2.1, Taylor expanding $\exp[\beta u_m(r)]$ to the first order, PY closure becomes $N_m^2 c^{mm}_{\alpha,\beta}(r) = -(\bar{\kappa}/\sqrt{\bar{\mathcal{N}}}) g^{mm}_{\alpha,\beta}(0) R^3_{e,0} \delta(r)$, which gives finite $C_{\alpha,\beta} \equiv N_m^2 \hat{c}^{mm}_{\alpha,\beta}(q)/R^3_{e,0} = -(\bar{\kappa}/\sqrt{\bar{\mathcal{N}}}) g^{mm}_{\alpha,\beta}(0) \le 0$ and thus

$$h^{mm}_{\alpha,\beta}(0) = -\frac{C_{\alpha,\beta}\sqrt{\bar{\mathcal{N}}}}{\bar{\kappa}} - 1. \tag{4.4}$$

With the above definition of $C_{\alpha,\beta}$, Eq. (4.2) then becomes

$$\frac{\hat{\mathbf{h}}^{mm}}{R^3_{e,0}} = \left(N^2\mathbf{I} - \sqrt{\bar{\mathcal{N}}}\hat{\boldsymbol{\omega}}^{mm}\mathbf{C}\right)^{-1} \hat{\boldsymbol{\omega}}^{mm}\mathbf{C}\hat{\boldsymbol{\omega}}^{mm}, \tag{4.5}$$

where $\mathbf{I}$ is the $N \times N$ identity matrix and $\mathbf{C}$ has $N \times N$ elements of $C_{\alpha,\beta}$. Taking the inverse Fourier transform of $\hat{h}^{mm}_{\alpha,\beta}$ and using Eq. (4.4), we can obtain $C_{\alpha,\beta}$ (and thus $\hat{h}^{mm}_{\alpha,\beta}$) as a function of $\bar{\kappa}$ and $\bar{\mathcal{N}}$. Note that, in the limit of $\bar{\kappa} \to \infty$, PY closure gives $h^{mm}_{\alpha,\beta}(0) = -1$;[16] since Eq. (4.4) with the right-hand-side (RHS) replaced by -1 still gives finite $C_{\alpha,\beta}$ at finite $\bar{\mathcal{N}}$ (see Sec. 4.3.1, it can be used at any $\bar{\kappa}$ (for finite $\bar{\mathcal{N}}$).

In this study, we assume for $\hat{\boldsymbol{\omega}}^{mm}$ the ideal conformations of CGC. For given $\bar{\kappa}$, $\bar{\mathcal{N}}$ and N, we numerically solve for $\mathbf{C}$ (and thus $\hat{\mathbf{h}}^{mm}$) from Eqs. (4.4) and (4.5) as follows: With

an initial guess of $\mathbf{C}$, we calculate $\hat{\mathbf{h}}^{mm}$ from Eq. (4.5), and

$$h^{mm}_{\alpha,\beta}(0) = \frac{1}{2\pi^2}\int_0^{q_c} \mathrm{d}q q^2 \hat{h}^{mm}_{\alpha,\beta}(q) + \frac{1}{2\pi^2}\int_0^{q_c^{-1}} \mathrm{d}z z^{-4} \hat{h}^{mm}_{\alpha,\beta}(z^{-1}) \tag{4.6}$$

with $q_c = 10^4\pi/R_{e,0}$, where both integrals are evaluated using Romberg integration[26] and the second one is used to integrate from $q = q_c$ to ∞ with $z = 1/q$. We then use Broyden's method[26] to converge $\mathbf{C}$ such that the maximum absolute residual error over all segment pairs in Eq. (4.4) is less than 10^{-12}.

Once $C_{\alpha,\beta}$ (and thus $\hat{h}^{mm}_{\alpha,\beta}$) are obtained for all segment pairs, we calculate the structural and thermodynamic properties of the original system. Its normalized isothermal compressibility is calculated as[27]

$$\kappa_{T,m} \equiv -\frac{\rho_c k_B T}{V}\left(\frac{\partial V}{\partial p}\right)_T = 1 + \frac{\sqrt{\bar{\mathcal{N}}}}{N^2}\sum_{\alpha,\beta=1}^{N}\frac{\hat{h}^{mm}_{\alpha,\beta}(0)}{R^3_{e,0}} = \frac{1}{1 - C_0\sqrt{\bar{\mathcal{N}}}}, \tag{4.7}$$

where p denotes pressure and $C_0 \equiv \sum_{\alpha,\beta=1}^{N} C_{\alpha,\beta}/N^2$. Note that $\kappa_{T,m} = 1$ for ideal chains since $\hat{h}^{mm}_{\alpha,\beta}(0) = 0$ at $\bar{\kappa} = 0$. With the ideal-chain conformations, we only examine the interchain thermodynamic properties. In particular, the interchain internal energy per chain and (virial) pressure are given by

$$\beta u_{c,m} = 2\pi\sqrt{\bar{\mathcal{N}}} l^2 \sum_{\alpha,\beta=1}^{N}\int_0^{\infty} \mathrm{d}r \frac{r^2}{R^3_{e,0}} g^{mm}_{\alpha,\beta}(r)\beta u_m(r) = -\frac{C_0\sqrt{\bar{\mathcal{N}}}}{2}, \tag{4.8}$$

$$\beta R^3_{e,0} P_m = -\frac{2\pi\bar{\mathcal{N}} l^2}{3}\sum_{\alpha,\beta=1}^{N}\int_0^{\infty} \mathrm{d}r \frac{r^2}{R^3_{e,0}} g^{mm}_{\alpha,\beta}(r)\frac{\mathrm{d}\beta u_m(r)}{\mathrm{d}\ln r} = -\frac{C_0\bar{\mathcal{N}}}{2}, \tag{4.9}$$

respectively, where we have used $\mathrm{d}\delta(r)/\mathrm{d}\ln r = -3\delta(r)$ in 3D obtained from $\nabla\cdot\delta(r)\mathbf{r} = 0$.

4.2.3 Structure-based coarse graining using BPRISM theory

Introducing the center-of-mass of each subchain (segment) as an auxiliary (non-interacting) site in the system, we extend Eq. (4.2) as[14,15]

$$\begin{bmatrix} \hat{\mathbf{h}}^{mm} & \hat{\mathbf{h}}^{ms} \\ \hat{\mathbf{h}}^{sm} & \hat{\mathbf{h}}^{ss} \end{bmatrix} = \begin{bmatrix} \hat{\boldsymbol{\omega}}^{mm} & \hat{\boldsymbol{\omega}}^{ms} \\ \hat{\boldsymbol{\omega}}^{sm} & \hat{\boldsymbol{\omega}}^{ss} \end{bmatrix} \begin{bmatrix} \hat{\mathbf{C}}^{mm} & l\hat{\mathbf{c}}^{ms} \\ l\hat{\mathbf{c}}^{sm} & \hat{\mathbf{c}}^{ss} \end{bmatrix} \left\{ \begin{bmatrix} \hat{\boldsymbol{\omega}}^{mm} & \hat{\boldsymbol{\omega}}^{ms} \\ \hat{\boldsymbol{\omega}}^{sm} & \hat{\boldsymbol{\omega}}^{ss} \end{bmatrix} + \rho_c \begin{bmatrix} \hat{\mathbf{h}}^{mm} & \hat{\mathbf{h}}^{ms} \\ \hat{\mathbf{h}}^{sm} & \hat{\mathbf{h}}^{ss} \end{bmatrix} \right\}, \tag{4.10}$$

where all of the bold symbols represent symmetric matrices of $N \times N$ elements corresponding to segment pairs, and the superscripts "ms" and "ss" denote the monomer-segment and segment-segment correlations, respectively; note that $\hat{\mathbf{h}}^{ms} = \hat{\mathbf{h}}^{sm}$, $\hat{\mathbf{c}}^{ms} = \hat{\mathbf{c}}^{sm}$, and $\hat{\boldsymbol{\omega}}^{ms} = \hat{\boldsymbol{\omega}}^{sm}$. For example, the element $\hat{h}^{sm}_{\alpha,\beta}$ is the interchain total PCF between the α^{th} segment and a monomer in the β^{th} segment on different chains, $\hat{h}^{ss}_{\alpha,\beta}$ is the interchain total PCF between the α^{th} and β^{th} segments on different chains, $\hat{\omega}^{sm}_{\alpha,\beta} \equiv \sum_{j=1}^{l} \hat{\omega}_{\alpha,\beta j}/l$ is the intrachain *average* PCF between the α^{th} segment and the monomers in the β^{th} segment with $\hat{\omega}_{\alpha,\beta j}$ being the intrachain PCF between the α^{th} segment and the j^{th} monomer in the β^{th} segment. Also note that all the intrachain PCFs are normalized, i.e., $\hat{\omega}^{mm}_{\alpha,\beta}(0) = \hat{\omega}^{ms}_{\alpha,\beta}(0) = \hat{\omega}^{ss}_{\alpha,\beta}(0) = 1$. For ideal CGC, $\hat{\boldsymbol{\omega}}^{ms}$ and $\hat{\boldsymbol{\omega}}^{ss}$ are derived in Ref. [15]; in Sec. 4.2.6, we derive them for ideal DGC, which recover those of ideal CGC in the limit of $N_m \to \infty$. Under the assumption[28–30] of $\hat{c}^{ms}_{\alpha,\beta} = \hat{c}^{sm}_{\alpha,\beta} = \hat{c}^{ss}_{\alpha,\beta} = 0$, which is exact with either PY or RPA closure, Eq. (4.10) gives

$$\hat{\mathbf{h}}^{ss} = \hat{\boldsymbol{\omega}}^{sm}(\hat{\boldsymbol{\omega}}^{mm})^{-1}\hat{\mathbf{h}}^{mm}(\hat{\boldsymbol{\omega}}^{mm})^{-1}\hat{\boldsymbol{\omega}}^{ms}. \tag{4.11}$$

4.2.4 RISM theory for the coarse-grained system

For CG system with N segments on each chain, RISM equation gives[8]

$$\hat{\mathbf{c}}^{ss} = (\hat{\boldsymbol{\omega}}^{ss})^{-1}\hat{\mathbf{h}}^{ss}(\hat{\boldsymbol{\omega}}^{ss} + \rho_c\hat{\mathbf{h}}^{ss})^{-1}, \tag{4.12}$$

where $\hat{\mathbf{h}}^{ss}$ is calculated from Eq. (4.11). The effective segmental pair potentials are then obtained as

$$\beta v_{\alpha,\beta}(r) = \begin{cases} -c^{ss}_{\alpha,\beta}(r) & \text{with RPA closure} \\ -c^{ss}_{\alpha,\beta}(r) + h^{ss}_{\alpha,\beta}(r) - \ln[1 + h^{ss}_{\alpha,\beta}(r)] & \text{with HNC closure} \\ \ln[1 - c^{ss}_{\alpha,\beta}(r) + h^{ss}_{\alpha,\beta}(r)] - \ln[1 + h^{ss}_{\alpha,\beta}(r)] & \text{with PY closure} \end{cases}, \tag{4.13}$$

where we use FFTW[31] to perform the inverse Fourier transform of $\hat{\mathbf{c}}^{ss}$ and $\hat{\mathbf{h}}^{ss}$ with a cut-off length of $r_c = 30R_{e,0}$ (which determines the discretization of q-space) and uniform discretization of $[0, r_c]$ into 3×10^5 subintervals (which determines the cut-off in q-space); our cut-off and discretization give negligible numerical errors. Note that these CG potentials depend on the segment pairs along the chain contour.

Finally, the structural and thermodynamic properties of CG system are calculated. Its normalized isothermal compressibility $\kappa_T = 1 + (\sqrt{\bar{\mathcal{N}}}/N^2)\sum_{\alpha,\beta=1}^{N}\hat{h}^{ss}_{\alpha,\beta}(0)/R^3_{e,0}$; this is the same as $\kappa_{T,m}$ because $\hat{\mathbf{h}}^{ss}(0) = \hat{\mathbf{h}}^{mm}(0)$ according to Eq. (4.11). Its interchain internal energy per chain and (virial) pressure are calculated as

$$\beta u_c = 2\pi\sqrt{\bar{\mathcal{N}}}\sum_{\alpha,\beta=1}^{N}\int_0^\infty \mathrm{d}r\frac{r^2}{R^3_{e,0}}g^{ss}_{\alpha,\beta}(r)\beta v_{\alpha,\beta}(r), \tag{4.14}$$

$$\beta R^3_{e,0}P = -\frac{2\pi\bar{\mathcal{N}}}{3}\sum_{\alpha,\beta=1}^{N}\int_0^\infty \mathrm{d}r\frac{r^2}{R^3_{e,0}}g^{ss}_{\alpha,\beta}(r)\frac{\mathrm{d}\beta v_{\alpha,\beta}(r)}{\mathrm{d}\ln r}, \tag{4.15}$$

where the integrals are numerically evaluated using Romberg integration[26] with the above cut-off and discretization.

4.2.5 Structure-based coarse graining using PRISM theory

If we assume that the interchain PCFs do not depend on the segment position along the chain contour for both original and CG systems by neglecting the chain-end effects,[32] i.e., $h^{mm}_{\alpha,\beta}(r) = h^{mm}(r)$, $c^{mm}_{\alpha,\beta}(r) = c^{mm}(r)$, $h^{ss}_{\alpha,\beta}(r) = h^{ss}(r)$ and $c^{ss}_{\alpha,\beta}(r) = c^{ss}(r)$, Eq. (4.2) becomes the PRISM equation proposed by Curro and Schweizer (which can also be obtained from Eq. (4.2) by setting $N = 1$),[9] given by

$$\hat{h}^{mm} = \hat{\omega}^{mm}\hat{C}^{mm}(\hat{\omega}^{mm} + \rho_c\hat{h}^{mm}), \tag{4.16}$$

where $\hat{C}^{mm} \equiv N_m^2\hat{c}^{mm}$, and $\hat{\omega}^{mm} \equiv \sum_{\alpha,\beta=1}^{N}\hat{\omega}^{mm}_{\alpha,\beta}/N^2$ is the normalized (i.e., $\hat{\omega}^{mm}(0) = 1$) single-chain structure factor. With $C_0 \equiv N_m^2\hat{c}^{mm}(q)/R^3_{e,0}$, Eq. (4.4) becomes $h^{mm}(0) = -C_0\sqrt{\bar{\mathcal{N}}}/\bar{\kappa} - 1$, and Eq. (4.5) becomes

$$\frac{\hat{h}^{mm}(q)}{R^3_{e,0}} = \frac{C_0P^2_{\mathrm{D}}(q)}{1 - C_0\sqrt{\bar{\mathcal{N}}}P_{\mathrm{D}}(q)}, \tag{4.17}$$

where $\hat{\omega}^{mm}$ for ideal CGC is given by the Debye function $P_{\mathrm{D}}(q) = 2(e^{-x} + x - 1)/x^2$ with $x \equiv q^2R^2_{e,0}/6$. Taking the inverse Fourier transform of the above, i.e., numerically solving

$$\frac{C_0}{2\pi^2}\int_0^\infty \mathrm{d}q\frac{R^3_{e,0}q^2P^2_{\mathrm{D}}(q)}{1 - C_0\sqrt{\bar{\mathcal{N}}}P_{\mathrm{D}}(q)} = -\frac{C_0\sqrt{\bar{\mathcal{N}}}}{\bar{\kappa}} - 1, \tag{4.18}$$

we can obtain C_0 (and thus $\hat{h}^{mm}$) as a function of $\bar{\kappa}$ and $\bar{\mathcal{N}}$; as shown in Sec. 4.2.2, Eq. (4.18) can be used at any $\bar{\kappa}$ (for finite $\bar{\mathcal{N}}$). Note that, if the Padé approximation $P_{\rm P}(q) = 1/(1+x/2)$ is used for $\hat{\omega}^{mm}$, C_0 can be obtained analytically as shown in Sec. 4.3.1. For the calculation of structural and thermodynamic properties, Eqs. (4.7)$\sim$(4.9) are used.

Next, Eq. (4.11) becomes

$$\frac{\hat{h}^{ss}}{R_{e,0}^3} = \frac{\hat{h}^{mm}}{R_{e,0}^3}\left(\frac{\hat{\omega}^{sm}}{\hat{\omega}^{mm}}\right)^2 = \frac{C_0(\hat{\omega}^{sm})^2}{1-\sqrt{\bar{\mathcal{N}}}C_0\hat{\omega}^{mm}}, \tag{4.19}$$

where Eq. (4.16) is used, and $\hat{\omega}^{sm} \equiv \sum_{\alpha,\beta=1}^{N}\hat{\omega}_{\alpha,\beta}^{sm}/N^2$ with $\hat{\omega}^{sm}(0) = 1$; and Eq. (4.12) becomes

$$\frac{\hat{c}^{ss}}{R_{e,0}^3} = \frac{\hat{h}^{ss}/R_{e,0}^3}{N^2\hat{\omega}^{ss}(\hat{\omega}^{ss}+\rho_c\hat{h}^{ss})} = \frac{(C_0/N^2)(\hat{\omega}^{sm}/\hat{\omega}^{ss})^2}{1-\sqrt{\bar{\mathcal{N}}}C_0[\hat{\omega}^{mm}-(\hat{\omega}^{sm})^2/\hat{\omega}^{ss}]}, \tag{4.20}$$

where $\hat{\omega}^{ss} \equiv \sum_{\alpha,\beta=1}^{N}\hat{\omega}_{\alpha,\beta}^{ss}/N^2$ with $\hat{\omega}^{ss}(0) = 1$. Expressions of $\hat{\omega}^{mm}$, $\hat{\omega}^{sm}$ and $\hat{\omega}^{ss}$ for ideal CGC are given in Ref. [19] and Sec. 4.2.6. Note that Eqs. (4.19) and (4.20) are also given in Ref. [19], and that the so-obtained $\hat{h}^{ss}$ and $\hat{c}^{ss}$ depend on N. Finally, one still has $\kappa_T = \kappa_{T,m}$ and can calculate βu_c and $\beta R_{e,0}^3 P$ according to Eqs. (4.14) and (4.15), respectively, once the effective potential $\beta v(r)$ between CG segments is obtained from a closure according to Eq. (4.13).

Fig. 4.1 summarizes the various quantities, parameters, and options in our systematic and simulation-free strategy of structure-based coarse graining for homopolymer melts, which has three steps:

- First, the chain connectivity (i.e., bonding interactions) in original system is described by $\boldsymbol{\omega}^{mm}$, which can be modeled by either ideal CGC (using either the Debye function $P_{\rm D}(q)$ or the Padé approximation $P_{\rm P}(q)$) or ideal DGC of N_m monomers; although not listed in Fig. 4.1, other chain models can also be used. Once $\boldsymbol{\omega}^{mm}$ is chosen, $\boldsymbol{\omega}^{sm}$ and $\boldsymbol{\omega}^{ss}$ are then obtained for given N. The non-bonded interaction between monomers, $\beta u_m(r)$ in our case, has two parameters $\bar{\kappa}$ and $\bar{\mathcal{N}}$ for CGC and an additional parameter σ_m/a for DGC. The original system is solved with either PRISM (for all N) or BPRISM

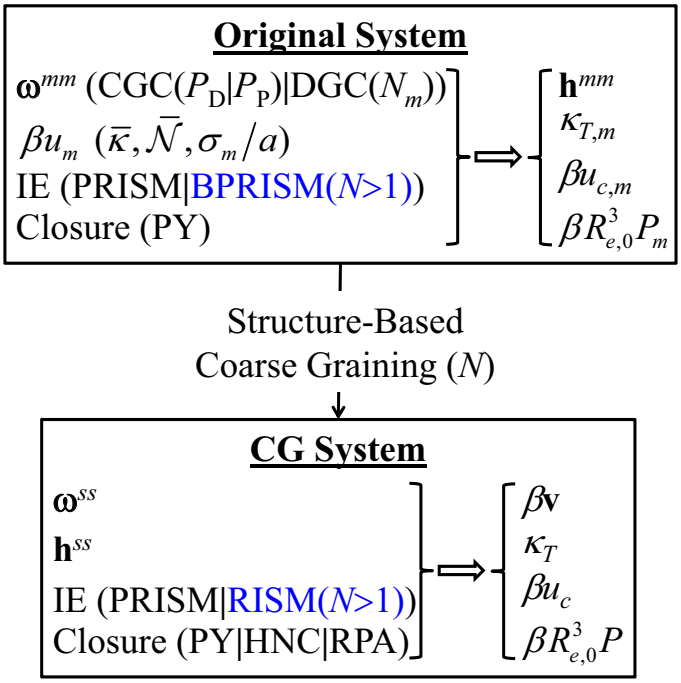

Figure 4.1: Our simulation-free strategy for structure-based coarse graining of homopolymer melts, where the various parameters and options (separated by "|") are listed in parentheses. See main text for details.

(for $N > 1$) theory, where we use PY closure (other closures can also be used); this gives $\mathbf{h}^{mm}$, as well as its structural and thermodynamic properties.

- Second, according to either Eq. (4.11) (when BPRISM theory is used for original system) or Eq. (4.19) (when PRISM theory is used), the structure-based coarse graining gives $\mathbf{h}^{ss}$, from which $\mathbf{c}^{ss}$ is obtained via either Eq. (4.12) (when BPRISM theory is used for original system, thus RISM theory for CG system) or Eq. (4.20) (when PRISM theory is used).

- Third, CG potentials $\beta\mathbf{v}$ are obtained via either PY, HNC, or RPA closure (other closures can also be used), which are segment-pair-dependent when BPRISM theory is used for original system, and the structural and thermodynamic properties of CG system are finally obtained and compared with those of original system.

4.2.6 Derivation of intrachain correlation functions used in structure-based coarse graining

Here we start from the ideal DGC model, which becomes the ideal CGC model as $N_m \to \infty$. To be general, we denote the number of monomers in the γ^{th} segment by l_γ. The ideal DGC model then gives

$$\begin{aligned}\hat{\omega}^{mm}_{\alpha,\beta}(q) &\equiv \frac{1}{l_\alpha l_\beta}\sum_{i=1}^{l_\alpha}\sum_{j=1}^{l_\beta}\hat{\omega}^{mm}_{\alpha i,\beta j}(q) \\ &= \begin{cases} \left\{l_\alpha - B(q)\left[2 + l_\alpha B(q) - 2B(q)^{l_\alpha}\right]\right\}/l_\alpha^2\left[1-B(q)\right]^2 & \text{if } \alpha = \beta \\ B(q)^{l_{\alpha\beta}+1}\left[1-B(q)^{l_\alpha}\right]\left[1-B(q)^{l_\beta}\right]/l_\alpha l_\beta[1-B(q)]^2 & \text{otherwise} \end{cases} \end{aligned} \tag{4.21}$$

where $B(q) = \exp(-q^2a^2/6)$, and $l_{\alpha\beta} = \sum_{\gamma=\alpha+1}^{\beta-1} l_\gamma$ if $\alpha < \beta$ and $\sum_{\gamma=\beta+1}^{\alpha-1} l_\gamma$ otherwise denotes the number of monomers between (not including those in) the α^{th} and β^{th} segments. For the case of $l_\gamma = l$, Eq. (4.21) becomes

$$\hat{\omega}^{mm}_{\alpha,\beta}(q) = \begin{cases} \left\{l - B(q)\left[2 + lB(q) - 2B(q)^{l}\right]\right\}/l^2[1-B(q)]^2 & \text{if } \alpha = \beta \\ B(q)^{(|\alpha-\beta|-1)l+1}\left[1-B(q)^{l}\right]^2/l^2[1-B(q)]^2 & \text{otherwise} \end{cases}. \tag{4.22}$$

In the limit of $l \to \infty$ (i.e., for the ideal CGC model), Eq. (4.22) recovers Eq. (8) of Ref. [15], which with $y^2 \equiv q^2R^2_{e,0}/6N$ becomes

$$\hat{\omega}^{mm}_{\alpha,\beta}(q) = \begin{cases} 2\left(e^{-y^2} + y^2 - 1\right)\Big/y^4 & \text{if } \alpha = \beta \\ \exp\left(y^2 - |\alpha-\beta|y^2\right)\left(1-e^{-y^2}\right)^2\Big/y^4 & \text{otherwise} \end{cases}. \tag{4.23}$$

We then obtain $\hat{\omega}^{mm}(q) \equiv \sum_{\alpha,\beta=1}^{N}\hat{\omega}^{mm}_{\alpha,\beta}(q)/N^2$ for ideal CGC, given by

$$\hat{\omega}^{mm}(q) = \frac{2}{N^2y^4}\left(e^{-Ny^2} + Ny^2 - 1\right). \tag{4.24}$$

Next we derive $\hat{\omega}^{sm}_{\alpha,\beta} \equiv \sum_{i=1}^{l_\beta}\hat{\omega}^{sm}_{\alpha,\beta i}/l_\beta$, which is given by

$$\hat{\omega}^{sm}_{\alpha,\beta}(q) = \begin{cases} \sum_{j=1}^{l_\alpha} B(q)^{l_\alpha/3+1/2+1/6l_\alpha - j + j^2/l_\alpha - j/l_\alpha}/l_\alpha & \text{if } \alpha = \beta \\ \left[1-B(q)^{l_\beta}\right]B(q)^{l_{\alpha\beta}+l_\alpha/3+1/2+1/6l_\alpha}/l_\beta[1-B(q)] & \text{otherwise} \end{cases}. \tag{4.25}$$

For the case of $l_\gamma = l$, Eq. (4.25) becomes

$$\hat{\omega}^{sm}_{\alpha,\beta}(q) = \begin{cases} \sum_{j=1}^{l} B(q)^{l/3+1/2+1/6l-j+j^2/l-j/l}/l & \text{if } \alpha = \beta \\ \left[1 - B(q)^l\right] B(q)^{|\alpha-\beta|l-2l/3+1/2+1/6l}/l[1-B(q)] & \text{otherwise} \end{cases}. \tag{4.26}$$

In the limit of $l \to \infty$, Eq. (4.26) recovers Eq. (13) of Ref. [15], given by

$$\hat{\omega}^{sm}_{\alpha,\beta}(q) = \begin{cases} \sqrt{\pi} e^{-y^2/12} \mathrm{erf}(y/2)/y & \text{if } \alpha = \beta \\ \exp\left(-|\alpha-\beta|y^2 + 2y^2/3\right) \left(1 - e^{-y^2}\right) \Big/ y^2 & \text{otherwise} \end{cases}. \tag{4.27}$$

We then obtain $\hat{\omega}^{sm}(q) \equiv \sum_{\alpha,\beta=1}^{N} \hat{\omega}^{sm}_{\alpha,\beta}(q)/N^2$ for ideal CGC, given by

$$\hat{\omega}^{sm}(q) = \frac{\sqrt{\pi} e^{-y^2/12}}{Ny} \mathrm{erf}\left(\frac{y}{2}\right) + \frac{2e^{-y^2/3}}{N^2 y^2} \frac{e^{-Ny^2} - Ne^{-y^2} + N - 1}{1 - e^{-y^2}}. \tag{4.28}$$

Note that $\hat{\boldsymbol{\omega}}^{ms} = \hat{\boldsymbol{\omega}}^{sm}$ when $l_\gamma = l$.

Finally we derive $\hat{\omega}^{ss}_{\alpha,\beta}$. For $\alpha = \beta$, $\hat{\omega}^{ss}_{\alpha,\alpha} = 1$. For $\alpha \neq \beta$, we have

$$\hat{\omega}^{ss}_{\alpha,\beta}(q) = B(q)^{l_{\alpha\beta} + \left(2l_\alpha^2+1\right)/6l_\alpha + \left(2l_\beta^2+1\right)(6l_\beta)}. \tag{4.29}$$

For the case of $l_\gamma = l$, Eq. (4.29) becomes

$$\hat{\omega}^{ss}_{\alpha,\beta}(q) = B(q)^{|\alpha-\beta|l-l/3+1/3l}. \tag{4.30}$$

In the limit of $l_\gamma \to \infty$, Eq. (4.30) recovers Eq. (16) of Ref. [15], given by

$$\hat{\omega}^{ss}_{\alpha,\beta}(q) = \exp\left(-|\alpha-\beta|y^2 + y^2/3\right). \tag{4.31}$$

We then obtain $\hat{\omega}^{ss}(q) \equiv \sum_{\alpha,\beta=1}^{N} \hat{\omega}^{ss}_{\alpha,\beta}(q)/N^2$ for ideal CGC, given by

$$\hat{\omega}^{ss}(q) = \frac{1}{N} + \frac{2e^{-2y^2/3}\left(e^{-Ny^2} - Ne^{-y^2} + N - 1\right)}{N^2\left(1 - e^{-y^2}\right)^2}. \tag{4.32}$$

4.3 Results

Since the focus of our work is on the general strategy of systematic and simulation-free coarse graining, instead of coarse graining of a specific polymer, we choose the hard-core

CGC-δ model as the original system. In the following, we first show how to solve the CGC-$\boldsymbol{\delta}$ model solved by PRISM theory and the correspondence between the hard-core CGC-δ model and specific polymers used in experiments. Using PRISM theory for structure-based coarse graining, we then examine how the effective CG potential varies with the coarse-graining level, and compare the structural and thermodynamic properties between original and CG systems. Finally, we compare the results of structure-based coarse graining between using PRISM and BPRISM theories to examine the chain-end effects neglected in the former.[32]

4.3.1 CGC-δ model solved by PRISM theory

As mentioned in Sec. 4.2.1, CGC-δ model is commonly used for polymer melts[16] or solutions in an implicit, good solvent;[22] in particular, CGC-δ model with finite $\bar{\kappa}$ is equivalent to the Edwards model[22] commonly used in polymer field theories. Here we first present the analytical results of CGC-δ model (including those at finite $\bar{\kappa}$) solved by PRISM theory with RPA and PY closures, then examine the accuracy of Padé approximation for $\hat{\omega}^{mm}$.

From RPA closure, $N_m^2 c^{mm}(r) = -(\bar{\kappa}/\sqrt{\bar{\mathcal{N}}})R_{e,0}^3\delta(r)$, we have $C_0^{\rm RPA} = -\bar{\kappa}/\sqrt{\bar{\mathcal{N}}}$. Eq. (4.7) then gives $\kappa_{T,m}^{\rm RPA} = 1/(1+\bar{\kappa})$, which approaches 1 as $\bar{\kappa} \to 0$ and 0 as $\bar{\kappa} \to \infty$. On the other hand, using $P_{\rm P}(q)$ instead of $P_{\rm D}(q)$ in Eq. (4.17) gives

$$h^{mm}(r) = \frac{3}{\pi\sqrt{\bar{\mathcal{N}}}r/R_{e,0}}\left\{\exp\left(-2\sqrt{3}\frac{r}{R_{e,0}}\right) - \exp\left[-2\sqrt{3\left(1-\sqrt{\bar{\mathcal{N}}}C_0\right)}\frac{r}{R_{e,0}}\right]\right\}, \quad (4.33)$$

which leads to

$$h^{mm}(0) = \frac{6\sqrt{3}}{\pi\sqrt{\bar{\mathcal{N}}}}\left(1-\sqrt{1-\sqrt{\bar{\mathcal{N}}}C_0}\right). \quad (4.34)$$

Combining RPA closure with Padé approximation then gives $h_{\rm RPA}^{mm}(0) = (6\sqrt{3}/\pi\sqrt{\bar{\mathcal{N}}})\left(1-\sqrt{1+\bar{\kappa}}\right)$. Clearly, for $\bar{\mathcal{N}} < (108/\pi^2)(\sqrt{1+\bar{\kappa}}-1)^2$ (or equivalently $\bar{\kappa} > \pi^2\bar{\mathcal{N}}/108 + \sqrt{3}\pi\sqrt{\bar{\mathcal{N}}}/9$), $h_{\rm RPA}^{mm}(0) < -1$, which indicates *qualitative* failure of RPA closure for CGC-δ model in such cases. We note that, when $P_{\rm D}(q)$ is used for ω^{mm}, PRISM theory with RPA closure is equivalent to the Gaussian-fluctuation (or the first-order perturbation[22]) theory;[39] our analysis here therefore reveals its limitation at small $\bar{\mathcal{N}}$ or large $\bar{\kappa}$.

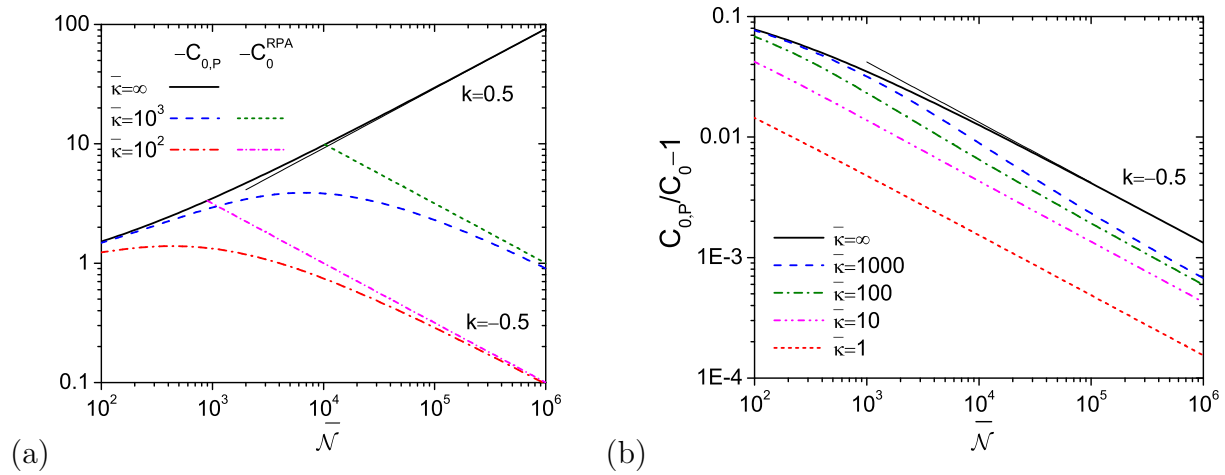

Figure 4.2: Logarithmic plots of (a) $-C_{0,\mathrm{P}}$ given by Eq. (4.35) and $-C_0^{\mathrm{RPA}} = \bar{\kappa}/\sqrt{\bar{\mathcal{N}}}$ and (b) the relative difference between $C_{0,\mathrm{P}}$ and C_0 obtained numerically from Eq. (4.18) vs. $\bar{\mathcal{N}}$ at various $\bar{\kappa}$ obtained from PRISM theory for CGC-δ model, where the slope of each straight line is given next to it.

Combining PY closure (see Sec. 4.2.2) with Padé approximation, we can analytically solve C_0 from Eq. (4.18) as[40]

$$C_{0,\mathrm{P}} = \frac{6\bar{\kappa}\sqrt{81\bar{\kappa}^2 + 3\pi^2\bar{\kappa}\bar{\mathcal{N}} + 18\sqrt{3}\pi\bar{\kappa}\sqrt{\bar{\mathcal{N}}} + 3\pi^2\bar{\mathcal{N}}}}{\pi^2\bar{\mathcal{N}}^{3/2}} - \frac{54\bar{\kappa}^2}{\pi^2\bar{\mathcal{N}}^{3/2}} - \frac{6\sqrt{3}\bar{\kappa}}{\pi\bar{\mathcal{N}}} - \frac{\bar{\kappa}}{\sqrt{\bar{\mathcal{N}}}}, \qquad (4.35)$$

which approaches C_0^{RPA} as $\bar{\kappa} \to 0$ or $\bar{\mathcal{N}} \to \infty$, and the hard-core result[16] $C_{0,\mathrm{P}}^{\infty} = -\pi^2\sqrt{\bar{\mathcal{N}}}/108 - \sqrt{3}\pi/9$ as $\bar{\kappa} \to \infty$. From Eq. (4.7), we then find that $\kappa_{T,m}^{\mathrm{PY}}$ approaches $\kappa_{T,m}^{\mathrm{RPA}}$ as $\bar{\kappa} \to 0$ or $\bar{\mathcal{N}} \to \infty$, and $1/(1 + \pi^2\bar{\mathcal{N}}/108 + \sqrt{12}\pi\sqrt{\bar{\mathcal{N}}}/18)$ as $\bar{\kappa} \to \infty$. While RPA closure includes only Gaussian fluctuations in the system, PY closure captures non-Gaussian fluctuations in an approximate way.

Fig. 4.2(a) shows how $-C_0^{\mathrm{RPA}}$ and $-C_{0,\mathrm{P}}$ at various $\bar{\kappa}$ (including $-C_{0,\mathrm{P}}^{\infty}$) vary with $\bar{\mathcal{N}}$. We see that $-C_0^{\mathrm{RPA}}$ is inversely proportional to $\sqrt{\bar{\mathcal{N}}}$, that $-C_{0,\mathrm{P}}^{\infty}$ increases monotonically with increasing $\bar{\mathcal{N}}$, and that $-C_{0,\mathrm{P}}$ at finite $\bar{\kappa}$ exhibits a maximum, both the location and value of which increase with increasing $\bar{\kappa}$. At large $\bar{\mathcal{N}}$, $-C_{0,\mathrm{P}}^{\infty} \propto \sqrt{\bar{\mathcal{N}}}$ but $-C_{0,\mathrm{P}}$ at finite $\bar{\kappa}$ approaches $-C_0^{\mathrm{RPA}}$ (i.e., $\propto 1/\sqrt{\bar{\mathcal{N}}}$). Note that any value of $-C_0$ above the curve of $-C_{0,\mathrm{P}}^{\infty}$ in Fig. 4.2(a) leads to the unphysical result of $h^{mm}(0) < -1$, as given by Eq. (4.34).

Finally, to examine the accuracy of Padé approximation used in the above derivation of

$C_{0,\mathrm{P}}$, Fig. 4.2(b) compares $C_{0,\mathrm{P}}$ with C_0 obtained numerically from Eq. (4.18) (where $P_{\mathrm{D}}(q)$ is used). We see that Padé approximation overestimates $-C_0$ by at most a few percent and becomes better with increasing $\bar{\mathcal{N}}$ or decreasing $\bar{\kappa}$. In addition, we find $C_{0,\mathrm{P}}/C_0 - 1 \propto 1/\sqrt{\bar{\mathcal{N}}}$ at large $\bar{\mathcal{N}}$ and at small $\bar{\kappa}$, as well as $C_{0,\mathrm{P}}/C_0 - 1 \propto \bar{\kappa}$ at small $\bar{\kappa}$ (data not shown).

4.3.2 Correspondence to experimental systems

In our original system of the hard-core CGC-δ model, there is only one parameter — the invariant degree of polymerization $\bar{\mathcal{N}}$. For an experimental system of polymer melts with hard excluded-volume interactions, since the monomer density $\rho_c N_m$ is nearly independent of N_m, one finds $\bar{\mathcal{N}} = a^6(\rho_c N_m)^2 N_m \propto N_m$, which has typical experimental values of at least 10^3. We therefore use $\bar{\mathcal{N}} = 10^4$ and 10^5 in this work, unless specified otherwise.

When the hard-core CGC-δ model is solved with PRISM-PY method, $\bar{\mathcal{N}}$ determines C_0 via Eq. (4.18) and thus $\kappa_{T,m}$ defined in Eq. (4.7). Fig. 4.3 compares the so-obtained $\kappa_{T,m}$ with that of polyethylene (PE) and polystyrene (PS) melts at 180°C and 280°C, respectively, and 1 atm, where we take the statistical segment length $a = 0.42$nm for PE[33] and 0.67nm for PS,[34] respectively, and the data for calculating their density and equation of state from Ref. [35]. We see that $\kappa_{T,m} \propto \bar{\mathcal{N}}^{-1}$ for both experimental systems, as well as the hard-core CGC-δ model at large $\bar{\mathcal{N}} \gtrsim 10^5$.

On the other hand, Fig. 4.3 also shows that $\kappa_{T,m}$ of the hard-core CGC-δ model is larger than those of PE and PS; in other words, the hard-core CGC-δ model is "softer". While this problem can be corrected by using an interaction potential of finite range (e.g., the Gaussian-core potential) instead of the δ-function potential, the hard-core CGC-δ model can nevertheless be used for our purpose of demonstrating the general strategy of systematic and simulation-free coarse graining. We therefore take it as the original system in this study due to its simplicity.

4.3.3 Coarse-grained potential

In this section, we examine the CG potential $\beta v(r)$ obtained from structure-based coarse graining using PRISM theory with various closures for CG system. We set $\bar{\mathcal{N}} = 10^4$ here; other values of $\bar{\mathcal{N}}$ do not qualitatively change our results. Fig. 4.4(a) shows the N-dependence of $\epsilon_0 \equiv \beta v(0)$, which measures the "hardness" of CG potential. We see that our numerical results of ϵ_0 obtained with both HNC and PY closures (denoted by $\epsilon_{0,\mathrm{HNC}}$ and $\epsilon_{0,\mathrm{PY}}$, respectively) monotonically increase with increasing N, which is expected since CG segments become softer as the coarse-graining level increases (i.e., N decreases); in the limit of $N \to N_m$, the CG system should reduce to the original system and we thus expect $\epsilon_0 \to \infty$. The RPA result, however, exhibits a maximum at $N = 48$ and then monotonically decreases with increasing N, which indicates *qualitative* failure of RPA closure for larger N. Nevertheless, at large $N \gtrsim 1000$, we find

$$\beta v_{\mathrm{RPA}}(r) = -c^{ss}(r) \approx -\frac{C_0}{N^2}\left(\frac{3R_{e,0}^2}{2\pi\sigma_0^2}\right)^{3/2} \exp\left(-\frac{3r^2}{2\sigma_0^2}\right) \tag{4.36}$$

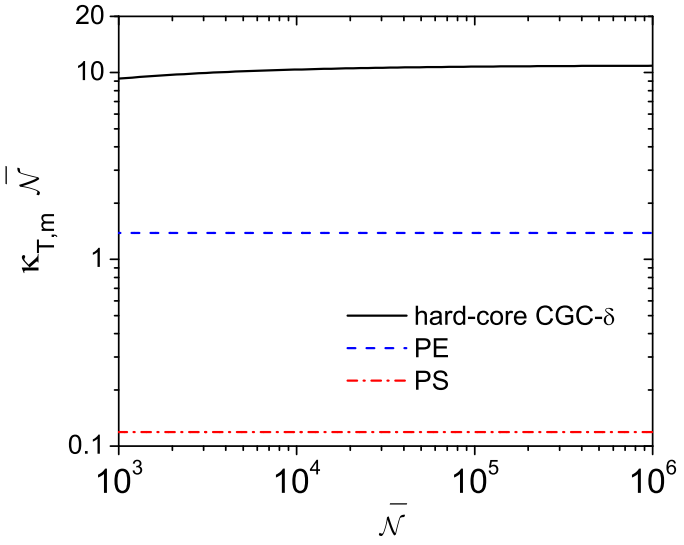

Figure 4.3: Logarithmic plot of the normalized isothermal compressibility $\kappa_{T,m}$ vs. the invariant degree of polymerization $\bar{\mathcal{N}}$ for the hard-core CGC-δ model, polyethylene (PE) and polystyrene (PS) melts.

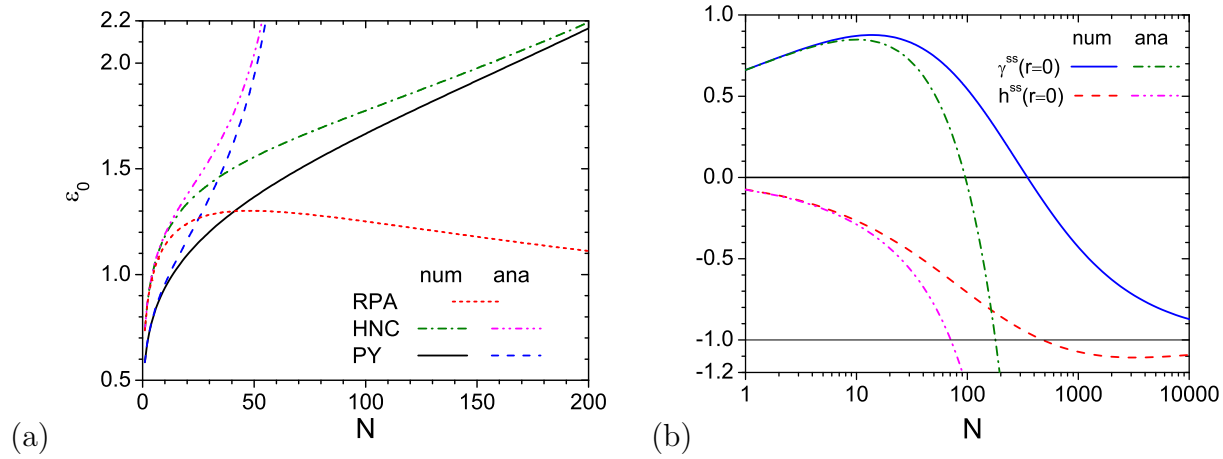

Figure 4.4: N-dependence of (a) ϵ_0 obtained with various closures for CG systems and (b) $\gamma^{ss}(0)$ and $h^{ss}(0)$, where PRISM theory is used for coarse graining, "num" denotes our numerical results, and "ana" the analytical results from Ref. [19]. $\bar{\mathcal{N}} = 10^4$.

with $\sigma_0^2/R_{e,0}^2 = 1/3N$ given by Eq. (4.37) below, which leads to $\epsilon_{0,\mathrm{RPA}} \propto N^{-1/2}$ consistent with our numerical results (data not shown). Note that Eq. (4.36) is the same as Eq. (37) in Ref. [19], which is for $N = 1$ and valid in the limit of $\bar{\mathcal{N}} \to 0$. On the other hand, Guenza and co-workers also suggested the validity of Eq. (4.36) for $N > 1$ in the limit of $-C_0\sqrt{\bar{\mathcal{N}}}/N \to 0$,[19] which is supported by our numerical results at $\bar{\mathcal{N}} = 10^4$ and $N \gtrsim 1000$ (i.e., $-C_0\sqrt{\bar{\mathcal{N}}}/N \lesssim 1$).

Our numerical results in Fig. 4.4(a) also show that, for small N, $\epsilon_{0,\mathrm{RPA}} \approx \epsilon_{0,\mathrm{HNC}}$ and both are considerably different from $\epsilon_{0,\mathrm{PY}}$, and that $\epsilon_{0,\mathrm{PY}}$ approaches $\epsilon_{0,\mathrm{HNC}}$ with increasing N for $14 < N < 349$. As mentioned in Sec. 4.2.2, RPA and PY closures can be obtained from the Taylor expansion of HNC closure at small $|h^{ss}(r)|$ and small $|\gamma^{ss}(r)|$, respectively. Fig. 4.4(b) shows that $|h^{ss}(r=0)|$ is small at small N, and that $|\gamma^{ss}(r=0)|$ is not so small at small N but monotonically decreases towards 0 for $14 < N < 349$; this explains the behavior of ϵ_0. We also note that both $\epsilon_{0,\mathrm{HNC}}$ and $\epsilon_{0,\mathrm{PY}}$ diverge for $N \geq 477$, due to the divergence of the potential of mean force $-\ln[1 + h^{ss}(r)]$ caused by the unphysical behavior of $h^{ss}(r) < -1$ at some r (e.g., $r = 0$ as shown in Fig. 4.4(b)). $h^{ss}(r)$ is calculated from Eq. (4.19), which involves only two approximations: the use of ideal-chain conformations

(i.e., $P_D(q)$) to obtain $\hat{\omega}$ and the use of PY closure to obtain C_0 for the original system. Since PY closure works well for hard-core repulsive potentials, we attribute this unphysical behavior mainly to the use of ideal-chain conformations, which is strictly valid only in the limit of $\bar{\mathcal{N}} \to \infty$.

Figs. 4.4(a) and 4.4(b) also compare our numerical results (denoted by "num") with those calculated from the analytical results of $h^{ss}(r)$ and $c^{ss}(r)$ obtained by Guenza and co-workers (given in Eqs. (20), (28) and (29) of Ref. [19], and denoted by "ana"); note that $\epsilon_{0,\mathrm{RPA}}$ obtained from their Eq. (29) is the same as our numerical result. While the analytical results of $\epsilon_{0,\mathrm{HNC}}$ and $\epsilon_{0,\mathrm{PY}}$ are consistent with our numerical results for $N \lesssim 10$, they deviate as N increases. In particular, we note that the analytical results of $\epsilon_{0,\mathrm{HNC}}$ and $\epsilon_{0,\mathrm{PY}}$ diverge for $N \geq 70$ (instead of $N \geq 477$ given by our numerical results) due to the approximation used in Eq. (20) of Ref. [19], which gives $h^{ss}(0) < -1$ as shown in Fig. 4.4(b).

Fig. 4.5(a) shows the CG potential $\beta v(r)$ normalized by ϵ_0, obtained with PY closure, as a function of r^2 normalized by the mean-square end-to-end distance of an ideal subchain having l monomers, $R_{e,s}^2 = R_{e,0}^2/N$; the latter normalization is chosen according to Eqs. (24) and (25) in Ref. [36], where it was suggested that the range of CG potential can be approximated by $\sigma_0 \equiv R_{e,0}/\sqrt{3N}$ based on the Gaussian distribution of polymer density around the subchain center-of-mass. We see that, with increasing N, $\beta v(r)/\epsilon_0$ approaches a straight line on this semi-logarithmic plot, suggesting that $\beta v(r)$ can be approximated by a Gaussian function. At larger r, however, $\beta v(r)/\epsilon_0$ exhibits small negative values (i.e., an attractive well), which approach 0 with increasing N, and thereafter slight oscillation around 0, as shown in Fig. 4.5(b). On the other hand, Figs. 4.5(c) and 4.5(d) compare $\beta v(r)/\epsilon_0$ obtained with various closures. In general, we see similar behavior to that of ϵ_0: At $N = 1$ the HNC and RPA results are indistinguishable and deviate from the PY result, and at $N = 100$ the HNC result is closer to the PY result and both deviate from the RPA result at small r. Note, however, that in the latter case the PY result is closer to RPA than to HNC result at large r (i.e., around the attractive well).

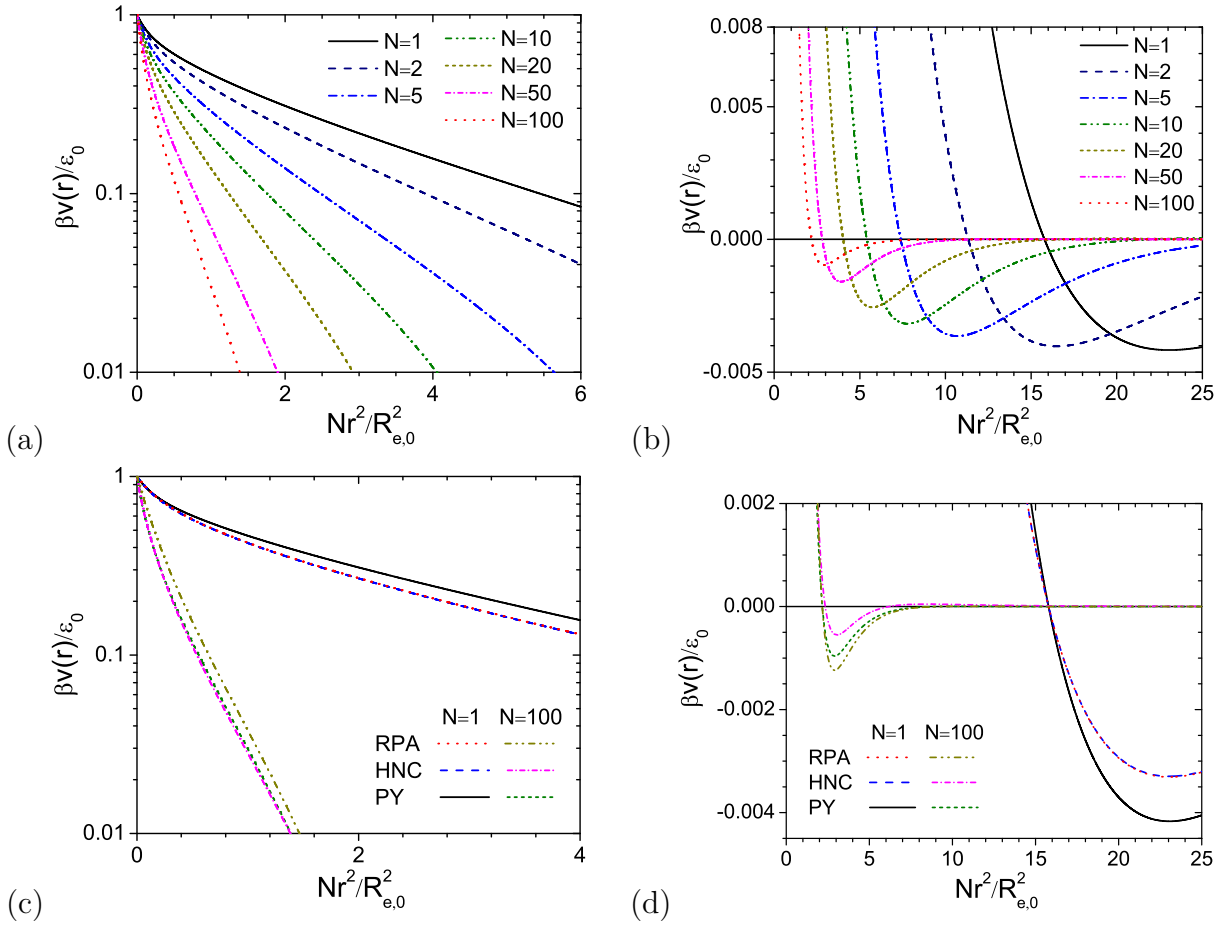

Figure 4.5: Effective pair potential between CG segments $\beta v(r)$ normalized by ϵ_0 as a function of r^2 normalized by $R_{e,0}^2/N$, obtained using PRISM theory for coarse graining. PY closure for CG systems is used in parts (a) and (b), and $\bar{\mathcal{N}} = 10^4$.

To quantify the range of CG potential, we define $\sigma_0 \equiv \sqrt{\int_0^\infty r^4 v(r)\mathrm{d}r / \int_0^\infty r^2 v(r)\mathrm{d}r}$ and $\sigma_i \equiv \sqrt{\int_0^{r_i} r^4 v(r)\mathrm{d}r / \int_0^{r_i} r^2 v(r)\mathrm{d}r}$, where r_i $(i = 1, 2, 3)$ is the i^{th} smallest r at which $\beta v(r) = 0$. Note that the RPA result of σ_0, denoted by $\sigma_{0,\text{RPA}}$, is given by

$$\sigma_{0,\text{RPA}}^2 = \frac{\int \mathrm{d}\mathbf{r} r^2 c^{ss}(r)}{\int \mathrm{d}\mathbf{r} c^{ss}(r)} = \frac{\left[-\nabla_{\mathbf{q}}^2 \hat{c}^{ss}(q)\right]\big|_{q=0}}{\hat{c}^{ss}(0)} = -\frac{1}{\hat{c}^{ss}(0)} \left[\frac{2}{q}\frac{\mathrm{d}\hat{c}^{ss}(q)}{\mathrm{d}q} + \frac{\mathrm{d}^2\hat{c}^{ss}(q)}{\mathrm{d}q^2}\right]\Bigg|_{q=0} = \frac{R_{e,0}^2}{3N}, \tag{4.37}$$

where Eq. (4.20) is used to obtain the final result, which is the same as the above σ_0 suggested in Ref. [36].

Fig. 4.6(a) shows σ_0 as a function of N obtained with various closures. We see that, at small N, $\sigma_{0,\text{HNC}}$ and $\sigma_{0,\text{RPA}}$ are indistinguishable and both are larger than $\sigma_{0,\text{PY}}$, consistent

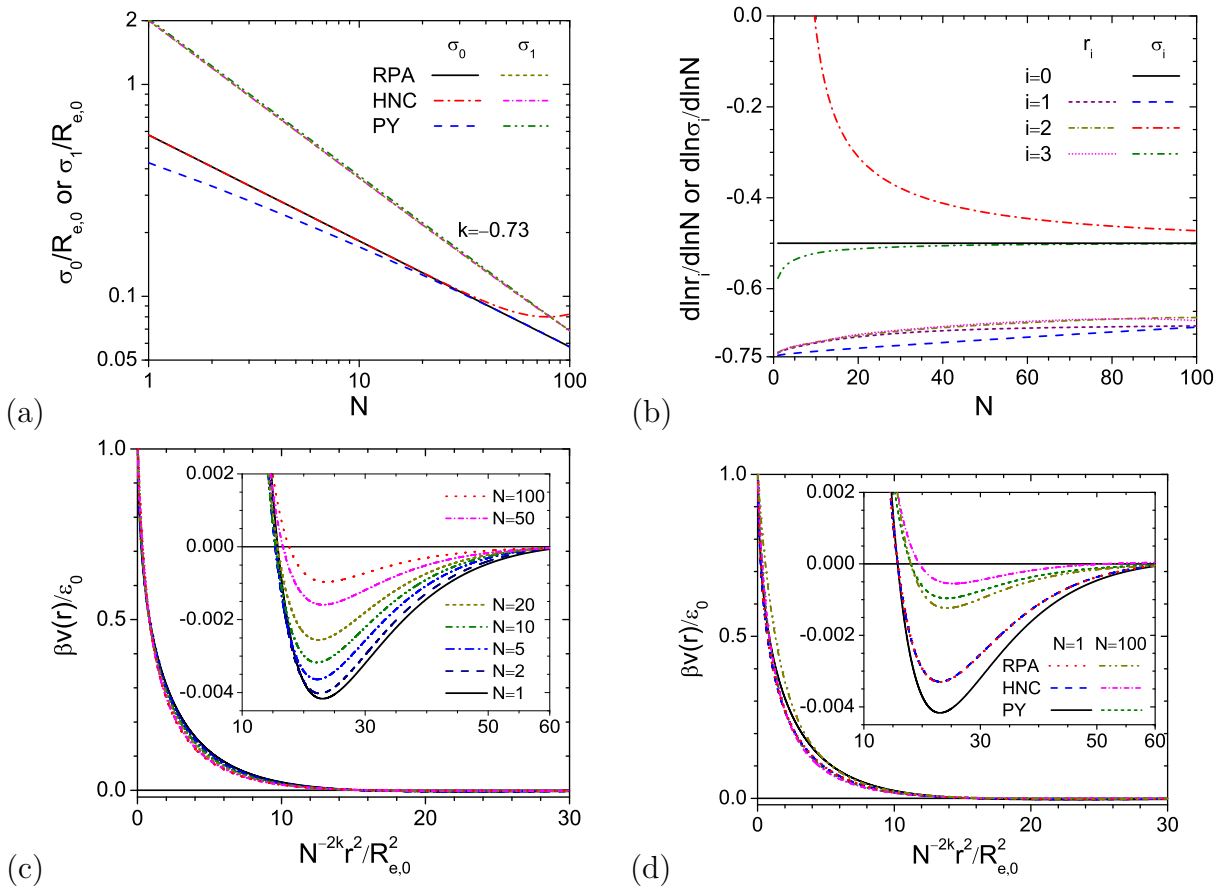

Figure 4.6: (a) Logarithmic plot of σ_0 and σ_1 vs. N, where "$k = -0.73$" denotes the fitted slope of σ_1 obtained regardless of the closure for CG systems. (b) Scaling exponent of r_i and σ_i with N, obtained with RPA closure for CG systems. Parts (c) and (d) show the effective pair potential between CG segments $\beta v(r)$ normalized by ϵ_0 as a function of r^2 normalized by $R_{e,0}^2/N^{2k}$ with $k = -0.73$, where PY closure for CG systems is used in (c). In all cases, PRISM theory is used for coarse graining and $\bar{\mathcal{N}} = 10^4$.

with the aforementioned behavior of ϵ_0 and $\beta v(r)/\epsilon_0$. For $N \gtrsim 30$, however, $\sigma_{0,\mathrm{PY}}$ merges with $\sigma_{0,\mathrm{RPA}}$ and both are smaller than $\sigma_{0,\mathrm{HNC}}$, which exhibits a shallow minimum at $N = 78$; this behavior, different from that of ϵ_0 and $\beta v(r < r_1)/\epsilon_0$ at large N, is due to the attractive well and oscillation of $\beta v(r)$ at $r > r_1$ shown in Fig. 4.5(d). Their effects can also be seen from the difference between σ_0 and σ_1 shown in Fig. 4.6(a). We note that σ_1 obtained with all three closures are larger than σ_0 (except for $N > 80$ obtained with HNC closure) and nearly collapse onto a straight line with a slope of $k \approx -0.73$ on this logarithmic plot (i.e., $\sigma_1^2/R_{e,0}^2 \propto N^{2k}$).

We further note that k slightly decreases with increasing $\bar{\mathcal{N}}$, i.e., $k \approx -0.74$ at $\bar{\mathcal{N}} = 10^5$. In Refs. [18, 19], Guenza and co-workers performed structure-based coarse graining using PRISM theory with the hard-core CGC-δ model as the original system, and obtained an analytical expression of $\beta v_{\mathrm{RPA}}(r) = -c^{ss}(r)$ for $r > R_{e,s}$ under the assumption of $-C_0\sqrt{\bar{\mathcal{N}}}/N \gg 1$; they found that the range of $\beta v_{\mathrm{RPA}}(r)$, when expressed in units of $R_{e,0}$, scales with $N^{-3/4}$. While this is consistent with our numerical results of $\sigma_{1,\mathrm{RPA}}$, we emphasize the different scalings of $\sigma_{0,\mathrm{RPA}}$ and $\sigma_{1,\mathrm{RPA}}$ with N shown in Fig. 4.6(a), caused by the small attractive well and oscillation of $\beta v_{\mathrm{RPA}}(r)$ at $r > r_1$; in other words, the scaling of CG potential range with N depends on how this range is measured.

Fig. 4.6(b) shows the scaling of r_i and σ_i with N, obtained numerically with RPA closure for CG systems. We see two groups of scaling behavior: One includes σ_0, σ_2 and σ_3, the scaling exponent of which is either $-1/2$ regardless of N (i.e., for $\sigma_{0,\mathrm{RPA}}$) or approaches $-1/2$ at large N, and the other includes r_i $(i = 1, 2, 3)$ and σ_1, the scaling exponent of which varies between $-3/4$ at small N (i.e., large $-C_0\sqrt{\bar{\mathcal{N}}}/N$) and -0.65 at large N. This is also found for PY results (note that $r_{i,\mathrm{PY}} = r_{i,\mathrm{RPA}}$ as easily seen from Eq. (4.13)), but not for HNC results as inferred from the non-monotonic behavior of $\sigma_{0,\mathrm{HNC}}$ shown in Fig. 4.6(a).

Finally, plotting $\beta v(r)/\epsilon_0$ as a function of r^2 normalized by $R_{e,0}^2/N^{-2k}$ instead of $R_{e,s}^2$, the PY results for various N collapse approximately onto the same curve as shown in Fig. 4.6(c), which can be compared with Figs. 4.5(a) and 4.5(b). The same is found for the HNC and RPA results as shown in Fig. 4.6(d), which can be compared with Figs. 4.5(c) and 4.5(d).

4.3.4 Comparisons of structural and thermodynamic properties between original and CG systems

By construction, structure-based coarse graining gives the same structural properties (i.e., $h_{\alpha,\beta}^{ss}(r)$) between original and CG systems. As explained in Sec. 4.2.4, they then have the same normalized isothermal compressibility, i.e., $\kappa_T = \kappa_{T,m}$. In the following we therefore only compare the thermodynamic properties of original and CG systems obtained using PRISM theory.

For the original system of hard-core CGC-δ model at $\bar{\mathcal{N}} = 10^4$, PRISM theory with PY closure gives the interchain pressure and internal energy per chain as $\beta R_{e,0}^3 P_m \approx 48111.4$ and $\beta u_{c,m} \approx 481.11$. For the CG system at given N, we use RPA, HNC and PY closures to numerically obtain the effective potential and then calculate $\beta R_{e,0}^3 P$ and βu_c, which are compared with the original system in Figs. 4.7(a) and 4.7(b), respectively. We see that, while HNC and RPA results at small N are very close to those of the original system, they are not exactly the same even at $N = 1$ (where $\beta R_{e,0}^3 P_{\rm HNC} \approx 48109.9$ and $\beta u_{c,\rm HNC} \approx 480.79$, and $\beta R_{e,0}^3 P_{\rm RPA} \approx 48109.0$ and $\beta u_{c,\rm RPA} \approx 480.78$), and the discrepancies increase with increasing N. The RPA results monotonically decrease with increasing N and underestimate the original system for all N, and the HNC results exhibit similar behavior to RPA results at small N, but have a minimum (at $N = 56$ for $\beta R_{e,0}^3 P$ and $N = 82$ for βu_c) and overestimate the original system at large $N \leq 477$. With RPA and HNC closures, even in the limit of $N \to N_m$ the original system cannot be recovered due to the different closures used for original and CG systems.

On the other hand, the PY results of CG systems at small N exhibit larger discrepancy (underestimate the original system more) than both RPA and HNC results. With increasing N, $\beta R_{e,0}^3 P_{\rm PY}$ exhibits a minimum at $N = 23$, and $\beta u_{c,\rm PY}$ monotonically decreases till $N = 477$ (after which $\beta v(r)$ obtained with both HNC and PY closures diverge as explained in Sec. 4.3.3). Only in the limit of $N \to N_m$, where both $\hat{\omega}^{ss}$ and $\hat{\omega}^{sm}$ become $\hat{\omega}^{mm}$, does the CG system with PY closure recover the original system (note that, as shown in Fig. 4.4(b), $h^{ss}(0)$ slowly approaches -1 for $N > 3242$).

To explain the above discrepancy in the thermodynamic properties between original and CG systems, we take βu_c as an example, which according to Eq. (4.14) is given by

$$\beta u_c = \frac{N^2\sqrt{\bar{\mathcal{N}}}}{2}\frac{\beta\hat{v}(0)}{R_{e,0}^3} + \frac{2\pi N^2\sqrt{\bar{\mathcal{N}}}}{R_{e,0}^3}\int_0^\infty {\rm d}r r^2 h^{ss}(r)\beta v(r). \tag{4.38}$$

If RPA closure is used, i.e., $\beta v(r) = -c^{ss}(r)$, and with $\hat{c}^{ss}(0)/R_{e,0}^3 = C_0/N^2$ from Eq. (4.20), we have the first term on RHS of Eq. (4.38) as $-\sqrt{\bar{\mathcal{N}}}C_0/2$, which is the same as the original system (see Eq. (4.8)). Fig. 4.7(c) shows that the ratio of the second to the first term on

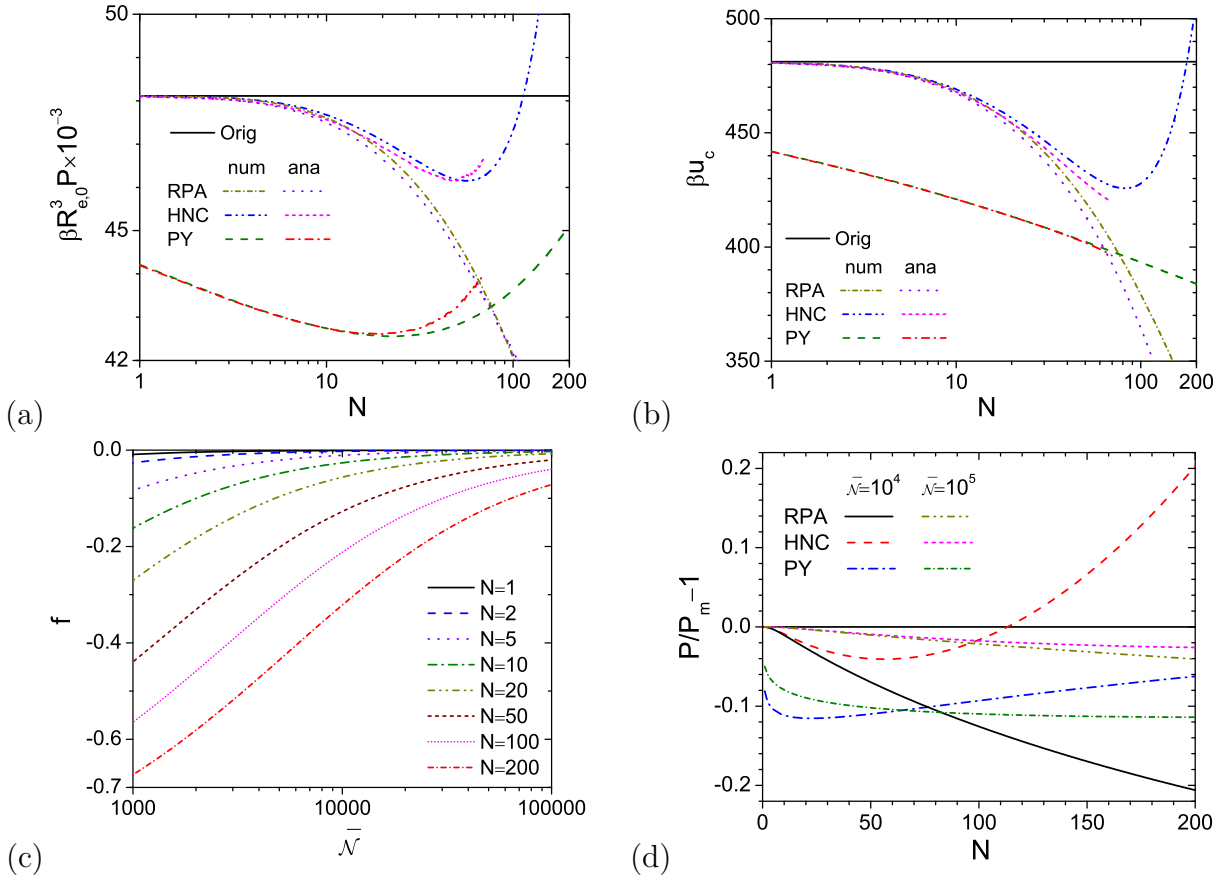

Figure 4.7: Semi-logarithmic plot of (a) the interchain (virial) pressure P and (b) the interchain internal energy per chain u_c vs. N obtained with various closures for CG systems, where "num" denotes our numerical results and "ana" the analytical results from Ref. [19], the result of the original system ("Orig") is also shown by a horizontal line, and $\bar{\mathcal{N}} = 10^4$. Part (c) shows the ratio of the second to the first term on RHS of Eq. (4.38), f, obtained with RPA closure for CG systems at various N. Part (d) shows the the relative difference in the interchain pressure between original and CG systems, $P/P_m - 1$, obtained with various closures for CG systems. PRISM theory is used for coarse graining in all the cases.

RHS of Eq. (4.38), $f = 4\pi \int_0^\infty \mathrm{d}r r^2 h^{ss}(r) c^{ss}(r)/\hat{c}^{ss}(0) < 0$, monotonically decreases with increasing N and decreasing $\bar{\mathcal{N}}$; the same behavior is therefore found for $\beta u_{c,\mathrm{RPA}}$, which underestimates $\beta u_{c,m}$. In contrast, Guenza and co-workers assumed $h^{ss}(r) = 0$ (i.e., structureless CG systems), which then leads to their claimed thermodynamic consistency[17–19] but clearly contradicts with Eq. (4.19). The same is for $\beta R_{e,0}^3 P_{\mathrm{RPA}}$ (data not shown).

As mentioned in Sec. 4.2.2, RPA closure can be obtained from the Taylor expansion of HNC closure at small $|h^{ss}(r)|$. At small N, since $|h^{ss}(r)|$ is indeed small as shown in

Fig. 4.4(b), HNC results exhibit similar behavior to RPA results. As N increases, while the second term in Eq. (4.38) monotonically decreases, its first term increases faster (data not shown), which is expected from the behavior of ϵ_0 obtained with HNC closure as shown in Fig. 4.4(a); this leads to the minimum in $\beta u_{c,\mathrm{HNC}}$ shown in Fig. 4.7(b). The same is found for $\beta R_{e,0}^3 P_{\mathrm{HNC}}$ (data not shown).

On the other hand, PY closure can be obtained from the Taylor expansion of HNC closure at small $|\gamma^{ss}(r)|$. At small N, however, $|\gamma^{ss}(r)|$ is not so small as shown in Fig. 4.4(b), which explains why PY results exhibit larger discrepancy than both HNC and RPA results. At large N ($N \gtrsim 155$ for $\beta R_{e,0}^3 P$ and $N \gtrsim 247$ for βu_c), while PY results still underestimate these properties of the original system, they exhibit smaller discrepancy than both HNC and RPA results, and we expect that they approach those of the original system in the limit of $N \to N_m$. Note that, at large N, while the HNC and PY predictions of ϵ_0 shown in Fig. 4.4(a), as well as $\beta v(r < r_1)/\epsilon_0$ shown in Fig. 4.5(c), approach each other, their predictions of βu_c and $\beta R_{e,0}^3 P$ are quite different due to their different attractive wells shown in Fig. 4.5(d).

Fig. 4.7(d) compares the relative deviation of the interchain pressure of CG systems from the original system, $P/P_m - 1$, at $\bar{\mathcal{N}} = 10^4$ and 10^5. We see that the relative deviation in general becomes smaller with increasing $\bar{\mathcal{N}}$, with the exception due to the minimum (thus the non-monotonic behavior) of the HNC and PY results. The same is found for $u_c/u_{c,m} - 1$ (data not shown). Our numerical results therefore clearly show that structure-based coarse graining cannot give the thermodynamic consistency between original and CG systems at any $N < N_m$, which is expected due to the information loss of coarse graining.

Finally, Figs. 4.7(a) and 4.7(b) also compare our numerical results with those obtained from the analytical expressions of $h^{ss}(r)$ and $c^{ss}(r)$ given in Ref. [19]. While the analytical results from Ref. [19] (without assuming $h^{ss}(r) = 0$) are consistent with our numerical results for small $N \lesssim 10$, they deviate as N increases. The analytical results also have another problem at large N when used to calculate the pressure; namely, the different approximations

of $c^{ss}(r)$ given in Eqs. (28) and (29) of Ref. [19], which are valid for $\sqrt{6N}r/R_{e,0} \gg 1$ and $\ll 1$, respectively, result in a mismatch of $c^{ss}(r)$ (thus discontinuous $\beta v(r)$) at the junction $\sqrt{6N}r/R_{e,0} = 4/3$ suggested in Ref. [19]. While this mismatch is small at small N, it increases with increasing N. We therefore conclude that the analytical results of Ref. [19] are only applicable for small $N \lesssim 10$ at $\bar{\mathcal{N}} = 10^4$; their applicable range increases with increasing $\bar{\mathcal{N}}$.

4.3.5 Comparison between PRISM and BPRISM results

In this section, we compare the results of structure-based coarse graining between using PRISM and BPRISM theories to examine the chain-end effects neglected in the former.[32] First, as shown in Eqs. (4.7)∼(4.9), the structural and thermodynamic properties of the original system at given $\bar{\mathcal{N}}$ depend only on C_0 in both theories. Fig. 4.8(a) therefore shows how $-C_0$ obtained from both theories with PY closure and their relative difference $C_{0,\mathrm{PRISM}}/C_{0,\mathrm{BPRISM}} - 1$ vary with N at $\bar{\mathcal{N}} = 10^4$; we only perform BPRISM calculations for $N \leq 40$ due to the expensive computation at larger N. We see that $-C_0$ in BPRISM theory slightly increases with increasing $N > 2$; in other words, PRISM theory slightly (by less than 0.03%) overestimates C_0 (i.e., $C_{0,\mathrm{PRISM}} > C_{0,\mathrm{BPRISM}}$) for $N > 2$ (they are the same for $N = 1$ and 2). According to Eqs. (4.7)∼(4.9), PRISM theory therefore slightly overestimates $\kappa_{T,m}$ (and κ_T of CG systems) and underestimates $\beta u_{c,m}$ and $\beta R_{e,0}^3 P_m$ in such cases.

Fig. 4.8(b) shows the relative difference in βu_c and $\beta R_{e,0}^3 P$ obtained from structure-based coarse graining between using PRISM and BPRISM theories with various closures for CG systems. We see that PRISM theory underestimates βu_c and $\beta R_{e,0}^3 P$ in all the cases for $N > 2$. While the chain-end effects are different for different properties and closures, the relative differences are less than 0.1% for $N \leq 40$. Similar results are found at $\bar{\mathcal{N}} = 10^5$ with even smaller relative differences (data not shown). Note that, although the relative differences vary monotonically with N in Fig. 4.8(b), the PRISM and BPRISM results are expected to be the same in the limit of $N \to \infty$, where the chain-end effects vanish.[32] Our

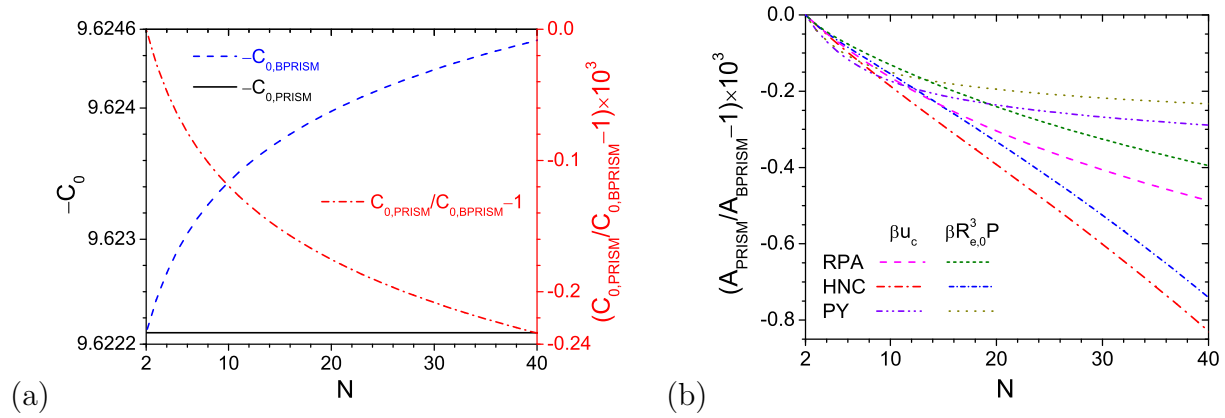

Figure 4.8: N-dependence of (a) $-C_0$ obtained from PRISM and BPRISM theories with PY closure for the original system and their relative difference and (b) the relative difference in the interchain internal energy per chain ($A = u_c$) and pressure ($A = P$) between using PRISM and BPRISM theories with various closures for CG systems. $\bar{\mathcal{N}} = 10^4$.

numerical results therefore show that, compared to BPRISM theory, PRISM theory can give quantitatively accurate results for both original and CG systems.

4.4 Discussions

In this section, we elaborate on a couple of issues related to this work.

4.4.1 Differences between this work and that of Guenza's group

Guenza and co-workers also applied structure-based coarse graining with PRISM theory to the original system of hard-core Gaussian thread model solved by PRISM theory with PY closure.[17–19] There are, however, several important differences between our work and theirs:

1. To pursue analytical results, Guenza and co-workers used the Padé approximation $P_{\rm P}(q)$ for the single-chain structure factor in the original system.[17–19] As shown in Fig. 4.2(b) below, this overestimates C_0 by up to a few percent (see Sec. 4.3.1 for more details). We use the exact Debye function $P_{\rm D}(q)$ instead, and pursue numerical results.

2. Again to pursue analytical results, Guenza and co-workers used RPA closure for CG systems in most cases.[17–19] As shown in Fig. 4.4(a), RPA closure *qualitatively* fails for

large N, which can be understood from Eq. (4.3) showing that RPA closure can be obtained from PY closure at *small* pair potential $\beta u(r)$ (and also assuming $g(r) = 1$); CG pair potential actually becomes larger as N increases, thus leading to the failure of RPA closure for CG systems. In contrast, we use RPA, HNC and PY closures for CG systems and compare in detail their performance for coarse graining; our numerical results in Fig. 4.7 show that, within the parameter range of our study, HNC closure gives the best agreement in the thermodynamic properties between the original and CG systems.

3. Most importantly, as explained in Sec. 4.3.4, Guenza and co-workers assumed $h^{ss}(r) = 0$ (i.e., structureless CG systems), which, together with RPA closure for CG systems, leads to their claimed thermodynamic consistency.[17–19] This assumption is inconsistent with the structure-based coarse graining, where $h^{ss}(r)$ should be obtained from Eq. (4.19). In contrast, our numerical results clearly show that structure-based coarse graining cannot give the thermodynamic consistency between original and CG systems at any $N < N_m$.

4. Last but not least, there is a philosophical difference on how to use integral-equation theories for coarse graining. As aforementioned, Guenza and co-workers pursued analytical results, which provide direct insights but inevitably involve uncontrolled approximations. In contrast, we pursue accurate numerical results without any unnecessary approximations, which are much faster to obtain than using molecular simulations, thus leading to the simulation-free strategy that practically solves the transferability problem. The issue of applicability and accuracy of our strategy will be discussed in Sec. 4.4.2 below.

In addition, as pointed out in our Introduction, Clark and Guenza also applied structure-based coarse graining with BPRISM theory to the original system of DGC (and CGC) model, but only examined structural correlations for $N \leq 4$; that is, they did not calculate

the effective pair potentials and thermodynamic properties of CG systems.[15] In contrast, we use RPA, HNC and PY closures for CG systems and compare in detail the coarse-graining performance between using BPRISM and PRISM theories for $N \leq 40$, as presented in Sec. 4.3.5.

Finally, we point out that, strictly speaking, molecular dynamics (MD) simulations of UA model used by Guenza and co-workers in Refs. [15, 18, 19] to support their coarse-graining results are irrelevant, because the UA model is not their original system for coarse graining. Similarly, MD simulations of CG systems used in Refs. [17–19] cannot support their coarse-graining results obtained from PRISM theory. Clearly, the use of such MD simulations differs from our simulation-free strategy for coarse graining.

4.4.2 Applicability and accuracy of PRISM theory and our simulation-free strategy

PRISM theory has been reviewed several times, and we refer readers to these reviews[11–13] for details. Here we just mention that PRISM theory can be applied to various models for real polymers including UA and explicit atom models, and for polymer melts can achieve quantitative agreement with molecular simulations.[11–13]

While in this work we choose the hard-core CGC-δ model as the original system, which can be viewed as a CG representation of real polymer melts and serves well for the purpose of demonstrating our systematic and simulation-free coarse-graining strategy, our strategy summarized in Fig. 4.1 is quite general and versatile, and is applicable to any more complicated chain models for real polymers and any more complex systems (e.g., polymer blends and nanocomposites) to which PRISM theory can be applied.

Note that, apart from the various closures needed for solving the integral-equation theories, the only assumption in our numerical calculations is the use of ideal-chain conformations in the original system, which is strictly valid only in the limit of $\bar{\mathcal{N}} \to \infty$. It can be removed by the self-consistent integral-equation theories,[37] but the single-chain simulations needed there precludes the use of simple CGC-δ model as the original system; discrete chain models

with nonzero-range interactions have to be used instead. On the other hand, such single-chain simulations are still much faster than many-chain simulations of original system, and readily give $\hat{\boldsymbol{\omega}}^{ms}$ and $\hat{\boldsymbol{\omega}}^{ss}$ needed in structure-based coarse graining for any chain model. The next step is therefore to apply our coarse-graining strategy to UA model of PE with the self-consistent PRISM theory,[37] which will be reported in a future publication.

Finally, because there is no exact closure, to obtain the most accurate results one can combine our coarse-graining strategy with fine graining using molecular simulations; one recent example is given in Ref. [38], where Kremer and co-workers successfully generated uncorrelated and equilibrated melt configurations of the microscopic bead-spring chains of $N_m = 2000$ ($\bar{\mathcal{N}} \approx 7 \times 10^3$). The basic idea is to first use molecular simulations of CG systems to generate uncorrelated configurations equilibrated at large (CG) scales, which is readily achieved because CG segments interact via soft potentials. Microscopic (or atomistic) details are then re-introduced into these configurations, and subsequent molecular simulations of these fine-grained configurations only need to equilibrate chains at small (local) scales, which is fast and independent of chain length. In Ref. [38], a hierarchy of CG systems at different coarse-graining levels were used to decompose the equilibration of long-chain melts into a sequence of steps involving fast relaxation of short (sub)chains; CG pair potentials obtained from our systematic and simulation-free coarse-graining strategy can well serve for this purpose, and small errors in CG potentials due to the use of approximate closures can be easily corrected by short molecular simulations of original system.

4.5 Conclusions

We have proposed a systematic and simulation-free strategy for coarse graining of homopolymer melts, where each chain of N_m monomers is divided into N subchains (segments) each containing $l \equiv N_m/N$ monomers. Instead of molecular simulations, we have used integral-equation theories, including the reference interaction site model (RISM),[8] the polymer reference interaction site model (PRISM),[9] and the multi-block PRISM[10] (denoted by BPRISM)

theories, to obtain the structural and thermodynamic properties of both original and coarse-grained (CG) systems, and quantitatively examined how the effective pair potentials between CG segments and the properties of CG systems vary with the coarse-graining level l. This is much faster than molecular simulations and provides the quantitative basis for choosing the appropriate N-values. For structure-based coarse graining, where the interchain radial distribution functions between CG segments (representing the center-of-mass of its monomers) are matched between original and CG systems, our strategy is summarized in Fig. 4.1, which is quite general and versatile.

Taking the hard-core Gaussian thread (referred to as "CGC-δ") model[16] as the original system, we have demonstrated our systematic and simulation-free strategy for structure-based coarse graining, and compared in detail the various integral-equation theories and closures (including the random-phase approximation (RPA) closure,[24,25] the hypernetted-chain (HNC) closure,[23] and the Percus-Yevick (PY) closure[20]) for coarse graining. While the hard-core CGC-δ model is "softer" than polyethylene and polystyrene melts (i.e., it has larger normalized isothermal compressibility defined in Eq. (4.7)), it has only one parameter — the invariant degree of polymerization $\bar{\mathcal{N}}$. In most cases, we numerically solve the hard-core CGC-δ model at $\bar{\mathcal{N}} = 10^4$ and 10^5 with PRISM theory and PY closure; in Sec. 4.3.1, we present the analytical results of the more general CGC-δ model (equivalent to the Edwards model[22]) solved by PRISM theory with RPA and PY closures.

Most of our numerical results for coarse graining are also obtained using PRISM theory. The effective pair potential $\beta v(r)$ (where $\beta \equiv 1/k_B T$ with k_B being the Boltzmann constant and T the thermodynamic temperature) between CG segments can be approximated by a Gaussian function at small r (where $\beta v(r) > 0$), and exhibits small negative values (i.e., an attractive well) at larger r, which approach 0 with increasing N, and thereafter slight oscillation around 0. We find that $\epsilon_0 \equiv \beta v(0)$ obtained with both HNC and PY closures (denoted by $\epsilon_{0,\mathrm{HNC}}$ and $\epsilon_{0,\mathrm{PY}}$, respectively) monotonically increases with increasing N; $\epsilon_{0,\mathrm{RPA}}$, however, exhibits a maximum (at $N = 48$ for $\bar{\mathcal{N}} = 10^4$), which indicates *qualitative* failure

of RPA closure for larger N. We also find that ϵ_0 and $\beta v(r)/\epsilon_0$ in general exhibit the same behavior: At small N the HNC and RPA results are close to each other and deviate from the PY result, and at large N the HNC and PY results are closer to each other (with the exception that the PY result of $\beta v(r)/\epsilon_0$ around the attractive well is closer to the RPA result); these are in accordance with the relations among these closures.

To quantify the range of $\beta v(r)$, we define $\sigma_0 \equiv \sqrt{\int_0^\infty r^4 v(r)\mathrm{d}r / \int_0^\infty r^2 v(r)\mathrm{d}r}$ and $\sigma_i \equiv \sqrt{\int_0^{r_i} r^4 v(r)\mathrm{d}r / \int_0^{r_i} r^2 v(r)\mathrm{d}r}$, where r_i $(i = 1, 2, 3)$ is the i^{th} smallest r at which $\beta v(r) = 0$, and find that $\sigma_{0,\text{RPA}}^2 = R_{e,0}^2/3N$ with $R_{e,0}^2$ denoting the mean-square end-to-end distance of an ideal chain in the original system. The scaling of CG potential range with N depends on how this range is measured. With RPA or PY closure for CG systems, we find two groups: One includes σ_0, σ_2 and σ_3, the scaling exponent of which is either $-1/2$ regardless of N (i.e., for $\sigma_{0,\text{RPA}}$) or approaches $-1/2$ at large N, and the other includes r_i $(i = 1, 2, 3)$ and σ_1, the scaling exponent of which varies between $-3/4$ at small N and -0.65 at large N. This difference is due to the attractive well and oscillation of $\beta v(r)$ at $r > r_1$. In particular, we find $\sigma_1^2/R_{e,0}^2 \propto N^{2k}$ with $k \approx -0.73$ regardless of the closure for CG systems. Plotting $\beta v(r)/\epsilon_0$ as a function of r^2 normalized by $R_{e,0}^2/N^{-2k}$, we further find that the results for various N and closures collapse approximately onto the same curve as shown in Figs. 4.6(c) and 4.6(d).

While structure-based coarse graining gives the structural consistency between original and CG systems (e.g., the same normalized isothermal compressibility), it cannot give the thermodynamic consistency at any $N < N_m$, which is expected due to the information loss of coarse graining. In particular, while the HNC and RPA results of the interchain internal energy per chain and (virial) pressure of CG systems at small N are very close to (but not exactly the same as) those of the original system, the RPA results monotonically decrease with increasing N and underestimate the original system for all N, and the HNC results exhibit similar behavior to RPA results at small N but have a minimum and overestimate the original system at large N. On the other hand, the PY results of CG systems at small N

underestimate the original system more than both RPA and HNC results. With increasing N, the PY result of the interchain pressure exhibits a minimum, and that of the interchain internal energy per chain monotonically decreases. The thermodynamic inconsistency in general becomes smaller with increasing $\bar{\mathcal{N}}$, with the exception due to the minimum (thus the non-monotonic behavior) of the HNC and PY results.

The thermodynamic inconsistency between the original and CG systems is in contrast to the claim of Guenza and co-workers;[17–19] their claim that the structure-based coarse graining gives full thermodynamic consistency regardless of N is actually due to the two approximations they used for obtaining analytical results: RPA closure for CG systems and the interchain total pair correlation function between CG segments $h^{ss}(r) = 0$ (i.e., structureless CG systems). Furthermore, comparisons between our numerical results and those obtained from the analytical expressions of $h^{ss}(r)$ and the interchain direct pair correlation function between CG segments $c^{ss}(r)$ given in Ref. [19] show that the analytical results (without assuming $h^{ss}(r) = 0$) are only applicable for small $N \lesssim 10$ at $\bar{\mathcal{N}} = 10^4$; their applicable range increases with increasing $\bar{\mathcal{N}}$.

Finally, we have also compared the results of structure-based coarse graining between using PRISM and BPRISM theories to examine the chain-end effects neglected in the former,[32] and concluded that, compared to BPRISM theory, PRISM theory can give quantitatively accurate results for both original and CG systems.

REFERENCES

[1] G. S. Grest and K. Kremer, Phys. Rev. A **33**, 3628 (1986).

[2] H. S. Ashbaugh, H. A. Patel, S. K. Kumar, and S. Garde, J. Chem. Phys. **122**, 104908 (2005).

[3] L.-J. Chen, H.-J. Qian, Z.-Y. Lu, Z.-S. Li, and C.-C. Sun, J. Phys. Chem. B **110**, 24093 (2006).

[4] Q. Wang and Y. H. Yin, J. Chem. Phys. **130**, 104903 (2009).

[5] F. A. Detcheverry, D. Q. Pike, P. F. Nealey, M. Muller, and J. J. de Pablo, Phys. Rev. Lett. **102**, 197801 (2009).

[6] Q. Wang, Soft Matter **5**, 4564 (2009); *ibid.* **5**, 6206 (2010).

[7] A. A. Louis, J. Phys.: Condens. Matter **14**, 9187 (2002).

[8] D. Chandler and H. C. Andersen, J. Chem. Phys. **57**, 1930 (1972).

[9] K. S. Schweizer and J. G. Curro, Phys. Rev. Lett. **58**, 246 (1987).

[10] E. F. David and K. S. Schweizer, J. Chem. Phys. **100**, 7767 (1994); *ibid.* **100**, 7784 (1994).

[11] K. S. Schweizer and J. G. Curro, Adv. Polym. Sci. **116**, 319 (1994).

[12] K. S. Schweizer and J. G. Curro, Adv. Chem. Phys. **98**, 1 (1997).

[13] D. R. Heine, G. S. Grest, and J. G. Curro, Adv. Polym. Sci. **173**, 209 (2005).

[14] V. Krakoviack, J. P. Hansen, and A. A. Louis, Europhys. Lett. **58**, 53 (2002).

[15] A. J. Clark and M. G. Guenza, J. Chem. Phys. **132**, 044902 (2010).

[16] K. S. Schweizer and J. G. Curro, Chem. Phys. **149**, 105 (1990).

[17] J. McCarty, A. J. Clark, I. Y. Lyubimov, and M. G. Guenza, Macromolecules **45**, 8482 (2012).

[18] A. J. Clark, J. McCarty, I. Y. Lyubimov, and M. G. Guenza, Phys. Rev. Lett. **109**, 168301 (2012).

[19] A. J. Clark, J. McCarty, and M. G. Guenza, J. Chem. Phys. **139**, 124906 (2013).

[20] J. K. Percus and G. J. Yevick, Phys. Rev. **110**, 1 (1958).

[21] E. Helfand and Y. Tagami, J. Polym. Sci., Part B: Polym. Lett. **9**, 741 (1971).

[22] S. F. Edwards, Proc. Phys. Soc. **88**, 265 (1966).

[23] J. P. Hansen and I. R. McDonald, *Theory of Simple Liquids* (Academic Press, London, 1976).

[24] A. Lang, C. N. Likos, M. Watzlawek, and H. Löwen, J. Phys.: Condens. Matt. **12**, 5087 (2000).

[25] A. A. Louis, P. G. Bolhuis, and J. P. Hansen, Phys. Rev. E **62**, 7961 (2000).

[26] W. H. Press, S. A. Teukolsky, W. T. Vetterling, and B. P. Flannery, *Numerical Recipes in C, 2nd ed.* (Cambridge University Press, New York, 1992).

[27] K. S. Schweizer, and J. G. Curro, J. Chem. Phys. **89**, 3342 (1988).

[28] C. S. Hsu, D. Chandler, and L. J. Lowden, Chem. Phys. **14**, 213 (1976).

[29] P. T. Cummings, C. G. Gray, and D. E. Sullivan, J. Phys. A: Math. Gen. **14**, 1483 (1981).

[30] L. Lue and D. Blankschtein, J. Chem. Phys. **102**, 5460 (1995).

[31] http://www.fftw.org.

[32] The chain-end effects are still taken into account in the single-chain structure factor.

[33] J. Schelten, D. G. H. Ballard, G. D. Wignall, G. L. Longman, and W. Schmatz, Polymer **17**, 751 (1976).

[34] D. G. H. Ballard, J. Schelten, and G. D. Wignall, Eur. Polym. J. **9**, 965 (1973).

[35] J. E. Mark, *Physical Properties of Polymers Handbook, 2nd ed.* (Springer, New York, 2007).

[36] T. Vettorel, G. Besold, and K. Kremer, Soft Matter **6**, 2282 (2010).

[37] K. S. Schweizer, K. G. Honnell, and J. G. Curro, J. Chem. Phys. **96**, 3211 (1992).

[38] G. Zhang, L. A. Moreira, T. Stuehn, K. Ch. Daoulas, and K. Kremer, ACS Macro Lett. **3**, 198 (2014).

[39] D. C. Morse, Ann. Phys. **321**, 2318 (2006).

[40] The other solution to Eq. (4.18) at finite $\bar{\kappa}$, which is the same as Eq. (4.35) but with a minus sign in front of its first term on RHS, is discarded due to the resulting unphysical behavior of $g^{mm}(0)$ (i.e., the first term on RHS of Eq. (4.18)), which for example approaches ∞ in the limit of $\bar{\kappa} \to \infty$.

CHAPTER 5

SYSTEMATIC AND SIMULATION-FREE COARSE GRAINING OF HOMOPOLYMER MELTS USING INTEGRAL EQUATION THEORY: A RELATIVE-ENTROPY-BASED STUDY

5.1 Introduction

Coarse graining of polymer melts[1–10] is an active research area, because full atomistic simulations of many-chain systems used in experiments are not feasible at present due to their formidable computational requirements. Various coarse-graining methods have been proposed in the literature,[2,11–17] in most of which molecular simulations (i.e., molecular dynamics or Monte Carlo simulations) are used to obtain the structural and/or thermodynamic properties of both original and coarse-grained (CG) systems that need to be matched. In Chapter 4, we proposed a systematic and simulation-free strategy for structure-based coarse graining of homopolymer melts, where we used integral-equation theories,[18–20] instead of molecular simulations, to obtain the structural and thermodynamic properties of both original and CG systems, and quantitatively examined how the effective pair potentials between CG segments and the thermodynamic properties of CG systems vary with the coarse-graining level. Our strategy is much faster than those using molecular simulations and provides the quantitative basis for choosing the appropriate coarse-graining level.[10]

The widely used structure-based coarse graining matches the interchain segment radial distribution functions between original and CG systems. As expected, it cannot give the thermodynamic consistency between original and CG systems due to the information loss

of coarse graining.[10] In this work, we apply our systematic and simulation-free strategy to the recently proposed relative-entropy-based coarse graining,[17,21,22] which minimizes the information loss quantified by the relative entropy. As shown by Shell, relative-entropy-based coarse graining provides a general framework and can be reduced, under further constraints, to the various coarse-graining methods previously proposed.[22] For example, when *pair* potentials are used between CG segments (which is the common practice in molecular simulations), relative-entropy-based coarse graining becomes equivalent to structure-based coarse graining if the functional form of CG potentials is unconstrained (i.e., contains an infinite number of parameters).[22] It can therefore be used to parameterize CG potentials with a given analytic functional form containing finite number of parameters, which is much more convenient to use in molecular simulations than the numerically obtained CG potentials from structure-based coarse graining. The values of relative entropy obtained from relative-entropy-based coarse graining with different CG potential functional forms can further be compared to determine the appropriate functional form or number of parameters.

To the best of our knowledge, relative-entropy-based coarse graining has not been applied to polymeric systems. In this work, we first describe our systematic and simulation-free strategy of relative-entropy-based coarse graining for homopolymer melts using the polymer reference interaction site model (PRISM) theory,[19] then present our numerical results with the hard-core Gaussian thread model[23] (referred to as the "CGC-δ" model below) solved by PRISM theory with the Percus-Yevick closure[24] as the original system, which was also used in Chapter 4. We compare the performance of various closures and CG potential functional forms for relative-entropy-based coarse graining, as well as the structural and thermodynamic properties of the original and CG systems at various coarse-graining levels. Our results obtained from relative-entropy-based coarse graining are also compared with those from structure-based coarse graining presented in Chapter 4.

5.2 Models and Methods

5.2.1 A general coarse-graining strategy using the relative-entropy framework

We consider an original system of homopolymer melts, which consists of n chains each of N_m monomers at a chain number density $\rho_c \equiv n/V$ with V being the system volume. The invariant degree of polymerization $\bar{\mathcal{N}} \equiv (\rho_c R_{e,0}^3)^2$ controls the system fluctuations with $R_{e,0}$ being the root-mean-square end-to-end distance of an ideal chain.

For coarse-graining purpose, similar to Chapter 4 we divide each original polymer chain into N subchains (segments) each containing l consecutive monomers, such that $Nl = N_m$. Let $\mathbf{r}_{k,t}$ be the spatial position of the t^{th} monomer on the k^{th} chain in the original system, and $\mathbf{R}_{k,s} = \sum_{t=(s-1)l+1}^{sl} \mathbf{r}_{k,t}/l$ the spatial position of the s^{th} segment (which corresponds to the center-of-mass of its monomers) on the k^{th} chain in the coarse-grained (CG) system; this defines the mapping operator $\mathbf{M}$ that gives $\mathbf{R} = \mathbf{M}(\mathbf{r})$, where $\mathbf{r}$ and $\mathbf{R}$ hereafter denote a configuration of original system and the corresponding configuration of CG system, respectively. Furthermore, let $Z_m = \int \mathrm{d}\mathbf{r} \exp(-\beta H_m^{\text{b}} - \beta H_m^{\text{nb}})$ be the canonical-ensemble configuration integral of the original system, where H_m^{b} and H_m^{nb} are its Hamiltonian due to chain connectivity and non-bonded interactions, respectively, and $\beta \equiv 1/k_B T$ with k_B being the Boltzmann constant and T the thermodynamic temperature. Similarly, we have the canonical-ensemble configuration integral of the corresponding CG system, $Z = \int \mathrm{d}\mathbf{R} \exp(-\beta H^{\text{b}} - \beta H^{\text{nb}})$, where H^{b} and H^{nb} are its Hamiltonian due to chain connectivity and non-bonded interactions, respectively.

Coarse graining using the relative-entropy (RE) framework[17] minimizes the relative entropy defined as[25]

$$S \equiv \int \mathrm{d}\mathbf{r} \mathcal{P}_m(\mathbf{r}) \ln \frac{\mathcal{P}_m(\mathbf{r})}{\mathcal{P}(\mathbf{M}(\mathbf{r}))}, \tag{5.1}$$

where the configurational probabilities $\mathcal{P}_m(\mathbf{r}) \equiv \exp(-\beta H_m^{\text{b}} - \beta H_m^{\text{nb}})/Z_m$ and $\mathcal{P}(\mathbf{M}(\mathbf{r})) \equiv \exp(-\beta H^{\text{b}} - \beta H^{\text{nb}})/Z$ are for the original and CG systems, respectively. Here we split S

into the bonding contribution $S^{\rm b}$ and the non-bonded contribution $S^{\rm nb}$, given by

$$S^{\rm b} \equiv \ln Z^{id} - \ln Z_m^{id} - \beta \left(\left\langle H_m^{\rm b} \right\rangle_m - \left\langle H^{\rm b} \right\rangle_m \right), \tag{5.2}$$

$$S^{\rm nb} \equiv \beta \left(n\Delta f_{c,m} - \left\langle H_m^{\rm nb} \right\rangle_m \right) - \beta \left(n\Delta f_c[v] - \left\langle H^{\rm nb}[v] \right\rangle_m \right), \tag{5.3}$$

respectively, where the superscript "*id*" denotes ideal chains (i.e., without non-bonded interactions), $\Delta f_{c,m}$ and Δf_c are the differences in the Helmholtz free energy per chain, $f_c \equiv -\ln Z/n\beta$, from ideal chains for the original and CG systems, respectively, and $\langle\rangle_m$ denotes the ensemble average of the original system, for example, $\left\langle H^{\rm nb} \right\rangle_m \equiv \int {\rm d}\mathbf{r} \mathcal{P}_m(\mathbf{r}) H^{\rm nb}(\mathbf{M}(\mathbf{r}))$. As noted in Eqs. (5.2) and (5.3), only $n\Delta f_c - \left\langle H^{\rm nb} \right\rangle_m$ in $S^{\rm nb}$ depends on the CG pair potential $v(r)$, which is solved by minimizing $S^{\rm nb}$ (thus S). With $v(r)$ parameterized as $v(r;\boldsymbol{\lambda})$, where $\boldsymbol{\lambda} = \{\lambda_i\}$ $(i = 1, ..., n_p)$ denotes the parameters to be solved and n_p the total number of parameters, minimizing $S^{\rm nb}$ is then equivalent to solving $\partial \left\langle H^{\rm nb} \right\rangle_m / \partial\lambda_i = \partial(n\Delta f_c)/\partial\lambda_i$ (hereafter, the operator $\partial/\partial\lambda_i$ denotes the partial derivative with respect to λ_i while keeping all $\lambda_{j\neq i}$ constant), which leads to[17]

$$\left\langle \frac{\partial(\beta H^{\rm nb})}{\partial\lambda_i} \right\rangle_m = -\frac{\partial}{\partial\lambda_i} \ln \frac{\int {\rm d}\mathbf{R} \exp(-\beta H^{\rm b} - \beta H^{\rm nb})}{\int {\rm d}\mathbf{R} \exp(-\beta H^{\rm b})} = \left\langle \frac{\partial(\beta H^{\rm nb})}{\partial\lambda_i} \right\rangle_{\rm CG} \tag{5.4}$$

for $i = 1, ..., n_p$, where $\langle\rangle_{\rm CG}$ denotes the ensemble average of CG system.

For the original system at given $\bar{\mathcal{N}}$, let $g^{ss}(r)$ be the interchain radial distribution function and $\omega^{ss}(r)$ the normalized intrachain pair correlation function (i.e., $4\pi \int_0^\infty {\rm d}r r^2 \omega^{ss}(r) = 1$) at given N, both for segments in the space of $\mathbf{M}(\mathbf{r})$.[10] We then have

$$\left\langle \frac{\partial(\beta H^{\rm nb})}{\partial\lambda_i} \right\rangle_m = 2\pi n N^2 \int_0^\infty {\rm d}r \frac{r^2}{R_{e,0}^3} \left[R_{e,0}^3 \omega^{ss}(r) + \sqrt{\bar{\mathcal{N}}} g^{ss}(r) \right] \frac{\partial\beta v(r;\boldsymbol{\lambda})}{\partial\lambda_i} - \frac{nN}{2} \frac{\partial\beta v(0;\boldsymbol{\lambda})}{\partial\lambda_i}, \tag{5.5}$$

where the last term is used to deduct the self-interaction of segments. Similarly, we have

$$\left\langle \frac{\partial(\beta H^{\rm nb})}{\partial\lambda_i} \right\rangle_{\rm CG} = 2\pi n N^2 \int_0^\infty {\rm d}r \frac{r^2}{R_{e,0}^3} \left[R_{e,0}^3 \omega(r) + \sqrt{\bar{\mathcal{N}}} g(r;\boldsymbol{\lambda}) \right] \frac{\partial\beta v(r;\boldsymbol{\lambda})}{\partial\lambda_i} - \frac{nN}{2} \frac{\partial\beta v(0;\boldsymbol{\lambda})}{\partial\lambda_i}, \tag{5.6}$$

where $g(r)$ is the interchain segment radial distribution function and $\omega(r)$ the normalized intrachain segment pair correlation function for the CG system at given N; note that $g(r)$

depends on $\beta v(r)$ (thus $\boldsymbol{\lambda}$) while $g^{ss}(r)$ does not. Under the assumption of $\omega(r) = \omega^{ss}(r)$, Eq. (5.4) finally becomes

$$\int_0^\infty \mathrm{d}r \frac{r^2}{R_{e,0}^3} \Big[g^{ss}(r) - g(r;\boldsymbol{\lambda}) \Big] \frac{\partial \beta v(r;\boldsymbol{\lambda})}{\partial \lambda_i} = 0 \tag{5.7}$$

for $i = 1, ..., n_p$, from which we solve for $\boldsymbol{\lambda}$. To better understand the above equation given by RE minimization, in Sec. 5.2.5 we show its relation with the least-squares fitting of $\beta v(r)$ to the CG potential $\beta v^{\mathrm{st}}(r)$ obtained from our structure-based coarse graining reported in Chapter 4.

5.2.2 Coarse graining of hard-core CGC-δ model using PRISM theory

To demonstrate our general coarse-graining strategy described above, as in Chapter 4 we take the hard-core CGC-δ model[23] as the original system, which consists of continuous Gaussian chains each of $N_m \to \infty$ monomers interacting with the non-bonded pair potential $\beta u_m(r) = (\bar{\kappa}/\rho_c N_m^2)\delta(r)$ with $\bar{\kappa} \to \infty$. This simple model system is solved using PRISM theory with the Percus-Yevick (PY) closure[24] and ideal-chain conformations, which then results in $\omega^{ss}(r)$ and $g^{ss}(r)$ for given N according to Eqs. (4.32) and (4.19), respectively, in Chapter 4, as well as its structural and thermodynamic properties; for more details, we refer readers to Chapter 4.

For the CG system at given N, PRISM theory gives

$$\hat{h} = N^2 \hat{\omega} \hat{c} (\hat{\omega} + \rho_c \hat{h}), \tag{5.8}$$

where $h(r) \equiv g(r) - 1$ and $c(r)$ are the interchain total and direct pair correlation functions (PCFs) between CG segments, respectively, and we use the short-hand notation $\hat{f} = (4\pi/q) \int_0^\infty \mathrm{d}r f(r) r \sin(qr)$ to denote the 3D Fourier transform of $f(r)$ with q being the wavevector length. Setting $\omega(r) = \omega^{ss}(r)$, we numerically solve Eq. (5.8) for given $\beta v(r;\boldsymbol{\lambda})$ with various closures, written in general as

$$c(r) = \exp[-\beta v(r) + \gamma(r) + B(r)] - [\gamma(r) + 1], \tag{5.9}$$

where $\gamma(r) \equiv h(r) - c(r)$ is the interchain indirect PCF and $B(r)$ the bridge function. In particular, we use three common closures in this work: $B(r) = 0$ for the hypernetted-chain (HNC) closure,[26] $\ln[\gamma(r)+1] - \gamma(r)$ for PY closure,[24] and $\ln[h(r)+1] - h(r)$ for the random-phase approximation (RPA) closure;[27] for the relation among these closures, we refer readers to Chapter 4.

Note that RPA closure can be written as $c(r) = -\beta v(r)$, which directly leads to $c(r)$ for given $\beta v(r; \boldsymbol{\lambda})$. On the other hand, to solve Eq. (5.8) with HNC and PY closures, we first re-write it as

$$\hat{\gamma} = \hat{\omega}^2 \hat{c} / (N^{-2} - \rho_c \hat{\omega} \hat{c}) - \hat{c}, \tag{5.10}$$

from which we obtain $\hat{\gamma}$ (and thus $\gamma(r)$) for given $c(r)$. We then obtain the new direct PCF from Eq. (5.9), and use the Anderson mixing method[28,29] to converge $c(r)$ till the maximum absolute residual error of Eq. (5.9) at all r is less than 10^{-14}. Note that $c(r)$ approaches 0 when r is on the order of the interaction range of βv, while $h(r)$ (and $\gamma(r)$) approaches 0 when r is on the order of $R_{e,0}$. We therefore use a cut-off length $r_c = 30R_{e,0}$ for $h(r)$ with $[0, r_c]$ uniformly discretized into 3×10^4 subintervals, and a cut-off length of $r_c/\sqrt{N}$ for $c(r)$; our cut-off and discretization give negligible numerical errors. We also use FFTW[30] to perform the Fourier transforms of PCFs with the above cut-off and discretization, where r_c determines the discretization of q-space and the subinterval size determines the cut-off in q-space.

Finally, we use the Newton's method combined with a globally convergent strategy[31] to solve for $\boldsymbol{\lambda}$ from Eq. (5.7) till the maximum absolute value of its left-hand-side is smaller than 10^{-12}, where the Romberg integration[31] is used to evaluate the integral with the cut-off r_c. We then calculate the minimized relative entropy, as well as the structural and thermodynamic properties of the CG system at given N (see Sec. 5.2.4 below).

5.2.3 Parameterization of CG pair potential

To reduce n_p, we take the functional form of $v(r)$ as suggested by the effective pair potential between CG segments $v^{\rm st}(r)$ obtained from our structure-based (st-based) coarse graining reported in Chapter 4. As shown there, $\beta v^{\rm st}(r)$ can be approximated by a Gaussian function at small r (where $\beta v^{\rm st}(r) > 0$). Our first way of parameterizing $\beta v(r)$ is therefore to represent it as a summation of $n_{\rm G}$ Gaussian functions, i.e.,

$$\beta v_{{\rm I},n_{\rm G}}(r;\boldsymbol{\lambda}) = \sum_{i=1}^{n_{\rm G}} A_i \exp\left(-B_i \tilde{r}^2\right) \tag{5.11}$$

with $n_p = 2n_{\rm G}$ parameters $A_i > 0$ and $B_i > 0$ ($i = 1, ..., n_{\rm G}$), where $\tilde{r} \equiv N^{3/4} r/R_{e,0}$ is used to take into account the $N^{-3/4}$ scaling of the CG potential range found in Refs. [7, 10].

On the other hand, $\beta v_{{\rm I},n_{\rm G}}(r;\boldsymbol{\lambda})$ cannot capture the attractive well of $\beta v^{\rm st}(r) < 0$ at large $\tilde{r}$, which has significant effects on both structural and thermodynamic properties of CG systems, especially at small N, as shown in Sec. 5.3.3. We therefore propose another way of parameterizing $\beta v(r)$ as

$$\beta v_{\rm II}(r;\boldsymbol{\lambda}) = A \exp\left(-B\tilde{r}^2\right) W(\tilde{r}) + C \frac{\sin(D\tilde{r})}{D\tilde{r}} \exp(-E\tilde{r}) \left[1 - W(\tilde{r})\right], \tag{5.12}$$

where the weighting function $W(\tilde{r}) = \exp(-F\tilde{r}^2)$ is used to combine the two terms on the right-hand-side of Eq. (5.12) dominating at small and large $\tilde{r}$, respectively. This leads to $n_p = 6$ parameters: A, B, C, D, E, and F, all of which are positive.

5.2.4 Calculation of structural and thermodynamic properties of CG systems and the minimized relative entropy using PRISM theory

Once the optimized pair potential $\beta v(r)$ is obtained for the CG system at given N, its normalized isothermal compressibility[10] is given by $\kappa_T = 1 + \sqrt{\bar{\mathcal{N}}}\hat{h}(0)/R_{e,0}^3$, where $\hat{h}(0)$ is solved from Eq. (5.8) with a closure, and its interchain internal energy per chain and (virial) pressure are calculated as

$$\beta u_c = 2\pi N^2 \sqrt{\bar{\mathcal{N}}} \int_0^\infty {\rm d}r \frac{r^2}{R_{e,0}^3} g(r) \beta v(r), \tag{5.13}$$

$$\beta R_{e,0}^3 P = -\frac{2\pi N^2 \bar{\mathcal{N}}}{3} \int_0^\infty {\rm d}r \frac{r^2}{R_{e,0}^3} g(r) \frac{{\rm d}\beta v(r)}{{\rm d}\ln r}, \tag{5.14}$$

where the integrals are numerically evaluated using Romberg integration[31] with the aforementioned cut-off and discretization.

The minimized relative entropy per chain $s_c \equiv \left\langle \beta H^{\rm nb} \right\rangle_m / n - \beta \Delta f_c$ provides a quantitative measure of the overall quality of coarse graining,[22] with which various closures for CG systems and various ways of parameterizing $\beta v(r)$ can be compared. Note that the intrachain contribution to s_c vanishes because we assume ideal-chain conformations, which are independent of $\beta v(r)$. We therefore show here how to calculate its interchain contribution (denoted by the superscript "inter") $s_c = \left\langle \beta H^{\rm inter} \right\rangle_m / n - \beta \Delta f_c^{\rm inter}$. $\left\langle \beta H^{\rm inter} \right\rangle_m / n$ can be calculated as

$$\frac{\left\langle \beta H^{\rm inter} \right\rangle_m}{n} = 2\pi N^2 \sqrt{\bar{\mathcal{N}}} \int_0^\infty {\rm d}r \frac{r^2}{R_{e,0}^3} g^{ss}(r) \beta v(r). \tag{5.15}$$

Defining $\epsilon^* \equiv \beta v(r=0)$ and $\beta v_0(r) \equiv \beta v(r)/\epsilon^*$, we can calculate $\beta \Delta f_c^{\rm inter}$ using the thermodynamic integration,

$$\beta \Delta f_c^{\rm inter} = 2\pi N^2 \sqrt{\bar{\mathcal{N}}} \int_0^{\epsilon^*} {\rm d}\epsilon \int_0^\infty {\rm d}r \frac{r^2}{R_{e,0}^3} g(r;\epsilon) \beta v_0(r), \tag{5.16}$$

where $g(r;\epsilon)$ is the interchain segment radial distribution function of the CG system with non-bonded pair potential $\epsilon v_0(r)$ and is obtained from PRISM theory with a closure. We use Romberg integration[31] to evaluate the integrals, where the cut-off r_c is used for the integration over r, and uniformly discretize $[0, \epsilon^*]$ into enough subintervals so that the accuracy of s_c is about in the order of 10^{-7} (at $N = 1$) to 10^{-5} (at $N = 100$). Finally, we note that Eqs. (5.15) and (5.16) can also be used to calculate s_c for our st-based coarse graining reported in Chapter 4.

5.2.5 Relation between RE minimization and least-squares fitting

Here we elucidate the relation between minimization of the relative entropy and the least-square fitting of $\beta v(r)$ to the CG potential $\beta v^{\rm st}(r)$ obtained from st-based coarse graining.

At given N, we define $\chi_v^2 \equiv 4\pi \int {\rm d}r r^2 \beta^2 [v^{\rm st}(r) - v(r;\boldsymbol{\lambda})]^2$, where the functional form of $\beta v(r;\boldsymbol{\lambda})$ is given with $\boldsymbol{\lambda} \equiv \{\lambda_i\}$ $(i = 1, \cdots, n_p)$ to be obtained by minimizing χ_v^2 with respect

to λ_i. This minimization is equivalent to solving $\partial\chi_v^2/\partial\lambda_i = 0$, i.e.,

$$\int \mathrm{d}qq^2[\hat{v}^{\mathrm{st}}(q) - \hat{v}(q;\boldsymbol{\lambda})]\hat{v}_i'(q;\boldsymbol{\lambda}) = 0, \tag{5.17}$$

where $v_i'(r;\boldsymbol{\lambda}) \equiv \partial v(r;\boldsymbol{\lambda})/\partial\lambda_i$ and $\hat{v}_i'(q;\boldsymbol{\lambda})$ represents its Fourier transform. On the other hand, minimizing the relative entropy (i.e., Eq. (5.7)) is equivalent to

$$\int \mathrm{d}qq^2[\hat{h}^{ss}(q) - \hat{h}(q;\boldsymbol{\lambda})]\hat{v}_i'(q;\boldsymbol{\lambda}) = 0. \tag{5.18}$$

where $\hat{h}^{ss}(q;\boldsymbol{\lambda})$ is obtained from st-based coarse graining and $\hat{h}(q;\boldsymbol{\lambda})$ from solving the CG system at $\boldsymbol{\lambda}$ using PRISM theory with a closure.

From PRISM equation (i.e., Eq. (5.8)), we have $\hat{h} = N^2\hat{\omega}^2\hat{c}/(1-\rho_c N^2\hat{\omega}\hat{c})$, which still holds by replacing $\hat{h}$ and $\hat{c}$ by $\hat{h}^{ss}$ and $\hat{c}^{ss}$, with $\hat{\omega} = \hat{\omega}^{ss}$. Eq. (5.18) then becomes

$$\int \mathrm{d}qq^2[\hat{c}^{ss}(q) - \hat{c}(q;\boldsymbol{\lambda})]S^{\mathrm{st}}(q)S(q;\boldsymbol{\lambda})\hat{v}_i'(q;\boldsymbol{\lambda}) = 0. \tag{5.19}$$

where $S^{\mathrm{st}} \equiv (1/\hat{\omega} - \rho_c N^2\hat{c}^{ss})^{-1}$ and $S \equiv (1/\hat{\omega} - \rho_c N^2\hat{c})^{-1}$ are the structure factor of CG systems obtained from st- and RE-based coarse graining, respectively.

If RPA closure is used for CG systems, i.e., $c^{ss}(r) = -\beta v^{\mathrm{st}}(r)$ and $c(r) = -\beta v(r;\boldsymbol{\lambda})$, Eq. (5.19) becomes

$$\int \mathrm{d}qq^2[\hat{v}^{\mathrm{st}}(q) - \hat{v}(q;\boldsymbol{\lambda})]S^{\mathrm{st}}(q)S(q;\boldsymbol{\lambda})\hat{v}_i'(q;\boldsymbol{\lambda}) = 0. \tag{5.20}$$

Comparing Eq. (5.20) to Eq. (5.17), we see that, RE minimization with RPA closure for CG systems is equivalent to a weighted (by $S^{\mathrm{st}}(q)S(q;\boldsymbol{\lambda})$) least-square fitting of $\beta v(r)$ to $\beta v^{\mathrm{st}}(r)$.

With HNC closure, i.e., $c^{ss}(r) = -\beta v^{\mathrm{st}}(r) + h^{ss}(r) - \ln[1+h^{ss}(r)] = -\beta v^{\mathrm{st}}(r) + \Delta h^{ss}(r)$ and $c(r) = -\beta v(r;\boldsymbol{\lambda}) + h(r;\boldsymbol{\lambda}) - \ln[1+h(r;\boldsymbol{\lambda})] = -\beta v(r;\boldsymbol{\lambda}) + \Delta h(r;\boldsymbol{\lambda})$, where $\Delta h^{ss}(r) \equiv h^{ss}(r) - \ln[1+h^{ss}(r)] \sim O((h^{ss})^2)$ and $\Delta h(r;\boldsymbol{\lambda}) \equiv h(r;\boldsymbol{\lambda}) - \ln[1+h(r;\boldsymbol{\lambda})] \sim O(h^2)$. Eq. (5.19) becomes

$$\int \mathrm{d}qq^2 \left\{\beta\left[\hat{v}^{\mathrm{st}}(q) - \hat{v}(q;\boldsymbol{\lambda})\right] - \left[\widehat{\Delta h}^{ss}(q) - \widehat{\Delta h}(q;\boldsymbol{\lambda})\right]\right\} S^{\mathrm{st}}(q)S(q;\boldsymbol{\lambda})\hat{v}_i'(q;\boldsymbol{\lambda}) = 0. \tag{5.21}$$

which can be compared to Eq. (5.17).

5.3 Results and Discussions

In this paper, we set $\bar{\mathcal{N}} = 10^4$; other values of $\bar{\mathcal{N}}$ do not qualitatively change our results. In the following, for different closures, coarse-graining strategies and CG potential parameterizations, we first analyze the behaviors of CG potential, then compare the relative entropy per chain and the structural and thermodynamic properties with the original systems.

5.3.1 CG potential

Fig. 5.1(a) compares CG potentials between st- and RE-based coarse graining obtained with HNC closure, where different N and parameterization of $\beta v(r)$ are used. We see that $\beta v_{\mathrm{I},2}(r)$ is overall smaller than $\beta v^{\mathrm{st}}(r)$, especially at small N; note that $\beta v_{\mathrm{I},1}(r)$ is even much smaller than $\beta v_{\mathrm{I},2}(r)$ (data not shown). We attribute this mainly to the absence of the attractive well in $\beta v_{\mathrm{I}}(r)$. As N increases, $\beta v_{\mathrm{I}}(r)$ approaches $\beta v^{\mathrm{st}}(r)$ because the attractive well of $\beta v^{\mathrm{st}}(r)$ becomes relatively (compared to $\beta v^{\mathrm{st}}(r=0)$) small as shown in Fig. 5.1.

$\beta v_{\mathrm{II}}(r)$, on the other hand, is much closer to $\beta v^{\mathrm{st}}(r)$ than $\beta v_{\mathrm{I}}(r)$. As shown in Fig. 5.1(a), $\beta v_{\mathrm{II}}(r)$ and $\beta v^{\mathrm{st}}(r)$ are almost indistinguishable at small N; as N increases, $\beta v_{\mathrm{II}}(r)$ slightly deviates from $\beta v^{\mathrm{st}}(r)$ at small $\tilde{r}$. Note that $\beta v_{\mathrm{II}}(r)$ can quantitatively capture the attractive well of $\beta v^{\mathrm{st}}(r)$ as shown in the inset of Fig. 5.1(a), although the attractive well of $\beta v_{\mathrm{II}}(r)$ is

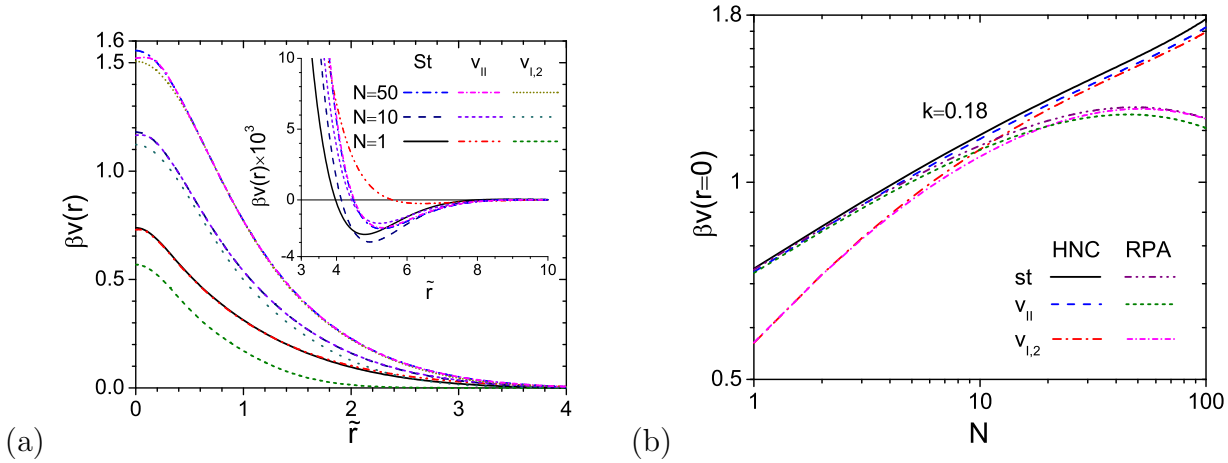

Figure 5.1: Comparison of (a) CG potential at different N and (b) its value at $r = 0$ as a function of N among st- and RE-based coarse graining

shallower than that of $\beta v^{\rm st}(r)$. Similar results are found for RPA and PY closures for CG systems (data not shown).

Fig. 5.1(b) shows $\beta v(r=0)$ as a function of N for st- and RE-based coarse graining obtained with HNC and RPA closures. In all cases, we see that the corresponding HNC and RPA results are close at small N but deviate at large N. In particular, while all HNC results monotonically increase with increasing N as expected, all RPA results exhibit a maximum around $N = 40$, indicating the qualitative failure of RPA closure for CG systems at larger N. The results of st-based coarse graining were discussed in detail in Chapter 4, so we focus here on the difference between the two coarse-graining methods.

For both closures, we see that $\beta v^{\rm st}(r=0)$ is the largest and that $\beta v_{\rm II}(r=0)$ only slightly smaller than $\beta v^{\rm st}(r=0)$ with $\beta v^{\rm st}(r=0) - \beta v_{\rm II}(r=0)$ monotonically increasing with increasing N. In particular, both of them obtained from HNC closure scales approximately with $N^{0.18}$. $\beta v_{\rm I,2}(r=0)$, however, is significantly different from (smaller than) $\beta v^{\rm st}(r=0)$ at small $N \lesssim 10$; as N increases, $\beta v^{\rm st}(r=0) - \beta v_{\rm I,2}(r=0)$ monotonically decreases for RPA closure but exhibits a minimum at $N = 27$ for HNC closure. While $\beta v_{\rm II}(r=0)$ is always larger (i.e., closer to $\beta v^{\rm st}(r=0)$) than $\beta v_{\rm I,2}(r=0)$ for HNC closure, they cross around $N = 20$ for RPA closure. We therefore conclude that $\beta v_{\rm II}(r)$ is a better parameterization for $\beta v^{\rm st}(r)$, which has a non-trivial attractive well, and that the absence of this attractive well in $\beta v_{\rm I}$ deceases $\beta v(r=0)$ (and $\beta v(r)$ at small $\tilde{r}$) even at $N = 100$.

As shown in Chapter 4, $\tilde{v}^{\rm st}(r) \equiv v^{\rm st}(r)/v^{\rm st}(r=0)$ for various N collapse approximately onto the same curve, if r is normalized by $R_{e,0}/N^{-k}$ with $k \approx -0.73$ at $\bar{\mathcal{N}} = 10^4$; note that k approaches $-3/4$ as $\bar{\mathcal{N}} \to \infty$.[7,10] Fig. 5.2(a) shows that the RE-based CG potential $\tilde{v}_{\rm II}(r)$ also exhibits the same behavior, where $k = -3/4$ is used. The inset of Fig. 5.2(a) shows that the attractive well is approximately located around $\tilde{r} \approx 5$.

Since $\tilde{v}_{\rm II}(r)$ approximately collapses for various N, we expect a rather weak N-dependence of all parameters in the functional form of $\beta v_{\rm II}(r)$; this is examined in Fig. 5.2(b). Writing $\tilde{v}_{\rm II}(r) = \exp[-(B+F)\tilde{r}^2] + (C/A)[\sin(D\tilde{r})/D\tilde{r}]\exp(-E\tilde{r})[1-\exp(-F\tilde{r}^2)]$, we see that the

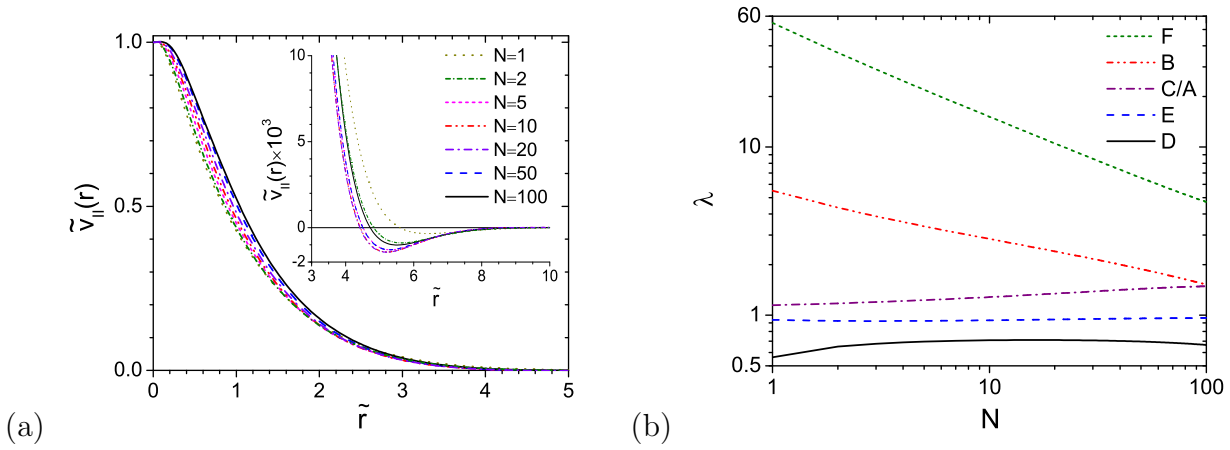

Figure 5.2: (a) Normalized CG potential $\tilde{v}_{\rm II}(r)$ as a function of $\tilde{r}$ and (b) the corresponding parameters from RE-based coarse graining using HNC closure for CG systems.

parameters C/A, E and D are indeed weakly dependent on N, but B and F are not. Note that the large value of $B+F$ makes the first term of $\tilde{v}_{\rm II}(r)$ decay very fast with $\tilde{r}$; in other words, this term only affects $\tilde{v}_{\rm II}(r)$ at small $\tilde{r}$. Similarly, the term $1-\exp(-F\tilde{r}^2)$ is approximately 1 at large $\tilde{r}$ because of the large value of F. This explains why $\tilde{v}_{\rm II}(r)$ is more collapsed at large $\tilde{r}$ than at small $\tilde{r}$ as shown in Fig. 5.2(a). The large value of $B+F$ makes the first term of $\tilde{v}_{\rm II}(r)$ negligible at large $\tilde{r}$, so that π/D approximately gives the first root $\tilde{r}_1$, at which $\tilde{v}_{\rm II}(r)=0$; our numerical results gives the average value (over $3\le N\le 100$) of $D\approx 0.69$ and thus $\tilde{r}_1\approx 4.53$, which is consistent with the inset of Fig. 5.2(a).

5.3.2 Relative entropy

Fig. 5.3(a) compares the relative entropy per chain $s_c^{\rm st}$ for st-based coarse graining with various closures for CG systems. Note that, in the calculation of s_c, we do not consider the contributions from the mapping entropy defined in Ref. [22] and the first term on the right-hand-side of Eq. (5.3), both of which are independent of CG potential; in addition, the former stems from the degeneracy of different original configurations that map to the same CG configuration and should decrease with increasing N, and the latter does not depends on N and actually diverges (its absence therefore leads to negative s_c) due to the divergence of $\Delta f_{c,m}$.[32] We see that $s_c^{\rm st}$ decreases with increasing N for all closures, which is also the case

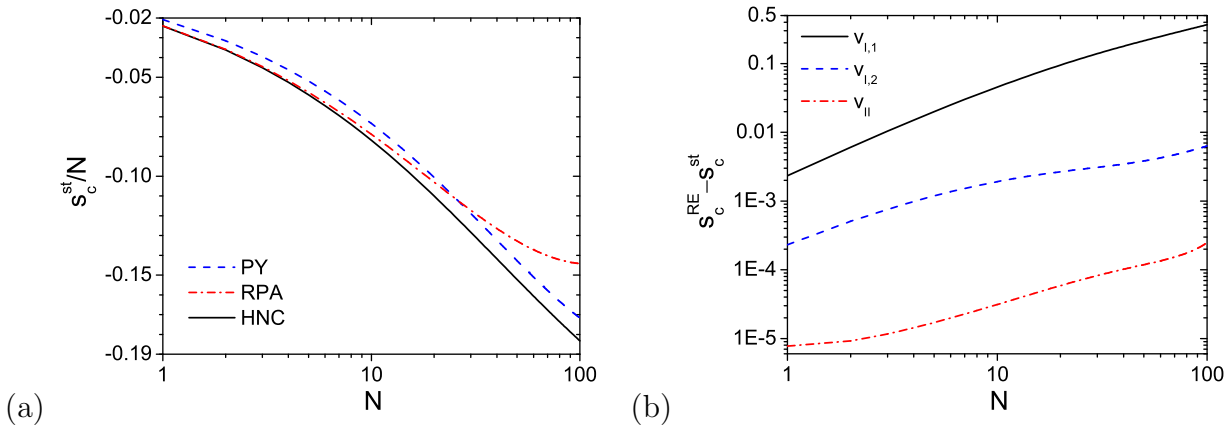

Figure 5.3: (a) Relative entropy per chain s_c of st-based coarse graining obtained from different closures; (b) Comparison of s_c between st- and RE-based coarse graining among different closures and potential parameterizations.

when the above two contributions are included; in other words, the information loss due to coarse graining decreases with increasing N, which is well expected.

We also find that $s_c^{\rm st}$ obtained from HNC and RPA closures, denoted by $s_{c,\rm HNC}^{\rm st}$ and $s_{c,\rm RPA}^{\rm st}$, respectively, are nearly indistinguishable at small N. Furthermore, $s_{c,\rm HNC}^{\rm st}$ is always smaller than both $s_{c,\rm RPA}^{\rm st}$ and $s_{c,\rm PY}^{\rm st}$, while $s_{c,\rm RPA}^{\rm st} < s_{c,\rm PY}^{\rm st}$ for $N \leq 26$ and the opposite occurs for larger N. Compared to Fig. 4.7 in Chapter 4, we see that the information loss due to coarse graining quantified by $s_c^{\rm st}$ is qualitatively consistent with the deviation in thermodynamic properties between original and CG systems; that is, for both the interchain internal energy per chain and (virial) pressure of CG systems, HNC results are always closer to the original system (better) than RPA and PY results, and RPA results are better than PY results for small N and the opposite occurs for large N. Note that, because RPA closure for CG systems qualitatively fails for large $N \gtrsim 40$ as shown in Chapter 4 and in Fig. 5.1(b), in the following we mainly focus on HNC closure unless specified otherwise.

Fig. 5.3(b) compares s_c between st- and RE-based coarse graining with various CG potential parameterization for the latter, both using HNC closure for CG systems. We see that the difference in s_c between these two coarse-graining methods $s_c^{\rm RE} - s_c^{\rm st} > 0$ in all cases; in other words, st-based coarse graining gives less information loss than RE-based coarse

graining at the same N. This is expected according to Ref. [22], where it was shown that st-based coarse graining is equivalent to RE-based coarse graining with an infinite number of parameters in $\beta v(r)$. We also find in Fig. 5.3(b) that s_c^{RE} decreases with increasing N, by noting the variation of s_c^{st} (from 0 to -20 as shown in Fig. 5.3(a)) and $s_c^{\mathrm{RE}} - s_c^{\mathrm{st}}$ (from 0 to 0.5) for $1 \leq N \leq 100$.

Our st-based coarse-graining results reported in Chapter 4 suggest that CG potential can be approximated by a Gaussian function. Fig. 5.3(b) shows that using two Gaussian functions (i.e., $\beta v_{\mathrm{I},2}(r)$) gives much less information loss than using just one (i.e., $\beta v_{\mathrm{I},1}(r)$). Furthermore, our results in Chapter 4 show that $\beta v^{\mathrm{st}}(r)$ exhibits an attractive well (i.e., $\beta v^{\mathrm{st}}(r) < 0$) at large $\tilde{r} \approx 5$, which has significant effects on both structural and thermodynamic properties of CG systems, and Fig. 5.3(b) shows that capturing this attractive well with the second term in Eq. (5.12) (i.e., $\beta v_{\mathrm{II}}(r)$) gives even better coarse-graining performance. Finally, Fig. 5.3(b) shows that $s_c^{\mathrm{RE}} - s_c^{\mathrm{st}}$ increases with increasing N, indicating that all three ways parameterizing CG pair potentials work better for smaller N. In particular, $\beta v_{\mathrm{II}}(r)$ gives the smallest $s_c^{\mathrm{RE}} - s_c^{\mathrm{st}} < 3 \times 10^{-4}$ for HNC closure and is good enough to analytically represent CG potential in the N-range considered in this paper.

5.3.3 Comparison of structural and thermodynamic properties

In this section we compare the normalized isothermal compressibility κ_T and interchain virial pressure $\beta R_{e,0}^3 P$ between st- and RE-based coarse graining with HNC closure for CG systems. Note that the st-based results κ_T^{st} is the same as the original system and independent of N, and that we refer readers to Chapter 4 for the calculation of thermodynamic properties of CG systems in st-based coarse graining.

As aforementioned, RE-based coarse graining using $\beta v_{\mathrm{I},1}(r)$ gives poor performance. This is also shown in Fig. 5.4(a), where we see that κ_T obtained from RE-based coarse graining using $\beta v_{\mathrm{I},1}(r)$ is significantly larger than κ_T^{st}. Using $\beta v_{\mathrm{I},2}(r)$ in RE-based coarse graining, the results are closer to κ_T^{st}, but still overestimate it at small $N \lesssim 10$. The poor performance of

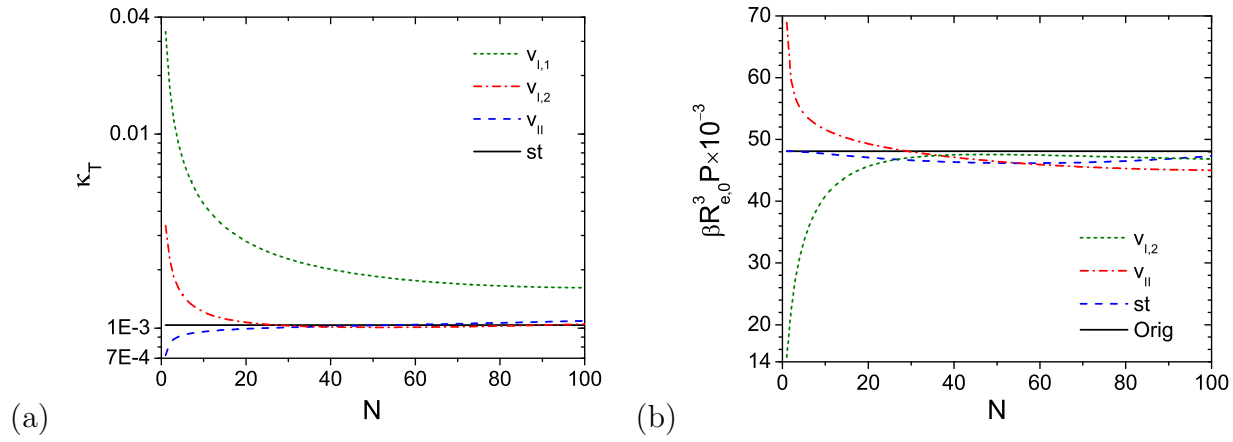

Figure 5.4: Comparison of (a) the normalized isothermal compressibility and (b) interchain virial pressure between st- and RE-based coarse graining.

$\beta v_{\rm I}(r)$ is again due to the absence of the attractive well in its functional form. Using $\beta v_{\rm II}(r)$ in RE-based coarse graining gives better results than using $\beta v_{\rm I}(r)$, although $\kappa_T^{\rm st}$ is somewhat underestimated at small $N \lesssim 10$.

Fig. 5.4(b) shows that using $\beta v_{\rm I,2}(r)$ in RE-based coarse graining always underestimates the pressure of the original system, P_m, particularly at small $N \lesssim 20$, again due to the absence of the attractive well. Note, however, that the results for $27 \leq N \leq 91$ obtained from RE-based coarse graining using $\beta v_{\rm I,2}(r)$ are closer to P_m than the corresponding st-based results. Using $\beta v_{\rm II}(r)$ in RE-based coarse graining, on the other hand, gives much better results than using $\beta v_{\rm I,2}(r)$ at small N. Unlike $\beta v_{\rm I,2}(r)$, $\beta v_{\rm II}(r)$ overestimates P_m for small $N \lesssim 30$. Fig. 5.4(b) also shows that using $\beta v_{\rm I,2}(r)$ in RE-based coarse graining gives closer prediction of $\beta R_{e,0}^3 P$ to the original system than using $\beta v_{\rm II}(r)$ for $N \gtrsim 36$, although the latter is closer to $\beta v^{\rm st}(r)$ and gives much smaller $s_c^{\rm RE}$. Finally, we note that the behavior of internal energy is similar to pressure and thus not shown.

5.4 Conclusions

We applied our systematic and simulation-free strategy to the recently proposed relative-entropy-based coarse graining,[17,21,22] which minimizes the information loss quantified by the

relative entropy, and becomes equivalent to structure-based coarse graining if the functional form of CG potentials is unconstrained (i.e., contains an infinite number of parameters).[22] It was then used to parameterize CG potentials with a given analytic functional form containing finite number of parameters, and the values of the minimized relative entropy with different CG potential functional forms can further be compared to determine the appropriate functional form or number of parameters. In this work, we first describe our systematic and simulation-free strategy of relative-entropy-based coarse graining for homopolymer melts using the polymer reference interaction site model (PRISM) theory,[19] then present our numerical results with the hard-core Gaussian thread model[23] (referred to as the "CGC-δ" model below) solved by PRISM theory with the Percus-Yevick closure[24] as the original system.

Here we proposed several parameterizations of CG pair potential, the performance of which was compared comparing to the results of st-based coarse graining presented in Chapter 4, and we found that the proposed functional form of CG pair potential $\beta v_{\mathrm{II}}(r)$ is good enough to represent the CG potential in the range of $1 \leq N \leq 100$; this is because it can capture the attractive well at around $\tilde{r} \approx 5$, which, on the other hand, cannot be captured by other parameterizations, i.e., summation of several Gaussians. We also found that $\tilde{v}_{\mathrm{II}}(r)$ for various N collapse approximately onto the same curve, if r is normalized by $R_{e,0}/N^{3/4}$, similar to the results of st-based coarse graining.

By comparing the relative entropy per chain s_c^{st} for st-based coarse graining with various closures for CG systems, we found s_c^{st} decreases with increasing N for all closures, indicating the information loss due to coarse graining decreases with increasing N, which is well expected. We also find that the information loss due to coarse graining quantified by s_c^{st} is qualitatively consistent with the deviation in thermodynamic properties between original and CG systems. The difference in s_c between st- and RE-based coarse graining shows that st-based coarse graining gives less information loss than RE-based coarse graining at the same N, and all three ways parameterizing CG pair potentials work better for smaller N.

The normalized isothermal compressibility κ_T obtained from RE-based coarse graining using $\beta v_{\mathrm{I},1}(r)$ is significantly larger than κ_T^{st}; using $\beta v_{\mathrm{I},2}(r)$ gives closer results to κ_T^{st}, but still overestimate it at small $N \lesssim 10$; $\beta v_{\mathrm{II}}(r)$, however, gives better results than using $\beta v_{\mathrm{I}}(r)$, although κ_T^{st} is somewhat underestimated at small $N \lesssim 10$. $\beta v_{\mathrm{I},2}(r)$ always underestimates the pressure of the original system, P_m, particularly at small $N \lesssim 20$. Note, however, that the results for $27 \leq N \leq 91$ obtained from RE-based coarse graining using $\beta v_{\mathrm{I},2}(r)$ are closer to P_m than the corresponding st-based results. Using $\beta v_{\mathrm{II}}(r)$ in RE-based coarse graining, on the other hand, gives much better results than using $\beta v_{\mathrm{I},2}(r)$ at small N. The behavior of internal energy is similar to pressure and thus not shown.

REFERENCES

[1] R. L. C. Akkermans and W. J. Briels, J. Chem. Phys. **114**, 1020 (2001).

[2] F. Müler-Plathe, Chem. Phys. Chem. **3**, 754 (2002).

[3] H. S. Ashbaugh, H. A. Patel, S. K. Kumar, and S. Garde, J. Chem. Phys. **122**, 104908 (2005).

[4] L.-J. Chen, H.-J. Qian, Z.-Y. Lu, Z.-S. Li, and C.-C. Sun, J. Phys. Chem. B **110**, 24093 (2006).

[5] A. J. Clark and M. G. Guenza, J. Chem. Phys. **132**, 044902 (2010).

[6] J. McCarty, A. J. Clark, I. Y. Lyubimov, and M. G. Guenza, Macromolecules **45**, 8482 (2012).

[7] A. J. Clark, J. McCarty, I. Y. Lyubimov, and M. G. Guenza, Phys. Rev. Lett. **109**, 168301 (2012).

[8] A. J. Clark, J. McCarty, and M. G. Guenza, J. Chem. Phys. **139**, 124906 (2013).

[9] J. McCarty, A. J. Clark, J. Copperman, and M. G. Guenza, J. Chem. Phys. **140**, 204913 (2014).

[10] D. Yang and Q. Wang, J. Chem. Phys. submitted.

[11] A. P. Lyubartsev and A. Laaksonen, Phys. Rev. E **52**, 3730 (1995).

[12] A. K. Soper, Chem. Phys. **202**, 295 (1996).

[13] A. P. Lyubartsev, A. Mirzoev, L. J. Chen, and A. Laaksonen, Faraday Discuss. **144**, 43 (2010).

[14] S. Izvekov and G. A. Voth, J. Phys. Chem. B **109**, 2469 (2005).

[15] S. Izvekov and G. A. Voth, J. Chem. Phys. **123**, 134105 (2005).

[16] W. G. Noid, J. W. Chu, G. S. Ayton, V. Krishna, S. Izvekov, G. A. Voth, A. Das, and H. C. Andersen, J. Chem. Phys. **128**, 244114 (2008).

[17] M. S. Shell, J. Chem. Phys. **129**, 144108 (2008).

[18] D. Chandler and H. C. Andersen, J. Chem. Phys. **57**, 1930 (1972).

[19] K. S. Schweizer and J. G. Curro, Phys. Rev. Lett. **58**, 246 (1987); J. G. Curro and K. S. Schweizer, Macromolecules **20**, 1928 (1987).

[20] E. F. David and K. S. Schweizer, J. Chem. Phys. **100**, 7767 (1994); *ibid.* **100**, 7784 (1994).

[21] A. Chaimovich and M. S. Shell, Phys. Rev. E. **81**, 060104 (2010).

[22] A. Chaimovich and M. S. Shell, J. Chem. Phys. **134**, 094112 (2011).

[23] K. S. Schweizer and J. G. Curro, Chem. Phys. **149**, 105 (1990).

[24] J. K. Percus and G. J. Yevick, Phys. Rev. **110**, 1 (1958).

[25] In our definition of relative entropy, we do not consider the mapping entropy defined in Ref. [17], which does not depend on CG potential.

[26] J. P. Hansen and I. R. McDonald, *Theory of Simple Liquids* (Academic Press, London, 1976).

[27] A. A. Louis, P. G. Bolhuis, and J. P. Hansen, Phys. Rev. E **62**, 7961 (2000).

[28] R. B. Thompson, K. Ø. Rasmussen, and T. Lookman, J. Chem. Phys. **120**, 31 (2004).

[29] M. W. Matsen, Eur. Phys. J. E **30**, 361 (2009).

[30] http://www.fftw.org.

[31] W. H. Press, S. A. Teukolsky, W. T. Vetterling, and B. P. Flannery, *Numerical Recipes in C* (Cambridge University Press, New York, 2nd edn, 1992).

[32] $\Delta f_{c,m}$ is calculated by thermodynamic integration for CGC-δ model solved with PRISM theory and PY closure, i.e., $\beta\Delta f_{c,m} = -(\sqrt{\mathcal{N}}/2)\int_0^\infty \mathrm{d}\bar{\kappa}(C_0/\bar{\kappa})$ with C_0 defined in Chapter 4 remaining finite in the limit of $\bar{\kappa} \to \infty$. On the other hand, the interchain internal energy per chain, $\left\langle H_m^{\mathrm{inter}} \right\rangle_m / n = -C_0\sqrt{\mathcal{N}}/2$, is finite.

CHAPTER 6

CONCLUDING REMARKS AND FUTURE WORK

In this section, all the studies in this dissertation will be summarized briefly, and we then point out one extension that can be possibly made based on the current work.

6.1 Concluding Remarks

Full atomistic simulations of many-chain systems such as polymer melts are not feasible at present, because of their formidable computational requirements, coarse-grained (CG) models with polymer segments interacting with soft potentials thus have to be used instead. As explained in a series of paper of our group,[1–6] simulations with CG models provide a powerful means for unambiguously and quantitatively revealing the effects of fluctuation/correlation (F/C) by comparing simulation results with the corresponding field theories, such as the self-consistent field (SCF) theory and Gaussian fluctuation (GF) theory, based on the same model system. A less intuitive reason for using soft potentials is that one can simulate condensed polymeric systems with experimentally accessible fluctuations (i.e., with $\bar{\mathcal{N}} \gtrsim 10^3$).

In this work we first investigated two CG models, polymer mushrooms in poor solvents on a lattice and disordered symmetric diblock copolymers (DBC) in continuum, to unambiguously quantify F/C effects in CG models by comparing Monte Carlo (MC) simulations with SCF, GF and integral-equation (IE) theories based on the same model systems, where the theories either totally neglect or approximately take into account of F/C effects.

For polymer mushroom systems in poor solvent, phase transitions for both one- and two-mushroom systems are involved. Based on the CG lattice model, we systematically constructed the phase diagrams of them as a function of the average polymer volume fraction,

the Flory-Huggins interaction parameter χ, and grafting distance (for two-mushroom systems) using lattice SCF calculations. While one expects that the simulation results approach the SCF predictions with increasing average segment number density ρ_0, contradiction to this expectation leads us to the discovery of a second-order symmetric-asymmetric transition in polymer mushrooms in a poor solvent (i.e., in the globule state), which, to the best of our knowledge, has not been reported in the literature.

For symmetric DBCs, we only focused on their disordered phase, where F/C effects were unambiguously quantified based on the same model system, by comparing the thermodynamic and structural properties obtained from fast off-lattice MC (FOMC) simulations and various theories, including SCF, GF, and IE theories. We have also analyzed the trends of ordered-disordered transition (ODT) by comparing the rates of how the normalized inverse composition structure factor $S_{\psi}^{-1}(q^*)/S_{\psi}^{-1}(q^*, \chi N = 0)$ approaches 0 obtained from the reference interaction site model with PY closure, which captures some of the qualitative behavior of the ODT determined in our recent FOMC simulations of symmetric DBC.[7]

While CG models with soft potentials has great advantages, there are still some open questions about how to obtain the CG model and how the coarse-graining level affects the properties of CG model. In this work, we therefore proposed the systematic and simulation-free strategy of coarse graining: we use integral equation theories,[8,9] instead of molecular simulations, to obtain the structural and thermodynamic properties of both original and CG systems, by matching their segmental pair correlation functions (structure-based) or minimizing the relative entropy (RE) between two systems.[10,11] We mainly have several remarks about coarse graining of homopolymer melts: (1) CG systems cannot reproduce all aspects of the original systems due to the information loss of coarse graining; (2) the normalized CG potentials as a function of normalized distance $\tilde{r}$ for various N and closures can be collapsed approximately onto the same curve; (3) an analytical functional form for the CG potential was proposed according to the structure-based coarse graining and optimized by RE-based coarse graining, which can capture the attractive well at $\tilde{r} \approx 5$ (see Fig. 5.2).

6.2 Future Work: Coarse-Graining using Self-Consistent Integral Equation Theories

In both structure-based and relative-entropy-based coarse-graining strategies as shown in Chapters 4 and 5, the use of ideal-chain conformations is an assumption based on the fact that the excluded-volume effects are mostly screened by the surrounding identical chains for large $\bar{\mathcal{N}}$ systems. For systems with strong pair interactions or small $\bar{\mathcal{N}}$, however, ideal-chain conformations are not appropriate for both original and CG systems. In such cases, molecular simulations or the self-consistent integral-equation (SCIE) theories should be used to obtain more accurate intrachain pair correlations functions.[12–15] As mentioned earlier, molecular simulations for the original system with long chain length are extremely computational expensive; the strategy of SCIE theories, however, is a good choice with less simulation time but high accuracy.

In SCIE theories, developed by Schweizer and co-workers,[12] the intra- and interchain correlation functions are obtained self-consistently by combining P/RISM equation with single-chain simulation in solvation potential. In this approach, the interchain interactions are accounted by an effective solvation potential acting on a single chain. The widely-used HNC-style solvation potential[16–18] in Fourier space is given by

$$\beta\hat{\mathbf{w}}(q) = -\hat{\mathbf{c}}(q)\hat{\mathbf{S}}(q)\hat{\mathbf{c}}(q) \tag{6.1}$$

where $\hat{\mathbf{S}}(q) = \hat{\boldsymbol{\omega}}(q) + \rho_c\hat{\mathbf{h}}(q)$ is the structure factor matrix. In the SCIE calculation, we initially solve P/RISM equation with a closure (such as PY closure) and ideal-chain conformations, $\hat{\mathbf{c}}(q)$, $\hat{\mathbf{h}}(q)$ and thus $\hat{\mathbf{S}}(q)$ and $\beta\hat{\mathbf{w}}(q)$ are obtained; single-chain simulations are then performed with bonded and nonbonded potentials and $\beta\hat{\mathbf{w}}(q)$ present, which leads to new single-chain structure factor, $\hat{\boldsymbol{\omega}}(q)$. This sequence is repeated until $\beta\hat{\mathbf{w}}(q)$ converges.

In order to reduce calculation time, a reweighting scheme[19,20] is applied to reuse the conformations previously generated. The new $\hat{\boldsymbol{\omega}}(q)$ are calculated from the old one by

$$\hat{\boldsymbol{\omega}}\{\mathbf{w}_{\text{new}}\} = \frac{1}{Z}\sum_{j=1}^{M}\hat{\boldsymbol{\omega}}^{(j)}\{\mathbf{w}_{\text{old}}\}\exp\left[\beta\mathbf{w}_{\text{new}}^{(j)} - \beta\mathbf{w}_{\text{old}}^{(j)}\right] \tag{6.2}$$

where $Z = \sum_{j=1}^{M} \exp\left[\beta \mathbf{w}_{\text{new}}^{(j)} - \beta \mathbf{w}_{\text{old}}^{(j)}\right]$, and M is the number of configurations used in the sample average. If the criterion, $\min\{Z, 1/Z\} < M/4$, is not satisfied, a new set of configurations is generated by single-chain simulation.

Once we obtain the single-chain conformations from SCIE theory, we then calculate the intrachain correlation functions, $\hat{\omega}_{\alpha,\beta}^{mm}(q)$, $\hat{\omega}_{\alpha,\beta}^{sm}(q)$ and $\hat{\omega}_{\alpha,\beta}^{ss}(q)$, which then replace the ideal-chain conformations used in the above coarse-graining procedures. Note that, while we have chosen continuous Gaussian chains with Dirac-δ-function non-bonded interactions as the original system here, which prevent us from using SCIE method, our coarse-graining approach can be readily extended to other (more realistic) models representing chemically specific polymers, such as discrete Gaussian chains, free joined chain, bead-spring model, and etc, for which the single-chain simulation in the solvation potential can be implemented.

REFERENCES

[1] Q. Wang, Soft Matter **5**, 4564 (2009); *ibid.* **5**, 6206 (2010).

[2] P. Zhang, X. Zhang, B. Li, and Q. Wang, Soft Matter **7**, 4461 (2011).

[3] P. Zhang, D. Yang, and Q. Wang, J Phys. Chem. B in press (2014).

[4] P. Zhang, B. Li, and Q. Wang, Macromolecules **44**, 7837 (2011).

[5] P. Zhang, B. Li, and Q. Wang, Macromolecules **45**, 2537 (2012).

[6] P. Zhang and Q. Wang, J. Chem. Phys. **140**, 044904 (2014).

[7] J. Zong and Q. Wang, J. Chem. Phys. **139**, 124907 (2013).

[8] D. Chandler and H. C. Anderson, J. Chem. Phys. **57**, 1930 (1972).

[9] K. S. Schweizer and J. G. Curro, Phys. Rev. Lett. **58**, 246 (1987).

[10] M. S. Shell, *J. Chem. Phys.*, **129**, 144108 (2008).

[11] A. Chaimovich and M. S. Shell, *J. Chem. Phys.*, **134**, 094112 (2011).

[12] K. S. Schweizer, K. G. Honnell, and J. G. Curro, *J. Chem. Phys.*, **96**, 3211 (1992).

[13] A. Yethiraj and K. S. Schweizer, *J. Chem. Phys.*, **97**, 1455 (1992).

[14] J. Melenkevitz, K. S. Schweizer, and J. G. Curro, *Macromolecules*, **26**, 6190 (1993).

[15] D. G. Gromov and J. J. de Pablo, *J. Chem. Phys.*, **103**, 8247 (1995).

[16] D. Chandler, Y. Singh, D. M. Richardson, *J. Chem. Phys.*, **81**, 1975 (1984).

[17] A. L. Nichols, D. Chandler, Y. Singh, D. M. Richardson, *J. Chem. Phys.*, **81**, 5109 (1984).

[18] D. Laria, D. Wu, D. Chandler, *J. Chem. Phys.*, **95**, 4444 (1991).

[19] M. Pütz, J. G. Curro, G. S. Grest, *J. Chem. Phys.*, **114**, 2847 (2001).

[20] R. H. Swendsen, R. H. Ferrenberg, *Phys. Rev. Lett.*, **61**, 2635, (1988).

APPENDIX A

A UNIFIED VIEW ON THE MEAN-FIELD ORDER OF COIL-GLOBULE TRANSITION

It is well known that a polymer chain immersed in a small-molecule solvent undergoes the coil-globule transition (CGT) between the expanded (coil) and collapsed (globule) states as the solvent quality changes, which has been the subject of extensive research.[1,2] In the study of CGT, a mean-field theory, either of the Flory-type[3–12] or the self-consistent field theory,[13,14] has been commonly used; the predicted transition order, however, has been controversial. For example, in Refs. [3–9, 13] it is predicted to be either a first-order phase transition, a critical point, or a crossover depending on the chain stiffness, while in Refs. [10, 11, 14] it is predicted to be a second-order phase transition. Here we therefore clarify the mean-field behavior of CGT and resolve the controversy on its transition order.

A.1 Implicit-Solvent Model

Let us consider the Flory-type Helmholtz free energy f_c of a single chain with N segments,

$$\beta f_c = \frac{3}{2}\alpha^2 - 3\ln\alpha + \frac{1}{2}va^3N\bar{\rho} + \frac{1}{6}wa^6N\bar{\rho}^2, \tag{A.1}$$

which was first used by Ptitsyn and Eizner[3] to investigate CGT, and was further developed in Refs. [4, 5] and by other researchers.[6–13] In Eq. (A.1), $\beta \equiv 1/k_BT$ with k_B being the Boltzmann constant and T the thermodynamic temperature; the first two terms on its right-hand-side represent the elastic free energy of the chain, where $\alpha \equiv \sqrt{R_e^2/R_{e,0}^2}$ is the chain expansion factor with R_e^2 and $R_{e,0}^2 = Na^2$ being the mean-square end-to-end distance of the real chain and that of an ideal chain, respectively, and a is the statistical segment length; and the last two terms represent the polymer-solvent interaction energy, where v and w are

the second and third virial coefficients, respectively, and $\bar{\rho} \equiv N/V_c$ is the average number density of polymer segments within the chain volume $V_c = R_e^3/k$ with k being a numerical constant (e.g., $k = 6/\pi$). With $\bar{\rho}a^3 = kN^{-1/2}\alpha^{-3}$, Eq. (A.1) can be rewritten as

$$\beta f_c = \frac{3}{2}\alpha^2 - 3\ln\alpha + \frac{1}{2}kvN^{1/2}\alpha^{-3} + \frac{1}{6}k^2w\alpha^{-6}. \tag{A.2}$$

Minimizing βf_c with respect to α, with $p \equiv k^2w/3$ and $q \equiv kvN^{1/2}/2$, gives

$$\alpha^5 - \alpha^3 - \frac{p}{\alpha^3} = q. \tag{A.3}$$

Note that Eq. (A.3) exhibits similar behavior to a cubic equation of state (in terms of α^3); that is, for $p > p_c = (9/20)^3/4$ the value of α continuously and monotonically increases with increasing q (or equivalently $vN^{1/2}$), and for $0 < p < p_c$ three different values of α can be found at given $q > q_c = -(4/5)(9/20)^{3/2}$. This behavior of α is regardless of the value of N (including the limit of $N \to \infty$), and has been reported in many studies.[3–9,13] Here we examine the first- and second-order derivatives of βf_c with respect to q, the continuity of which *defines* the transition order of CGT but has not been reported in the literature. Substituting Eq. (A.3) into Eq. (A.2), we obtain the minimized βf_c as

$$\beta f_c = \frac{5}{2}\alpha^2 - 3\ln\alpha - 1 - \frac{1}{2}p\alpha^{-6}. \tag{A.4}$$

At given p, the above gives $\mathrm{d}\beta f_c/\mathrm{d}\alpha = 5\alpha - 3\alpha^{-1} + 3p\alpha^{-7}$ and Eq. (A.3) gives $\mathrm{d}q/\mathrm{d}\alpha = 5\alpha^4 - 3\alpha^2 + 3p\alpha^{-4}$. With $\alpha(p,q)$ given by Eq. (A.3), we then have

$$\frac{\mathrm{d}\beta f_c}{\mathrm{d}q} = \frac{\mathrm{d}\beta f_c}{\mathrm{d}\alpha}\frac{\mathrm{d}\alpha}{\mathrm{d}q} = \frac{1}{\alpha^3(p,q)}, \tag{A.5}$$

$$\frac{\mathrm{d}^2\beta f_c}{\mathrm{d}q^2} = \frac{\mathrm{d}}{\mathrm{d}\alpha}\left(\frac{\mathrm{d}\beta f_c}{\mathrm{d}q}\right)\frac{\mathrm{d}\alpha}{\mathrm{d}q} = -\frac{1}{5\alpha^8(p,q)/3 - \alpha^6(p,q) + p}, \tag{A.6}$$

Fig. A.1 clearly shows that, for $p < p_c$, $\mathrm{d}\beta f_c/\mathrm{d}q$ (and $\mathrm{d}^2\beta f_c/\mathrm{d}q^2$) exhibits a discontinuity (due to the existence of two different α-values) at $q > q_c$, indicating that CGT is a first-order phase transition; at $p = p_c$, $\mathrm{d}\beta f_c/\mathrm{d}q$ is continuous but $\mathrm{d}^2\beta f_c/\mathrm{d}q^2$ diverges at $q = q_c$, indicating a critical point; and for $p > p_c$, both derivatives are continuous, indicating a

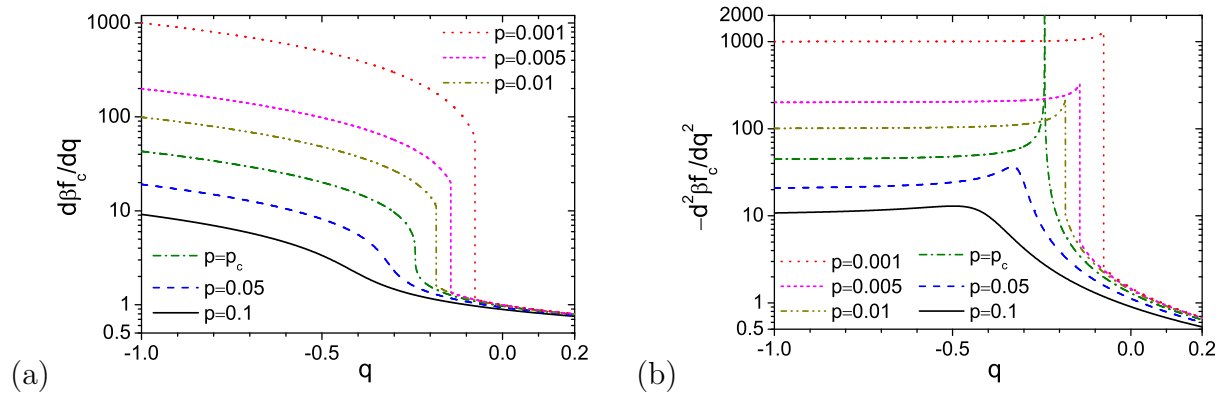

Figure A.1: Semi-logarithmic plots of (a) the first- and (b) the second-order derivatives of βf_c with respect to q at various p, given by Eqs. (A.5) and (A.6), respectively.

"crossover" (termed for our purpose; strictly speaking, one needs to prove that all higher-order derivatives are continuous). This behavior of CGT is referred to as "type-I" hereafter.

A.2 Explicit-Solvent Model

Eq. (A.1) is for an implicit solvent. One can also consider an explicit solvent, where βf_c is given by[3–5,7]

$$\beta f_c = \frac{3}{2}\alpha^2 - 3\ln\alpha + n_{\rm S}\ln(1-\phi_{\rm P}) + \chi n_{\rm S}\phi_{\rm P}. \tag{A.7}$$

Here $\phi_{\rm P} \equiv v_{\rm P}\bar{\rho}$ and $n_{\rm S} \equiv (1-\phi_{\rm P})V_c/v_{\rm S}$ are the average polymer volume fraction and the number of solvent molecules within the volume V_c, respectively, with $v_{\rm P}$ and $v_{\rm S}$ being the volume of each polymer segment and solvent molecule, respectively, and χ is the Flory-Huggins interaction parameter between a polymer segment and a solvent molecule. Defining $r_f \equiv v_{\rm P}/a^3$, which measures the chain stiffness, and $r_s \equiv v_{\rm P}/v_{\rm S}$, which measures the size ratio between a polymer segment and a solvent molecule, and Taylor-expanding $\ln(1-\phi_{\rm P})$ to the third order in $\phi_{\rm P}$, we have

$$\beta f_c \approx \frac{3}{2}\alpha^2 - 3\ln\alpha + \frac{1}{2}kr_s r_f(1-2\chi)N^{1/2}\alpha^{-3} + \frac{1}{6}k^2 r_s r_f^2 \alpha^{-6}, \tag{A.8}$$

where an unimportant constant is omitted. Comparing Eq. (A.8) to Eq. (A.1), we find $v = (1-2\chi)r_s r_f$ and $w = r_s r_f^2$.

While the above expansion of $\ln(1-\phi_{\rm P})$ is only valid for $\phi_{\rm P} \ll 1$ (i.e., large N in the coil and θ-states) with higher-order terms needed when $\phi_{\rm P} \sim O(1)$, it does not qualitatively change the type-I behavior of CGT, but only changes the exact location of the critical point.[3,4,10] Similarly, using either a more accurate expression of the elastic free energy,[8,9,12] a Gaussian (instead of uniform) distribution of polymer segments in V_c,[5,7] or the expansion factor based on the chain radius of gyration,[5,8,9,12] as well as varying r_s[5] or r_f,[3–5,7,13] do not qualitatively change the type-I behavior of CGT.

On the other hand, in the limit of $N \to \infty$, Moore,[14] Sanchez[10] and Di Marzio[11] concluded that CGT is a second-order phase transition with respect to T (or equivalently v or χ). In particular, Sanchez[10] pointed out that, since α of the coil state diverges in the limit of $N \to \infty$, it is better to use $\phi_{\rm P}$, which is bounded for all N, as an order parameter for CGT. Replacing α^3 by $\phi_0/\phi_{\rm P}$, where ϕ_0 is the corresponding value of $\phi_{\rm P}$ in the θ-solvent (i.e., where $\alpha = 1$), we obtain from Eq. (A.7)

$$\beta f_c = \frac{3}{2}\left(\frac{\phi_0}{\phi_{\rm P}}\right)^{2/3} - \ln\frac{\phi_0}{\phi_{\rm P}} + N_e\frac{1-\phi_{\rm P}}{\phi_{\rm P}}\ln(1-\phi_{\rm P}) - N_e\chi\phi_{\rm P}, \tag{A.9}$$

where $N_e \equiv r_s N$ is the effective chain length taking into account the size ratio between a polymer segment and a solvent molecule, and an unimportant constant is omitted. Note that, with $r_s = 1/2$ and $\chi = \theta/2T$, where θ denotes the θ-temperature, Eq. (A.9) reduces to the free-energy expression used by Sanchez (i.e., Eq. (25b) in Ref. [10]), with the only difference being that the coefficient 3/2 in our Eq. (A.9) is replaced by 7/2, which does not qualitatively change the phase behavior of CGT. At given χ, minimizing βf_c with respect to $\phi_{\rm P}$ gives

$$\frac{1}{N_e} - 1 - \frac{1}{N_e}\left(\frac{\phi_0}{\phi_{\rm P}}\right)^{2/3} - \frac{\ln(1-\phi_{\rm P})}{\phi_{\rm P}} = \chi\phi_{\rm P} \tag{A.10}$$

and the minimized free energy

$$\beta f_c = \frac{5}{2}\left(\frac{\phi_0}{\phi_{\rm P}}\right)^{2/3} - \ln\frac{\phi_0}{\phi_{\rm P}} + N_e\frac{2-\phi_{\rm P}}{\phi_{\rm P}}\ln(1-\phi_{\rm P}) + N_e - 1. \tag{A.11}$$

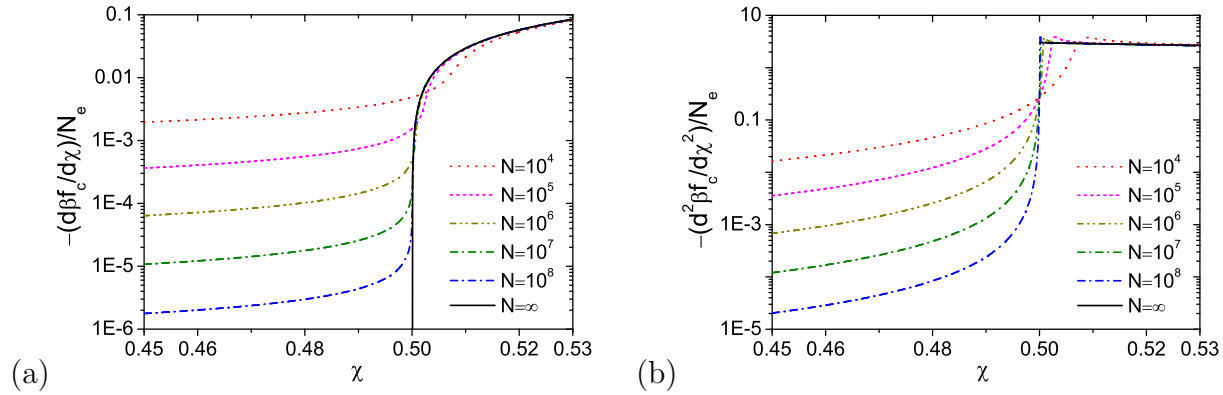

Figure A.2: Semi-logarithmic plots of (a) the first- and (b) the second-order derivatives of βf_c with respect to χ at various N, given by Eqs. (A.12) and (A.13), respectively. Note that in the limit of $N \to \infty$ both the derivatives divided by N_e are 0 for $\chi < 1/2$, and that $p = 0.1$ and $r_s = 1$ are used here.

The first- and second-order derivatives of βf_c with respect to χ are then obtained as

$$\frac{\mathrm{d}\beta f_c}{\mathrm{d}\chi} = \frac{\mathrm{d}\beta f_c}{\mathrm{d}\phi_\mathrm{P}} \frac{\mathrm{d}\phi_\mathrm{P}}{\mathrm{d}\chi} = -N_e \phi_\mathrm{P}(\chi, \phi_0, N_e) \tag{A.12}$$

$$\frac{\mathrm{d}^2\beta f_c}{\mathrm{d}\chi^2} = \frac{\mathrm{d}}{\mathrm{d}\phi_\mathrm{P}} \left(\frac{\mathrm{d}\beta f_c}{\mathrm{d}\chi} \right) \frac{\mathrm{d}\phi_\mathrm{P}}{\mathrm{d}\chi} = \frac{-3N_e\phi_\mathrm{P}^2}{2/N_e - 2 - 5\chi\phi_\mathrm{P} + \ln(1-\phi_\mathrm{P})/\phi_\mathrm{P} + 3/(1-\phi_\mathrm{P})} \tag{A.13}$$

with $\phi_\mathrm{P}(\chi, \phi_0, N_e)$ given by Eq. (A.10).

Fig. A.2 shows $\mathrm{d}\beta f_c/\mathrm{d}\chi$ and $\mathrm{d}^2\beta f_c/\mathrm{d}\chi^2$ for various N at $p = \phi_0^2 N_e/3 = 0.1 > p_c$ (thus in the crossover region predicted by Eq. (A.2)), where $r_s = 1$ is used. We find that $\mathrm{d}\beta f_c/\mathrm{d}\chi$ is continuous for all N, and that $\mathrm{d}^2\beta f_c/\mathrm{d}\chi^2$ is continuous for all finite N but exhibits a discontinuity at $\chi = 1/2$ in the limit of $N \to \infty$. In this limit (denoted by the superscript "∞" hereafter), we note that $\phi_\mathrm{P} \to 0$ in both the coil and θ-states, and that ϕ_P is independent of N in the globule state but is small just below the θ-temperature. Taylor-expanding $\ln(1-\phi_\mathrm{P})$ in Eq. (A.10) to the fourth order in ϕ_P, which is valid near the θ-temperature, then gives $\chi \approx -(1/N_e\phi_\mathrm{P})(\phi_0/\phi_\mathrm{P})^{2/3} + 1/2 + \phi_\mathrm{P}/3 + \phi_\mathrm{P}^2/4$. Since $(1/N_e\phi_\mathrm{P})(\phi_0/\phi_\mathrm{P})^{2/3} = (kr_f/r_s)\phi_\mathrm{P}^{-5/3}N^{-4/3} \to 0$ in the globule (G) state, we obtain $\phi_{\mathrm{P,G}}^\infty = (2/3)\left(\sqrt{9\chi - 7/2} - 1\right)$ just below the θ-temperature, and can write $\phi_\mathrm{P}^\infty = \phi_{\mathrm{P,G}}^\infty H(\chi - 1/2)$ with $H(x)$ denoting the Heaviside step-function. Finally, Eqs. (A.12) and (A.13) give, respectively, $-(\mathrm{d}\beta f_c/\mathrm{d}\chi)^\infty/N_e = \phi_\mathrm{P}^\infty$, which is continuous at $\chi = 1/2$, and

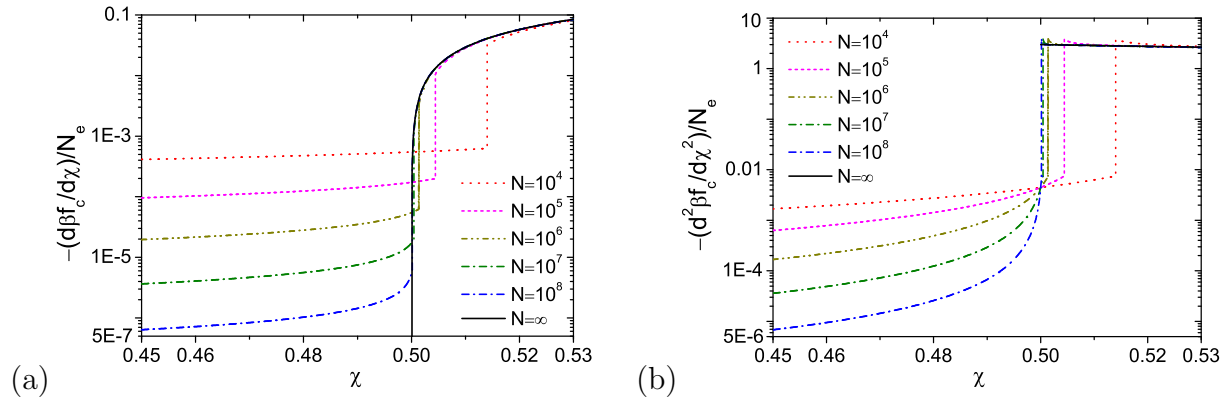

Figure A.3: Same as Fig. A.2 but with $p = 0.001$.

$-(\mathrm{d}^2\beta f_c/\mathrm{d}\chi^2)^\infty/N_e = 3(9\chi - 7/2)^{-1/2}H(\chi - 1/2)$, which is discontinuous at $\chi = 1/2$. Our analysis here is supported by the fact that the numerical results of $\mathrm{d}\beta f_c/\mathrm{d}\chi$ and $\mathrm{d}^2\beta f_c/\mathrm{d}\chi^2$ approach these limiting values with increasing N as shown in both Figs. A.2 and A.3. For the case shown in Fig. A.2, CGT is therefore a crossover for finite N but becomes a second-order phase transition with respect to χ only in the limit of $N \to \infty$.

Fig. A.3 shows $\mathrm{d}\beta f_c/\mathrm{d}\chi$ and $\mathrm{d}^2\beta f_c/\mathrm{d}\chi^2$ for various N at $p = 0.001 < p_c$ (thus in the first-order transition region predicted by Eq. (A.2)), where $r_s = 1$ is used. We see that $\mathrm{d}\beta f_c/\mathrm{d}\chi$ exhibits a discontinuity for all finite N but becomes continuous in the limit of $N \to \infty$, and that $\mathrm{d}^2\beta f_c/\mathrm{d}\chi^2$ is discontinuous for all N.

We therefore conclude that CGT has the type-I behavior for finite N, and becomes a second-order phase transition with respect to χ only as $N \to \infty$. Even in this limit, CGT still has the type-I behavior with respect to $vN^{1/2}$ (or equivalently $(1 - 2\chi)N^{1/2}$).

REFERENCES

[1] C. Williams, F. Brochard, and H. L. Frisch, Ann. Rev. Phys. Chem. **32**, 433 (1981).

[2] B. M. Baysal and F. E. Karasz, Macromol. Theory Simul. **12**, 627 (2003).

[3] O. B. Ptitsyn and Yu. Ye. Eizner, Biofizika **10**, 3 (1965).

[4] O. B. Ptitsyn, A. K. Kron, and Yu. Ye. Eizner, J. Polym. Sci.: Part C **16**, 3509 (1968).

[5] Yu. Ye. Eizner, Polym. Sci. USSR. **11**, 409 (1969).

[6] P. G. de Gennes, J. Phys. (Paris) **36**, L-55 (1975).

[7] C. B. Post and B. H. Zimm, Biopolym. **18**, 1487 (1979).

[8] T. M. Birshtein and V. A. Pryamitsyn, Macromolecules **24**, 1554 (1991).

[9] A. Y. Grosberg and D. V. Kuznetsov, Macromolecules **25**, 1970 (1992).

[10] I. C. Sanchez, Macromolecules **12**, 980 (1979).

[11] E. A. Di Marzio, Macromolecules **17**, 969 (1984).

[12] S. L. Shmakov, Polym. Sci. Ser. B **44**, 310 (2002).

[13] M. Muthukumar, J. Chem. Phys. **81**, 6272 (1984).

[14] M. A. Moore, J. Phys. A: Math. Gen. **10**, 305 (1977).